

TESIS DOCTORAL

ESTUDIO DE LA FIBROSIS PATOLÓGICA MIOCÁRDICA  
MEDIANTE NANOMATERIALES DIRIGIDOS POR PROTEÍNAS  
COMO HERRAMIENTA TERAGNOSTICA Y SISTEMA DE  
EXPRESIÓN GÉNICA DIRIGIDA

PHP TESIS

STUDY OF MYOCARDIAL PATHOLOGICAL FIBROSIS  
USING PROTEIN-PROTEIN-DIRECTED  
NANOMATERIALS AS THERACNOSTIC TOOL AND  
TARGETED GENE EXPRESSIN SYSTEM

AUTOR

DAVID MAESTRO LAVÍN

DIRECTOR/ES

ANA VICTORIA VILLAR

UNIVERSIDAD DE CANTABRIA

Escuela de **Doctorado** de la Universidad de Cantabria

Santander 2022





# Table of Contents

<b>1. INTRODUCTION</b> .....	10
1.1 THE HEART :.....	10
1.1.1 Function and Structure.....	10
1.1.2 Cellular composition.....	12
1.1.2.1 Characteristics of the Myocardial main cell types:.....	13
1.1.3 Extracellular matrix in cardiovascular physiology.....	14
1.1.3.1 Structure and composition.....	14
1.2 CARDIOVASCULAR DISEASES.....	16
1.2.1 Adaptive response.....	17
1.2.1.1 Remodelling of the myocardium.....	17
1.2.1.2 Cardiac fibrosis process and evolution.....	20
1.2.2 Fibroblast, the remodelling agent.....	22
1.2.2.1 Origin of cardiac fibroblasts in the disease heart.....	22
1.2.3 TGF $\beta$ signalling pathways in cardiac Fibroblast activation and regulation during fibrosis.....	23
1.2.3.1 TGF- $\beta$ signaling.....	23
1.2.3.2 TGF $\beta$ Production and Activation.....	23
1.2.3.3 TGF $\beta$ canonical signaling pathway (Smad-based).....	24
1.2.3.4 TGF $\beta$ non-canonical signaling pathway (non-Smad-based).....	25
1.2.3.5 The role of Hsp90 and other partners in TGF $\beta$ signaling cascade.....	26
<b>2. AIMS OF THE STUDY</b> .....	32
2.1 SPECIFIC OBJECTIVES:.....	33
<b>3. MATERIAL AND METHODS</b> .....	36
3.1 MATERIAL.....	36
3.1.1 Animals.....	36
3.1.2 Primary cells.....	36
3.1.3 Cellular Lines.....	37
3.1.4 Solutions and reagents used in the experiments.....	37
3.1.4.1 Cell culture médium.....	37
3.1.4.2 Cell culture reagents.....	37
3.1.4.2 Protein purification/extraction and Western Blot.....	38
3.1.4.3 Hsp90 refolding assay.....	39
3.1.4.4 RNA extraction and purification.....	39
3.1.4.5 RT and qPCR.....	39
3.1.4.6 PCR and agarose gels.....	39
3.1.4.7 Immunofluorescence and live cell microscopy reagents.....	40
3.1.4.8 Masson trichrome and Picrosirius red staining reagents.....	40
3.1.4.9 Laboratory solutions and buffers.....	41
3.1.4.10 SEM and TEM electron microscopy.....	41
3.1.4.11 Designed oligonucleotides.....	41
3.1.4.12 Inhibitors.....	42
3.1.4.13 Competent bacteria.....	43
3.1.4.14 Plasmid library.....	43
3.1.4.15 Heat shock competent cells.....	44
3.1.4.16 Bacterial culture and Transformation.....	44
3.1.4.17 Antibodies.....	44
3.1.4.18 Restriction enzymes.....	45
3.1.4.18 Kits used for extraction and purification.....	45
3.1.5 Laboratory equipment.....	45
3.1.5.1 Animal handling equipment.....	45
3.1.5.2 Fungible Material.....	46
3.1.5.3 Equipment used.....	47
3.1.5.4 Software.....	47
3.2 METHODS.....	47
3.2.1 Cell Culture, cellular insulation, and maintenance.....	47



3.2.1.1 Standard procedures for all working cell types .....	47
3.2.1.2 Cell Freezing .....	50
3.2.1.3 Thawing of cells .....	50
3.2.2 TGF- $\beta$ stimulation assay and treatments (CTPR-17AAG) .....	50
The inhibitors were added 1 hour after the addition of TGF $\beta$ , and then the cultures were incubated for 10 hours at 37°C. To reduce interference due to external factors, Opti-MEM culture medium supplemented with 5% serum FBS and 1% antibiotic was used. ....	51
3.2.3 Cell lysis obtaining total protein extracts-WB analysis .....	51
3.2.3.1 WB assays .....	52
3.2.4 Total RNA isolation and purification .....	53
3.2.5 Retrotranscription .....	54
3.2.6 Gene expression analysis by qPCR .....	54
3.2.7 Refolding assay in the presence of CTPR-17AAG-EGCG .....	54
3.2.8 Microscopy techniques .....	55
3.2.8.1 Immunofluorescence assay, confocal microscopy .....	55
3.2.8.2 Internalisation , Microscopic observations .....	56
3.2.9 Three-dimensional cardiac fibroblast culture construction and experiments .....	56
3.2.9.1 Flexible ring-shaped model .....	57
3.2.9.2 3D cell culture model generation .....	57
3.2.9.3 Organoid rheological analysis .....	58
3.2.10 Genetic Alert System (GAS) Plasmid Construction .....	60
3.2.10.1 Cloning procedures .....	60
3.2.10.2 Isothermal assembly .....	60
3.2.11 Analysis of MMP2 functionality and localisation by zymography assay .....	61
3.2.11 Animal handling procedures and protocols .....	62
3.2.11.1 Extraction of cardiac tissue for primary cell isolation .....	62
3.2.11.2 Mini-osmotic pump implantation surgery .....	62
3.2.11.3 Compound administration .....	63
<b>4. RESULTS</b> .....	<b>65</b>
4.1 DETECTION OF CTPR AND ITS INTERFERING WITH THE KEY SIGNALLING PATHWAY OF CARDIAC FIBROSIS IN VITRO AND IN VIVO .....	65
The results presented in this section will focus on the in vitro and in vivo evaluation of the behaviour of CTPR390-488 on reducing cardiac fibrosis. ....	65
4.1.1 Cellular location of CTPR390-488 in cell culture primary cardiac fibroblasts and observation of fibroblasts ultrastructural changes .....	65
4.1.1.1 CTPR390 detection in fibroblasts .....	65
4.1.1.2 Cell viability in the presence of CTPR390 .....	67
4.1.1.3 CTPR induces fibroblasts ultrastructural changes .....	70
4.1.1.4 Description of the CTPR390-Hsp90-TGF $\beta$ RI interaction and its consequences in terms of the TGF $\beta$ profibrotic signaling cascade .....	79
4.1.1.5 Mechanism of action of CTPR390 altering TGF $\beta$ dependent profibrotic signaling .....	82
4.1.2 In vivo antifibrotic effect of CTPR in cardiac remodelling. Evaluation of CTPR as a biomarker (theragnostic molecule) and its biodistribution. ....	85
4.1.2.1 CTPR390 counteracts hypertrophic remodelling in the heart of hypertensive mice .....	86
4.1.2.2 CTPR390 counteracts fibrotic remodelling in the heart of hypertensive mice .....	88
4.1.2.3 Detection of the differences in CTPR390 accumulation between the fibrotic and the CTPR390-treated hearts by SXRF microscopy .....	90
4.1.2.4 CTPR390 theragnostic capacity .....	93
4.1.2.5 CTPR390 biodistribution .....	95
4.1.3 Antifibrotic effect and changes in the biomechanical parameters of a human cardiac 3-dimensional model treated with CTPR .....	96
4.1.3.1 CTPR390 mechanical behavior and antifibrotic effect on human engineered organoids ...	97
4.1.3.2 CTPR390 distribution and gene regulation in cardiac organoids .....	99
4.2 GENETIC ALERT SYSTEM (GAS), CONSTRUCTION AND THE EVALUATION OF ITS ACTIVITY .....	103
4.2.1 Construction and development of POSTN variant promoters for GAS. ....	103
4.2.2 Evaluation of the activity of the constructs GAS AV and GAS iii .....	105
<b>5. DISCUSSION</b> .....	<b>108</b>

4.1 CTPR390 IS LOCALIZED INTRA AND EXTRACELLULARLY WITHOUT AFFECTING THE FIBROBLASTS HOMEOSTASIS .....	109
4.1.1 The intravesicle ultrastructural location of CTPR390 activates cell trafficking.....	110
4.1.2 Ultrastructural and cell signalling effects of CTPR390 .....	110
4.1.3 Action model of the CTPR390-Hsp90 and Hsp90-TGF $\beta$ RI physical interactions....	112
4.2 IN VIVO THERAGNOSTIC CAPABILITIES OF CTPR390 .....	113
4.2.1 CTPR interferes with cardiac remodelling in vivo.....	113
4.2.2 CTPR testing, potential theranostic capacity through Hsp90 inhibition and fluorescence capacity .....	114
4.2.3 CTPR390 acummulation in the cardiovascular system of fibrotic mice .....	116
4.3 PRESERVATION OF HEALTHY MECHANICAL BEHAVIOUR IN A FIBROTIC 3D HUMAN CARDIAC ORGANOID IN THE PRESENCE OF CTPR390 .....	117
4.3.1 Restoration of basal mechanical capabilities through the action of CTPR390 .....	118
4.3.2 3D human culture model, under the action of the CTPR .....	120
4.4 FIRST STEPS IN THE CONSTRUCTION AND ASSESSMENT OF THE FUNCTIONING OF THE GENETIC ALERT SYSTEM.....	120
<b>5. CONCLUSIONS .....</b>	<b>124</b>
<b>7. SUMMARY IN SPANISH .....</b>	<b>127</b>
7.1 INTRODUCCIÓN .....	127
7.2 OBJETIVOS .....	130
7.3 RESULTADOS.....	131
7.3.1 Detección de CTPR y su interferencia en la vía de señalización clave de la fibrosis cardíaca in vitro e in vivo .....	131
7.3.1.1 Localización celular de CTPR390-488 en fibroblastos cardíacos primarios de cultivo celular y observación de los cambios ultraestructurales de los fibroblastos .....	131
7.3.2 Efecto antifibrótico in vivo del CTPR en el remodelado cardíaco. Evaluación del CTPR como biomarcador (molécula de diagnóstico).....	134
7.3.2.1 CTPR390 counteracts cardiac remodelling in hypertensive mice .....	135
7.3.2.2 Detección de CTPR390 entre los corazones fibróticos y los tratados con CTPR390 mediante microscopía SXRF capacidad de teragnóstica.....	137
7.3.3 Efecto antifibrótico y cambios en los parámetros biomecánicos de un modelo cardíaco humano tridimensional tratado con CTPR .....	138
7.3.3.1 Comportamiento mecánico de CTPR390 y efecto antifibrótico en organoides de ingeniería humana.....	138
7.3.3.2 Distribución y regulación génica de CTPR390 en organoides cardíacos.....	139
7.3.4 Sistema de Alerta Genética (siglas en ingles "GAS"), construcción y evaluación de su actividad .....	140
7.3.4.1 Construcción y desarrollo de promotores de variantes de POSTN para GAS .....	140
7.3.4.2 Evaluation of the activity of the constructs GAS AV and GASiii .....	141
7.4 DISCUSION .....	142
7.5 CONCLUSIONES .....	150
<b>8. PUBLICATIONS .....</b>	<b>154</b>
<b>REFERENCES .....</b>	<b>156</b>

<b>Figure 1 Structural illustration of the heart.....</b>	<b>10</b>
<b>Figure 2 Heart wall structure.....</b>	<b>12</b>
<b>Figure 3 adaptive response in cardiac tissue in response to stimuli of different nature. ....</b>	<b>19</b>
<b>Figure 4 Summary of Left Ventricular Remodeling and Decompensation in Patients With Aortic Stenosis.....</b>	<b>21</b>
<b>Figure 5 Schematic representation of the TGF<math>\beta</math> canonical pathway. ....</b>	<b>25</b>
<b>Figure 6 Stress curve obtained after rheological measurements. ....</b>	<b>60</b>
<b>Figure 7 CTPR detection in fibroblast. ....</b>	<b>67</b>
<b>Figure 8 Analysis of fibroblasts viability through 24 hours cell proliferation assays under conditions of Hsp90 inhibition.....</b>	<b>68</b>
<b>Figure 9 Luminescent analysis of Hsp90 refolding activity in the present of Hsp90 inhibitors. ....</b>	<b>69</b>
<b>Figure 10 Electron microscopy assays to detect fibroblasts ultrastructural changes of CTPR390-treated cells and CTPR390 localization.....</b>	<b>71</b>
<b>Figure 11 Correlation of a CTPR390-488-Au treated NIH-3T3 cell using cryo-3D-SIM Correlation obtained in NIH/3T3 using cryo-3D-SIM and cryo-SXT.....</b>	<b>73</b>
<b>Figure 12 Colocalisation study of CTPR390-488-Au in the presence of vesicle markers in NIH/3T3 fibroblasts.. ....</b>	<b>74</b>
<b>Figure 13 Comparison of MVB median volumes (Med V) of both NIH-3T3 and primary fibroblast cells measured after segmentation using Amira software. ....</b>	<b>75</b>
<b>Figure 14 Comparison of mitochondrial sphericity and volumes of both NIH/3T3 and primary fibroblast using Amira.....</b>	<b>78</b>
<b>Figure 15 Effects of CTPR390 on protein levels of proteins linked to TGF<math>\beta</math> activation.....</b>	<b>80</b>
<b>Figure 16 Effects of CTPR390 on SMAD2 levels.....</b>	<b>81</b>
<b>Figure 17 Analysis of the inhibitory capacity of CTPR390 in COL1 gene, at protein and genetic level.....</b>	<b>82</b>
<b>Figure 18 In-silico simulation of CTPR390-Hsp90-TGF<math>\beta</math>RI interaction. ....</b>	<b>83</b>
<b>Figure 19 Confocal microscopy images showing direct protein–protein interaction of Hsp90 and TGF<math>\beta</math>RI in NIH/3T3 and primary fibroblast detected by Proximity Ligation Assay (PLA).....</b>	<b>84</b>
<b>Figure 20 Analysis of CTPR390 effect on Hsp90. ....</b>	<b>85</b>

<b>Figure 21 Assessment of hypertrophic remodelling in an in vivo hypertensive mouse model.....</b>	<b>87</b>
<b>Figure 22 Analysis of fibrotic remodelling.....</b>	<b>89</b>
<b>Figure 23 Quantification of the gene and protein expression of fibrotic markers (A-D).....</b>	<b>90</b>
<b>Figure 24 Localisation and quantification of CTPR390-Au by soft X-ray fluorescence microscopy (SXRF).....</b>	<b>91</b>
<b>Figure 25 Quantification of CTPR390-Au in the heart of mice and its correlation analysis with the percentage of fibrosis.....</b>	<b>92</b>
<b>Figure 26 Analysis of the theranostic by Masson's trichrome and confocal microscopy .....</b>	<b>93</b>
<b>Figure 27 Analysis of the theranostic capability of CTPR390Au based on a new detection of fibrosis using XRF.....</b>	<b>94</b>
<b>Figure 28 ICP-MS analysis of various tissues from the CTPR390-Au hypertensive and healthy models.....</b>	<b>96</b>
<b>Figure 29 Mechanical analysis of TGF<math>\beta</math>-activated 3D cardiac organoids treated with CTPRs.....</b>	<b>98</b>
<b>Figure 30 Analysis of the human cardiac organoids hECT mechanical capabilities .....</b>	<b>99</b>
<b>Figure 31 CTPR390 visualization in human 3D organoids.....</b>	<b>100</b>
<b>Figure 32 Multiphoton imaging in organoids.....</b>	<b>100</b>
<b>Figure 33 CTPR390 accumulation in human cardiac fibroblasts of 3D organoids.....</b>	<b>101</b>
<b>Figure 34 Gene expression analysis of the fibrotic markers.....</b>	<b>102</b>
<b>Figure 35 Periostin promoter and variants, enhancer and repressor sequences.....</b>	<b>104</b>
<b>Figure 36 Amplification of GAS system elements.....</b>	<b>105</b>
<b>Figure 37 proMMP2 activity in GAS systems.....</b>	<b>106</b>



TABLE 1 PRIMARY CELL LINES. ....	36
TABLE 2 IMMORTALISED CELL LINES .....	37
TABLE 3 PRIMARY ANTIBODIES.....	44
TABLE 4 SECONDARY ANTIBODIES. ....	45
TABLE 5 CTPR390-488 INTERNALISATION RATES MEASURED BY ABSORBANCE AND AUTOFLUORESCENCE, 24 HOURS AFTER ITS ADMINISTRATION. ....	66
TABLE 6 IN WHICH AVG # REPRESENTS THE AVERAGE NUMBER OF SEGMENTED MVBS IN A TOMOGRAM, AVG V STANDS FOR AVERAGE VOLUME. ....	76
TABLE 7 IN WHICH AVG # REPRESENTS THE AVERAGE NUMBER OF SEGMENTED MITOCHONDRIAIN A TOMOGRAM, AVG V STANDS FOR AVERAGE VOLUME. ....	76



# 1. INTRODUCTION

## 1.1 The Heart :

### 1.1.1 Function and Structure

It could be defined as the muscular organ with the function of providing a constant flow of blood to the rest of the organs. Is structured in 4 chambers, 2 upper (atria) and 2 lower (ventricles) (¡Error! No se encuentra el origen de la referencia.), being the movements of relaxation (diastole) and contraction (systole) the ones that would promote the filling and emptying of the different chambers in a coordinated way and thus generate the flow of blood through the body. The passage of blood between the different chambers would be limited by the opening and closing processes of the valve system, which would guarantee the flow of blood in the same direction, preventing backward movement. Within this system are the atrioventricular and arterial valves. The first control the flow of blood from the atria to the ventricles, being constituted by the tricuspid valve (right atrium-right ventricle) and the mitral valve (left atrium-left ventricle). The arterial valves control the flow from the ventricles to the vascular system, consisting of the pulmonary (right ventricle-pulmonary artery) and aortic (left ventricle-aortic artery) valves (¡Error! No se encuentra el origen de la referencia.).

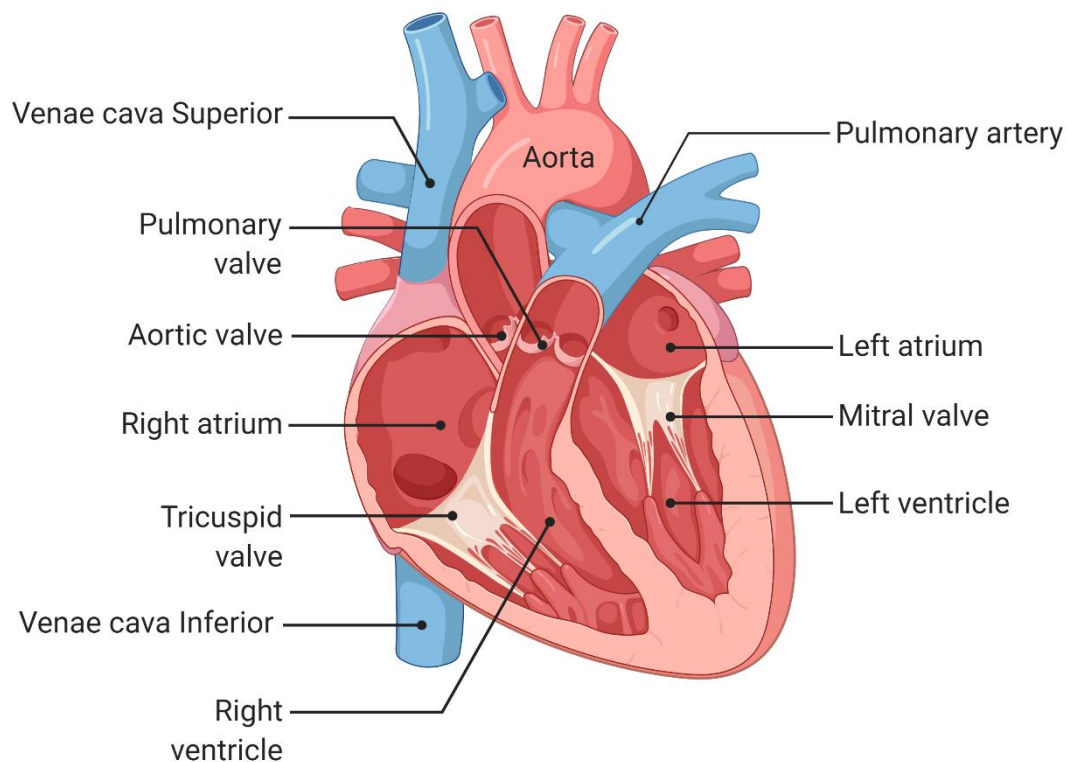


Figure 1 Structural illustration of the heart. Created with BioRender.com



Regarding the structure of the cardiac tissue, the wall of the heart is composed of three distinct layers. Looking at it from the outside in, the outermost part is the epicardium **Figure 2**, a layer of mesothelium that lines the outermost cell layer of the heart in vertebrates and plays an important role during the development and growth of cardiac mesenchyme, being a major source of multipotent cells and molecules produced in its cells. Recent studies in other organisms define it as a player during tissue repair. Its composition is reduced to a single layer of mesothelial cells, flattened in shape [1, 2]. As the intermediate and largest layer, we have the myocardium **Figure 2**, which originated from areas of mesoderm, and whose growth and development during our growth involves both the original myocytes and their expansion (originating from the mesoderm), and cardiomyocytes from neighbouring extra- and intracardiac tissues, whose migration into the tissue occurs during its expansion. As already mentioned, the main cellular component of this layer would be the cardiomyocyte [3]. Finally, in the innermost part and covering the heart chambers, there is the endocardium **Figure 2**, formed by endothelial cells and separated from the myocardium by a layer made up of the extracellular matrix. This layer of cells would be a continuation of the endothelium of the blood vessels, appearing at an early stage of development [4].

It should be mentioned that the epicardium can also be encompassed within another structure, called the pericardium, membrane, or sac, which surrounds the heart and which, as shown in **Figure 2**, would consist of an outer layer called the fibrous pericardium and an inner structure called the serous pericardium. In the latter part we would find an inner layer that would form the epicardium (visceral layer) and the so-called parietal layer[5].

## The heart wall

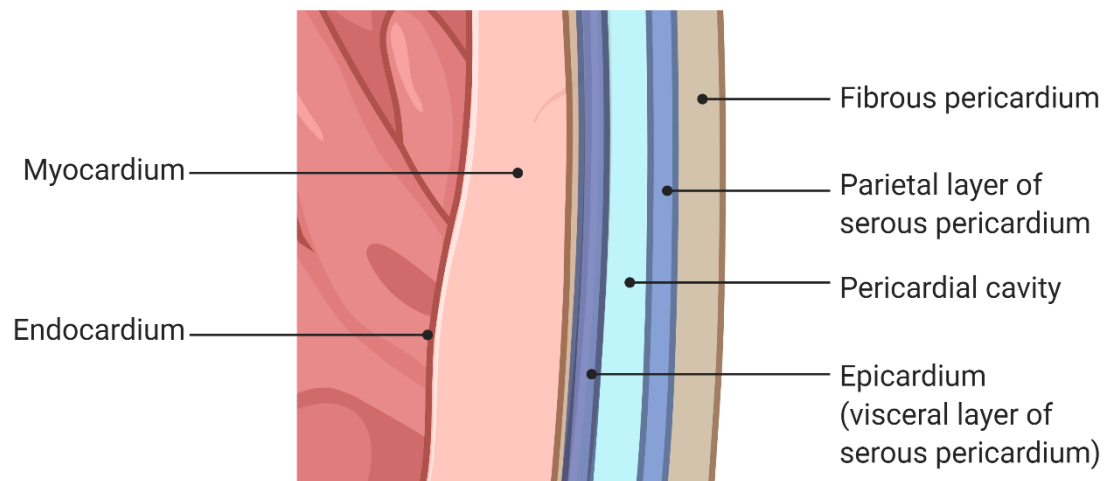


**Figure 2 Heart wall structure.** Created with BioRender.com

In addition to the structure described above, it is worth mentioning the ducts through which the blood will reach and leave the heart, being the venae cava and the pulmonary vein, which bring the blood to the heart, to the right and left atrium, respectively (¡Error! No se encuentra el origen de la referencia.) and on the other side would be the pulmonary artery and the aorta, which carry the outgoing blood from the right and left ventricles, respectively (¡Error! No se encuentra el origen de la referencia.). The last mentioned are extremely important because, these are the areas affected during hypertensive phenomena related to be addressed later cardiovascular diseases. It is these pathological situations that are the focus of this study [6].

The aorta and pulmonary arteries are blood vessels designed to handle the pulsatile flow of blood generated by the heart and transform it into a continuous flow. These vessels can withstand the stress produced by the cardiac Systole/Diastole cycles that generate the blood flow, thanks mainly to the elastin fibers present in their structure. Over time, the elastin fibers naturally wear down and become brittle, causing a loss of elasticity and a transfer of tension to the collagen fibers in the arterial wall [7-9].

### 1.1.2 Cellular composition

The cell populations located in cardiac tissue are diverse. However, some of them have been shown to constitute the basic or most abundant components in each of the tissue layers that make up the heart. Three cell populations have been identified as the majority

populations, either because of the total number of cells in the organ they represent or because of the volume of the organ they constitute, these cell groups are cardiomyocytes, fibroblasts and endothelial cells.

Regarding cardiomyocytes, in different studies it has been possible to observe the large volume of the organ that corresponds to this cell type reaching values close to 75%, this is understandable if we take into account that the myocardium, of which they are the main cellular component, represents practically the totality of the organ. However through studies on the cell populations present in the organ, it has been possible to observe populations of non-myocytic cells, such as endothelial cells, fibroblasts, vascular smooth muscle cells and hematopoietic-derived cells, which would make up about 70% of the total cellular content of the heart [10-12].

Overall, although the percentages may vary depending on the cell population studies used, a consensus has been reached that cardiomyocytes, fibroblasts and endothelial cells represent more than 2/3 of the total cells of the heart, all of which play important structural and functional roles [12].

#### **1.1.2.1 Characteristics of the Myocardial main cell types:**

**-Cardiomyocytes:** Specialised cell population, to take care of the rhythmic and coordinated contraction of the cardiac organ, its rate of renewal varies throughout life, maintaining a constant total number of cells in healthy tissue, seeing that after birth for the development and growth of the organ, it goes from a process of hyperplasia to one of hypertrophy. Heart muscle cells, with not only the ability to contract, but also to conduct electrical signals for coordinated contraction. They are located in the middle layer, myocardium [13, 14].

**-Endothelial cells:** Cells that line the inside of blood vessels and in the heart, they would go on to form the endocardium in the atria and ventricles. Their arrangement in the tissue allows them to be the cell group with the closest contact with the blood flow, which can quickly determine changes in the physiological conditions and thus react to these changes by producing and secreting molecules and peptides into the environment that affect the remodelling process and cardiac contractility that stands out, either by stimulating inflammatory pathways, or by affecting the activity of other cell populations [15-17]. Studies on the role of this cell population in remodelling situations have shown the capacity to originate active fibroblasts from the endothelial cell population, which is an important source of proliferation of new CFs and therefore affects the production and deposition capacity of ECM components [18].

**-Cardiac Fibroblast:** Fibroblasts would form a population of cells with a spindle-shaped body and an indeterminate number of projections. They represent essential developmental agents for their activity in the deposition of ECM components during growth, and in adulthood they show consistent activity in ECM degradation and deposition. Allowing it to adapt to the environment, thanks to its involvement in the secretion and production of matrix components, as well as the production of proteins such as metalloproteinases (MMPs), with the capacity to degrade it [19, 20]. Within this cell type, of mesenchymal origin, a great heterogeneity has been found within the same tissue, as well as between organs, depending on the physiological conditions to which they are subjected. Observing a different composition of membrane proteins or showing a different gene expression profile with regard to matrix proteins such as collagen or other molecules [20, 21].

### **1.1.3 Extracellular matrix in cardiovascular physiology**

The ECM has been seen from the beginning as an inert structure, whose basic purpose was to provide structural support for cells and tissues. Nowadays, however, the perception of the ECM has changed, seeing its capacity for plasticity and dynamism, which allow it to respond to external stimuli, as well as its role in cell-to-cell interaction and its ability to function as a reservoir of molecules, being very important for the development of the organ, as well as the maintenance of cell homeostasis and differentiation in early stages of development [22-24].

In many cardiovascular diseases, both the extent and composition of the ECM are altered, contributing to the pathogenesis of the disease by affecting organ structure and function or even altering signal transduction at the cellular level, leading to tissue maladaptation [22].

#### **1.1.3.1 Structure and composition**

The ECM is essentially composed of structural and non-structural proteins, that can be divided into 3 main groups, glycoproteins, proteoglycans and glycosaminoglycans, some of which, such as fibronectin or laminin, have the capacity to provide both functions, the common factor in these groups is glycosylation, which refers to the decoration of proteins or lipids with sugars [25].

The structural ones, as their name indicates, have a more structural function, such as Collagen I and III (which constitute about 90% of the collagen in the heart) which would represent the main structural components. The non-structural ones would fulfil other

roles, as is the case of the matricellular proteins, all of them vital for ECM plasticity [26, 27].

Within the structural components, collagen type I would be responsible for providing resistance to the 3D framework on which the cells are based, through the formation of thick fibres, while collagen III would constitute finer fibres whose structural function is to provide elasticity to the framework [28]. In addition, as major components, they are expected to play an important role in tissue, with some studies noting the importance of maintaining the ratio between these two isoforms collagen I:III, for the functional integrity of various organs[29], and how disruption of the balance can affect tissue stiffness and strength which subsequently leads to cardiomyopathy. [29-31]. With minor presence, but playing important roles, would be other minority components present in the matrix range from collagen V, with the formation of heterotypic fibres with collagen I, regulating its fibrinogenesis, or collagen IV, the main component of the basement membrane, involved in maintaining the functions of the endothelial cells. Other molecules such as Elastin and Fibronectin, would provide resilience and elasticity in the case of elastin and for the fibronectin a fibrillar network on the cell surface, which facilitates cell-matrix interaction, facilitating the transmission of information and stimuli from one side to the other [23, 28]. In the case of fibronectin, it is worth highlighting its importance during wound healing processes or tissue damage, thanks to the aforementioned capacities for interaction and transmission of information between different components, which will allow it to play the role of early ECM formation [32, 33].

Among the non-structural proteins are the matricellular proteins, macromolecules routinely expressed and secreted into the matrix, their levels being affected during stressful situations in the tissue, with a function of communication between cells and matrix proteins, with the aim of controlling the behaviour of the cells. Within this group of macromolecules we find thrombospondin (TSP), osteopontin (OPN), tenascin-C (TNC), periostin (POSTN) and SPARC (secreted acidic protein rich in cysteine) [26, 27, 34]. Some of them have been shown to have a high impact on the correct development and function of the cardiac organ, such as POSTN, a gene coding for a protein with a role during the development of the cardiac organ, with a high expression profile during the early stages of development, which is strongly reduced in adulthood [35, 36]. Studies have shown the ability of this protein to induce the re-entry of adult cardiomyocytes into the cell cycle [37]. Mismatches in the expression of proteins such as this one have been shown to promote alterations at the organ level, which can lead to cardiomyopathy, linking the dysregulation of periostin to situations of stress, during situations of damage to cardiac tissue, when the levels of expression of this gene increase [37, 38].

## INTRODUCTION

It should not be forgotten to mention an essential function, for the correct functioning and maintenance of homeostasis in the tissue, carried out by the ECM and which is related to molecules such as cytokines or TGF $\beta$ , which are regularly released by cells, with the aim of performing their activity in the same cell or in neighboring cells. These and other cytokines and growth factors can be stored in a latent form through binding and association with other molecules and fibers, and their release can then be controlled in a controlled manner. During the remodelling processes initiated by stressful situations, proteinases such as MMPs, which can also be found stored in the matrix, degrade these complexes, triggering the release of the molecules and facilitating their interaction with the cells in the area [27, 39-41].

### **1.2 Cardiovascular diseases**

The latest data collected by the World Health Organization (WHO) dating from 2019, show a scenario in which cardiovascular diseases (CVD) represent the leading cause of death in the world, affecting to a greater extent country with a medium/low level of development [42]. CVD represent disorders that affect the heart and blood vessels, affecting their proper functioning, these disorders would be associated with, partial or total blockages of blood flow to the affected areas, mechanical or electrical dysfunctions [43-45].

An underlying factor in many of these diseases, which is not always taken into account in the monitoring of patients, is the adaptive response that these phenomena initiate in the affected tissue. Within this group of pathologies, we can find ischaemia, infarction, cardiomyopathies, hypertension and myocarditis, would have the capacity to generate tissue damage or stress that would cause this adaptive response, giving rise to the phenomenon known as cardiac fibrosis, the pathology that is the objective of this study [46, 47]. All of the aforementioned pathologies will, to a greater or lesser extent, require short- and long-term monitoring due to possible heart dysfunction and myocardial stiffness. Factors that show a close relationship are an unhealthy diet or lifestyle, advanced age and stress, among others [48, 49]. Within these conditions we can differentiate between those such as myocardial infarction (MI), which cause massive damage in a localized period, and pathologies such as aortic stenosis or arterial hypertension, which would subject the tissue to a situation of prolonged stress over time, although both can lead to a fibrotic process, the mechanism and the response generated will be different [50, 51].

### **1.2.1 Adaptive response**

The key factor in relation to heart disease is the ability of the organ, tissue and ultimately the cells to adapt and adapt their environment to new environmental conditions, always with the aim of maintaining their capabilities and functions. This response exists from the earliest moments in the organ's development [52], and continues throughout adult life, in an ever-changing environment [53].

The latter is of great importance as it highlights that this adaptation process does not have to be linked only to health conditions, but may be due to intentionally generated stimuli, such as a change of lifestyle in terms of increased physical activity on the part of the individual [54]. All this leads to changes in the composition and structure of the organ, to ensure that it meets the needs of the individual. These adaptive processes, which will be discussed in the next section, would be cardiac hypertrophy, a process by which an increase in cardiac muscle [55] is produced, with the aim of maintaining or increasing blood flow to support the demands of the organism. The other process would be fibrotic remodelling, more focused at the level of the extracellular matrix [56] and whose purpose would be to maintain the structural integrity of the tissue by altering the composition of the ECM. This process of adaptation can result in a phenomenon known as myocardial remodelling, a process that involves different approaches to this process of adaptation and whose understanding is of vital importance.

#### **1.2.1.1 Remodelling of the myocardium**

Previously it was described the structure and composition of the cardiac organ, according to which in the heart it was possible to differentiate between two fractions, the first consisting mainly of cardiomyocytes and interstitial cells (cellular part, mentioned above) and the part that supports the cells and allows their interaction, the extracellular matrix (ECM). Having identified the tissue components in a simplified way, it is clear that it is on these two elements that the different remodelling responses should act. Next, the adaptive response to changes in the environment will be analysed and the different responses will be analysed. However, it is worth noting that because of what has been described above about the ECM and its complexity, this represents an element of great importance due to the fact that most myocardial diseases are associated with the expansion of the interstitium accompanied by an alteration in the composition of the ECM, showing that the ECM is not simply a network that supports the cells, but also have a role in the cellular responses of cardiomyocytes and interstitial cells [22].

Back to cardiac remodelling, one of the main mechanisms involved in the adaptive response would be a process of hypertrophy, a process in which the heart and individual

## INTRODUCTION

cardiomyocytes often undergo enlargement, but which also involves a process of cell proliferation.

Hypertrophy can be classified as physiological or pathological depending on the processes to which the response is associated [57]. Cardiac hypertrophy associated with normal cardiac organ function would be referred to as physiological hypertrophy or remodelling, with examples of stimuli for this remodelling being stress generated during training in athletes, during pregnancy or during normal growth in children [58, 59]. This response would be characterised by a slight increase in cardiac mass by a cardiomyocyte growth in length and width (hypertrophy) and renewal (proliferation of endogenous cardiac stem cells). In hearts with this remodelling, there is no loss of contractility, increased cell death, replacement of muscle cells by interstitial cells or an expansion of the ECM due to increased production of its components, and unlike pathological remodelling. This is a reversible process in most cases, except for post-natal hypertrophy, the result of this process would be a decrease in cardiac wall stress, increased pumping performance and improved vascularization [50, 60]. Several cell signalling pathways have been associated with this remodelling, including vascular endothelial growth factor B (VEGF-B), insulin, growth hormone (GH) and insulin-like growth factor 1 (IGF1), as well as the thyroid hormone triiodothyronine (T3) [50, 61].

On the other hand, pathological hypertrophy or pathological remodelling, usually occurs in the presence of cardiovascular disease (CVD). Would be related to a dysfunction in the normal functioning of the cardiac organ, loss of myocytes, fibrotic replacement, cardiac dysfunction, all this in order to reduce the stress on the ventricular wall to temporarily preserve cardiac pump function, the problem begins when this response leads to a series of maladaptive changes that can culminate in heart failure and death, an important event to note is that in this type of hypertrophy, the other remodelling process mentioned above, cardiac fibrosis, would also be present. [57, 58, 62, 63]. This process of pathological hypertrophic remodelling is characterized by the action of multiple mechanisms, the effect of which would be maladaptive, such as changes in metabolic patterns and gene expression, impairment of the fate and survival of individual cells, as well as modifications of the extracellular environment due to fibrosis [61, 64, 65].

Studies have shown that the development of physiological or pathological hypertrophy depends on the nature of the stimuli and signalling mechanisms used, rather than the duration of cardiac stress. It has been shown that in situations that generate similar conditions, the response in the organ differs [50, 66]. As an example of the latter, it can



be observed in studies in which the adaptive response was analysed, how stimuli of a different nature, but which generate similar situations of "overload" for the heart, cause apparently identical remodelling processes in the heart, but which, due to the origin of the stimulus, will be classified as pathological [67] and physiological [68] processes, due to the situations that will underlie each situation. In these studies, what can be classified as two subtypes of hypertrophy, based on changes in form, were analysed, these being concentric hypertrophic processes (during which a reduction in load volume may occur) and eccentric (where an increase in load volume may occur) (**Figure 3**). In the case of eccentric hypertrophy, in the aforementioned cases, in physiological situations, it would be characterised by chamber enlargement and a proportional change in wall thickness, whereas eccentric hypertrophy in pathological situations would be associated with thinning of the ventricular walls.

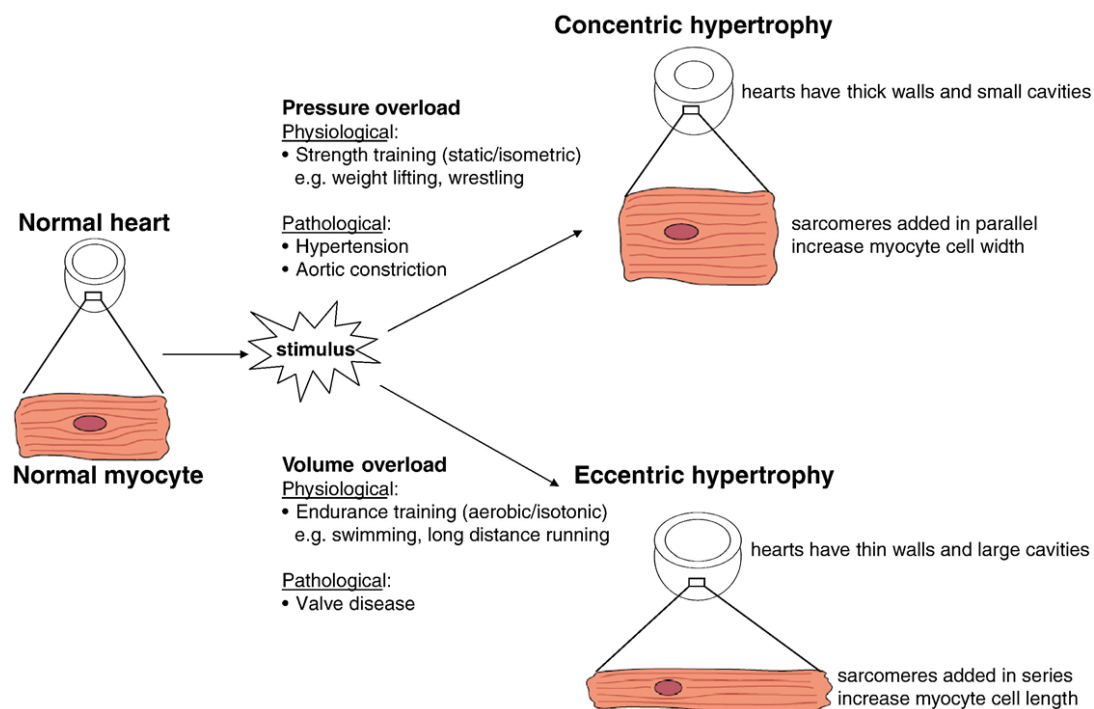


**Figure 3 adaptive response in cardiac tissue in response to stimuli of different nature.** Representation of two hypertrophic adaptations of the heart to overload stimuli, both physiological and pathological. From (Bianca C. Bernardo. et al., 2010).

Even so, there are several elements that can share both processes of hypertrophy, however, 2 are the major differences that can differentiate between the two processes, and that is that unlike pathological hypertrophy, physiological hypertrophy lacks inflammatory response and fibrosis during the process [69, 70]. Of these two elements, fibrosis will be the one we will focus on in our study, trying to reduce the impact of fibrosis on the pathological remodelling and therefore on the cardiovascular patient.

### **1.2.1.2 Cardiac fibrosis process and evolution**

As mentioned above, after the heart suffers damage or stress, these events would trigger a series of responses at the tissue and cellular level, which would trigger a transduction of these signals, altering gene expression, ECM homeostasis and metabolism, ultimately affecting normal cellular functioning [71, 72]. These processes would eventually lead to the fibrotic response, which can be shown in two non-exclusive ways. On the one hand the one known as replacement or reparative and on the other the one known as reactive fibrosis [73, 74]. As an example of reparative fibrosis, we would have that generated in response to phenomena such as myocardial infarction, which would be a rapid and immediate response, with a reparative and scarring character, what would be sought would be the substitution or reinforcement of an area of damaged tissue, in a localised manner [75]. On the other hand, in our study we are more interested in reactive response, typical of conditions characterised by overload, as in the case of hypertension or aortic stenosis [76]. In the latter case, there would be a diffuse and progressive fibrosis, being situations in which over time, the cardiac function is affected, presenting dysfunctions.

In the context of reactive fibrosis, the processes would be characterised by an imbalance between the degradation and production of extracellular matrix elements in the interstitial or perivascular zone during the remodelling process [77]. This excess of extracellular matrix protein deposition is associated with impaired organ functional capacities, such as increased myocardial stiffness, reduced ventricular compliance and impaired physical capacity.

This response can be divided into 3 major phases, looking at the events and actions that take place in each phase, the first being a phase of inflammation, a fibrosis/proliferative phase and finally a long-term response/remodelling, being this last phase necessary for the development of the pathology. [72, 78-80].

Unlike the situation of a myocardial infarction, where tissue damage occurs in a localised manner over time, the first phase of inflammation would take place during the first week, in the case of the model we are working with in this study, it would be more of a hypertension model, so we are working with a situation of stress that is maintained over time, leading to a phase of inflammation that is more distended over time. The stress to which the tissue is subjected would eventually lead to the migration of inflammatory cells, such as macrophages and neutrophils among others, which would trigger the inflammation process in the affected area, through the release of proinflammatory cytokines such as Interleukin-6 and 8 (IL-6 and IL-8) or tumour necrosis factor (TNF) [79, 81].

A release of cytokines into the environment will also take place, with the aim of favouring the proliferation of cardiac fibroblasts, their activation and their differentiation into myofibroblasts, thus favouring the formation of scars with excess deposition of structural fibres [81, 82].

The latter would be located within the proliferation/fibrosis phase, where the progressive replacement of healthy tissue by fibrotic tissue and initial remodelling would take place, aiming to maintain the integrity of the tissue [83, 84]. This phase would be dominated by the presence of myofibroblasts. During this phase, the number of fibroblasts in the cardiac tissue would increase, thanks to a combination of phenomena such as migration from adjacent tissues, proliferation and differentiation of cells from other populations to active fibroblasts and myofibroblasts. This fibrosis would be called reparative fibrosis, as it would seek to remodulate and repair the fibrosis [85, 86].

Finally, if the process is not terminated, it would lead to the maintenance of a long-term response, resulting in reactive fibrosis, in which the adjacent tissue would be affected, causing dysfunctional remodelling, which would not be aimed at preserving the capacity of the cardiac organ [87-89].

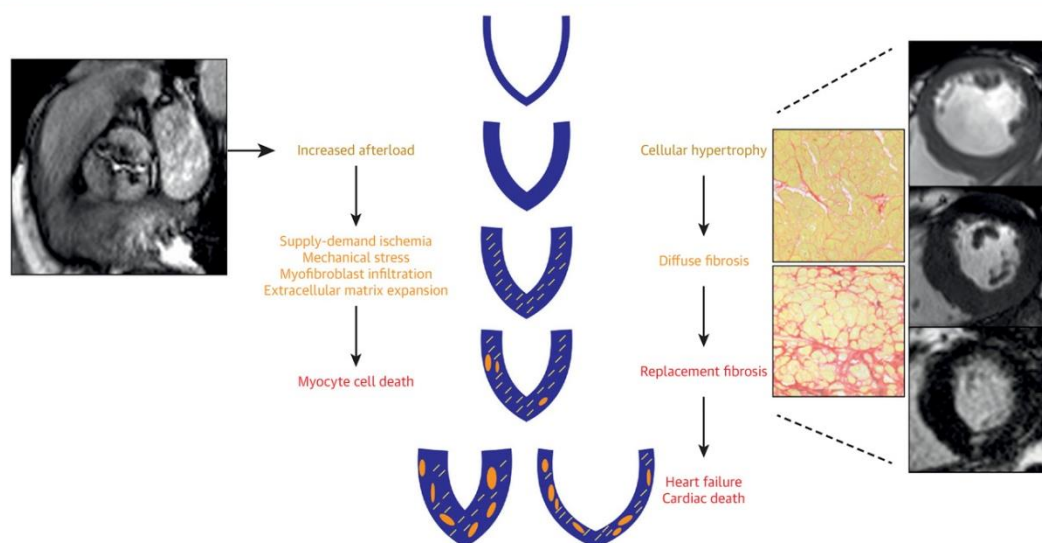


**Figure 4 Summary of Left Ventricular Remodeling and Decompensation in Patients With Aortic Stenosis.** The diagram shows the effects of aortic stenosis on left ventricular remodelling and its evolution over time. On the left side we have the effects that the cardiac tissue suffers and on the right side the responses that it would generate. The colour coding would match each action with its reaction. Bing, R. et al. *J Am Coll Cardiol Img.* 2019;12(2):283-96

Long-term maladaptive remodelling, due to the spread of the response in the tissue, would generate an excess of fibrotic tissue, which would affect not only the mechanical capacities of the tissue, but would threaten the homeostasis of the tissue by hindering

## INTRODUCTION

cell-cell communication and nutrient uptake by the cells, potentially subjecting the tissue and cells to further stress and feeding back into the response [90-92].

As mentioned above, the processes of ECM degradation and formation are strongly related to cardiac fibroblasts, which are the main remodelling agents in cardiac tissue [93].

### **1.2.2 Fibroblast, the remodelling agent**

Cardiac fibroblasts are key players in cardiac physiology and cardiovascular disease, functioning as major producers of ECM components, such as different types of collagens, fibronectin or vimentin among others. Although fibroblasts are the main producers of these proteins, other cell populations, endothelial cells, pericytes or smooth muscle cells, that can produce them to a lesser extent have been identified as contributing to the fibrotic process [93, 94]. Fibroblasts are primarily responsible for cardiac fibrosis. When these cells go into an activated state, due to damage or an inflammatory process, they show up-regulation of collagen production to stabilize cardiac function.

#### **1.2.2.1 Origin of cardiac fibroblasts in the disease heart**

When talking about the origin of fibroblasts in cardiac tissue, some studies differentiate between two stages, during development and the origin in a diseased heart, both involving different cell populations, but with a change in their relevance.

During development, cardiac fibroblasts would derive from mesenchymal cells. Being pro-epicardial cells present in the heart of the embryo, those who would undergo a process of epithelial to mesenchymal transformation, which would end with the differentiation of the latter to fibroblasts, but differentiation from the endocardium would also be present [20, 95, 96].

In contrast is the scenario of a diseased heart in which the remodelling process, or fibrotic process, involves the activation of cardiac fibroblasts, proliferation and their differentiation into myofibroblasts. Several studies analysed the possible origin for these cells, using markers and probes, and identified, as expected, fibroblasts resident in cardiac tissue as the source with the greatest contribution to these new cell populations [97, 98]. In addition, studies in mice using specific cell population markers showed that the process of transition from endothelial or endocardial cells to cardiac fibroblasts observed during development did not show a significant change, with the contribution of these cell populations being minimal compared to the primary source [99-101].

### **1.2.3 TGF $\beta$ signalling pathways in cardiac Fibroblast activation and regulation during fibrosis**

During the processes described above, cytokine production, mechanical signals produced through the extracellular environment, are initiated, which will cause the activation of cardiac fibroblasts, as well as the transdifferentiation of some of the into myofibroblasts. There are several signalling cascades that intervene or have some effect on these activation and differentiation processes, some of the most important and studied ones would include RhoA/ROCK, Renin-angiotensin system and the TGF $\beta$  pathway[102, 103].

#### **1.2.3.1 TGF- $\beta$ signaling**

Many cytokines and growth factors have been studied for their effects and their role in regulating fibroblast activation, their differentiation into myofibroblasts and their effects on ECM production and remodelling, but TGF $\beta$  has been shown to be one of the main agents with the most potent effect on all these phenomena, found to be a versatile cytokine that can play both pathological and physiological roles. Like Angiotensin II, TGF $\beta$  acts at different levels and may affect cell proliferation, cell differentiation ( ) as well as the production of ECM components regulates phenotype and function of all cells involved in tissue injury) [104-106]. In the first moments of its activation, during a situation of stress or damage to cardiac tissue, it appears to play a protective role in the tissue, promoting repair of the damaged area or promoting proliferation or non-pathological remodelling of the organ to maintain optimal organ function, but it is in the sustained response that problems are generated, promoting excess ECM deposition, affecting tissue stiffness and affecting its function [107].

#### **1.2.3.2 TGF $\beta$ Production and Activation**

TGF $\beta$  in its physiological state is produced and secreted by many cells as part of a latent complex, lacking the ability to interact with its receptor. The activation of its signalling pathway is preceded by the release of a molecule of active TGF $\beta$  from the latent complex, which is stored in significant quantities through its association with matrix components [108].

TGF $\beta$  is synthesised as an homodimeric proproteins, which undergoes proteolytic processing at the RXXR consensus sequence by Furin, an endopeptidase present under profibrotic conditions. As a result, it will result in a mature TGF $\beta$  dimer joined by disulfide bridges, and a peptide called "Latent Associated Peptide" (LAP)[108]. This processing can occur in the Golgi apparatus, although cases of unprocessed proTGF $\beta$  protein being secreted from cell lines have been observed [109]. LAPs remain non-covalently associated with the mature TGF $\beta$  dimer while maintaining its latency, in complexes that

## INTRODUCTION

are termed "small latent complexes" (SLC). SLC then covalently binds to a multidomain protein called "Latent TGF $\beta$  Binding Protein" (LTBP) via LAP-bound forms the "Large Latent Complex" (LLC). Finally, LTBP directs the latent TGF $\beta$  to the extracellular matrix (ECM) for its storage [110, 111].

In a physiological state, the balance of the content of latent TGF $\beta$  and TGF $\beta$  free at the matrix, would be maintained, displaying a higher latent complex content than the free form [112, 113].

Activating this latent state, causing the release of the TGF  $\beta$  molecule, would be the next step in TGF $\beta$  signalling and there are several actors that can induce this process. Plasmin, metalloproteinases and thrombospondin 1, are identified factors that can cause degradation of the complex facilitating the release of TGF $\beta$  [114]. The physiological levels of these molecules remain stable, guaranteeing levels of free TGF $\beta$  that are necessary for the proper functioning of the tissue, being altered in pathological situations.. In addition to these factors, Integrins which are a type of embedded membrane proteins have also been identified as important factors regarding activation of TGF $\beta$  [115, 116].

### **1.2.3.3 TGF $\beta$ canonical signaling pathway (Smad-based)**

The main TGF $\beta$  pathway would begin with the binding of the cytokine to the TGF $\beta$  type II receptor (TGF $\beta$ R2), which would allow it to recruit and phosphorylate the TGF $\beta$  type I receptor (TGF $\beta$ R1), initiating a cascade of phosphorylations that would allow signal transduction. Once TGF $\beta$ R1 is activated, it phosphorylates serine residues at the C-terminal end of the effector Smads (Smad2 and Smad3), which, once phosphorylated, dissociate from TGF $\beta$ R1, and form a heterotrimer, consisting of Smad2, Smad3 and Smad4 [117, 118]. This complex would have the capacity to translocate into the cell nucleus and act together with transcription factors to affect the transcription of specific genes, which may encode for structural fibres, such as Collagen I and III, as well as proteins that are markers of the overload environment in which they may be found and that fulfil an antagonistic function to that generated by TGF $\beta$ , such as in the case of hypertensive environments, where an increase in the expression of natriuretic peptides a and b (Nppa and Nppb) is observed. [119]. In addition to the Smad proteins that have been seen in the canonical pathway, another of these proteins that act as second messengers and that functions as a counterbalance, acting as an inhibitor of the pathway, is known as Smad7, which competes with Smad2/3 for binding and interaction with TGF $\beta$ R1 [120].

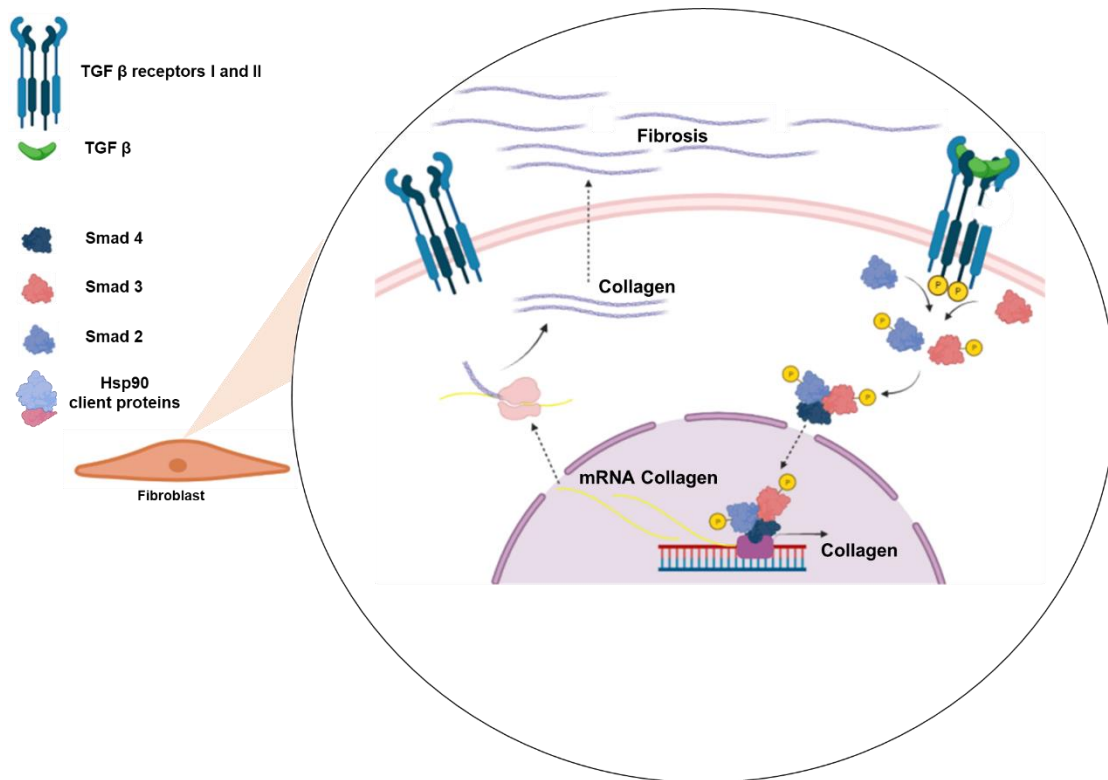


**Figure 5 Schematic representation of the TGFβ canonical pathway.** Canonical route with the main elements described. At the membrane level in shades of blue the TGFβ type 1 and type 2 receptors are arranged. In green we have a TGFβ molecule that is being recognised. After the recognition process we will have the phosphorylation processes, represented by the yellow spheres (phosphate groups) and which would allow the transduction and transmission of the signal from the membrane to the nucleus, where the complex constituted by the Smad2/3/4 effectors would enter, a complex with the capacity to interact with transcription factors to exacerbate the expression of target genes. These processes would end in the transcription of a gene and their translation into proteins, in the image are present collagen fibres as an example of a gene affected by the TGFβ pathway.

#### 1.2.3.4 TGFβ non-canonical signaling pathway (non-Smad-based)

In addition to the canonical pathway, there are accessory pathways that would be responsible for downstream signal transduction. In this group we find the extracellular signal-regulated kinase (Erk)/mitogen-activated protein kinase (MAPK) signalling pathway. In the same way, recognition of the cytokine TGFβ by type I and II receptors would occur, causing phosphorylation at tyrosine residues in the intracellular domain. From this point on, signalling would diverge [118].

TGFβ stimulation can also generate a non-canonical mitogen-activated protein kinase (MAPK)-dependent response, which transmits the signal from the cell membrane to the nucleus and regulates gene expression [121]. The conventional ones would be mitogen-activated protein kinases (MAPK), p38 MAPK (p38), c-Jun terminal kinase (JNK) and extracellular signal-regulated kinase (ERK). These are thought to play an important role in the effector response, by regulating transcriptional cofactors that co-operate with

## INTRODUCTION

Smad proteins [121, 122]. Their role in fibrotic processes has been confirmed in studies analysing the presence and concentrations of active MAPKs, showing an increase in these forms in pathological situations, as well as a worsening of the situation in cases where their concentration was increased [123, 124].

One of the independent Smad pathways would be the RhoA/ROCK axis-dependent signalling pathway. RhoA would function as a switch protein, alternating between an active (RhoAGTP) and an inactive (RhoAGDP) form. It belongs to the GTPase family associated with the control of the cytoskeleton, cell motility and gene expression, using a variety of effectors, of all the effectors Rho-associated, coiled-coil-containing protein kinases (ROCKs) has been defined as the main [121]. Two isoforms ROCK1 and ROCK2 were found. RhoA and ROCK can be activated indifferently by Smad-dependent or Smad-independent mechanisms. They would affect the induction of actin polymerisation and stress fibre formation during epithelial to mesenchymal transition (EMT) [125]. Tests in cell culture and in mouse models showed the importance of this signalling pathway, as it was observed that models with the deletion of the ROCK1 isoform gene showed a lower production of matrix components [126] and also affected the processes of transdifferentiation to fibroblasts [127, 128].

Another alternative route would be that of phosphatidylinositol-3-kinase (PI3K), with the capacity to activate protein kinase B (Akt), which would act through different effectors, some of which are well studied, such as glycogen synthase kinase-3 $\beta$  (GSK-3 $\beta$ ) or mammalian target of rapamycin (mTOR) [129]. Its relevance at the level of the fibrotic process has been demonstrated by the effects observed in the increase of collagen production after its activation, and the inhibitory effects brought about by the use of inhibitors or the generation of mutants for some of the components of the pathway [121, 130].

### **1.2.3.5 The role of Hsp90 and other partners in TGF $\beta$ signaling cascade**

In addition to intracellular components, it is important to highlight the role of different partners, at the membrane level, with the capacity to modulate the signalling pathway by exerting their activity during TGF $\beta$ -receptor recognition. This is the case for TGF $\beta$ RIII (also known as betaglycan), a membrane receptor with a high affinity for TGF $\beta$ , which may affect the availability of TGF $\beta$  with TGF $\beta$ RII [131]. Another example of an accessory receptor is the Bone Morphogenetic Protein and Activin Membrane-Bound Inhibitor (BAMBI), which acts as a pseudoreceptor similar to TGF $\beta$ RI, but lacks the intracellular



kinase domain. Its action would be based on preventing the formation of the receptor complex, preventing the propagation of the signal downstream [132]. The last example of an accessory receptor is Endoglin, a membrane glycoprotein with TGF $\beta$  coreceptor function, with high levels of expression in endothelial cells, due to its role in angiogenesis. Mutations in its expression (silencing) show attenuation in myocardial fibrosis [133].

In addition to the membrane coreceptors, there is also a pull of proteins in the extracellular matrix, which have been studied in recent years and which are being assigned functions in this signalling pathway. In this group we have the presence of Connective Tissue Growth Factor (CTGF) and the chaperone Heat shock protein 90 (Hsp90). CTGF is a matricellular protein, with a very important role in the activation of cardiac fibroblasts and TGF $\beta$ . In different studies, the effect of suppressing its production and secretion to the outside of the cell by fibroblasts, the inhibitory effect on fibrotic remodelling has been observed [134].

Hsp90, on the other hand, has been found to be present in the extracellular matrix in different studies, showing that it was not due to fractions produced by the cell sample in the organ [135]. This protein would have the ability to mediate cellular processes through protein-protein interactions. It functions as a cofactor together with TGF $\beta$ RI during cytokine recognition, affecting the initiation of the cell signalling pathway [135, 136].

#### Hsp90

- The target of action of these nanoparticles would be Heat shock protein 90 (Hsp90) [9], which has been described in different articles as an important component in the TGF- $\beta$  signalling pathway [10,11]. Hsp90 has a putative energetically favourable TPR-binding domain with which it could bind to various proteins to form functional multi-protein complexes [11]. Inhibition of these bindings may affect various cellular functions [12]. In this project we work with a hypothesis, according to which Hsp90 exerts a role as a cofactor of the TGF- $\beta$  type I receptor (TGF- $\beta$ RI) whose presence in the protein complex allows optimal action of the TGF- $\beta$  signalling cascade [11]. This hypothesis is based on insilico simulations, which show a thermodynamically favourable model showing the interaction between TGF- $\beta$ RI and a homodimer of Hsp90 [7,11].

1. Couleaud, P., Adan-Bermudez, S., Aires, A., Mejías, S. H., Sot, B., Somoza, A., & Cortajarena, A. L. (2015). Designed modular proteins as scaffolds to stabilize fluorescent nanoclusters. *Biomacromolecules*, 16(12), 3836-3844.
2. Datta, R., Bansal, T., Rana, S., Datta, K., Chattopadhyay, S., Chawla-Sarkar, M., & Sarkar, S. (2015). Hsp90/Cdc37 assembly modulates TGF $\beta$  receptor-II
  - Therapy of fibrosis

## INTRODUCTION

Fibrotic remodelling is a major contributor to HF progression as it causes contractile dysfunction and arrhythmia in heart disease of various aetiologies [43, 60-63]. In the treatment of HF, fibrosis can potentially be targeted indirectly or directly by drug therapies to ameliorate cardiac function [298, 299]. Despite the mechanistic understanding of heart diseases generated over the years, the therapeutics can only slow down fibrosis [300]. According to the European Society of Cardiology (ESC) guidelines for the diagnosis and treatment of acute and chronic HF [301], neurohormonal antagonists are the currently used drugs to treat patients with HFrEF or after a MI. The recommended pharmacological treatments [301] for all patients with symptomatic HFrEF Class II-IV (graded according to the New York Heart Association – NYHA – functional classification), or after MI, are angiotensin-converting enzyme inhibitors (ACEI) for blockade of the renin-Ang II-aldosterone system (RAAS) and  $\beta$ -adrenergic receptor blockers ( $\beta$ -blockers). This treatment aims to ameliorate the symptoms of HF, improve functional capacity and reduce mortality, and is also recommended for patients with asymptomatic left ventricular (LV) systolic dysfunction [301]. Treatment with ACEI (e.g. Captopril, Lisinopril) and  $\beta$ -blockers (e.g. Bisoprolol, Carvedilol) are recommended to be coupled with diuretics, if it is necessary to reduce symptoms of circulatory congestion and peripheral edema [301]. ACEI have been shown to help recovering LV systolic function and reduce fibrosis [302, 303]. In patients with coronary artery disease, who do not present LV systolic dysfunction,

27

ACEI prevent or delay the onset of HF [301, 304]. In case ACEI are not well tolerated, patients can be alternatively treated with AT1R blockers, such as Candesartan and Valsartan. AT1R blockers suppress the RAAS via selective inhibition through AT1R and are indicated to reduce vasoconstriction, sodium and water retention, myocardial hypertrophy and fibrosis [301, 305-307]. When HFrEF patients are resilient to treatment with an ACEI and a  $\beta$ -blocker, they can subsequently be treated with mineralocorticoid/aldosterone receptor antagonists (MRA), such as Spironolactone and Eplerenone. The MRA block receptors of aldosterone and other

steroid hormone receptors (e.g. corticosteroids, androgens) [301]

. LCZ696

(Sacubitril/Valsartan), a new dual-acting compound in the class of angiotensin receptor neprilysin inhibitors (ARNI) [308], showed to be more effective than the ACEI Enalapril alone [309, 310], but it is being only used in patients intolerant to ACEI and MRA [301].

Besides ACEI and AT1R blockers which are considered to slow down fibrosis, no therapeutic strategy is yet available that is specifically designed to target CF and is able to fully halt or reverse the effects of pathological cardiac remodelling [298, 299].

- Emerging anti-fibrotic strategies and pharmacological targets

Despite the critical impact of cardiac fibrosis in the progress of HF, only very few new therapeutic approaches are currently in clinical trials.

## AIMS OF THE STUDY



## 2. AIMS OF THE STUDY

The introduction section shows the high impact of cardiac fibrosis pathology on the patient., as well as its complexity in terms of the approach to the problem, which is reflected in the lack of effective and efficient treatment. This explains the need to develop effective anti-fibrotic drugs for the treatment and improvement of patients' lives.

In this work, we propose to analyse and study the behaviour of an experimental antifibrotic drug (CTPR) whose action would prevent the generation and accumulation of an excessive overexpression of extracellular matrix components (mainly collagen), with special focus on its cellular and extracellular localization. We also aimed to advance in the knowledge of the antifibrotic mechanism of action of the drug giving an insight of the the in vivo response of the heart after its administration. This general objective inherently involves the objective of maintaining the cellular homeostasis of the target organ by not altering the main action of the CTPR target protein (the folding capacity of the Hsp90 chaperone).

With a molecule such as CTPR we aim to combine its use as an anti-fibrotic with its possible use as a tracer agent to demonstrate its theranostic capacity by monitoring it in cardiac fibrotic models.

We also propose an alternative approach to the problem of reducing myocardial fibrosis. This objective focuses on degrading already accumulated pathological fibrosis rather than preventing its excessive accumulation as in the proposed treatment with CTPR. We want to apply a system based on the use of a plasmid construct, aiming at a controlled degradation of the extracellular matrix, as mentioned above. The degrading system, that we called Genetic Alert system (GAS), pretends to use the matrix metalloproteinase MMP2 as an effector protein based on the importance and capacity of this protein in the task of ECM degradation. We propose to activate GAS function only in pathological situations to prevent degradation of healthy ECM fibres by selecting a promoter (periostin) whose specific expression profile ensures a controlled and selective activation of the system only in pathological conditions.

## 2.1 Specific objectives:

Research line: Modular nanobiotechnological tools designed to detect and interfere with the key signalling pathway of cardiac fibrosis in vitro and in vivo:

1. Characterisation of CTPR nanoparticles localisation in fibroblasts. Study of cell viability and ultrastructural changes of fibroblasts in the presence of CTPR.
2. Evaluation and quantification of the antifibrotic impact of CTPR and the alteration of different profibrotic signalling pathways in embryonic and primary cardiac fibroblasts. Comparison of the antifibrotic effect of CTPR and some commercial Hsp90 inhibitors such as 17AAG or EGCG.
3. Unraveling CTPR antifibrotic mechanism of action focusing on the study of profibrotic signaling-related protein expression.
4. Study of the in vivo effect of CTPR on cardiac remodelling. Evaluation of hypertrophy and fibrosis changes in a hypertensive mouse model.
5. Evaluation of CTPR as a biomarker and/or theragnostic marker and its biodistribution in a hypertensive mouse model.
6. Evaluation of the antifibrotic capabilities and biomechanical changes of a three-dimensional human cardiac organoid treated with CTPR.

Research line: Genetic Alert System (GAS), active therapy for the degradation of excess extracellular matrix components in pathological situations.

1. Generation of the "genetic alert system" (GAS) molecule;
2. Demonstration of the GAS (MMP2-psecTag2-POSTN) latence in healthy conditions and observation of its gelatinase activity in cardiac remodelling conditions.







### 3. MATERIAL AND METHODS

#### 3.1 MATERIAL

##### 3.1.1 Animals

Live animals' studies were approved by the University of Cantabria Institutional Laboratory Animal Care and Use Committee in compliance with the Guide for the Care and Use of Laboratory Animals (ILAR, 1985) and were conducted in accordance with the “European Directive for the Protection of Vertebrate Animals Used for Experimental and Other Scientific Purposes” (European Communities Council Directive 86/606/EEC). The animals were provided by the Animal Housing and Experimentation Service of the University of Cantabria (In Spanish SEEA).

During the study, mice of the C57BL6 strain, aged between 3 and 8 months, were used for isolation for primary cultures as well as for the generation of animal models for experiments in the field.

##### 3.1.2 Primary cells

Two different populations of primary cultures were used in the study.

Heart tissue cells were obtained from C57/BL6 mice of the SEEA. In addition, we worked with a cell line provided in collaboration with the group led by Prof. Dr. rer. nat. Susanne Lutz from the Institute of Pharmacology and Toxicology, University Medical Center Goettingen. Information on the crops is given in the table below.

Cell type	Name	Source	Application
Cardiac Fibroblasts from the mouse heart.	mCF	C57/BL6 mouse processed heart (3-8 months).	monolayer and coculture cultures, RNA extraction, western blotting, microscopy.
Normal human cardiac fibroblasts from the ventricle.	hCF	cell extracts from male patient, marketed by the company LONZA, LOT NO.: 0000421712 (Lonza #CC-2904).	hECT formation, RNA extraction, western blot, microscopy.

Table 1 Primary cell lines.

### 3.1.3 Cellular Lines

In addition to primary cells, cell lines were used in the work.

They are listed in the table.

Cell type	Name	Source	Application
Mouse embryo fibroblasts	NIH/3T3	<i>Mus musculus</i> , mouse, Embryo fibroblast.	monolayer and coculture cultures, RNA extraction, western blotting, microscopy.
Rat cardiomyocytes	H9C2	<i>Rattus norvegicus</i> , rat, Heart; Myocardium, cardiomyocytes	monolayer and coculture cultures, RNA extraction, western blotting, microscopy.

Table 2 Immortalised cell lines

### 3.1.4 Solutions and reagents used in the experiments

#### 3.1.4.1 Cell culture médium

##### Culture medium for NIH/3T3 and H9C2

DMEM High Glucose medium (4.5 g/l), with L-Glutamine, with Sodium Pyruvate (#11965092, gibco or #BE12-604F, Lonza) supplemented with 10% heat-inactivated FBS serum (#10082147, gibco) and 1% antibiotic Penicillin/Streptomycin (#11548876, gibco).

##### Culture medium for primary mouse cardiac fibroblasts

DMEM High Glucose medium (4.5 g/l), with L-Glutamine, with Sodium Pyruvate (#11965092, gibco or #BE12-604F, Lonza) supplemented with 10% heat-inactivated FBS serum (#10082147, gibco), 10% of DBS serum (#16030074, gibco) and 1% antibiotic Penicillin/Streptomycin (#11548876, gibco).

##### Culture medium for primary human cardiac fibroblasts

Fibroblast Growth Medium 3 (#C-23230, PromoCell), supplemented with Growth Medium 3 SupplementMix (#C-39345, PromoCell) and 1% antibiotic Penicillin/Streptomycin (#11548876, gibco).

##### Transfection culture medium

Opti-MEM™ (#11058021, gibco) unsupplemented.

#### 3.1.4.2 Cell culture reagents

**PBS** phosphate buffer for washes NaCl 154 mM, Na<sub>2</sub>HPO<sub>4</sub> 8.1 mM KH<sub>2</sub>PO<sub>4</sub> 1.9 mM, pH 7.4 (preparation in house).

## MATERIAL AND METHODS

**Trypsin 1X** for cell-culture plate dissociation TrypLE™ (# 12604021, gibco).

**Trypsin Solution 10X** for cell-culture plate dissociation (#59427C-100ML, Merck).

**Trypsin powder** for tissue dissociation, cell extraction (#T8003, Merck).

**Dimethyl sulfoxide (DMSO)** for cell cryopreservation (#40470004-3, Quimigen).

**Collagen solution** for the production of 3D cultures (#5010-50ML, CellSystems).

**DMEM powder** for preparation of more concentrated solutions, 3D cultures preparation (#52100039, gibco).

**NaOH 0.2M solution** used for pH modifications (preparation in house).

**Lipofectamine™ LTX Reagent** (#10573013, invitrogen) used for transfection processes in cell cultures.

**Gelatine from porcine skin** (#G1890-100G, Merck), used for coating cell culture surfaces and for zymography.

### 3.1.4.2 Protein purification/extraction and Western Blot

**Detergent-free lysis buffer (DFB)** (10mM Hepes, 100mM KCl and 1.5mM MgCl) (preparation in house).

**RIPA Extraction and Lysis Buffer** (#10017003, Scientific).

**Protease inhibitor**, Thermo Scientific™ Halt™ protease inhibitor cocktail, EDTA-free (100X) (#10320015, Scientific).

**Protease and Phosphatase Inhibitor Cocktail** (#PPC2020-1ML, Merck).

**Acrylamide, 30%** Acrylamide/Bis Solution, 29:1 (#1610156, BIO-RAD).

**Ammonium Persulfate (APS)** (#1610700, BIO-RAD).

**Tetramethylethylenediamine (TEMED)** (#1610801, BIO-RAD).

**SDS 10%** Sodium dodecyl sulfate in ddH<sub>2</sub>O (preparation in house).

**Laemmli 4x Sample Buffer** (#1610747, BIO-RAD).

**Tris-HCl 1.0M pH 6.8 with HCl** (preparation in house).

**Tris-HCl 1.5M pH 8.8 with HCl** (preparation in house).

**Protein Weight Marker**, Precision Plus Protein Dual Color Standards (#1610374, BIO-RAD).

**Tween 20**, Detergent 100% no iónico (#1706531, BIO-RAD).

**Tris buffered saline solution 10X** (TBS 10X) (preparation in house).

**Tris buffered saline solution – Tween** (TBST) (preparation in house).

**Ponceau Solution** (#10776454, Scientific).

**Methanol ≥98.5%**, TECHNICAL (#20903.368P, VWR).

### 3.1.4.3 Hsp90 refolding assay

**Stability buffer**, 25mM Tris-HCl 1.5M pH 7.8, 8mM MgSO<sub>4</sub>, 10% Glycerol, 1% Triton X100 and 10mg/mL (BSA).

**Cold mix**, 100mM Tris-HCl pH7.7, 10mM Mg(OAc)<sub>2</sub>, 375mM KCl, 15mM ATP and 25mM creatine phosphate.

**Luciferase** (#16176, Thermo Fisher).

**Reticulocyte extract** (#L4960, Promega).

**CPK solution**, Creatine phosphokinase at 5mg/mL in 50% glycerol.

**Buffer 7.1**, 8mL of cold mix, 1.6mL of CPK solution, 1.075mL of deionized water and 125µL of desnaturated luciferase 0.5mg/mL

### 3.1.4.4 RNA extraction and purification

**Trizol** RNA, DNA and protein extraction and purification, NZYol (#MB18501, NZYTech).

**Isopropanol**, Purificación de RNA, 2-Propanol, ≥99% grado biotecnología (#0918-1L, VWR).

**Chloroform**, RNA purification, Chloroform ≥98% stabilised, TECHNICAL (#22720.550, VWR).

**Water, nuclease-free** (#11893933, Scientific).

### 3.1.4.5 RT and qPCR

**High-Capacity cDNA Reverse Transcription** PCR High-Capacity cDNA Reverse Transcription Kit (#4368814, Scientific).

**qPCR master mix** reaction, gene expression PowerUp™ SYBR™ Green Master Mix (#A25777, Scientific).

### 3.1.4.6 PCR and agarose gels

**DreamTaq Green PCR Master Mix (2X)** (#K1082, Scientific).

**KAPA Taq PCR Kit** (#KK1015, Merck).

## MATERIAL AND METHODS

**Phusion High-Fidelity DNA Polymerase kit** (#F553L, Scientific).

**dNTP mixture** (10 mm each) (# 18427013, Scientific).

**DNA size marker**, GeneRuler 1 kb DNA Standard (#SM0311, Scientific).

**DNA Loading Buffer** (#10816015, Scientific).

**Agarose**, Electran, high resolution, low melting for electrophoresis (#MFCD00081294, VWR).

**TAE buffer 10X** (Tris-base, pH 8 EDTA Acetic acid) (preparation in house).

### 3.1.4.7 Immunofluorescence and live cell microscopy reagents

**Paraformaldehyde (PFA) 4%** Solution in PBS (#AR1068, Quimigen).

**Triton X-100 Detergent** (#1610407, BIO-RAD).

**PBS phosphate buffer** for washes NaCl 154 mM, Na<sub>2</sub>HPO<sub>4</sub> 8.1 mM KH<sub>2</sub>PO<sub>4</sub> 1.9 mM, pH 7.4 (preparation in house).

**Tween 20**, Detergent 100% no iónic (#1706531, BIO-RAD).

**ProLong™** Diamond Antifade Mountant with DAPI (#P36962, Scientific).

**ProLong™** Diamond Antifade Mountant (#P36961, Scientific).

**Reactivo NucBlue™** Live ReadyProbes™ (#R37605, Scientific).

**Invitrogen™ NucRed™** Dead 647 ReadyProbes™ Reagent (#15139325, Scientific).

**Invitrogen™ LysoTracker™** Green DND-26 (#11594976, Scientific).

**MitoTracker®Red CMXRos** (#9082, Cell Signaling).

### 3.1.4.8 Masson trichrome and Picrosirius red staining reagents

**Hematoxylin Solution**, Harris (#1.09253.0500, Merck).

**Acid Fuchsin** (#1.05231.0025, Merck).

**Xylidine Ponceau** (#P2395-25G, Merck).

**Light Green** (#1.15941.0025, Merck).

**Phosphomolybdic acid** (#131031.1608, Panreac).

**Xylene** (mixed isomers) for analysis (#MFCD00077264, VWR).

**Picro-Sirius Red Solution** (#SRS500, Quimigen).

### 3.1.4.9 Laboratory solutions and buffers

**Absolute ethanol, ≥99.9%** (by GC), EMSURE® ACS, ISO, Reag. Ph. Eur. for analysis, Supelco® (#MFCD00003568, Merck).

**Acetic acid ≥96%**, EMSURE® for analysis, Supelco® (#MFCD00036152, Merck).

**Bovine serum albumin (BSA)** (#A7906-50G, Merck).

**Hydrochloric acid** (#1.00317.1000, Merck).

**Glacial Acetic Acid** (#211008, Panreac).

**Ethanol ≥70%** (v/v), Biotechnology Grade (#MFCD00003568, VWR).

### 3.1.4.10 SEM and TEM electron microscopy

**Phosphate buffer 0.1M** (preparation in house).

**Osmium tetroxide** (#75633, Merck).

**Acetone** (#67-64-1, Merck).

**Durcupan™ ACM** ( # 44610, Merck).

**Paraformaldehyde (PFA) 4%** Solution in PBS (#AR1068, Quimigen).

**Sodium cacodylate Buffer pH 6.5; 50 mM** (#97068, Merck).

### 3.1.4.11 Designed oligonucleotides

**Mouse:**

**Col1A2 (Collagen type I: alpha 2)**

FW 5'-TGAGACCCTTCTCACTCCTGA-3' / RV 5'-CCTTGGTTAGGGTCAATCCA-3'

**Col1A1 (Collagen, type I, alpha 1)**

FW 5'- CGACCTCAAGATGTGCCACT-3' / RV 5'- CCATCGGTCATGCTCTCTCC-3'

**Col3A1 (Collagen, type III, alpha 1)**

FW 5'- TCGGAAGTGCAGAGACCTAA-3' / RV 5'- TGTTTCCCAGTTTCCATGT-3'

**FN (Fibronectin)**

FW 5'- CCT GCG GTA GTC TCT CCT TG -3' / RV 5'- GCA TCG TAG TTC TGG GTG GT-3'

**HSP90aa1 (Heat shock protein HSP 90-alpha)**

FW 5'- TTCCAGAAGATGAAGAGGAAAA-3' / RV 5'- GTCACCAGTCGGTTTGACAC-3'

**HSP90 ab1 (Heat shock protein HSP 90-beta)**

FW 5'- TCTACTTCATGGCTGGGTCA-3' / RV 5'- AACTCGGGAAGAGCCTGAAT-3'

**Nppa (Natriuretic peptide A)**

## MATERIAL AND METHODS

FW 5'- GGCAGAGACAGCAAACATCA-3' / RV 5'- GTCCCAGTCTGTGTCCCACT-3'

### **Nppb (Natriuretic peptides B)**

FW 5'-TCCTAGCCAGTCTCCAGAGC-3' / RV 5'- CCTTGGTCCTTCAAGAGCTG-3'

### **Smad2 (Mothers against decapentaplegic homolog 2)**

FW 5'-GAGGAGGAACTGTATCAAAGTGC-3' / RV 5'-GGAGCCTTCAGAGTGGACC-3'

### **S14 (Ribosomal protein S14)**

FW 5'- AGTGACTGGTGGGATGAAGG-3' / RV 5'-CTTGGTCCTGTTTCCTCCTG-3'

**Human:**

### **LOX (Lysyl Oxidase)**

FW5'-CAAGGGACATCAGATTTCTTAC-3'/RV5'-CCATACTGTGGTAATGTTGATGA-3'

### **PDGFRA (Platelet Derived Growth Factor Receptor Alpha)**

FW 5'-GCTCTTTACTCCATGTGTGGGA-3' / RV 5'-ATTAGGCTCAGCCCTGTGAGA-3'

### **FN (Fibronectin)**

FW 5'-GGTCTACTCTGTGGGGATGC-3' / RV 5'-TGTGGTGCAGGAGTAGAACG-3'

### **Col3A1 (Collagen, type III, alpha 1)**

FW 5'- GACCAAAAGGTGGATGCTGGC-3' / RV 5'-ACCGTTAGCTCCTGGTTTCC-3'

### **S14 (Ribosomal protein S14)**

FW 5'- GGGGTGACATCCTCAATCC-3' / RV 5'- TATCACCGCCCTACACATCA-3'

### **3.1.4.12 Inhibitors**

**17-allylamino-17-demethoxygeldanamycin (17-AAG)** (#A8476-500UG, Merck).

**Epigallocatechin gallate (EGCG)** (#989-51-5, Merck).

**Tetratricopeptide repeat domain clusters (CTPR)** (Centre for Cooperative Research in Biomaterials CIC biomaGUNE, Prof. Cortajarena, A. Aires Postdoctoral Researcher). Different variants of the CTPR, provided by the collaborating group, will be used during the study. The molecules will be obtained through protein production and purification processes, at the end of which the protein structure of the CTPR will be obtained.

The molecules will be obtained through processes of protein production and purification, finally obtaining the protein structure of the CTPR, to which the component in charge of providing the fluorescence will be added.

#### **- The variants used in the study will be:**

- 1. CTPR390-488:** It will contain a structure composed of TPR modules forming the main protein structure, to which a TPR



module binding to Hsp90 will be added. Additionally, Alexa-488 groups will be added by conjugation to provide the fluorescent characteristic.

2. **CTPR390-Au:** It will contain a structure composed of TPR modules forming the main protein structure, to which a TPR module binding to Hsp90 will be added. In this case of this variant, the fluorophore Alexa-488 was replaced by metallic gold nanoclusters, which will be associated to the protein structure, by means of an intelligent design of the TPR domains, generating regions rich in histidines and cysteines to which they will be associated, providing through these links the fluorescent capacities [137].
3. **CTPR390-488-Au:** It will contain a structure composed of TPR modules forming the main protein structure, to which a TPR module binding to Hsp90 will be added. En esta variante se realizara una combinacion de las tecnologias previas, para la generacion de un CTPR con capacidades fluorescentes mixtas.
4. **CTPR-488-Au:** It will contain a structure composed of TPR modules forming the main protein structure. As with the previous molecule, a combination of the two systems will be used to generate fluorescence. A key aspect in the design of this CTPR will be the removal of the Hsp90-interacting module from the protein structure. The main objective of this variant will be to serve as an additional control in assays against the so-called functional versions, which will contain the Hsp90 binding module.

#### 3.1.4.13 Competent bacteria

**E. coli strain DH5 $\alpha$**  (preparation in house).

**E. coli strain TOP10** (preparation in house).

#### 3.1.4.14 Plasmid library

**pSecTag A**, Mammalian expression vector for the secretion of C-terminally 6xHis-tagged proteins.

**proMMP2**, variant of pSecTagA, with the gene coding for proMMP2 arranged in open reading frame under the control of the CMV promoter (designed in house).

## MATERIAL AND METHODS

**GASpostnAv**, proMMP2 variant with CMV promoter substitution, with a variant of the periostin promoter (POSTN) (designed in house).

**GASpostniii**, proMMP2 variant with CMV promoter substitution, with a variant of the periostin promoter (POSTN), variant taken from the literature [138].

### 3.1.4.15 Heat shock competent cells

**Buffer TFB1**, 100mM KCl, 50mM MnCl<sub>2</sub>, 30mM KAcetat, 10mM CaCl<sub>2</sub>, 15% Glycerol and ddH<sub>2</sub>O (preparation in house).

**Buffer TFB2**, 10mM MOPS, 10mM KCl, 75mM CaCl<sub>2</sub>, 15% Glycerol and ddH<sub>2</sub>O (preparation in house).

### 3.1.4.16 Bacterial culture and Transformation

**Ampicillin**, antiviotic (preparation in house).

**Glycerol 87 %** BioChemica (#A0970, PanReac).

**LB Broth** (preparation in house).

**LB Agar** (preparation in house).

### 3.1.4.17 Antibodies

**Primary:**

Name	Host	Supplier	Catalogue number	Dilution
CTPR	Rabbit	TSS UniOvi	-	1:50
Alix	Mouse	Santa Cruz	sc53540	1:50 1 : 100 1:2000
Flotillin-1	Mouse	Santa Cruz	sc74566	1 : 100
antiCD9	Mouse	Donation from Sanchez-Madrid	-	1 : 100
Smad2/3	Mouse	Santa Cruz	sc133098	1:2000
p-Smad2/3	Goat	Santa Cruz	sc-11769	1:2000
ERK	Mouse	Santa Cruz,	sc-514302	1:1000
p-ERK	Mouse	Santa Cruz	sc-7383	1:2000
GAPDH	Mouse	Santa Cruz	sc-365062	1:5000
Hsp70	Mouse	abcam	ab2787	1:2000
Hsp90 $\beta$	Mouse	abcam	ab53497	1:2000
Hsp90 $\alpha$	Mouse	abcam	ab282108	1:2000
AKT	Mouse	Santa Cruz	sc-55523	1:2000
p-AKT	Mouse	Santa Cruz	sc-377556	1:2000
COL I	Mouse	Santa Cruz	sc-59772	1:1000
COL III	Mouse	Santa Cruz	sc-271249	1:2000
FN	Mouse	Santa Cruz	sc-8422	1:1000
$\alpha$ RSK	Mouse	Santa Cruz	sc-9986	1:5000
TGF $\beta$ RI	Rabbit	abcam	AB31013	1:2000

Table 3 Primary antibodies.

**Secondary:**

Name	Host	Supplier	Catalogue number	Dilution
Anti-mouse	Goat	ThermoFisher	A-21124	1:10000
anti-mouse	Donkey	JIR, USA	715-166-150	1:10000 1:20000
Anti-mouse	Donkey	LI-COR	926-32212	1:10000
Anti-rabbit	Donkey	LI-COR	926-32213	1:10000
Anti-rabbit	Mouse	Santa cruz	sc-2357	1:10000

**Table 4 Secondary antibodies.****3.1.4.18 Restriction enzymes**

**FastDigest Value Pack** (#K1991, Scientific).

**FastDigest DpnI** (#FD1704, Scientific).

**Nsbl (FspI)** (10 U/ $\mu$ L) (#10641811, Scientific).

**Cfr42I (SacII)** (10 U/ $\mu$ L) (#10568180, Scientific).

**FastDigest BgIII** (#10282970, Scientific).

**FastDigest HindIII** (#10101380, Scientific).

**3.1.4.18 Kits used for extraction and purification**

**GeneJET Plasmid Mini-Preparation Kit** (#K0503, Scientific).

**GeneJET PCR Purification Kit** (#K0701, Scientific).

**GeneJET Genomic DNA Purification Kit** (#K0722, Scientific).

**3.1.5 Laboratory equipment****3.1.5.1 Animal handling equipment**

**Scalpel** (#705-001, Medical express).

**Swann-Morton blades** (#705-015, Medical express).

**Absorbable suture thread** (#743-1229, Medical express).

**Non-absorbable suture thread** (#743-21107, Medical express).

**Surgical scissors blunt tip** (#710-988, Medical express).

**Curved scissors** (#710-980, Medical express).

**Syringe** (#791-435, Medical express).

**Syringe 2mL** (#154-001, Medical express).

## MATERIAL AND METHODS

**Syringe 1mL** (#154-030, Medical express).

**Needle 25G** (#740-003, Medical express).

**Mini osmotic pumps 2 and 4 weeks** (#1002 and 1004, Alzet).

**Isofluorane** (#13400264, Animal Housing and Experimentation Service, University of Cantabria).

### 3.1.5.2 Fungible Material

**Pipette tip from 0.1 to 10ul** (#301-01, Deltalab).

**Pipette tip from 2 a 200 ul natural** (#200078, Deltalab).

**Pipette tip from 100 a 1.000 ul** (#200070, Deltalab).

**Serological pipette 2mL** (#612-3704, VWR).

**Serological pipette 10mL** (#612-3700, VWR).

**Serological pipette 25mL** (#612-3698, VWR).

**Glass Pasteur pipettes** (#701, Deltalab).

**Cell culture plates 100mm diameter** (#734-2817, VWR).

**Cell culture dishes 60 mm diameter** (#734-2815, VWR).

**Culture plates multiwell, 6-well** (#734-2798, VWR).

**Culture plates multiwell, 12-well** (#734-2799, VWR).

**Culture plates multiwell, 24-well** (#7734-2800, VWR).

**Millipore® Millicell® cell culture plate inserts** (#Z353086, Merck).

**Cryovials for preservation at -80°C and -140°C** (#409002.1, Deltalab).

**Falcon tube 50mL** (#525-0155, VWR).

**Falcon tube 15mL** (#BDAA352196, VWR).

**Amicon Ultra-15, PLGC Ultracel-PL membrane, 10 kDa** (#UFC901024, Meck).

**Microcentrifuge tubes, Safe-Lock, Eppendorf® 1.5 and 2mL** (#211-2130 and #211-2120, VWR).

**Polystyrene seeding handle** (#10160721, Scientific).

**Cell Scrapers** (#179693, Scientific).

### **3.1.5.3 Equipment used**

**Pipette Eppendorf Research® plus, 1 channel, fixed, 10 µL, clear** (#3124000016, Eppendorf).

**Pipette Eppendorf Research® plus, 1 canal, fijo, 200 µL, amarillo** (#3124000083, Eppendorf).

**Pipette Eppendorf Research® plus, 1 canal, fijo, 1,000 µL, blue** (#3124000121, Eppendorf).

**Pipetboy acu 2** (#015 1, Integra).

### **3.1.5.4 Software**

**Image J/ FIJI** (LOCI, University of Wisconsin, (NIH, U.S.)).

**GraphPad Prism 8.0 Project** (San Diego, CA).

**ClusPro** (docking algorithm ClusPro).

## **3.2 METHODS**

### **3.2.1 Cell Culture, cellular insulation, and maintenance**

During the study, different immortalized cell lines were used, as well as primary cells extracted from tissues. Due to their requirements, a specific maintenance procedure was used for each of them.

#### **3.2.1.1 Standard procedures for all working cell types**

All manipulation of the different cell lines used was carried out following standard procedures for the maintenance of sterility. The cells were handled in a class II laminar flow cabinet, with High-efficiency particulate air (HEPA) filters, allowing a minimum of 10 minutes from start-up to ensure the establishment of laminar air flow. Subsequently, the work surface in the cabin is sterilised by UV radiation and 70% ethanol solution. At the same time, all materials brought into the cabin are sterilised by applying a 70% ethanol solution.

The different cell cultures are kept growing in incubators at 37°C, with 5% CO<sub>2</sub> and in a humid atmosphere. The culture media used together with the necessary supplements are stored according to the instructions of the distributor.

For use, they should be brought to room temperature or placed in a dry bath for 20 minutes before use.

## MATERIAL AND METHODS

### **NIH/3T3 and H9C2 immortalised cell lines**

For the culture and maintenance of cell lines 3T3 and H9C2 (fibroblasts and myocardiocytes respectively), the same medium and supplements are used, DMEM High Glucose medium (4.5 g/l), with L-Glutamine, with Sodium Pyruvate, supplemented with 10% Fetal bovine serum (FBS) and 1% antibiotic Penicillin-Streptomycin.

Periodically, once 80% confluence has been reached in the cell culture, a pass is performed. This process is carried out by discarding the culture medium present in the culture plate, using a vacuum pump, then the culture is washed with a PBS solution (1/5 of the volume of the culture medium used) for a few seconds to remove any remaining medium, and finally the TrypLE compound is added (half the volume of PBS used). The cell-plate dissociation process is completed in the incubator at 37°C after 5 minutes. After dissociation, the cells are resuspended in culture medium supplemented to inactivate the TrypLE compounds, 3mL of medium for every 1mL of TrypLE used.

If it is necessary to plate a specific number of cells per plate for an assay, a cell count shall be performed, otherwise a 1:10 dilution of the cell suspension shall be seeded in a new culture plate.

### **Primary C57BL/6 mouse cardiac fibroblasts**

The isolation is based on the cardiac organ of the mouse obtained in the animal facilities of the University of Cantabria, respecting at all times the current regulations for the use and manipulation of animals.

Once the organ has been obtained, the first step will be to preserve it until its immediate processing in a PBS solution on ice. Prior to the enzymatic treatment, the tissue will be mechanically disintegrated using surgical scalpels. Once the initial dissociation is complete, the organ fragments are immersed in a trypsin solution, vortexing the mixture periodically every 10 minutes, during the 30 minutes that this step lasts. Incubation of the tissue in the solution is carried out at 37°C in the incubator.

At the end of the incubation period, the solution with the cells in suspension is filtered using a 35 µm pore nylon filter, in order to remove any tissue fragments that may remain undissociated. The filtered solution shall be centrifuged at 500 g for 10 minutes to pellet the cells present in the solution. Once pelleted, the medium shall be removed from the falcon tube and the cells shall be resuspended in a solution containing antitrypsin, and this solution shall be plated, distributing the volume obtained in two 60 mm diameter plates. To the plated volume, supplemented culture medium is added until the maximum volume recommended by the distributor is reached. The medium used is DMEM High

Glucose medium (4.5 g/l), with L-Glutamine, supplemented with 10% FBS, 10% Donor Bovine Serum (DBS) and 1% of the antibiotics Penicillin/Streptomycin. The presence of the two serums aims to stimulate and facilitate the establishment of the extracted cells, the cell population obtained is heterogeneous and it will be the culture conditions that will allow us to maintain only the fibroblast populations.

The medium is changed the day after the extraction and the medium is removed from the plate, in which the unattached cells remain. In the course of the first week, cardiac fibroblasts will be the majority cell population in the plaque, displacing others.

Due to the slow growth rate the cells may show, it may be necessary to use a Trypsin Solution 10X, due to the high adhesion the cells may show after a prolonged period of time.

The passages and expansion of the primary cells will be carried out after reaching confluence percentages of around 90%, adapting the number of cells seeded in the new plates to their format, trying to maintain seeding densities of around 40%.

These primary cells were successfully maintained for 10 passages before growth rate and cell abnormalities were observed. Due to the limited expansion of these cells, early passages are used for the assays in which they are involved.

### **Primary human cardiac fibroblasts**

For the culture of these primary cells, a kit containing Fibroblast Growth Medium 3, supplemented with 10% serum FBS and 1% antibiotic (Penicillin-Streptomycin) purchased separately will be used. Due to the characteristics of the culture medium, a change should be made every 2 days, due to nutrient depletion. T75 Flasks are used for the culture of these cells, always maintaining percentages above 40% during the expansion process, avoiding passages before reaching confluences close to 100%.

In order to carry out the tests with these cells, they are used in 4th passages, to avoid morphological abnormalities and affections.

### **Cocultures Model**

In addition to traditional cell culture, variants such as co-culture will be used as a means of analysing the interaction between different cell populations. Using the Millipore® Millicell® cell culture plate inserts, different cell populations will be cultured in the same well, sharing the medium, keeping the cell populations separate by means of a membrane that only allows the nutrients and compounds produced by the cells to pass through.

## MATERIAL AND METHODS

### **3.2.1.2 Cell Freezing**

In order to preserve the different cell lines for future assays, vials with the cell lines preserved in liquid nitrogen are preserved. Attempts are made to cryopreserve cells in low passages.

The process for freezing and preservation of viability begins with obtaining 80-90% confluent cultures. It is important that the cells are in the exponential growth phase before freezing.

Once this confluence has been reached, the cells are dissociated from the culture plate, a count is made, and the final volume needed to have a solution with a cell concentration of about  $4 \times 10^6$  cells is calculated, after which the cells are pelleted by centrifugation at 500 g for 10 minutes, and the medium is then removed. The cells are then resuspended in a solution of pure FBS with 8% dimethyl sulfoxide (DMSO) divided into 1ml cryovials and stored in a freezing container at  $-80^{\circ}\text{C}$  for the first 24 hours. After this time, the vials are transferred to nitrogen containers. Timing is more important to respect with primary cells due to their greater fragility.

### **3.2.1.3 Thawing of cells**

Before removing the cryovial from the liquid nitrogen, prepare the culture plate in which the cells will be seeded with a minimum of 9mL of supplemented medium. The designated volume is necessary to dilute the concentration of DMSO present in the frozen cells from 8% to values below 1%, due to its toxicity. Once this step is completed, the vial is removed and placed in the dry bath for 1 minute. Finally, a micropipette is used to collect the total volume of the cryovial (1mL), and if necessary, supplemented medium can be used to facilitate the use of the entire contents of the cryovial. Finally, gentle cross-shaped movements are made in order to achieve a homogeneous distribution of the cells.

24 hours after plating the cells, remove the medium from the plate, which contains a small concentration of DMSO, wash the cells with 2-3mL of PBS and add fresh medium, in order to remove any remaining DMSO from the culture.

### **3.2.2 TGF- $\beta$ stimulation assay and treatments (CTPR-17AAG)**

Fibrotic marker expression stimulation assays are performed in 6-well and 12-well plates. Three identical wells are prepared from each of the experimental sites, one of which is used for RNA extraction, another for obtaining total proteins for WB analysis and the third is reserved for use in case there is a problem with the previous wells or for other techniques such as microscopy, which will be discussed later.



For the stimulation of the cell culture by TGF $\beta$ , it is expected to reach 60-70% confluence, which is about  $9 \times 10^5$  cells in the wells of the 6-well plates and  $4 \times 10^5$  cells per well in the 12-well plates. Numbers may vary depending on the cell type being used. Prior to the start of the assay, the culture medium of the plates shall be changed with fresh medium supplemented with the defined concentration of the cytokine.

In the first assays, we compared the stimulation of gene expression with different concentrations of the cytokine and at different times, in order to identify the optimal stimulation. Cells were cultured using supplemented DMEM culture medium until the desired confluency was reached, and then the culture medium was changed to Opti-MEM medium during the assay. These assays were performed every time a new stock was started. The TGF $\beta$  concentrations and incubation times used in the assays were 0.3ng/mL and 1ng/mL TGF $\beta$  depending on the stock used, and the incubation times were 8 and 10 hours, to observe the genetic level and change in the expression profile of marker genes.

Once the conditions for optimal stimulation have been identified, the cell cultures will be exposed to the different compounds to be tested, by a single addition of the inhibitors to the culture medium, from the stock solutions, until the desired concentration is reached.

In the cell cultures, confluence 60-70%, TGF $\beta$  a at the aforementioned concentrations was used to simulate a pathological situation and thus exacerbate the expression of fibrotic markers. At the same time, the cells were incubated in the presence of different concentrations (0.4, 0.8, 1 and 2  $\mu$ M) of the CTPR molecule, as well as another commercial molecule 17AAG, whose inhibitory capacity is known, in order to be able to make a comparison of the expression levels between cultures treated with different inhibitors.

The inhibitors were added 1 hour after the addition of TGF $\beta$ , and then the cultures were incubated for 10 hours at 37°C. To reduce interference due to external factors, Opti-MEM culture medium supplemented with 5% serum FBS and 1% antibiotic was used.

### **3.2.3 Cell lysis obtaining total protein extracts-WB analysis**

To obtain the protein extract from a cell culture or tissue, two different buffers, each with its own indications, were used interchangeably.

The DFB buffer was mainly used to obtain extracts from cell cultures, while the commercial buffer RIPA was used for tissue samples, which showed low protein values.

## MATERIAL AND METHODS

In cell culture, an average of 1 mL of the DFB lysis buffer solution is used, after which the cells are lifted from the culture plate and the volume is placed in an **Eppendorf** at 0°C. The solution of DFB and cells is incubated for 30 minutes on ice, after which it is centrifuged at 4°C and 4000g for 10 minutes. This centrifugation process will allow us to separate the cell debris, forming a pellet, from the cytoplasmic protein fraction of interest, located in the supernatant, which will be collected and stored at -20°C until use.

In the case of tissues, RIPA buffer shall be used, following the manufacturer's protocol. Add a total of 1mL of buffer for every 20mg of tissue. Subsequently, using a blender, homogenise the tissue with the lysis buffer, keeping the tube with the mixture on ice at all times. Once homogenised, the mixture is incubated for a further 5 minutes and then centrifuged at 4°C, 4000 g for 10 minutes to separate the cellular debris from the proteins. Finally, the supernatant obtained is transferred to a tube for storage at -20°C until use.

Additionally and specifically in some cell cultures, in parallel to the analysis of the proteins present at cellular level, an analysis of the protein content of the medium will be carried out. This will be done by recovering and concentrating the protein content using Amicon Ultra devices, with a 10kDa membrane. The process for the concentration of the medium is based on a centrifugation process at 4000g in the case of the model used in the laboratory, at 4°C and for 20 minutes, obtaining at the end of the process a volume of 200µL of concentrated medium.

At this point, the protein extract will be available for analysis by different techniques:

### **3.2.3.1 WB assays**

The separation and identification of the proteins, obtained during the extraction and cell lysis process, is carried out by electrophoresis in acrylamide gels of variable percentage, depending on the size of the protein. In this study, 12% gels were used for the analysis of proteins whose size varies between 10-70kDa, and 15% gels were used to obtain a better resolution in the case of proteins at 40kDa.

The amount of protein loaded per well varies 5µg-50µg depending on the purity of the starting sample, and how enriched it is in our protein. Likewise, all samples analysed by this process will undergo an initial denaturation by heating at 100°C for 5 minutes in Laemmli buffer (LB), maintained afterwards by the denaturing conditions of the gels used (SDS-PAGE).

The initial electrophoresis step is carried out at a constant voltage of 120V for 40 minutes and may be left longer if a better separation is required.

Once migration is complete, the proteins present in the gel are transferred to a nitrocellulose membrane, using a wet system, with a constant current of 400mA. The duration of the process depends largely on the size of the protein analysed, following a rule of 1 minute for each kDa of size. During the process of optimising transfer times, reversible staining of the membrane with Ponceau Red solution was used to ensure the transfer of the protein of interest.

Once the transfer has been completed, the membrane is treated with a 10% BSA solution to avoid unspecific binding of the antibodies for 1 hour under agitation, dissolving the BSA in TBST buffer, the same buffer that will be used for the preparation of the antibody solution. Subsequently, once the membrane has been treated with BSA, incubate the membrane in the presence of the primary antibody specific for the protein of interest under constant agitation, at 4°C o/n. At the end of this part, the antibody solution is recovered for future use, and the membrane is washed several times with TBST solution, 10 minutes each time, under constant agitation. Finally, the membrane is incubated with a TBST solution with the secondary antibody, again under constant agitation for 1 hour at room temperature, and then the membrane is washed twice with the TBST solution, to avoid excess of secondary antibody and signal that we can detect.

For the detection and identification of the signal provided by the secondary antibody, an Odyssey® DLX system is used. For the analysis of the bands obtained, the intensity and density of the bands, which is proportionally related to the amount of protein, will be analysed using Image J. Several proteins will be used as loading controls.

### **3.2.4 Total RNA isolation and purification**

For the extraction of total RNA in the different assays, the product NZYol from nzytech was used. NZYol is a ready-to-use reagent that combines a mixture of phenol and other components for the isolation of total RNA. Initially, the culture medium present in the different cultures is removed and stored at -80°C until use. Immediately afterwards, the culture plate is collected without the medium and the necessary volume of NZYol, 1mL, is added, at the distributor's suggestion and to improve extraction and purification, it is stored at -80°C. After this initial incubation, follow the established protocol. To each sample and for each 1 mL of NZYol, add 200 µL of chloroform, incubate the mixture for 5 minutes at room temperature and centrifuge at 12,000 xg for 15 min at 4°C to cause phase separation. Subsequently, precipitate the RNA present in the aqueous phase, the upper phase, add 500 µL of isopropanol followed by incubation for 20 minutes (for better separation it is recommended to incubate at -20°C) and centrifuge at 12,000 xg for 10

## MATERIAL AND METHODS

min at 4°C. The supernatant is then decanted. Subsequently, the supernatant is discarded and the precipitate at the bottom of the tube is washed with 75% ethanol, followed by another centrifugation at 12,000 xg for 10 min, and after removal of the ethanol from the tube, the pellet is resuspended in DEPC water.

Subsequently, after following the extraction protocol, an RNA sample resuspended in DEPC-treated Water. Once purified, the concentration of the solution was measured using the NanoDrop™ 2000, which allows us to measure the degree of purity and integrity of the sample. In addition to collecting outliers, the degree of degradation of the sample will be analysed by migration and visualisation of the samples on a 1% agarose gel.

### **3.2.5 Retrotranscription**

The Thermo Fisher High-Capacity kit is used to obtain cDNA from the extracted RNA. Following the protocol designated by the manufacturer, 2µg of the extracted RNA is used, prepared in a volume of 10µL, to which 10µL of a 2X mix is added, containing all the elements necessary to carry out the retrotranscription reaction (reaction buffer, dNTPs, random primers and the retrotranscriptase). The reaction programme consists of an incubation at 25°C for 10 minutes, followed by 2 hours at 37°C, 5 minutes at 85°C and a final incubation step at 4°C until sample collection. During the reaction, the cDNA sequence is obtained and the RNA present in the mixture is removed.

### **3.2.6 Gene expression analysis by qPCR**

For expression analysis we will use a qPCR kit (SYBR™ Green PCR Master Mix) from Thermo Fisher, consisting of a mix containing all components (SYBR® Green I dye, the dNTPs mix and AmpliTaq Gold® DNA polymerase). The substrate in the reaction will be the cDNA obtained in the retrotranscription, using a 1:10 dilution of the product obtained in the retrotranscription reaction. The programme used is composed of a denaturation step of 5 minutes at 95°C, followed by a banding step of 30 seconds at 60°C and a 5-second run at 72°C. This was carried out on a StepOnePlus™ Real-Time PCR System thermal cycler. completar explicando como los analizamos

### **3.2.7 Refolding assay in the presence of CTPR-17AAG-EGCG**

For the analysis of the effects of Hsp90 inhibitors on its protein folding function, a luciferase refolding assay was performed.

To carry out the assay, the cell lysate was obtained separately from all the experimental conditions, using two commercial Hsp90 inhibitors, 17AAG and EGCG, to which the CTPR was added. Different concentrations were used for all of them (0.4, 4, 40µM).

Once the lysates have been obtained following the process described in the section on **Methods 3.2.3**, the different components shall be mixed and incubated.

The first step will be the measurement of the total protein concentration of the different lysates, both the experimental conditions, with their controls, as well as the commercial control constituted by a pericytes lysate, rich in Hsp90. The aim was to equalise the stock concentrations of the solutions.

Once the concentrations have been equalised, a first 1:3 dilution process of each of the lysates will be carried out, and they will be centrifuged at 25000g for 20 minutes to remove any particles found in the solution. At this point in our case we will have solutions with a protein concentration of 0.1mg/mL.

Subsequently, 10µL of the dilutions of the different lysates are added to each well of a 96-well plate, to which 20µL of deionised water and 10µL of the denatured luciferase (0.5mg/mL) solution and the luciferase reagent (Buffer 7.1), previously prepared, for a final volume of 40µL per well. The reaction is now started and incubated in the dark for 2 hours at room temperature. Finally, after the incubation time has elapsed, 40-100µL of luciferase reagent is added and the signal intensity is measured with the Luminometer.

### **3.2.8 Microscopy techniques**

#### **3.2.8.1 Immunofluorescence assay, confocal microscopy**

The cultures used for this technique were grown on plates, on the bottom of which several coverslips were placed before seeding the cells, in order to encourage their growth on the crystals. Once a confluence in the crystals of no more than 70% has been reached, in order to have a good visual of the cells under the microscope, the crystals were removed with tweezers, always manipulating the edge of the crystals to avoid damaging the cells that had grown on them. The crystals are washed in 1X PBS solution to remove any remaining medium, and immediately afterwards the crystals shall be placed in a 4% PFA solution for 30 minutes, at room temperature and with slow agitation. The crystals with cells should be kept in the dark throughout the process, in the case of working with any fluorescent molecule present in the sample.

After inclusion in 4%PFA, the crystals are washed in PBS1X briefly and the crystals are immersed in a solution of PBS1X with 0.5% Triton X-100, to permeabilize the sample and allow access of the antibody to the cell interior, for 30 minutes, at room temperature and slow agitation. Subsequently, 3 washes are performed, under the same conditions, consecutively for 5 minutes, each one, under agitation in a solution of PBS1X with 0.05% Tween-20 (PBS-T). At this point, the sample is prepared for incubation with the primary

## MATERIAL AND METHODS

antibody. A dilution of the primary antibody is prepared, which is usually 1:100, although it may vary with the antibody used, follow the manufacturer's instructions, to optimize the amount of antibody, 10µl of the solution is placed on each crystal, the surface tension will allow the solution to remain in the crystals. Incubation shall be o/n at 4°C, and to avoid evaporation of the antibody, the crystals shall be incubated in a humid chamber. The following day, the sample is washed three times with PBS-T washing solution, at room temperature and shaking, to remove any remaining primary antibody on the sample, and then the sample is incubated with the secondary antibody (1:1000) for 30 minutes at room temperature and in the dark, and finally the sample is washed with PBS1X and mounted with prolonged DAPI or without DAPI.

During the whole process it is very important that the sample with the cells never dries out completely, as this could affect the signal emitted by the sample.

### **3.2.8.2 Internalisation , Microscopic observations**

The samples obtained for this assay shall be treated according to the guidelines described in the methods section "Immunofluorescence assay, confocal microscopy", once the desired confluence and incubation time of 10 hours had been reached.

The samples used in this assay have been incubated in the presence of two variants of the CTPR molecule used in the assay. On the one hand, the CTPR molecule was used, consisting of a protein structure formed by the TPR modules, bound with the Alexa 488 flourophore, and on the other hand, a variant was also used, consisting of the protein structure formed by the TPR repeats, inside which gold nanoclusters are found, which will be responsible for providing the fluorescence to the sample. In both cases, due to the fluorescent signal of the CTPRs, the samples will be processed in the dark to avoid signal loss by bleaching.

### **3.2.9 Three-dimensional cardiac fibroblast culture construction and experiments**

The use of human organoids in experimentation has long proved to be a very attractive experimental model. Its versatility in allowing us to generate miniaturized and simplified versions of organs lets us to study cell behavior in conditions similar to those native to the tissue, while maintaining a controlled environment. In this study, we worked collaboratively to learn and generate a 3D culture, aimed at mimicking cardiac connective tissue.

The model selected for use was developed at the Institute of Pharmacology and Toxicology of the Medical University of Goettingen under the direction of Prof. Dr. med. Wolfram-Hubertus Zimmermann.

### **3.2.9.1 Flexible ring-shaped model**

The model used consists of a matrix made up of a bovine collagen solution, which will provide the support for the cells. The structure elaborated to support the organoid will be placed in the wells of a plate constructed and designed for this purpose by Tim Meyer, and marketed by Startups myriamed GmbH. The company in charge markets plates with the same design, but with a difference in the stiffness of the columns, due to changes in their composition. On the advice of our collaborators, we experimented with the model called TM5.

The design of the plaque consists of the following elements:

- 48-well plate, with a working volume of 500 $\mu$ L per well.
- A removable structure, consisting of two columns, well defined and joined at the base.
- A lower cavity in which the structure will fit with the columns.
- An upper head, where all the manipulation of the culture will be carried out.

### **3.2.9.2 3D cell culture model generation**

For the elaboration of the organoid we need 4 main components, the bovine collagen solution, with a concentration of 6mg/mL, a 2X DMEM solution, the solution with the cells and finally a 0.2M NaOH solution to regulate the pH.

For the correct polymerisation and gelation of the organoid, it is necessary to maintain a strong control on parameters such as temperature or pH of the mixture, therefore it is extremely important to keep the temperature low (4°C), by using ice in the case of solutions, or directly cooling the consumables to -20°C, such as pipette tips or tubes that may come into contact with the solutions shortly before their use, in order to avoid premature gelation of the mixture.

With these basic handling considerations in mind, the protocol followed is described below.

The first step is to prepare two of the main elements mentioned above:

- The 2X DMEM and the cell solution. The DMEM 2X solution contains 20% FBS and 2% antibiotic Penicillin/Streptomycin. The reason for preparing it at a higher concentration than normally used in laboratory tests is due to its role

## MATERIAL AND METHODS

in regulating the osmolarity changes that the mixture may undergo due to the action of the collagen solution to be used and which may affect not only the gelation process, but also the cell population of the culture.

- The necessary number of cells for the tissues must also be available. This cell population will be in pass 4, and will have been resuspended in FGM3 medium supplemented at a concentration of  $9.056 \times 10^6$  cells/mL.

The combination of the components should be done in a pre-established order, with DMEM 2X being the initial one, followed by the addition of the collagen solution at 6mg/mL and 0.2M NaOH. Once this step has been reached, the mixture should be homogenised gently and smoothly before proceeding. In the case of collagen, it is advisable to use micropipette tips with a wide mouth to avoid the formation of bubbles and damage to the collagen fibres, and the addition of the NaOH solution should be progressive as the colour of the solution changes from yellow to red, indicating a pH of 7-8.

Once the mixture is ready, the cell solution is added, in the volume necessary to obtain a final cell concentration of  $0.75 \times 10^6$  cells/mL.

The final volume for each organoid is 180uL, of which 46.52uL of collagen solution, 46.52uL of DMEM 2X solution, 4uL of NaOH and 82.96uL of cell solution.

The designated volumes may vary depending on the concentrations of the stock solutions used. These amounts correspond to the working concentrations used.

Once the mixture has been prepared, all that remains is to distribute the 180uL of the mixture around the two columns in a circular motion.

Once finished, the mixture is incubated for 1 hour inside the incubator at 37°C, this is because the optimal solidification conditions are physiological, hence the maintenance of the osmolarity, pH and temperature during the process.

### **3.2.9.3 Organoid rheological analysis**

For the analysis of the mechanical properties of the generated organoid, the 3D model will be subjected to a stress process in an RSA-2 rheometer. The process consists of placing the ring-shaped organoid around two prongs, one of which is fixed, and the other is placed on a movable arm.

During the whole process the organoid will remain in a chamber generated around it, to keep it immersed in a DPBS1X buffer solution at 37°C, in order to maintain optimal



hydration and to maintain stable measurement conditions, to reduce disturbances in the system as far as possible.

Once the process has been started, the probe located on the movable arm will start to move, generating a constant stretching of the organoid at 0.03mm/s. This process will continue until the organoid ruptures. During the whole process the device will keep track of the tensile strength and resistance offered by the organoid. The data collected during the process can be represented in a curve, similar to the one shown in **Figure 6**, in which three well-defined areas can be identified, the **toe region**, the **elastic region** and the **plastic region**.

The regions of the curve of interest, because it is from these that the parameters to be evaluated are obtained, are the elastic region, the end of which would be identified by the yield point, identified in **Figure 6**, and the plastic region, which would be between the yield point and the failure point **Figure 6**. From the elastic region, we obtain the parameters of **Young's modulus**, which represents the slope of the curve in that region, and which shows us information about the elasticity of the organoid (higher values = steeper slopes, which indicates a lower elasticity of the model) **Figure 6**. Also, by measuring the area under the curve in that region, the **Resilience** will be obtained, this parameter will show us the amount of force that the organoid can absorb before suffering an irreversible deformation (it gives us an idea of the robustness of the system against stress situations). Finally, the last parameter analysed will be obtained by calculating the area under the curve of the plastic region, which will give us an idea of the energy that the system is capable of absorbing before collapsing and breaking, this parameter will be the **Toughness**. In addition to the aforementioned points, the ultimate strength point, which indicates the point of greatest resistance during the measurement process, is also worth mentioning.

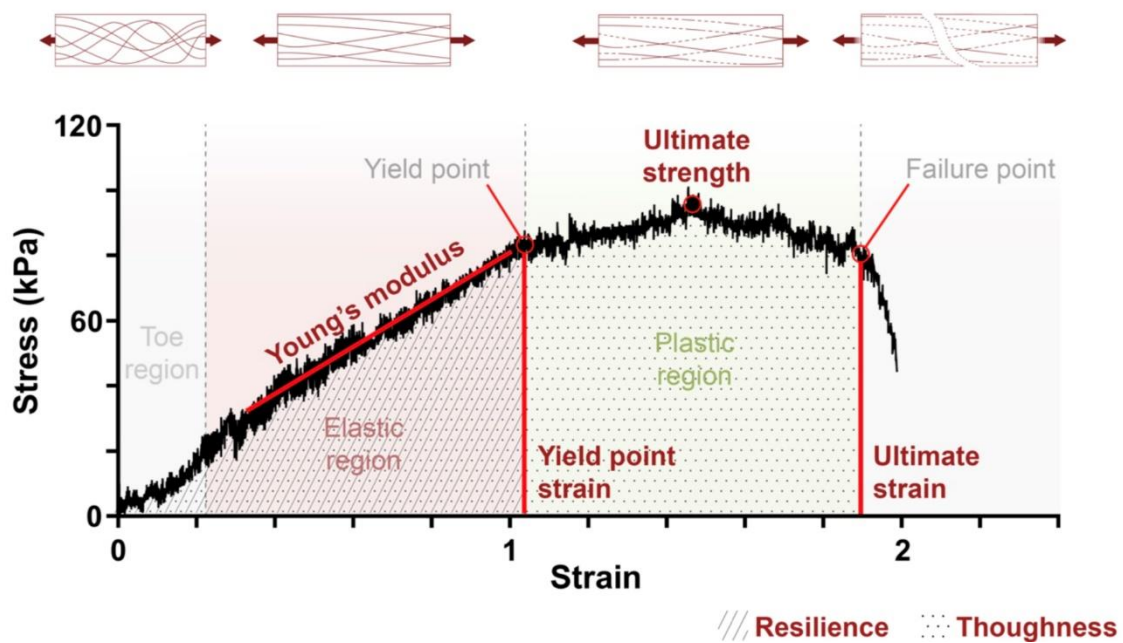


**Figure 6 Stress curve obtained after rheological measurements.** It would identify the Toe region (it would represent the first phase in which the organoid is not yet stressed by the apparatus). Then we would have the elastic region whose end would be indicated by the Yield point, in it through the calculation we would obtain the Young's modulus, related to the elasticity of the 3D model, the area under the curve of this region would provide the resilience (parameter related to the stability of the system against external stress). Between the Yield point and the Failure point, the plastic region would be located, in which the Ultimate strength (point of minimum stress) can be identified and by measuring the area under the curve we would calculate the hardness parameter, which would be related to the amount of energy that the system can absorb. The failure point would represent the point at which the organoid suffers a rupture [139].

### 3.2.10 Genetic Alert System (GAS) Plasmid Construction

#### 3.2.10.1 Cloning procedures

The plasmid constructs generated in the laboratory followed the Isothermal assembly (IA) procedure. The starting construct used as a template has been designed by members of the research group, which, starting from the commercial plasmid psectaq, originated the plasmid called proMMP2, which consisted of the introduction of the MMP2 gene under the control of the cytomegalovirus (CMV) promoter.

#### 3.2.10.2 Isothermal assembly

The process defined as isothermal assembly is a one-step cloning process, which dispenses with the action of restriction enzymes. This process is based on the generation of DNA fragments, the ends of which show a high level of homology between them.

The proposed constructs are based on the substitution of the CMV promoter, present in the proMMP2 plasmid, by different variants of the POSTN gene, enabling us to maintain gene expression, but allowing us to maintain greater control in relation to the time of expression.

For the amplification of the DNA fragments, the Phusion High-Fidelity DNA Polymerase kit (Thermo Scientific) was used, in combination with primers designed for the generation of the fragments, with a length of about 40 nucleotides. For its design, the proMMP2 plasmid sequence was used as template DNA to obtain the vector fragment, and the MGI:MGI:1926321 mouse genome was used as template for the primers that amplified the different fragments of the POSTN promoter.

With the primers designed, the next step is the amplification of the fragments themselves using the purified proMMP2 plasmid and the mouse genome of the C57/BL6 strain. Once the fragments are obtained and before starting the technique, the fragments are purified to eliminate any background contamination generated by the moulds used, in the case of the linearised vector, the Thermo Scientific DpnI restriction enzyme is used and in the case of the fragments, an electrophoresis is carried out to check if any prior purification step is necessary and if necessary, the Thermo Scientific GeneJET PCR Purification Kit is applied to purify the PCR product.

With the purified fragments we proceeded with the Isothermal assembly, due to the variety in the size of the fragments and their influence on the reaction, different insert/vector ratios were tested. The reaction components to work with would be: 5uL of the vector/insert mixture together with 15uL of the Isothermal reaction mixture containing T5 exonuclease (NEB), Phusion High-Fidelity DNA Polymerase (Thermo Scientific) and the Taq ligase (NEB) together with the buffer (1M Tris-HCL pH7.5, 2M MgCl<sub>2</sub>, 100mM dNTPs, 1M DTT, 1.5g PEG 8000 and 100mM NAD).

Incubation time would be 1 hour at 50°C in a thermocycler, followed by microdialysis of the sample for a minimum of 30 minutes. Finally, competent bacteria will be transformed with the obtained product, and a PCR verification of those selected will be performed, having as a last step the sequencing of the construct.

### **3.2.11 Analysis of MMP2 functionality and localisation by zymography assay**

The zymography technique is intended to detect and assess the presence of proteolytic enzymes capable of degrading gelatin. Among the enzymes with this capacity we will highlight MMP9 and MMP2. The latter, as already mentioned, is the metalloproteinase whose gene is present in the GAS constructs and variants, so the aim is to assess the functionality and quantity of this protein that the system is capable of producing.

This technique consists of a migration phase in an acrylamide gel, for common proteins, in which the proteins are separated by size. The gel composition for the separation will

## MATERIAL AND METHODS

also consist of a specific compound for this technique, pig skin gelatin (Merk) at a concentration of 2.65 mg/mL.

Once the migration phase is finished, the gel will be washed and incubated for 1 hour under gentle agitation, to eliminate denaturing agents and facilitate the renaturation of the proteins in the gel, the solution "A" used consists of 2.5% TritonX100, 50mM TrisPH7.4, 5mM CaCl<sub>2</sub> and 1mM ZnCl<sub>2</sub>. After renaturation it will be necessary to remove the residual solution in the gel, and it will be incubated again at 37°C or/and embedded in a solution "B" with TritonX100, 50mM TrisPH7.4, 5mM CaCl<sub>2</sub> and 1mM ZnCl<sub>2</sub>. The presence of Zn is necessary as it is a catalytic component of matrix metalloproteinases such as MMP2. Once the incubation is finished and by using a 0.5% coomassie solution and 10 minutes of incubation under agitation, it will be possible to visualize any band resulting from gelatin degradation in the gel, product of the gelatinases presents in the analyzed sample, being able to analyze the intensity and size of the band and relate it to the amount of relative protein present in the sample in comparison to a control. If necessary and if the signal appears to be weak, a wash at the end of the process to remove excess staining is possible.

### **3.2.11 Animal handling procedures and protocols**

The extraction process was carried out the animal facilities of the University of Cantabria, respecting at all times the current regulations for the use and manipulation of animals. At all times, qualified personnel were on hand to assist with animal handling and procedures.

#### **3.2.11.1 Extraction of cardiac tissue for primary cell isolation**

The animals were anaesthetized by inhalation of a mixture of isoflurane and O<sub>2</sub> prior to sacrifice by cervical dislocation.

Once the animals were sacrificed, the extraction process was carried out immediately, by means of a cut in the thorax area, allowing access to the diaphragm, the heart being located between the lungs and in front of the esophagus and the aorta.

The removal of the cardiac organ was performed by excising the organ from the main veins and arteries, immediately placing it in a PBS solution on ice, and then transferring the organ for processing.

#### **3.2.11.2 Mini-osmotic pump implantation surgery**

For the generation of the in-vivo hypertensive model, mini-osmotic pumps are used, containing a solution of Angiotensin II 7mg/mL, which is released in a maintained and controlled manner for periods of time ranging from 2 to 4 weeks, depending on the model

used. The mini-pumps were implanted subcutaneously, at the level of the scapulae, and the incision was then sewn with suture thread. At all times, the aim was to avoid causing discomfort in the mobility of the mouse, due to the implantation of the device.

### **3.2.11.3 Compound administration**

All drug delivery, independent of implanted devices, is by intraperitoneal injections.

## MATERIAL AND METHODS

## 4. RESULTS

### 4.1 Detection of CTPR and its interfering with the key signalling pathway of cardiac fibrosis *in vitro* and *in vivo*

The first studies related to CTPR are performed with CTPR conjugated to the fluorophore Alexa 488 (CTPR390-488) (Methods **3.1.4** section **Inhibitors**). The main features of all CTPR molecules used in this study include the specific Hsp90 binding capability by binding to the MEEVD motif located at the carboxyl-terminal end of Hsp90. CTPR390-488 presents fluorescence due to the fluorophore Alexa488 conjugated to the particle [140].

The results presented in this section will focus on the *in vitro* and *in vivo* evaluation of the behaviour of CTPR390-488 on reducing cardiac fibrosis.

#### 4.1.1 Cellular location of CTPR390-488 in cell culture primary cardiac fibroblasts and observation of fibroblasts ultrastructural changes

It is known that Hsp90 $\alpha$  and  $\beta$  present different locations within the cell. The classical cytoplasmic presence of Hsp90  $\alpha$  and  $\beta$  isoforms [141], its relatively new detection of their nuclear translocation [142]; and the location of Hsp90 in close proximity with TGF $\beta$  signaling effectors [140, 143], such as TGF $\beta$ RI at the plasma membrane or internalized [140, 144]. There are also other Hsp90 isoforms such as Trap1 located in mitochondria [145] or GRP94 endoplasmic reticulum resident isoform [146]. The isoforms Trap1 and GRP94 do not include the MEEDV domain at the C-terminus, thus CTPR390-488 do not have the capability of binding these isoforms, thus it is not expected to be in those organelles.

##### 4.1.1.1 CTPR390 detection in fibroblasts

We tested the cellular internalization capacity of CTPR390-488 at concentrations of 0.2, 0.4 and 0.8 $\mu$ M in cultured fibroblast. The distribution of the CTPR between the extracellular and intracellular fractions was visualized by WB (**Figure 7A**) obtaining significant differences compared to control cells (**Figure 7B**) intracellular CTPR390-488 vs control \*\*p<0.005, extracellular CTPR390-488 vs control \*\*\*p<0.001 (**Figure 7B**).

WB analysis revealed that the CTPR390 antibody generated specifically for this molecule did not detect any endogenous TPR domain present in a wide variety of cytoplasmic proteins [140] (**Figure 7**). It also revealed that although internalisation occurs, it represents a small percentage of the total CTPR390-488 (**Figure 7B**). WB images

## RESULTS

indicate the higher amount of extracellular CTPR390-488 compared to the cytoplasmic fraction.

CTPR390-488 added to cell ( $\mu\text{M}$ )	Absorbance (A.U.)		Autofluorescence (A.U.)	
	%	<u>SD</u>	%	<u>SD</u>
0.0	0.0	0.0	0.0	0.0
0.2	7.5	1.0	7.3	5.9
0.4	10.8	1.7	8.6	6.7
0.8	8.4	1.3	9.8	3.4

**Table 5** CTPR390-488 internalisation rates measured by absorbance and autofluorescence, 24 hours after its administration.

**Table 5** shows the percentage of CTPR390–488 internalization detected by, autofluorescence and absorbance (**Table 5**). The quantification analysis indicates that the 92,70-89.1 $\pm$ 1,350% of CTPR-488 is outside the cell and that the 10.8-7.3 $\pm$ 1,350% of CTPR390-488 is maintained 24 hours after the treatment (**Table 5**).

Moreover, in order to check the stability of the molecule at the cellular level, samples were analysed (**Figure 7D**). The CTPR390-488 autofluorescence and the fluorescent signal of the immunofluorescence assay using specific antibody against CTPR390-488, presented colocalisation (**Figure 7D**), showing not only that the Alexa-488 fluorophore remains associated with the CTPR390 molecule, but also showing the absence of unspecificity coming from TPR endogenous domains present in a wide variety of cellular proteins [140], or any other sources when detecting CTPR390-488 by either autofluorescence or immunofluorescence (**Figure 7D**).



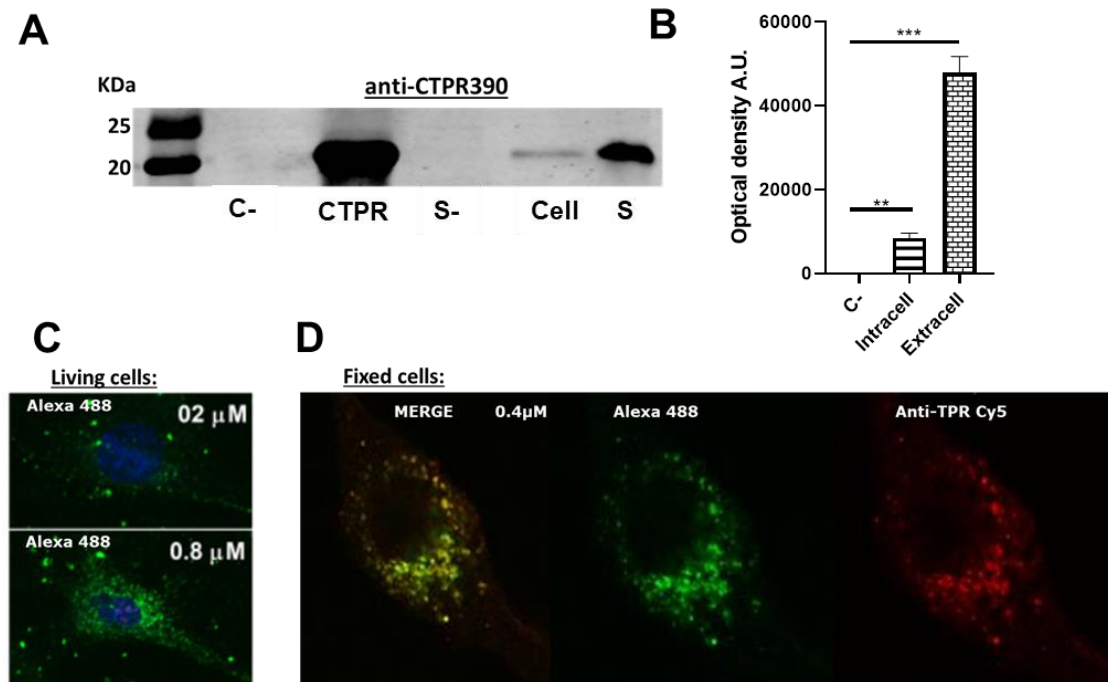


**Figure 7 CTPR detection in fibroblast.** (A) WB of TGF $\beta$ -activated fibroblasts (0.3 ng/ml of TGF $\beta$ ) incubated in the presence of CTPR390-488. **C-** indicates the negative control lysate used from a cell culture without the CTPR molecule. **CTPR** shows its signal in a pure solution. **S-** indicates supernatant collected from the culture used as a negative control. **Cell** would refer to the cell lysate from cells incubated with CTPR. **S** would show the supernatant from cell cultures incubated in the presence of the CTPR. (B) Measurement of the signal intensity through image J software to define the differences between intra and extracellular CTPR390-488, optical density signal obtained in the WB in arbitrary units (A.U.). The mean value corresponds to 3 independent WB experiments (\*\* $p < 0.005$ , \*\*\* $p < 0.001$  Mann–Whitney (C,D) Observation by confocal microscopy of in vivo cultures (C) and cells fixed (D) in the presence of CTPR390-488. (D) Fixed cells do not show extracellular CTPR390-488. and a specific antibody against the synthetic molecule was used. Adapted from (Cáceres, R. A. et al 2018).

#### 4.1.1.2 Cell viability in the presence of CTPR390

Once verified the internalization of CTPR390-488, we checked CTPR390 cellular viability. Hsp90 is a well-studied chaperone, with great importance in the maintenance of cellular homeostasis. Being Hsp90 the target of CTPR390, there is a risk of nullifying its homeostasis-dependent functions, as is the case with other Hsp90 inhibitors used in cancer therapies such as geldanamycin, or the improved (less toxic) 17AAG, 17DMAG [147, 148]. These commercial compounds bind to Hsp90 at the amino-terminal domain, where the main ATPase activity of the chaperone is located.

CTPR390 addresses the MEEDV C-terminal end of Hsp90 protein [149]. We will test whether MEEDV inhibition reduces the activity of the TGF $\beta$  signaling cascade, without affecting the ATPase domains of Hsp90, where the basis of chaperone activity and thus much of cellular homeostasis lies.

## RESULTS

We conducted cell proliferation assays performed in NIH/3T3 fibroblasts (**Figure 8A-D**) and cardiac primary fibroblasts (**Figure 10E-H**), using 17AAG (**Figure 8C,G**) and CTPR390 (**Figure 8D,H**) as inhibitors, at concentrations of  $0.8\mu\text{M}$  (**Figure 8C-D** and **G-H**), after an incubation period of 2 days, controls cells and cells treated with CTPR390-488 showed similar appearance in both cell types. Cells with 17AAG showed a greater number of cells in suspension (death cells), a situation typical of culture under stress conditions. These observations were supported by the cell counts of the cultures, which show a significant decrease in the total number of cells only in the 17AAG-treated group compared to TGF $\beta$  controls or CTPR390-488 treated cells ( $2.8 \times 10^6$  vs  $4.03 \times 10^6$  or  $4.2 \times 10^6$ ,  $*p < 0.05$ ) (**Figure 8I**).

These assays were performed with CTPR-488, however, they can be extrapolated to other variants such as those containing metal nanoclusters, as studies have shown similar action in fibroblasts [150].

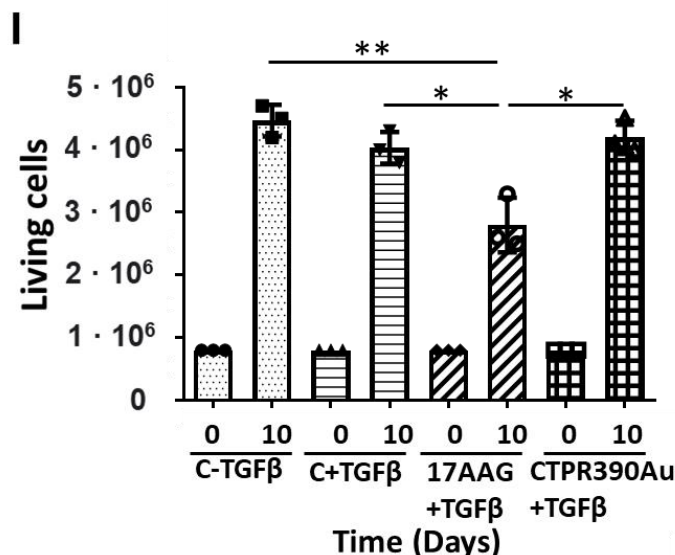
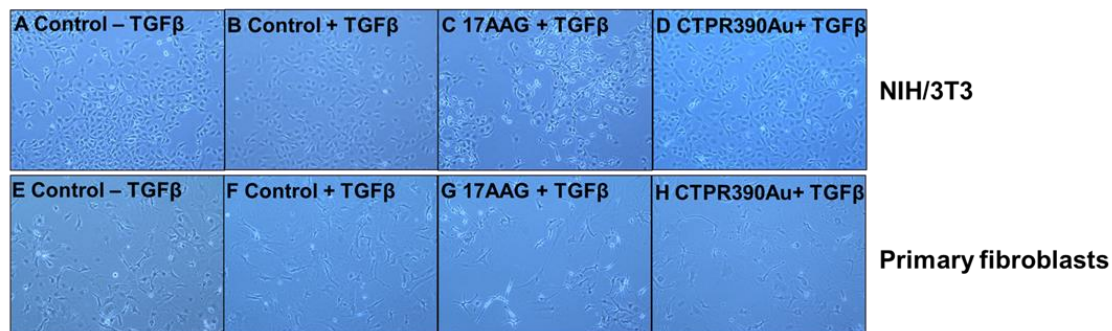


**Figure 8 Analysis of fibroblasts viability through 24 hours cell proliferation assays under conditions of Hsp90 inhibition.** NIH/3T3 fibroblasts (**A-D**) and cardiac primary fibroblasts (**E-H**), (**A,E**) Control cells in the absence of TGF $\beta$ . (**B,F**) Control cells treated with  $0.3 \text{ ng/ml}$  of TGF $\beta$  for 24 hours. (**C,G**) Cells treated with  $0.3 \text{ ng/ml}$  of TGF $\beta$  and  $0.8\mu\text{M}$  of 17AAG for 24 hours (**D,H**) Cells treated with  $0.3 \text{ ng/ml}$  of TGF $\beta$  and  $0.8\mu\text{M}$  of CTPR390 for 24 hours. (**I**) Counting of the total number of live cells on the culture plates using trypan blue to detect death cells and cell counter to evaluate living cells methods of the samples from **A-H**.  $*p < 0.05$ ,  $**p < 0.005$ ; Mann-Whitney test.

Epigallocatechin-gallate (EGCG) is another commercial Hsp90 inhibitor with its binding site in the carboxyl-terminal ATPase domain thought to place some action on the folding functionality of the chaperone [147, 151]. We evaluate the chaperone activity of Hsp90 through assays to measure Hsp90 refolding capability of denatured proteins. This refolding test measures the ability of Hsp90 to refold client proteins. Luciferase, which is one of the client proteins of Hsp90 will be used to test the refolding activity of Hsp90. The assay was performed in different fibroblast cell lysates, treated with the inhibitors 17AAG, EGCG and CTPR390 at concentrations of 0.4, 4 and 40 $\mu$ M.

Reticulocyte lysates, composed of a lysate of pericytes, are samples with high amount of Hsp90, thus an optimum positive control to compare the results of cardiac fibroblast samples. Another positive control (C) was a culture of TGF $\beta$ -activated cardiac fibroblasts. The results related to the refolding capacity of Hsp90 (**Figure 9**) do not show a significant deterioration in Hsp90 chaperone activity at different working concentrations (0.4, 4 and 40 $\mu$ M), in samples containing CTPR390 or EGCG, however in samples containing 17AAG a significant decrease of the ATPase-dependent refolding activity at all concentrations (0.4  $\mu$ M, \* $p$ <0.05) (4 and 40  $\mu$ M, \*\* $p$ <0.005) was observed.

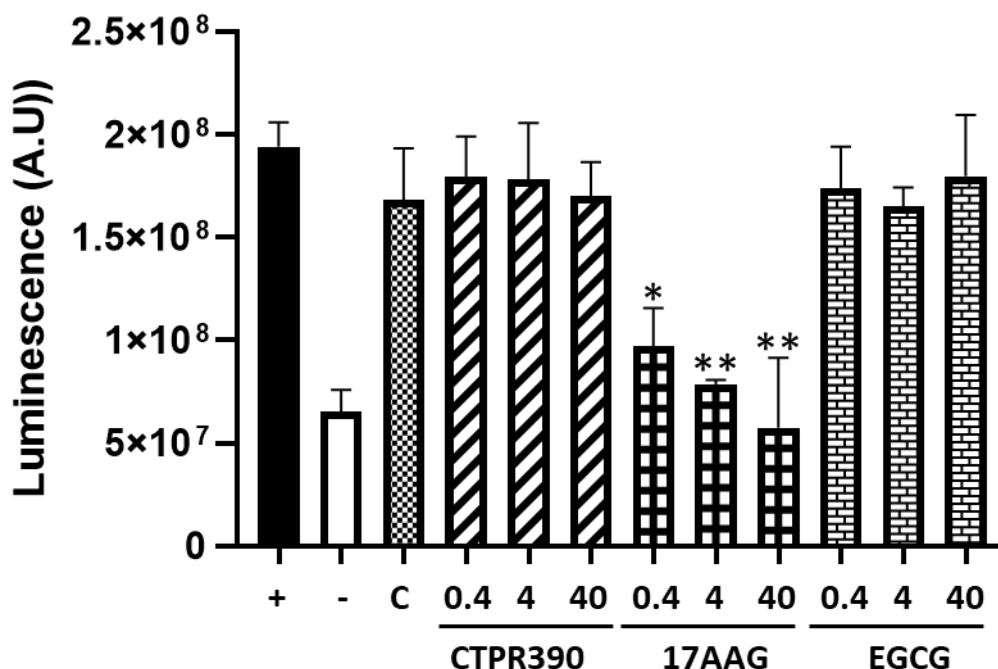


**Figure 9 Luminescent analysis of Hsp90 refolding activity in the present of Hsp90 inhibitors.** Hsp90-dependent refolding activity of lysates from myocardial fibroblasts in the presence of CTPR390–488, 17AAG and EGCG at different concentrations (0.4, 4 and 40  $\mu$ M); the negative control (-) was denatured luciferase at a concentration of 0.5mg/mL, the positive control (+) corresponded to rabbit reticulocyte lysate (protein concentration 0.1mg/mL) and the second control (C) corresponds to myocardial fibroblast lysate activated with TGF $\beta$  (0.3 ng/ml). Mean values in arbitrary units (A.U.) correspond to 3 independent assays. (\* $p$ <0.05, \*\* $p$ <0.005; Mann–Whitney test).

## RESULTS

### 4.1.1.3 CTPR induces fibroblasts ultrastructural changes

To observe the effects of the synthetic molecule CTPR390 at the ultrastructural level, EM techniques were used, observing the presence of the molecule at the cytoplasmic level in detail (**Figure 10**). The CTPR used in this part of the study includes apart from the fluorophore Alexa488, a gold cluster that will be crucial for the evaluation of the *in vivo* assays. The ultrastructural location of CTPR390 can be visualized through the fluorophore Alexa488 conjugated to the cluster.

The enlarged ERs (marked by arrow 2 in **Figure 10B**) observed in TGF $\beta$ -activated fibroblasts, indicated a general protein synthesis overexpression which is a regular event on activated fibroblasts to synthesized and secrete ECM fibres, mainly collagen (marked by arrow 1 in **Figure 10B** and arrow 3 in **Figure 10C**) [140]. CTPT390-treated cells presented basal ER size (**Figure 10D**) without the engrossment observed in the TGF $\beta$ -activated control cells (**Figure 10B**). Another observation in this case related to the intercellular collagen deposition is the reduction of collagen molecules visualized between fibroblasts in CTPR390-treated cells (marked by arrow 4 and 5 in **Figure 10E,F**) compared to non-treated ones (**Figure 10B,C**) [140]. For visualisation and verification of the presence of the CTPR at the intracellular level, magnified images of the cellular interior were taken, detecting the presence of the CTPR at the cytoplasmic level (marked with a C **Figure 10G**), using Immunogold labelling (marked by arrows **Figure 12G**).

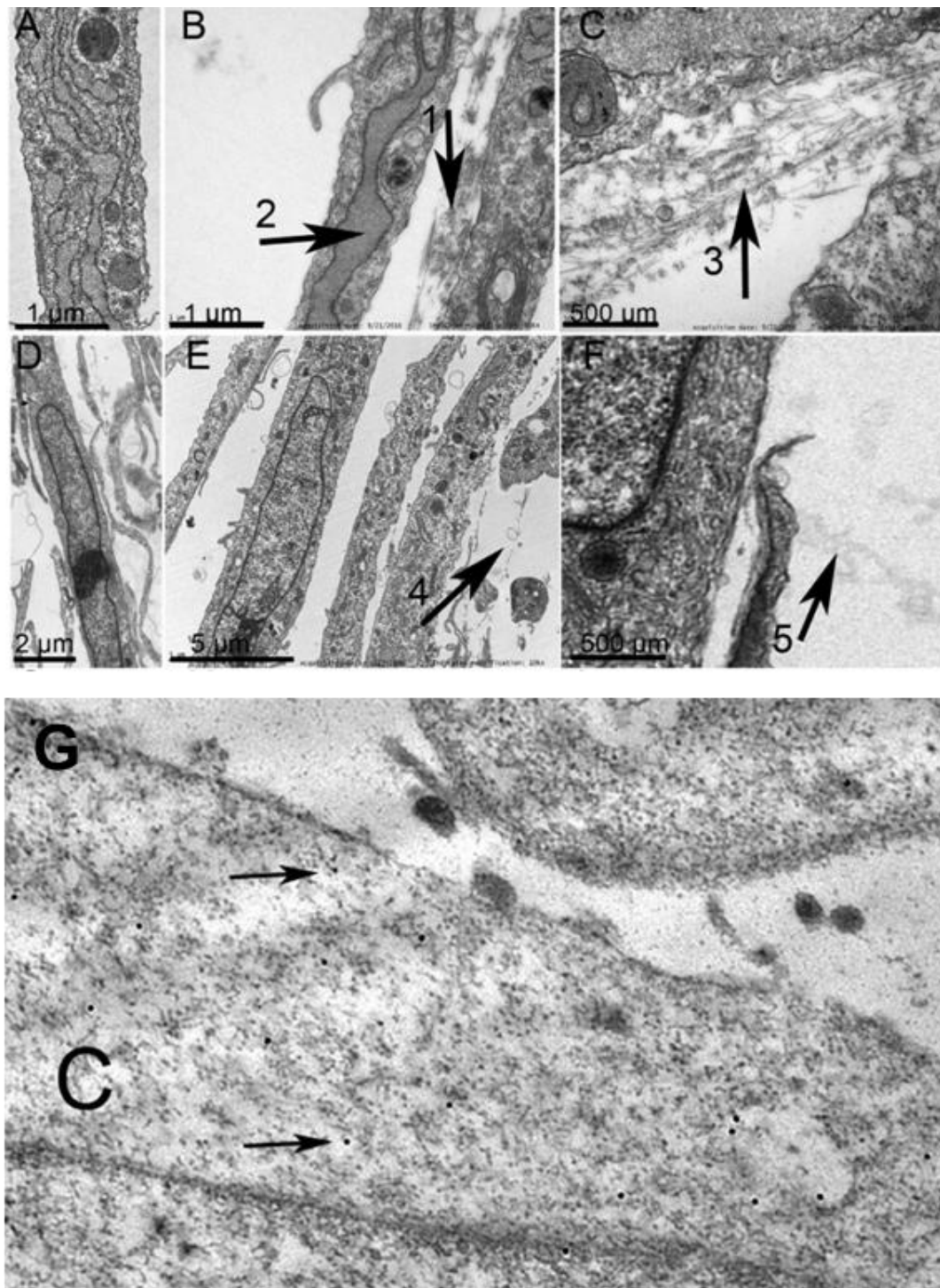


**Figure 10 Electron microscopy assays to detect fibroblasts ultrastructural changes of CTPR390-treated cells and CTPR390 localization.** (A) TGFβ-treated (0.3 ng/ml) fibroblasts with ER engrossment. (B) Detail of panel A in which arrow 1 marks intercellular collagen deposition and arrow 2 marks the engrossed ER. (C) Arrow 3 shows a detail of the deposited collagen showed in panel B by arrow 1. (D) TGFβ-activated fibroblasts treated with CTPR390 (E, F) Absence of intercellular deposited collagen marked by arrows 4 and 5 in TGFβ-activated fibroblasts treated with CTPR390 and incubated with CTPR390. Horizontal black bar indicate the electron microscopy magnification used (1 μm-500 μm) (G) Image of the cell cytoplasm "C" of a CTPR-treated fibroblast, using EM immuno-gold against CTPR390, visualised as electrodense particles, black dots (two of them marked by arrows). Adapted from (Cáceres, R. A. et al 2018).

## RESULTS

For a deeper study of the ultrastructural changes developed by fibroblasts in the presence of CTPR390, a 3D tomography was performed. We wanted not only to unveil changes in key cellular organelles but also describe in full detail CTPR390 location within the cell.

Higher resolution techniques such as cryo-3D-SIM and cryo-SXT techniques (never combined before to localize potential drugs inside the cell) were used to generate a reconstruction tomography at native conditions due to the cryopreservation of the cells and absence of fixation that could alter the real conformation and morphology of the cell.

Identification and visualisation of the effects of CTPR390 treatment in NIH/3T3 and primary fibroblast was carried out using the activation conditions of 1ng/mL TGF $\beta$ , and incubation time to 48 hours, and with a CTPR390-488-Au concentration of 0.8 $\mu$ M (the concentration and time parameters used showed by expression analysis increases in markers such as collagen comparable with the previously used conditions of 0.3ng/mL and 24 hours, results shown in the control groups versus those treated with inhibitors, in **Figure 17A, B and C**. In addition, due to the sensitivity of the analysis, long incubation times are used to ensure stability and the absence of stress caused by factors external to TGF $\beta$  stimulation, such as the handling process).

CTPR390-488-Au fluorescent signal was correlated, to cmxros mitotracker (mitochondria marker) to guide the correlative tomography. The samples analysed showed an increase in the number of multivesicles bodies (MVB) detected in the cell interior compared to controls, these vesicles contain CTPR390-488-Au, distributed homogeneously throughout the cytoplasm (**Figure 11E**). It is important to describe if those vesicles participate in apoptotic processes more related to cell elimination of the exogenous agent CTPR390 of generation of toxicity leading to apoptotic signals or they are joining the cell trafficking events to perform an intracellular action in the present or other cells once the intracellular traffic reaches other cells. For this purpose, the use of membrane markers will be used at a later stage.

The samples obtained using X-ray, were analysed in 2D projections of a single cell (**Figure 11A**) and selected areas of the same cell (**Figure 11C**). 2D projections were overlaid with cryo-SIM projections to obtain the superposition of the fluorescent signals from CTPR390-488-Au in green and mitochondria marker in red with the 3D tomogram (**Figure 11B and D**). By doing this a correlation between the fluorescent signal of CTPR390-488-Au, the mitochondrial membrane marker cmxros, and the X-ray projection of the same cell is provided. Subsequently, a 3D reconstruction of 5 regions close to the nucleus was performed overlaying a single slide of the tomography on the 2D X-ray projection (**Figure 11C**) and on a single slide of the reconstruction performed with the



cryo-3D-SIM (**Figure 11D**). By magnifying the analysed areas close to the nucleus, the CTPR390-containing multivesicular bodies (green) and mitochondria (red) could be better visualised, both in NIH/3T3 (**Figure 11E**) and in primary mouse cardiac fibroblasts (**Figure 11F**).

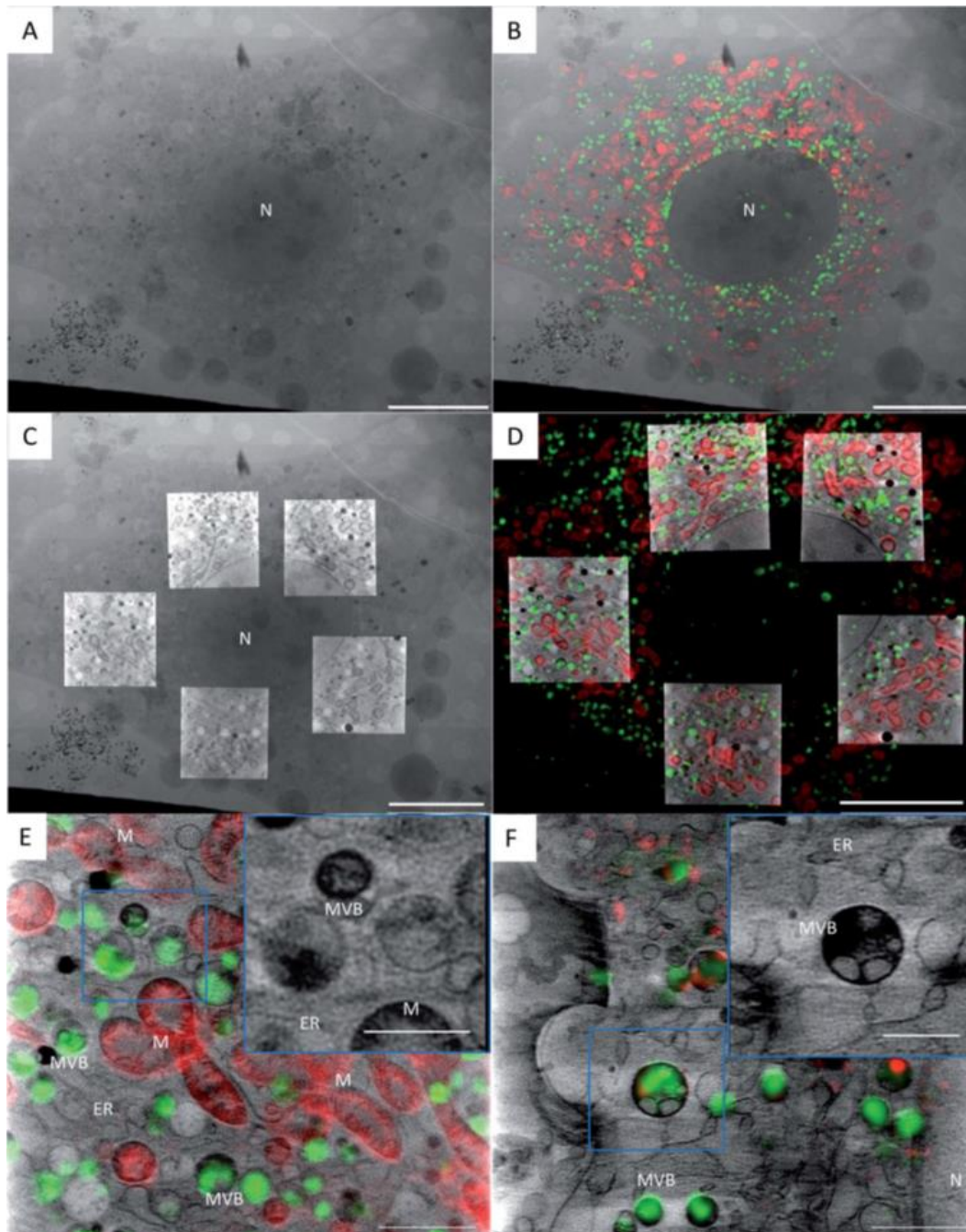


**Figure 11 Correlation of a CTPR390-488-Au treated NIH-3T3 cell using cryo-3D-SIM Correlation obtained in NIH/3T3 using cryo-3D-SIM and cryo-SXT. (A) X-ray projection mosaic, (B) cryo-SIM projection overlaid on X-ray mosaic, (C) tomographic reconstruction of 5 selected areas overlaid on X-ray mosaic, (D) tomographic reconstruction of 5 selected areas overlaid on cryo-SIM projection, (E) tomographic reconstruction overlaid on cryo-SIM projection in NIH/3T3 cell, CTPR390-488-Au:green and mitochondria:red, (F) tomographic reconstruction overlaid on cryo-SIM projection in primary fibroblasts, CTPR390-488-Au:green and mitochondria:red. Scale bar: (A-D) 10  $\mu$ m; Scale bar: (F) 2  $\mu$ m; inset 1  $\mu$ m. N: nucleus, M: mitochondria, MVB: multivesicular bodies, ER: endoplasmic reticulum. Adapted from (Groen, J. et al., 2021).**

## RESULTS

To elucidate the origin of these MVB where CTPR390 is encapsulated and understand their potential roles, markers of proteins associated with different types of cell vesicles were used to analyse their spatial association with the Alexa-488 signal present in CTPR390.

Markers related to the biogenesis of multivesicular bodies, such as Alix and Flotillin-1 [152, 153] and a marker associated with adhesion, motility, membrane fusion, and vesicle trafficking such as CD9 [154] were used. After analysis of confocal microscopy images using the above mentioned markers in CTPR390-treated NIH/3T3, colocalisation phenomena between Alix and CTPR390 (**Figure 12A, A', A'', A'''**) and between CD9 and CTPR390 (**Figure 12C, C', C'', C'''**) could be observed. In the case of Flotillin, the signal obtained was weak in the sample analysed and no colocalization was observed (**Figure 12B, B', B'', B'''**). Even though we did not detect a clear Flotillin and CTPR390 colocalization, the merged signals of Alix-CTPR390 and CD9-CTPR390 indicated that CTPR390 could be involved in events related to vesicle trafficking.

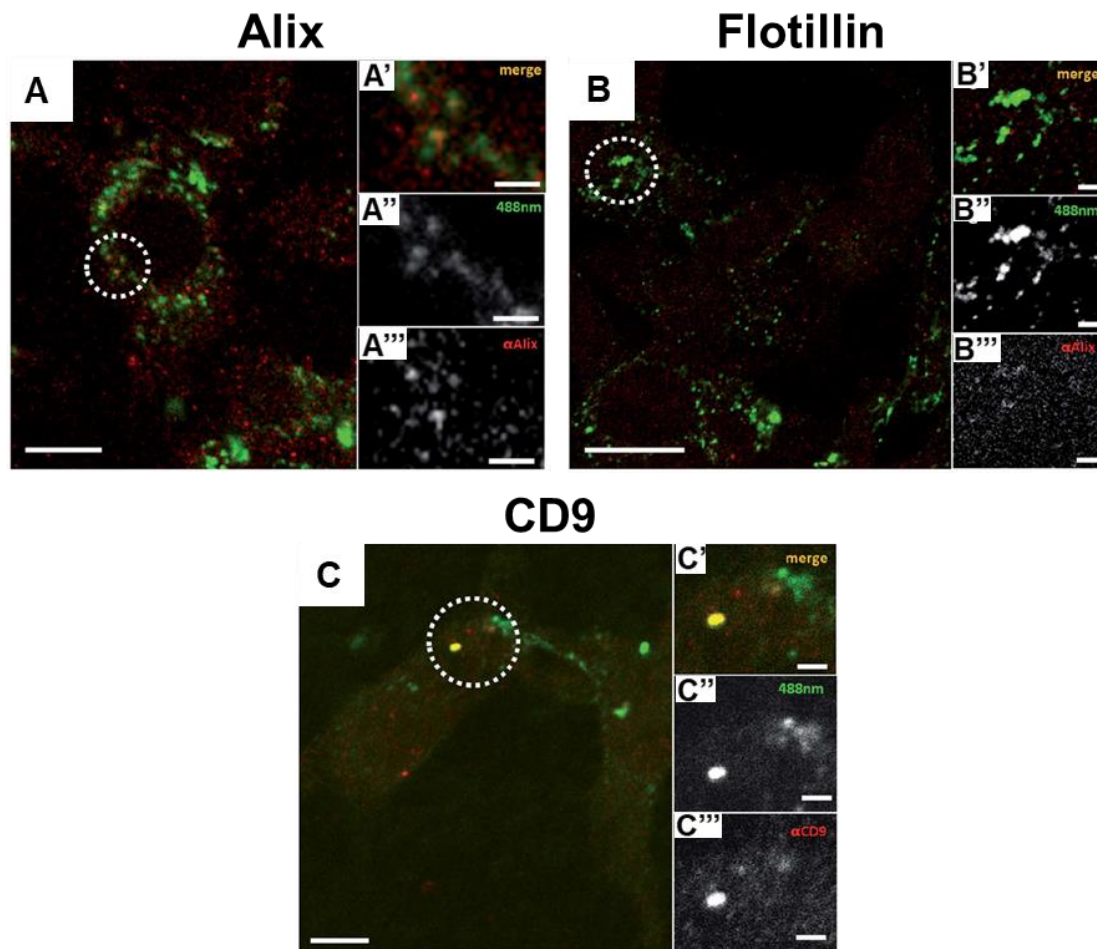


**Figure 12 Colocalisation study of CTPR390-488-Au in the presence of vesicle markers in NIH/3T3 fibroblasts.** (A-C) Confocal microscopy observations of CTPR390-488-Au (green). The inset shows the merged ('), green (alexa488, ") and red (from the respective antibody, ""'). Colocalisation (yellow). Scale bars: (A) 5  $\mu$ m; (B) 3  $\mu$ m; (C) 2  $\mu$ m. Adapted from (Groen, J. et al., 2021).



In addition to their visualisation using the markers, the Amira software was also used to evaluate the size and number of multivesicular bodies of the previously obtained reconstructions. An analysis to identify trends in the different experimental groups was carried out.

The results showed a similarity in the median volumens of the vesicles between the TGF $\beta$ -treated cells 136.4 $\mu\text{m}^3$  and control groups 172.1 $\mu\text{m}^3$  showing no significant differences in NIH-3T3 and the same happened for cardiac primary fibroblasts with values of 192.9  $\mu\text{m}^3$  and 216.8  $\mu\text{m}^3$ . This result could indicate that their presence may be typical of normal cell function in both cell types NIH-3T3 (**Figure 13A**) and primary cardiac fibroblasts (**Figure 13B**). In contrast, cells treated with CTPR390-488-Au showed an increase in cell number compared to the control, 85% in the case of NIH/3T3, or 74% of primary fibroblasts, without a significant decrease in volume (**Figure 13**).

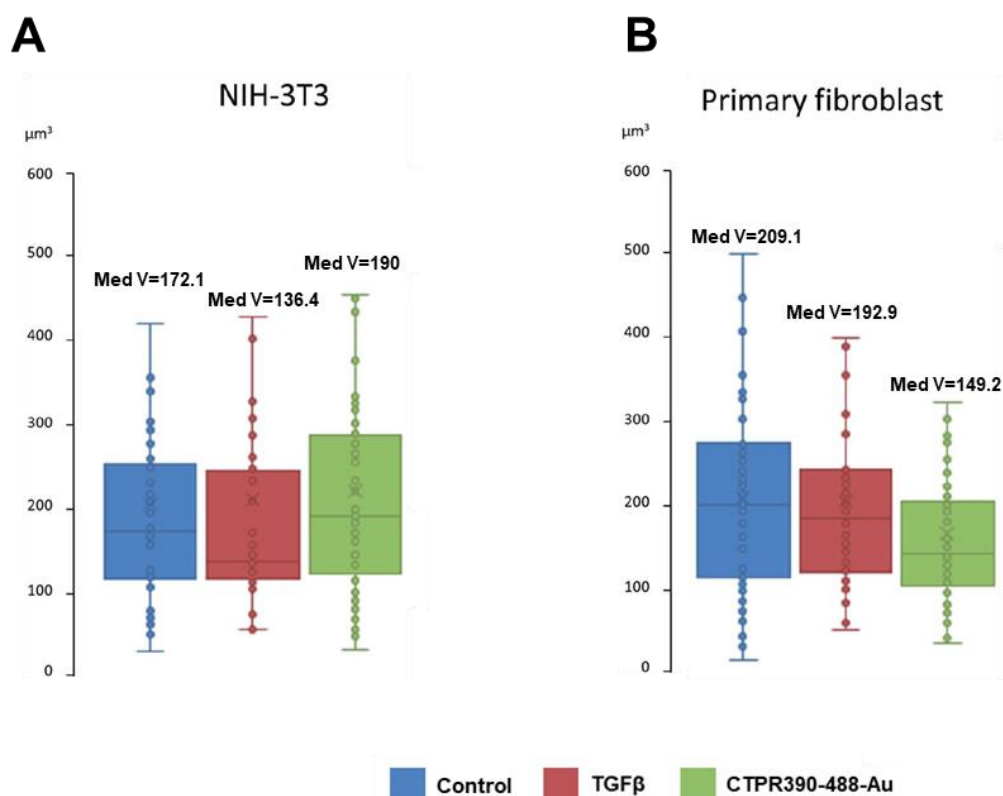


**Figure 13 Comparison of MVB median volumes (Med V) of both NIH-3T3 and primary fibroblast cells measured after segmentation using Amira software.** Colored bars show the absence of significant differences in the Med V (in  $\mu\text{m}^3$ ) of control cells (control in blue), TGF $\beta$  treated cells (TGF $\beta$  in red) and fibroblasts treated with 1ng/mL of TGF $\beta$  and 0.8 $\mu\text{M}$  of CTPR390-488-Au (CTPR390-488-Au in green). Adapted from (Groen, J. et al., 2021).

Moreover, we measured the average number of segmented MVBs in a tomogram (Avg#) and the average volume of segmented MVB (Avg V) Table 6 shows the absence of significant differences in these two parameters which complement the observations of Figure 7.

## RESULTS

	Avg#			Avg V		
	Control	TGF $\beta$	CTPR390-488-Au	Control	TGF $\beta$	CTPR390-488-Au
<b>NIH-3T3</b>	10.25	9	19	204.8	211.2	221
<b>Primary fibroblast</b>	13.25	12.25	23	216.8	213.3	176.5

**Table 6** in which Avg # represents the average number of segmented MVBs in a tomogram, Avg V stands for average volume.

In addition, using data obtained by cryo-SXT, a comparison of mitochondrial morphology directly related to cell health in both NIH-3T3 and primary fibroblasts was performed. Analyses performed using Amira software show significant effects of the treatment of CTPR390.

The results obtained with NIH-3T3 show an increase in the number of mitochondria (78% more compared to the control) together with a decrease in size and increased enlargement in the TGF $\beta$  treated group (**Figure 14B, Table 7**). Cultures treated with the CTPR390 molecule showed lower numbers (44% less compared to the control group) with an increase in volume (**Figure 14B**), this process may be related to stressful situations. [155].

	Avg#			Avg V		
	Control	TGF $\beta$	CTPR390-488-Au	Control	TGF $\beta$	CTPR390-488-Au
<b>NIH-3T3</b>	32.25	57.25	24.4	365.9	200	585.1
<b>Primary fibroblast</b>	23.5	21.5	19	382.5	478.3	393.1

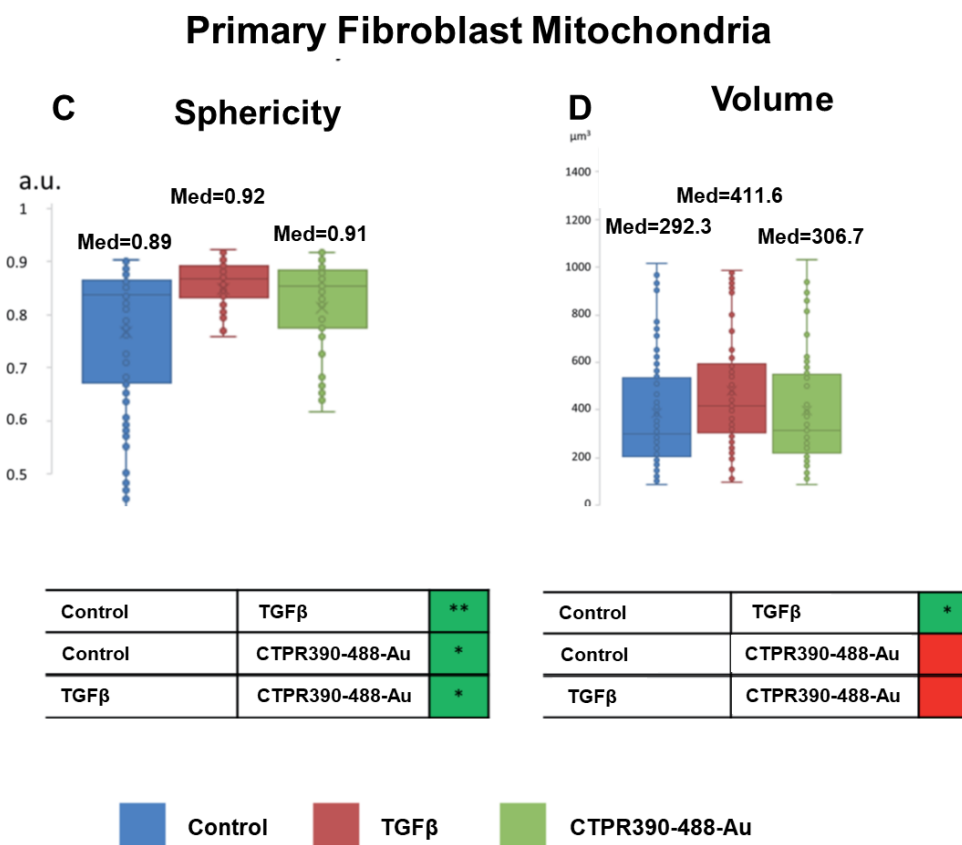
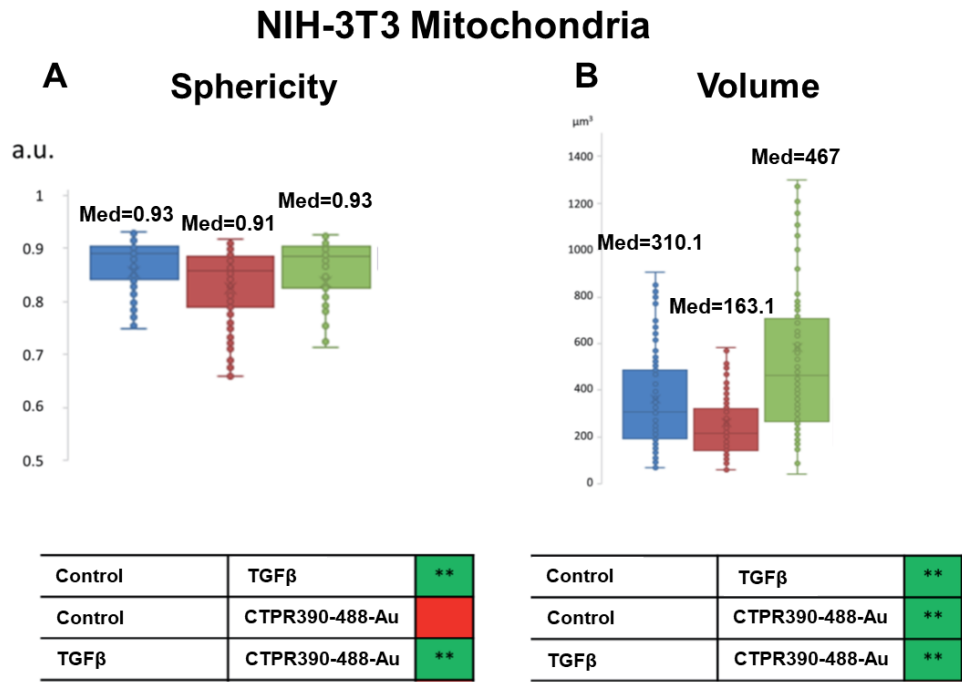
**Table 7** in which Avg # represents the average number of segmented mitochondria in a tomogram, Avg V stands for average volume.

In the analysis of primary fibroblasts, significant differences were found with respect to NIH/3T3. A similar number of mitochondria was observed in the experimental groups, although with a small decrease in the group treated with CTPR390, 20% compared to the control group, tendency also seen in NIH/3T3. It should not be forgotten that the activation of fibroblasts and the differentiation processes generated are processes with a high energy demand, and an increase in the number of mitochondria to meet the demand generated is not unusual [156]. Treatment with CTPR390 seems to prevent this increase in cardiac primary fibroblasts. In terms of volume, the group treated only with TGF $\beta$  showed a significant increase compared to the control group, maintaining the same level as that observed in the NIH/3T3 (**Figure 14D**), the same could be related to the increase in energy demand. In relation to sphericity, significant differences were found between the experimental groups, in contrast to NIH/3T3, where a certain

homogeneity between groups was maintained (**Figure 14A**), with the highest degree of diversity being found in the control group (**Figure 14C**).

Considering the data obtained in the two cell types, primary fibroblasts seem to be a system less prone to perturbations compared to NIH/3T3, although they are not exempt from presenting alterations with the different treatments. In contrast, in NIH/3T3, each of the treatments seems to generate a characteristic profile between groups, in terms of number, size and shape of mitochondria, showing a lower resilience. Many of these processes are related not only to an energetic adaptation of the cell, an increase in the number of mitochondria, but also in the case of a reduction in the size of the mitochondria, which can be related to an increase in fission processes, which can be used to reduce the mitochondrial damage that the cell may be suffering [157].

RESULTS



*t* ≤ 0.05: (\*) significant difference  
*t* ≤ 0.01: (\*\*) extremely significant difference

**Figure 14 Comparison of mitochondrial sphericity and volumes of both NIH/3T3 and primary fibroblast using Amira. Med V stands for median volume (both in μm<sup>3</sup>). \*p<0.05, \*\*p<0.005, t-test. Adapted from (Groen, J. et al., 2021).**

#### 4.1.1.4 Description of the CTPR390-Hsp90-TGF $\beta$ RI interaction and its consequences in terms of the TGF $\beta$ profibrotic signaling cascade

To describe the CTPR390 action on Hsp90 and subsequently the Hsp90 participation on the profibrotic TGF $\beta$  canonical and non-canonical signaling cascades, we developed *in silico* assays and assays at the protein level. The protein levels of different effectors of the TGF $\beta$  canonical and non-canonical signalling pathways were analysed. Primary cardiac fibroblasts activated by TGF $\beta$  were incubated in the presence of CTPR390 at concentrations of 0.1, 0.2 and 0.8 $\mu$ M.

The analysis focused on the quantification of the active or phosphorylated forms of the different actors, showing in the case of effectors from non-canonical TGF $\beta$  pathways such as p-AKT and p-ERK. Analyses showed a progressive decrease in the phosphorylated forms of AKT (**Figure 15A**) and ERK (**Figure 15B**). The non-phosphorylated variants maintain constant levels, making it clear that CTPR390 has no effect on the protein synthesis of the proteins analysed (**Figure 15A** and **B**). Of the different concentrations tested, only the 0.8 $\mu$ M concentration showed a significant reduction in p-AKT (**Figure 15A**) and p-ERK (**Figure 15B**) levels compared to the control condition. Protein levels of Hsp70 and TGF $\beta$ RI, as examples of Hsp90 client proteins in the different conditions, were also analysed, showing constant levels (**Figure 15C**), allowing us to rule out the possibility of alterations in the levels of the effectors due to the availability of these proteins.

RESULTS

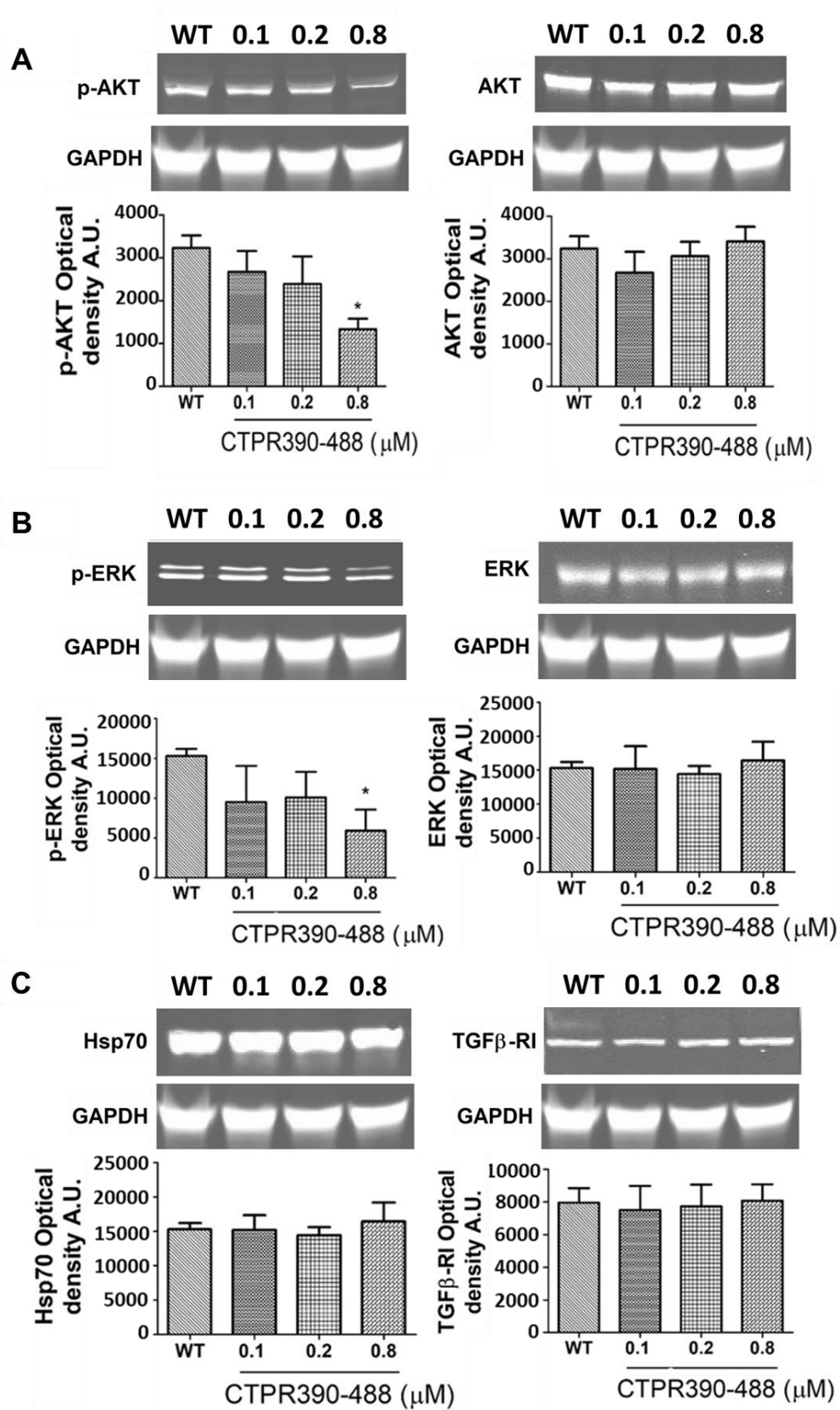


**Figure 15 Effects of CTPR390 on protein levels of proteins linked to TGF $\beta$  activation. (A and B) Quantification and analysis of the balance between active and non-active forms of effectors of the non-canonical TGF $\beta$  pathway, AKT and ERK. (C) quantification of Hsp90, Hsp70 and TGF $\beta$ RI client proteins in the presence of CTPR390. \* $p < .05$ ; Mann–Whitney test. Adapted from (Cáceres, R. A. et al 2018).**

In addition, the Smad2/3 complex of the canonical TGF $\beta$  pathway was also visualized, showing a significant reduction even at lower concentrations (0.1 and 0.2 $\mu$ M) (**Figure 16A**), neither the concentration of the non-phosphorylated form, nor the levels of SMAD2 expression were altered (**Figure 16A and B**). Likewise, the analysis of the gene expression of one of the effectors of the canonical pathway, Smad2, shows no alterations in the different conditions analysed (**Figure 16B**).

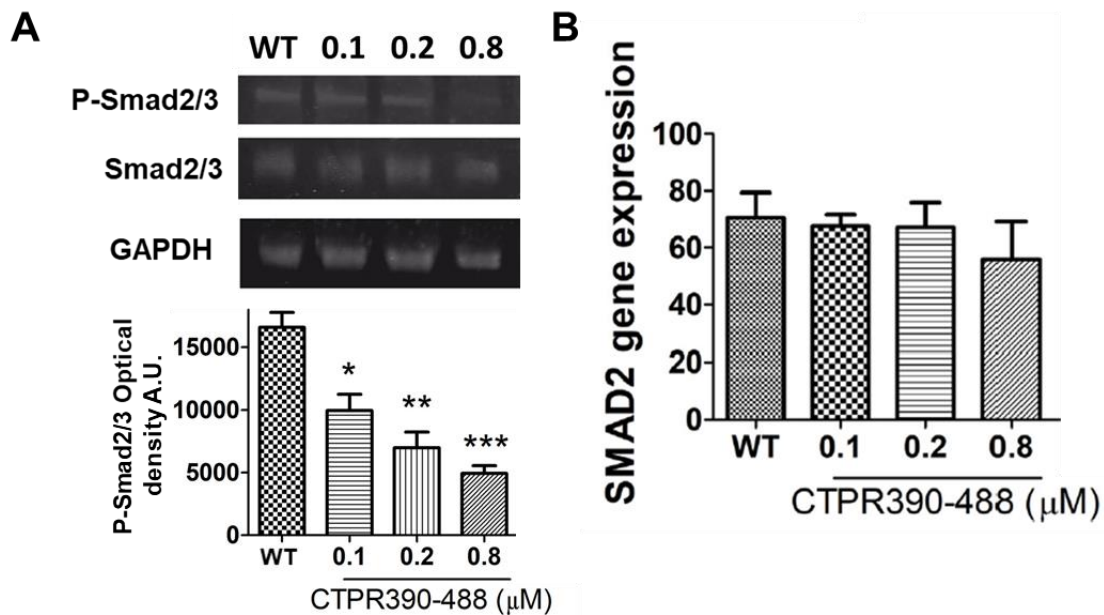


**Figure 16 Effects of CTPR390 on SMAD2 levels.** (A) Quantification of pSmad2/3 and Smad2/3 protein complex levels. (B) Smad2 expression levels at different concentrations of CTPR390. \* $p < .05$ , \*\* $p < .005$ , \*\*\* $p < .001$ ; Mann–Whitney test. Adapted from (Cáceres, R. A. et al 2018).

Once the effect of CTPR390 on different effectors of the signalling pathway had been analysed, its effect on the production of matrix elements was tested by performing a first analysis on COL1, which is the main ECM fiber to be overexpressed in pathological situations during remodelling. Therefore, primary cultures of cardiac fibroblasts will be incubated at different concentrations of CTPR390 to see its effects, been compare with compound 17AAG, a commercial Hsp90 inhibitor used in cancer treatments.

Assays performed on activated primary fibroblasts show a significant reduction in both protein concentration (**Figure 17A**) and COL1 expression (**Figure 17B**) at concentrations of 0.1, 0.2 and 0.8 $\mu$ M of CTPR390. For the comparative test, significant and similar levels of reduction in COL1 expression were achieved with both molecules (**Figure 17C**). In this last assay, we worked with concentrations of 1 $\mu$ M of CTPR390 and 17AAG, as these were the optimal concentrations to achieve the maximum effect.

## RESULTS

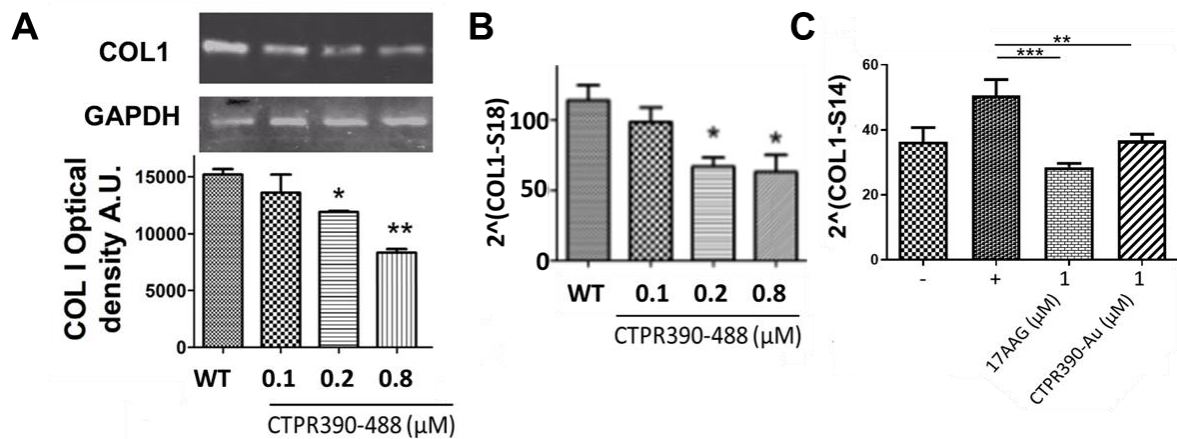


**Figure 17 Analysis of the inhibitory capacity of CTPR390 in COL1 gene, at protein and genetic level.** (A) Concentration of COL1 in the presence of CTPR390 at different concentrations. (B) COL1 expression levels in TGF $\beta$  activated primary fibroblasts at different concentrations of CTPR390. (C) Comparison of the effect at the gene expression level together with the commercial inhibitor 17AAG. \* $p < 0.05$ , \*\* $p < 0.005$ , \*\*\* $p < 0.001$ ; Mann–Whitney test. Adapted from (Cáceres, R. A. et al 2018).

### 4.1.1.5 Mechanism of action of CTPR390 altering TGF $\beta$ dependent profibrotic signaling

In previous studies focused on design and mechanism of action of CTPR390, we have demonstrated the binding capacity of the CTPR390 molecule to the carboxyl-terminal domain of Hsp90 via the MEEVD motif, a TPR-binding domain of importance in mediating protein-protein interactions [149, 158]. In this study, we design an *in silico* model using the docking algorithm ClusPro, according to which Hsp90 homodimer (green and blue structures of **Figure 18**) would interact with the TGF $\beta$ RI (yellow structure of **Figure 18**). In this model, CTPR390 (purple structure in **Figure 18**) interacts with the MEEVD motif of Hsp90, interfering with the ability of the chaperone to bind the extracellular domain of TGF $\beta$ RI, the expulsion of Hsp90 from the TGF $\beta$  multiprotein receptor complex could affect TGF $\beta$  signalling pathway and the profibrotic response.

By this thermodynamically favorable in-silico simulation the ability of Hsp90 to interact with the extracellular domain of the TGF $\beta$ RI and the conformational change from close to open of the Hsp90 homodimer promoted by the action of CTPR390 can be observed (**Figure 18**).



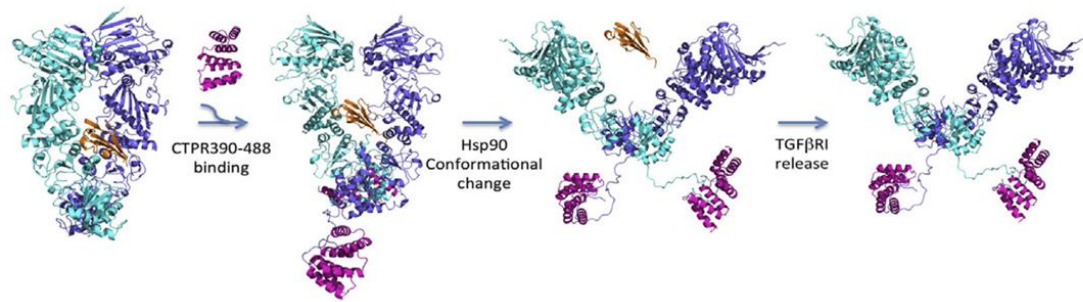


**Figure 18 In-silico simulation of CTPR390-Hsp90-TGFβRI interaction.** From left to right: Molecular model of the interaction between the TGFβRI extracellular domain (Yellow) and Hsp90 closed dimer (blue); Interaction of CTPR390–488 protein (purple) with the C-terminal end of Hsp90 domain; Hsp90 conformational change from the close to the open state upon CTPR390–488 interaction; disruption of the interaction between Hsp90 dimer. The TGFβRI domain was docked into the Hsp90 dimer using the docking algorithm ClusPro and the individual TGFβRI and Hsp90 structures as input. The molecular model from ClusPro was used as input for ROSIE Docking2. Adapted from (Cáceres, R. A. et al 2018).

To check the Hsp90-TGFβRI interaction, a proximity ligation assay (PLA) was performed at NIH/3T3 and primary cardiac fibroblasts. PLA assay determines that the distance between two proteins is lower than 40 Å (or direct interaction) when obtaining a fluorescence spot of colocalization.

Confocal microscopy images showed the Hsp90-TGFβRI interaction as a red spot in a NIH/3T3 cells visualized in bright field (**Figure 19A**), placing the complex (**Figure 19B**) at the plasma membrane. A positive control was also used in the system, based on the detection of the well documented Smad2 and Smad3 interaction (**Figure 19C**). The negative control, against non-directly connected proteins such as Elk1 and TGFβ was also performed and showed (**Figure 19D**).

The tests were also repeated in cardiac fibroblasts. Signal from the Hsp90-TGFβRI complex (**Figure 19E**) was also detected (green empty circle mark the red spot), with the Smad2-Smad3 complex (**Figure 19F**) as a positive control, and Elk1 and TGFβ as a negative control (**Figure 19G**). Thus, Hsp90 and TGFβRI was not only belonging to the same protein complex, but also interact directly to each other (¡Error! No se encuentra el origen de la referencia.).

## RESULTS

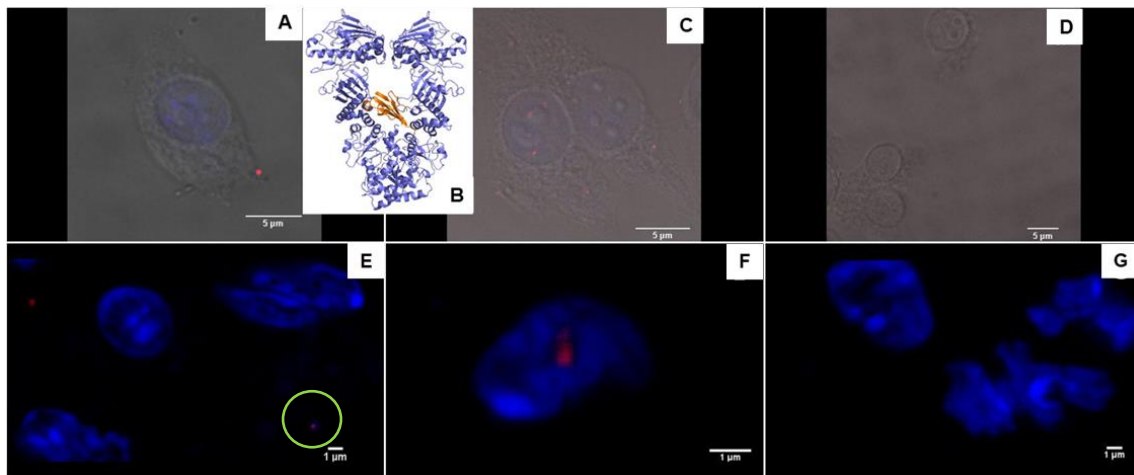


**Figure 19 Confocal microscopy images showing direct protein–protein interaction of Hsp90 and TGFβRI in NIH/3T3 and primary fibroblast detected by Proximity Ligation Assay (PLA).** (a) Red spot showed primary antibody detection of the Hsp90-TGFβRI direct interaction and differential interference contrast (DIC) showed cell surface of NIH-3T3 fibroblasts. (b) Molecular model of the interaction between TGFβRI extracellular domain (orange) and Hsp90 dimer (purple). (c): Red spots showed primary antibody detection of the positive control Smad2 and Smad3 interaction. (d) Negative control with non-interacting proteins TGFβ and Elk1. (e) Red spot showed primary antibody detection of the Hsp90-TGFβRI direct interaction in primary (not cultured) cardiac fibroblasts. (f) Positive control assay using primary antibodies directed against interacting proteins such as Smad2 and Smad3. (g) Negative control experiment with primary antibodies directed against non-interacting proteins such as TGFβ and Elk1. Dapi was used as a nuclear counterstain (blue). Adapted from (García, R. et al 2016).

We next tested whether the inhibition of Hsp90 by CTPR390 altered the gene expression of the constitutive isoform Hsp90β (Hsp90ab1), and the gene expression of the stress-inducible isoform Hsp90α (Hsp90aa1). We analysed the expression of these two isoforms of the chaperone, observing significant increases in the expression of the inducible isoform (**Figure 20A**) in activated fibroblasts, in the presence of CTPR390 at different concentrations, 0.2, 0.8 and 1.5μM. The constitutive isoform showed no significant differences (**Figure 20B**; Error! No se encuentra el origen de la referencia.).

To check that the inhibitory effect of CTPR390 is produced at the plasma level by the interaction to the TGFRI, we transfected fibroblasts with a plasmid construct encoding for constitutively active TGFβRI. The results showed a significant increase in protein levels of p-Smad2/3 (**Figure 20C**) and p-ERK (**Figure 20D**) even in the presence of CTPR390. Transfection of constitutively active TGFβRI eliminates the dependence of the Hsp90-TGFβRI interaction in terms of activation of the TGFβ profibrotic cascade, thereby eliminating the inhibitory effects previously achieved in the presence of CTPR390.

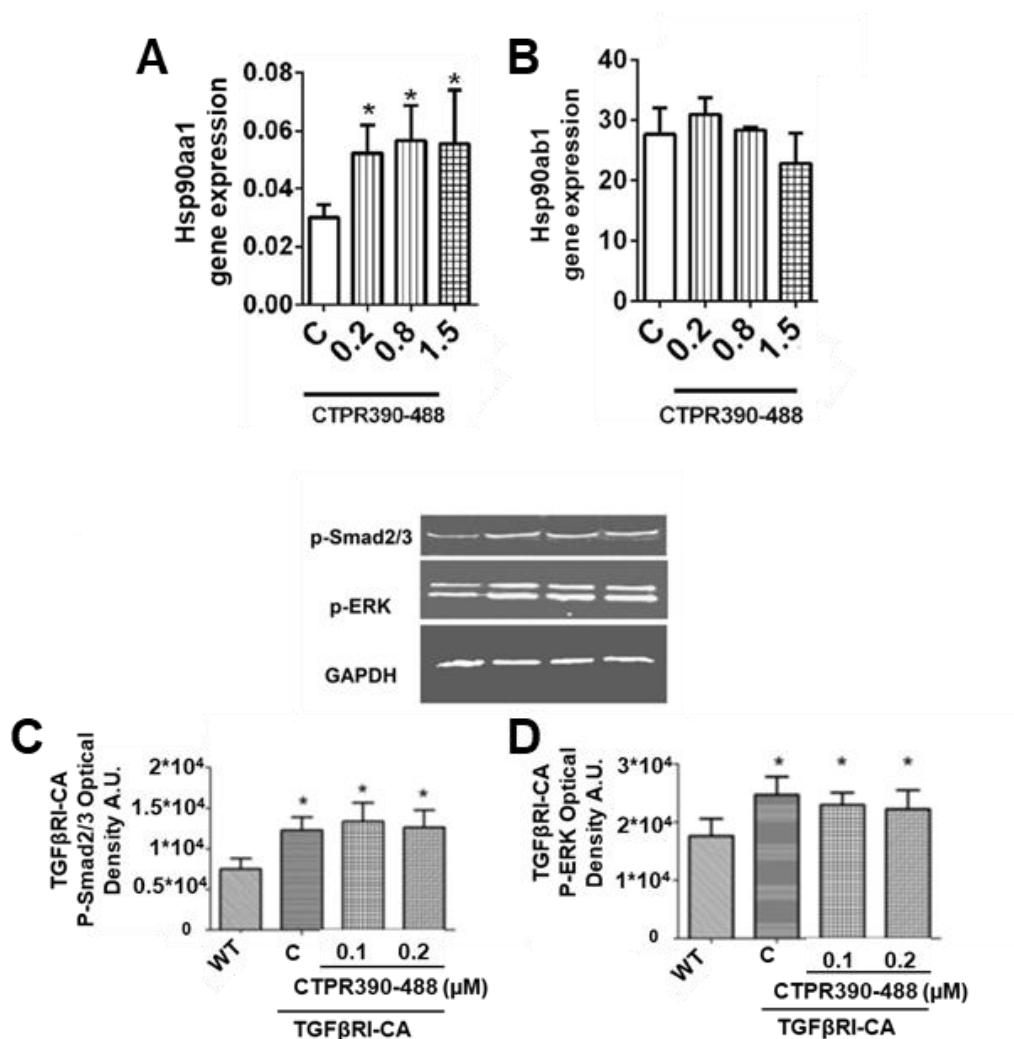


**Figure 20 Analysis of CTPR390 effect on Hsp90.** (A) Expression levels of Hsp90aa1. (B) Expression levels of Hsp90ab1 isoforms, under CTPR390-free conditions and at concentrations of 0.2, 0.8 and 1.5 μM. (C-D) Detection and analysis of the active phosphorylated forms of the TGFβ signalling effectors p-Smad2/3 (canonical) (C) and p-ERK (non-canonical) (D) in cell cultures transfected with constitutively activated TGFβ receptor 1. \* $p < 0.05$ . Mann–Whitney test. Adapted from (Cáceres, R. A. et al 2018).

#### 4.1.2 In vivo antifibrotic effect of CTPR in cardiac remodelling. Evaluation of CTPR as a biomarker (theragnostic molecule) and its biodistribution.

Once we described the results in which it is demonstrated that CTPR internalizes primary cardiac fibroblasts and reduce ECM collagen overexpression and deposition in vitro, we proceed to use of the CTPR390 in vivo, with the aim of analysing its capabilities in a complete organism. With this objective in mind, we proceeded to generate an in vivo model of a hypertensive mouse, allowing us to work in a fibrotic environment, (see

## RESULTS

material and methods section **3.2.11 Animal handling procedures and protocols**, for a description of the model).

### 4.1.2.1 CTPR390 counteracts hypertrophic remodelling in the heart of hypertensive mice

As we defined in the introduction, the remodelling process can be initiated in the cardiac organ in pathological situations. The alterations suffered in the cardiac organ due to damaging events promotes an adverse remodelling including hypertrophy and fibrosis.

The changes in size and weight of the heart indicates the hypertrophic process have started. We will differentiate two large groups, composed of mice operated with osmotic minipumps containing saline, which we will call the healthy group, and a group called fibrotic, which will contain osmotic minipumps with an AngII solution of 7mg/mL. In each of these groups, individuals will be administered CTPR390-Au or saline (vehicle), which will be administered at 3 hours, 4 and 8 days, prior to the end point of the assay, to have controls for each condition, as well as to analyse the differences between the different times of administration (¡Error! No se encuentra el origen de la referencia.) shows the groups included in this study.

Mice status	Vehicle			CTPR390 Au		
Healthy (saline)	3 hours	4 Days	8 Days	3 hours	4 Days	8 Days
Fibrotic (Ang II)	3 hours	4 Days	8 Days	3 hours	4 Days	8 Days

**Table 8 Description of the experimental groups for in vivo assays.** Mice were subjected to osmotic minipump implantation (saline solution or Ang II solution) and CTPR390 treatment at different time points of the study (3 hours, 4, 8 days before sacrifice them (n= x mice per group).

To test the increment in myocardial mass, we proceeded to measure the heart weight (HW) in relation to the body weight (BW) of each mouse under study. In **Figure 21A** representative images of hearts from each group under study are shown. The 3 hour group shows a significant increase in the HW/BW factor, for both fibrotic groups, regardless of intraperitoneal administration of CTPR390 (**Figure 21B**), compared to their controls, such that the fibrotic+vehicle group shows a  $37.78\pm 4.49\%$  increase compared to the healthy+vehicle group, ( $*p<0.05$ ), and the fibrotic+CTPR390 group shows a  $25.25\pm 5.3\%$  increase compared to the healthy+CTPR390 group. ( $**p<0.005$ ). Sham groups show similar values (**Figure 21B**).

On the other hand, with regard to the 8-day groups, they show similar HW/BW in the healthy sham groups (vehicle-treated or CTPR390-treated mice), (**Figure 21A and B 8Days**). However, the analysis of the fibrotic groups, shows a significant decrease in the HW/BW values, around  $13.89 \pm 2\%$  in the group treated with CTPR390 compared to the fibrotic+vehicle group ( $*p < 0.05$ ), no statistically significant difference was observed between the fibrotic group treated with CTPR390 and the control group treated with CTPR390 showing similar values (**Figure 21B 8 Days**). On the other hand, the untreated fibrotic group showed a significantly higher increase in values than the other 3 experimental groups ( $*p < 0.05$ ), Ang II+CTPR390 vs Sham+CTPR390; and  $**p < 0.005$  Ang II +CTPR390 vs Sham+Vehicle. (**Figure 21B 8 Days**).

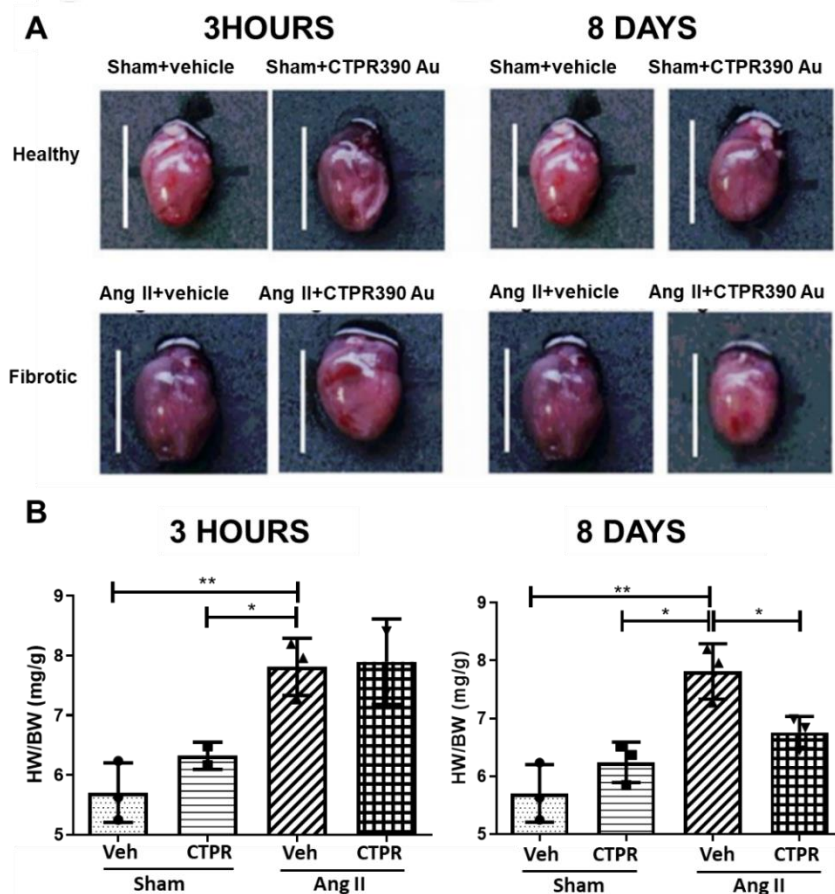


**Figure 21 Assessment of hypertrophic remodelling in an in vivo hypertensive mouse model.** (A) Representative Color pictures of the different group of hearts under study. From left to right healthy (sham+vehicle treatment for 3 hours), and (Sham+CTPR390 treatment for 3 hours), sham+vehicle treatment for 8 days), and (Sham+CTPR390 treatment for 8 days). From left to right Fibrotic (Ang II+vehicle treatment for 3 hours), and (Ang II+CTPR390 treatment for 3 hours), Ang II+vehicle treatment for 8 days), and (Ang II+CTPR390 treatment for 8 days). The white vertical scale bar represents 1 cm.(B) Assessment and comparison of the HW/BW in mg of heart/g of mouse units (mg/g). All groups are compared with the Fibrotic group without CTPR390 (Veh/Ang II).  $*p < 0.05$ ,  $**p < 0.005$ . Mann–Whitney test. Adapted from (Aires, A., Maestro, D. et al 2021).

## RESULTS

### 4.1.2.2 CTPR390 counteracts fibrotic remodelling in the heart of hypertensive mice

In addition to hypertrophic remodelling, fibrotic remodelling would also be present, so quantification of fibers expression analysis of fibers deposition were made of the main components of the ECM, more specifically, quantification of the collagen present in the tissue, as well as a study of the expression levels of profibrotic markers were performed.

The eight groups under study are the ones defined in the previous section, in brief: the group of "healthy" or Sham mice, the group of hypertensive or "fibrotic" mice. Each of these groups present 4 experimental conditions corresponding to mice treated with CTPR390 at 3 hours, 4 days and 8 days before the end of the trial, and a control group treated with saline (vehicle) instead of CTPR390. See methods section for the experimental design.

Myocardial cross sections were obtained and stained using Masson's trichrome to highlight the fibrotic areas of the hearts (**Figure 22A**), various areas of the section were randomly quantified using Image J software. The percentages of purple staining indicating collagen in the tissue showed similar values in the control groups ( $7.3-9.2\pm 1.4\%$ ), both in the control group not treated with CTPR390 and in the groups treated at 3 hours, 4 and 8 days (**Figure 22B**). On the contrary, significantly higher values are observed in the fibrotic groups, with the highest values being reached in the fibrotic group without CTPR390 administration. Specially the group treated 3 hours before the end of the assay, with no significant difference observed between this group and the fibrotic group, despite the administration of CTPR390 (**Figure 22B**). In contrast, the fibrotic groups with CTPR390 administration at 4 and 8 days showed a significant reduction in the percentage collagen area in the sections with respect to their fibrotic control without CTPR390 (4 days:  $12.3\pm 0.4\%$  and 8 days:  $9.7\pm 0.3\%$  compared to Ang II+veh:  $14.9\pm 1.2\%$ , with  $p<0.05^*$  and  $p<0.005^{**}$  respectively) (**Figure 22B**). These results indicate that the reduction is more remarkable in the group with the administration of the molecule 8 days before the end of the assay (**Figure 22B**).



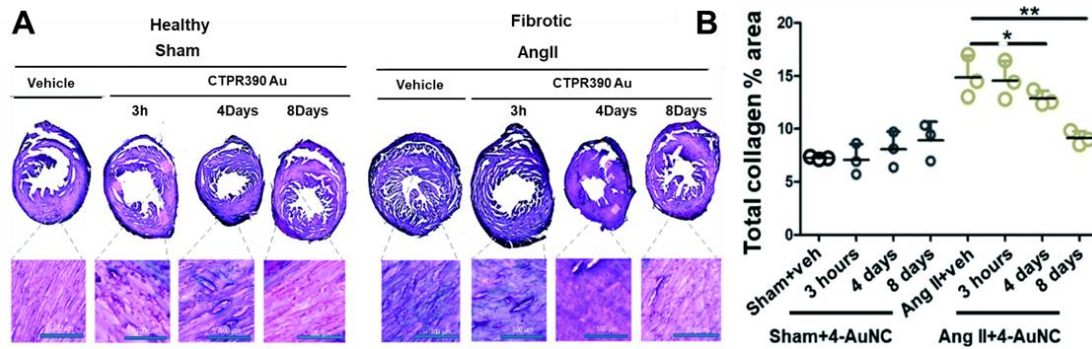


**Figure 22 Analysis of fibrotic remodelling.** (A) Heart sections of the different experimental groups with the different conditions, on the left the fourth healthy groups, without CTPR390 (Sham/Vehicle) and with CTPR390Au at 3 hours, 4 days and 8 days before the end of the assay. On the right the fourth fibrotic groups (Ang II/vehicle) without CTPR390 (Ang II/CTPR390Au) with CTPR390 at 3 hours, 4 and 8 days. All of them stained with Masson's trichrome as it is shown in the details below each section. The muscle is shown in pink and the fibrotic areas in purple. Blue horizontal bars of these details indicate xmm. (B) The quantification of the percentage of collagen in random areas of the cross sections from A. \* $p < 0.05$ , \*\* $p < 0.005$ . Mann-Whitney test. Adapted from (Aires, A., Maestro, D. et al 2021).

We next analysed the profibrotic marker gene expression and protein quantification, in control and fibrotic samples, both untreated and treated with CTPR390 at end point (8 days after the CTPR390 treatment).

A reduction in the gene expression of cardiac stress markers such as Nppa (**Figure 23A**) and Nppb (**Figure 23B**) was observed in the fibrotic group samples treated with CTPR390 (Ang II/CTPR390Au) compared to the untreated group (Ang II/Veh)\*  $p < 0.05$ . In the case of Nppb, the fibrotic group treated with CTPR390 (Ang II/CTPR390Au) presented similar values to those found in the healthy group (Sham) treated with CTPR390. A significant reduction (\*\* $p < 0.001$ ) in the gene expression levels of COL1A1 (**Figure 23C**) and FN (**Figure 23D**) structural fibres were observed in the mice with CTPR390 administration, which are comparable to those observed in sham animals (\*\* $p < 0.001$ ). Quantification of the protein levels of Ang II/CTPR390Au samples also showed a reduction of COL1A1 (**Figure 23E**) and FN (**Figure 23F**) to levels compared to the Ang II/Veh group. Ang II/Sham control group presented significant differences with Ang II/Veh as expected in all markers tested (**Figure 23**).

## RESULTS

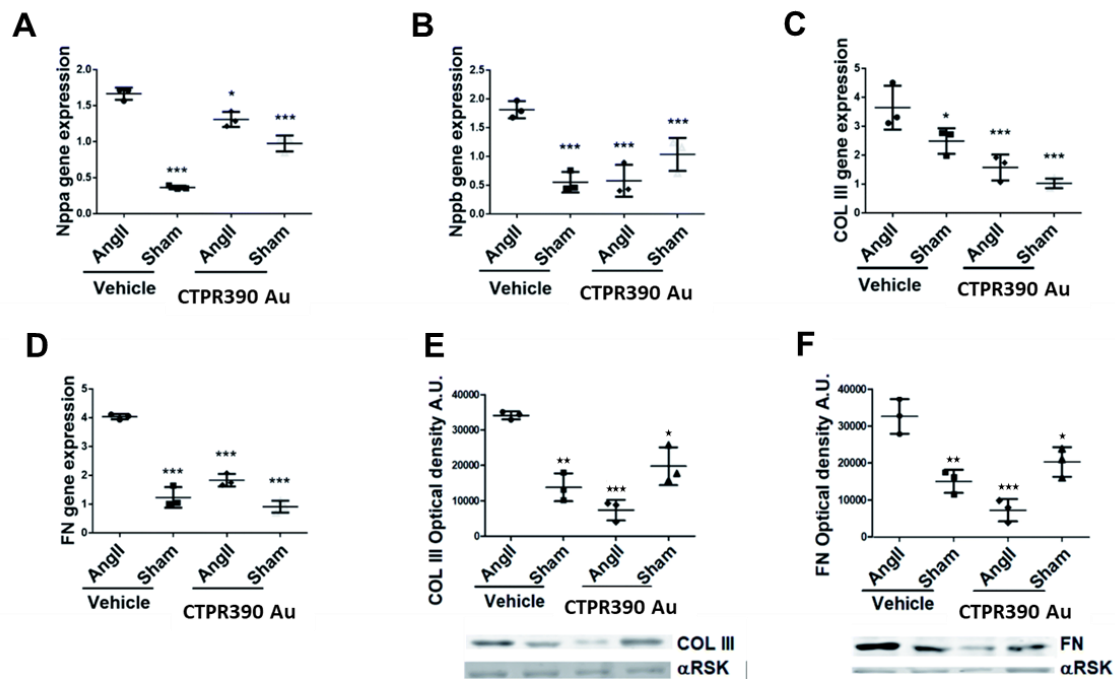


**Figure 23** Quantification of the gene and protein expression of fibrotic markers (A-D) Expression levels of profibrotic marker genes Nppa (A) and Nppb (B) as markers of cardiac stress and COLIII (C) and FN (D) as structural proteins of the extracellular matrix. (E-F) WB and quantification using Image J software of COLIII and FN protein levels  $\alpha$ RSK expression was used as loading control protein. N= 4 mice per group. \* $p < 0.05$ , \*\* $p < 0.005$ , \*\*\* $p < 0.001$ . Mann-Whitney test. Adapted from (Aires, A., Maestro, D. et al 2021).

### 4.1.2.3 Detection of the differences in CTPR390 accumulation between the fibrotic and the CTPR390-treated hearts by SXRF microscopy

Once the changes promoted by the CTPR390 on the profibrotic-related proteins were analyzed, its distribution in cardiac tissue was evaluated using the most powerful superresolution technique available which is the SXRF (described in the section on materials and methods).

Au SXRF elemental maps showing localization of the Au element from CTPR390-Au were taken in different regions of the whole heart. The analysis revealed the accumulation of Au (marking CTPR390-Au molecule) in the heart of fibrotic mice compared to healthy mice at the three experimental time points under study (3 hours, 4 and 8 days, prior to the end of the trial) (**Figure 24A-F**). With a thickness of 50 $\mu$ m, the myocardial samples analyzed here corresponded to the same and consecutive sections in which fibrosis was detected in section **4.1.2.2 CTPR390 counteracts fibrotic remodelling in the heart of hypertensive mice** of the results.

A lack of Au signal in the healthy groups treated with the CTPR390 (**Figure 24A, C and E**), with no gold detected at any time, in some cases a residual signal, identified as



background, was detected (**Figure 24C**). On the contrary, in the fibrotic group, a progressive increase of the Au signal in the tissue, as the time elapsed since the injection increases (**Figure 24B, D and F**), with the highest signal intensity being observed in the fibrotic group with the administration of CTPR390 8 days before sacrifice (**Figure 24F**). We calculated the concentration of ng Au per surface area ( $\text{mm}^2$ ), which clearly identified a differential accumulation in the fibrotic group treated with CTPR390 administration 8 days prior to sample collection (4-fold increase between 3 hours and 8 days) (**Figure 24H**).

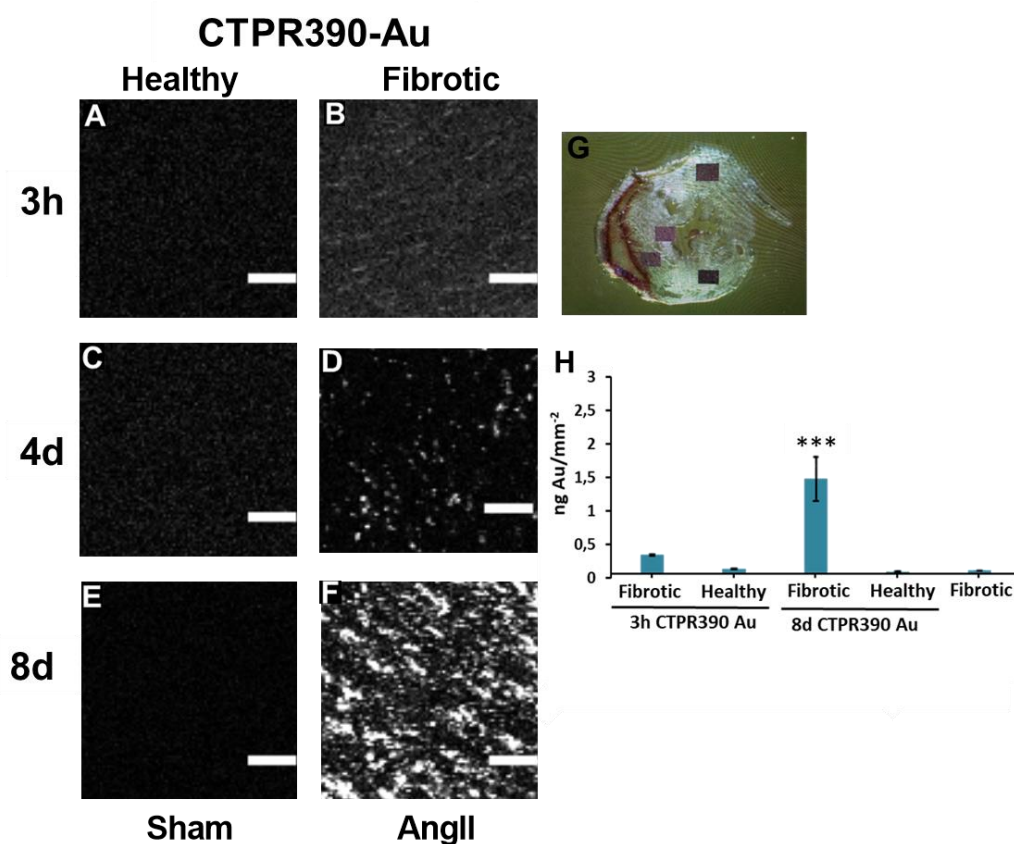


**Figure 24 Localisation and quantification of CTPR390-Au by soft X-ray fluorescence microscopy (SXRF).** (A-F) Images of the areas selected for analysis, of the heart sections by SXRF microscopy, in which the inorganic element gold from CTPR390Au present in the sample is quantified. (G) Cross-sectional view of a heart with the different areas of analysis highlighted defined as grey squares. (H) Graph with the quantification of Au in the myocardial sections of the groups under study. The groups analysed were both healthy (Sham) and fibrotic (AngII) at 3 hours, 4 and 8 days after administration of CTPR390-Au. The analysis areas were  $5 \times 5 \mu\text{m}^2$ . Scale bar is  $100 \mu\text{m}$ . \*\*\* $p < 0.001$ . Mann–Whitney test. Adapted from (Aires, A., Maestro, D. et al 2021).

The signal intensity is directly proportional to the amount of CTPR390 found in the analysed area, as well as the Au is linked to the CTPR390, so the higher the accumulation of CTPR390 is, the higher the signal detected. Thus, the analyses of the signal intensity detected showed that in the healthy tissues, the percentage of fibrosis

## RESULTS

remained stable at around  $7-9\pm 0.5\%$  (**Figure 25A**), both in the group without CTPR390 and in the CTPR390-treated groups at different times. No gold signal ( $\text{ng}/\text{mm}^2$ ) was detected in those groups (**Figure 25C**), and no correlation between the accumulation of CTPR390 (gold signal) and the percentage of fibrosis in the tissue was detected (**Figure 25E**). With regard to the fibrotic groups, high percentages of fibrosis were detected in the untreated group (Ang II) and in the group treated with CTPR390 3 hours before the end of the assay, showing a significant reduction of fibrosis with similar values the fibrotic groups treated with CTPR390Au at 4 and 8 days (**Figure 25B**). In terms of gold quantity ( $\text{ng}/\text{mm}^2$ ), a significant accumulation ( $***p<0.001$ ) was seen in the fibrotic group treated with CTPR390Au 8-days administration (**Figure 25D**). Correlation between the accumulation of CTPR390 (gold signal) and the percentage of fibrosis was detected in fibrotic tissues treated with CTPR390 (**Figure 25F**)  $R^2=0,7813$  and  $p<0.01$ , while in healthy tissues the nanoclusters data are residual and do not correlate with the percentage of fibrosis detected as we previously explained (**Figure 25E**).

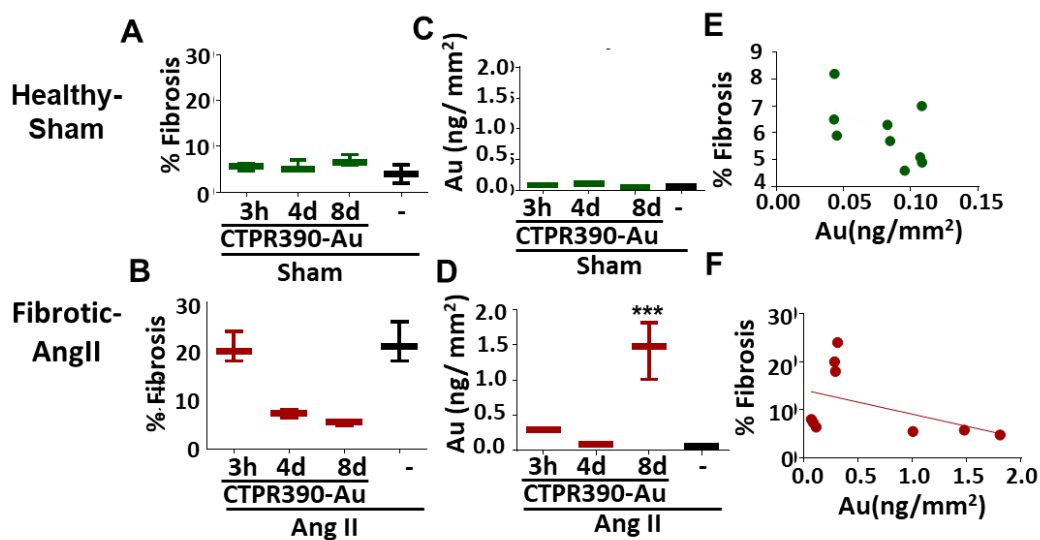


**Figure 25 Quantification of CTPR390-Au in the heart of mice and its correlation analysis with the percentage of fibrosis.** (A-B) Graphical representation of the percentages of fibrosis from the Sham (A) and Ang II (B) groups with or without CTPR390Au treatment, obtained in the 4 different areas analysed (see **Figure 24G**). (C-D) Concentration of Au per surface area of the Sham (C) and Ang II (D) groups with or without CTPR390Au treatment. (E-F) Correlation analysis between fibrosis percentages and Au concentration values in the myocardial tissue analysed of the Sham (E) and Ang II (F) groups with or without CTPR390Au treatment.  $***p<0.001$ . Mann-Whitney test.

#### 4.1.2.4 CTPR390 theragnostic capacity

The theragnostic capacity of a molecule is based on its characteristics to be detected (fluorescence in this case) and its therapeutic capacity checked in previous sections *in vitro* and *in vivo*. In this section, we combined both capabilities to observe a merged theragnostic event.

To this respect, cardiac tissue samples extracted from mice treated with CTPR390-488 were analysed. The healthy and the fibrotic groups treated with CTPR390 showed different signal intensity indicating different capacities in the accumulation of CTPR390 (**Figure 26**), as we previously detected with XRF technique (**Figure 24**). A reduction in the accumulation of fibrosis showed in **Figure 26C** is observed in heart sections of CTPR390-488 treated animals (**Figure 26B**). Only in the fibrotic group (**Figure 26D**) CTPR390-488 fluorescence signal is observed. Masson's trichrome staining assay revealed, the presence of collagen in the same areas where the CTPR390-488 was detected (**Figure 26A**) while this effect was not observed in healthy tissues, (**Figure 26E, F, H**) or negative control tissues from CTPR390-untreated mice (**Figure 26C, G**). These results showed a decrease in the fibrotic tissue under CTPR390 treatment (**Figure 26B**). Thus, using CTPR390 we observed fibrosis reduction and detection of CTPR390 in the tissue (**Figure 26D and H**).

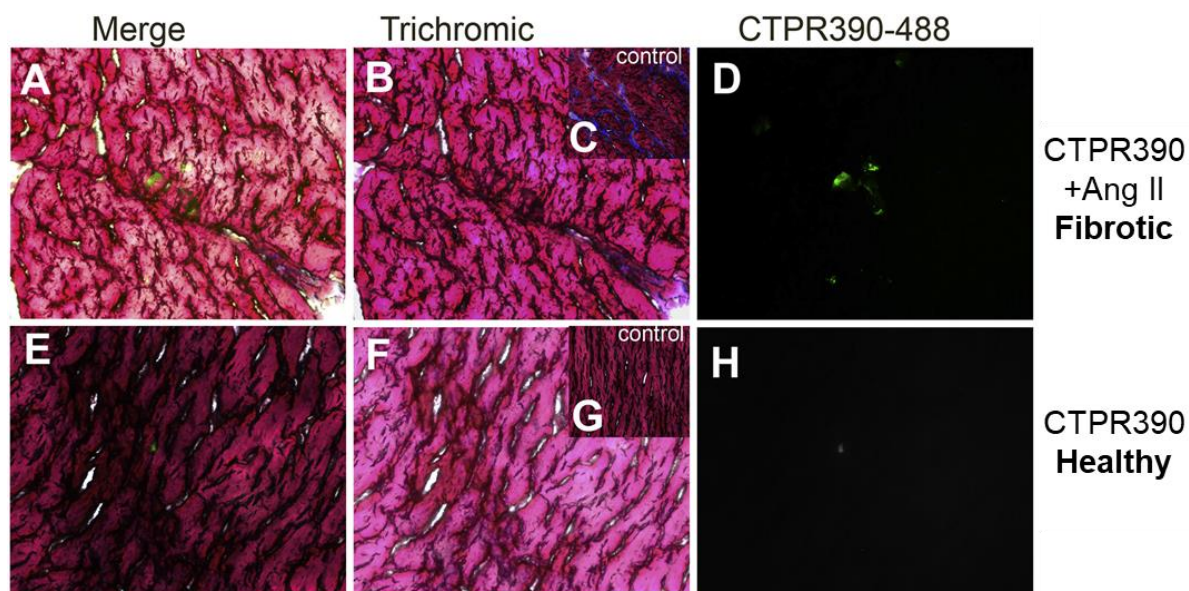


**Figure 26 Analysis of the theragnostic by Masson's trichrome and confocal microscopy (A-H)** Cross-section of the left ventricle of the heart of AngII+CTPR390-488 mouse model (**A-D**) and CTPR390-488 control mouse (**E-H**). A and E mixture of Masson's trichrome staining with Alexa-488 signal from CTPR390 obtained by confocal microscopy. B, C, F, G, tissue staining, with cardiac muscle in pink and areas of collagen deposition in blue. D, H, confocal microscopy images showing CTPR390-488 signal in green and its accumulation in areas.

## RESULTS

To reinforce these data, we developed a novel tungsten (W)-based labelling technique for collagen in tissue, which allowed fibrosis detection and visualisation by XRF (**Figure 27L** and **F**). The implementation of this technique is based on the use of a tungsten solution, that in contact with the myocardial tissue is linked to the collagen present in the tissue, due to its acidic character, which will allow it to associate with acidic elements, such as collagens. Due to the impermeability of the cells, the solution would not penetrate their interior, thus avoiding any interference from elements foreign to the collagen in the extracellular matrix. Thus, associated with the collagen fibres of the tissue, and visible through XRF. Once the solution is applied to the samples, the analysis of the tissue sections showed an accumulation of collagen fibres (**Figure 27L**) in areas where CTPR390Au was also accumulated, (**Figure 27K**). We did not observe W signal in healthy tissue (**Figure 27C, I**), but we can detect this W in the fibrotic tissue (**Figure 27F** and **L**). We observe a selective accumulation of CTPR390 in fibrotic tissue (**Figure 27K**) and not in healthy tissue (**Figure 27E**), which indicate the possibility of a potential molecule for diagnosis.

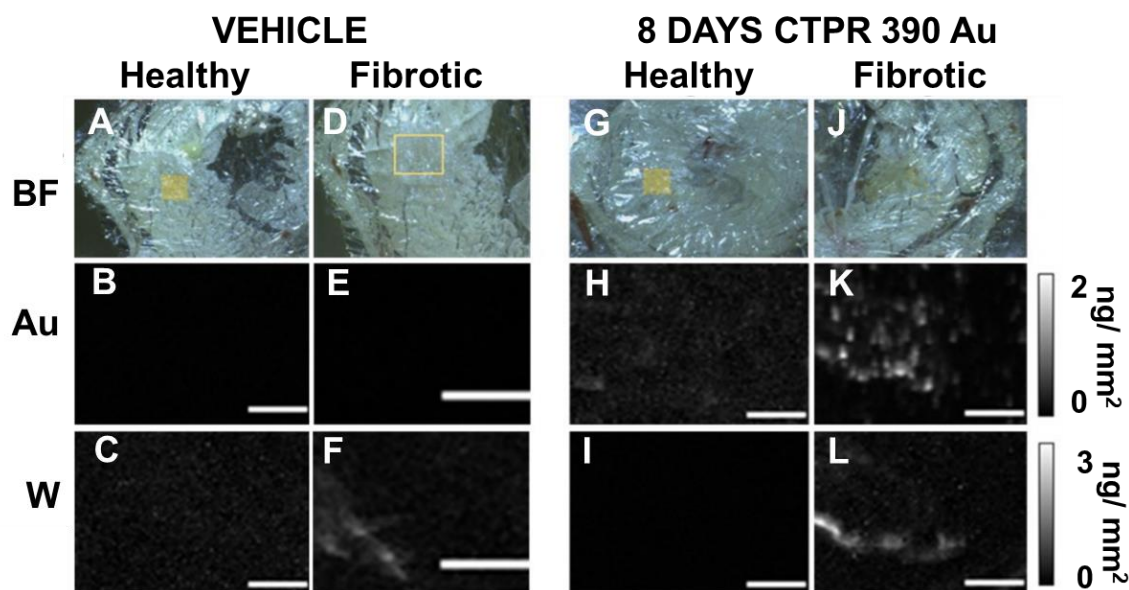


**Figure 27 Analysis of the theranostic capability of CTPR390Au based on a new detection of fibrosis using XRF.** (A-J) Bright field visualization (BF) of cross section areas of the heart of healthy (A,D) and hypertensive (G,J) mouse models, to be analysed by SXRF. Healthy and fibrotic groups, without CTPR390 administration or with CTPR390 administration 8 days before the end of the trial are analysed. Yellow squares indicate the area under study Au) representation of the signal obtained from the CTPR390 gold present in Healthy (B) and Fibrotic (E) CTPR390Au-untreated mice, and Healthy (H) and Fibrotic (K) CTPR390Au treated mice. Tungsten images (W) of Healthy (C) and Fibrotic (F) CTPR390Au-untreated mice, and Healthy (I) and Fibrotic (L) CTPR390Au treated mice obtained from the same areas, but showing only the tungsten signal, associated to the collagen fibres. White horizontal scale bar is 100 $\mu$ m and vertical grey bar indicates the intensity of accumulation in ng/mm<sup>2</sup> of the inorganic element under study.

#### 4.1.2.5 CTPR390 biodistribution

After observing that CTPR390 arrives to the heart we are interested in detecting which other tissues present CTPR390, in both healthy and fibrotic mouse models. The biodistribution of CTPR390 was carried out using the ICP-MS technique. During the assay, CTPR390 was administered via a single intraperitoneal injection, and due to the systemic administration of the CTPR390, a wide distribution of the molecule is assumed. We will calculate the percentage of CTPR390 present in the target tissue compared to the CTPR390 accumulated in other key organs of the mice.

The results obtained showed the presence of Au in a multitude of organs, showing a wide distribution of CTPR390-Au (**Figure 28**). A significative accumulation of CTPR390 was observed in areas of tissue belonging to or associated with the cardiovascular system, such as the atrium (control 7% of total vs. 9% in the fibrotic group \* $p < 0.05$ ), ventricle (control 0.8% of total vs. 3% in fibrotic group \*\* $p < 0.005$ ), and aorta (control 6% of total vs 8% in the fibrotic group \* $p < 0.05$ ).

CTPR390 is located in liver 38%, and kidney 38%, is higher percentage than in the cardiovascular system but without significant differences between healthy and fibrotic individuals, which may indicate the particle metabolism is carried on. Very revealing was the absence of signal from the brain and cerebellum (**Figure 28**), which may indicate the inability of CTP390 to cross the blood-brain barrier.



## RESULTS

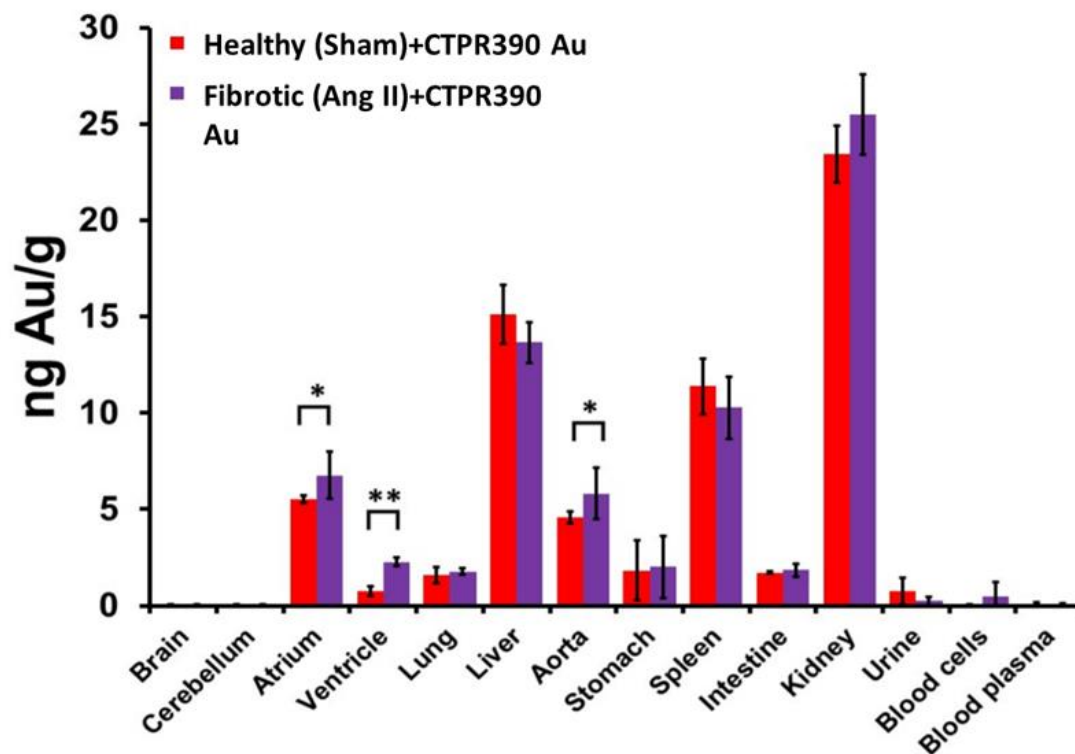


Figure 28 ICP-MS analysis of various tissues from the CTPR390-Au hypertensive and healthy models. Measured Au concentration per gram of tissue in the healthy and hypertensive model with CTPR390 administered 8 days before the end of the trial. \* $p < 0.05$ , \*\* $p < 0.005$ . Mann-Whitney test.

### 4.1.3 Antifibrotic effect and changes in the biomechanical parameters of a human cardiac 3-dimensional model treated with CTPR

With a view to translating the studies to models closer to the human environment generated during the development of cardiac fibrosis, we proceeded with the implementation of a 3D human organoid model, which resembles the mechanical conditions of human cardiac connective tissue, which will allow us to recreate the native environment and conditions more accurately, thus further advancing the study. Following the protocol explained in the method section **3.2.9 Three-dimensional cardiac fibroblast culture construction and experiments**.

This 3D model allows not only to test variations in gene and protein expression in the fibroblasts that make up the organoid, in an environment more in line with the physiological state, but also allows the assessment of morphological, structural and biomechanical characteristics. Thus, this model provides valuable information of the effects that the CTPR390 therapeutic strategy may have in patients.

#### 4.1.3.1 CTPR390 mechanical behavior and antifibrotic effect on human engineered organoids

For the observation of possible mechanical or structural effects of the therapy under study, we incorporated a control CTPR390 molecule that lacks the specific binding module to Hsp90 but maintains the cluster structure incorporating Au as well as fluorophore 488 (maintaining the basis of the fluorescent capabilities of the theragnostic therapy under study).

We will work with 4 experimental groups:

- 1) “control” organoids which will be maintained without exposing them to the CTPRs or to fibrotic activation by TGF $\beta$ .
- 2) “TGF $\beta$ ”-activated organoids that conform the fibrotic group
- 3) “Functional CTPR” organoids activated with TGF $\beta$  and treated with the CTPR390 molecule presenting the functional module to bind Hsp90.
- 4) “non-functionalCTPR” organoids activated with TGF $\beta$  and treated with the CTPR390 molecule without the functional module to bind Hsp90.

The measured parameters used to characterize each group are mentioned in the material and methods section **Organoid rheological analysis**.

A characteristic feature of this model is its generation on two poles that supports the organoid. During the culture of the organoids and by the action of the cells embedded in the matrix, the two poles will undergo a deflection generated by the contraction of the organoid. This parameter was used to establish the 13-day duration of the assay, as it allowed us to observe a differential response in the groups during that time (**Figure 29A**). As can be seen in the **Figure 29A**, from day 2 of culture, the fibrotic “TGF $\beta$ ” group shows a greater contraction than the rest of the experimental groups, which will be maintained until the end of the assay. Thus, “TGF $\beta$ ” group showed a significantly greater degree of deflection percentage compared to the rest of the groups tested (**Figure 29B**). The other 3 groups (“control”, “Functional CTPR” and “non-functional CTPR”) showed similar degree of deflection, with no differences in the mechanical behaviour of the tissues treated with functional CTPR or the non-functional CTPR.

## RESULTS

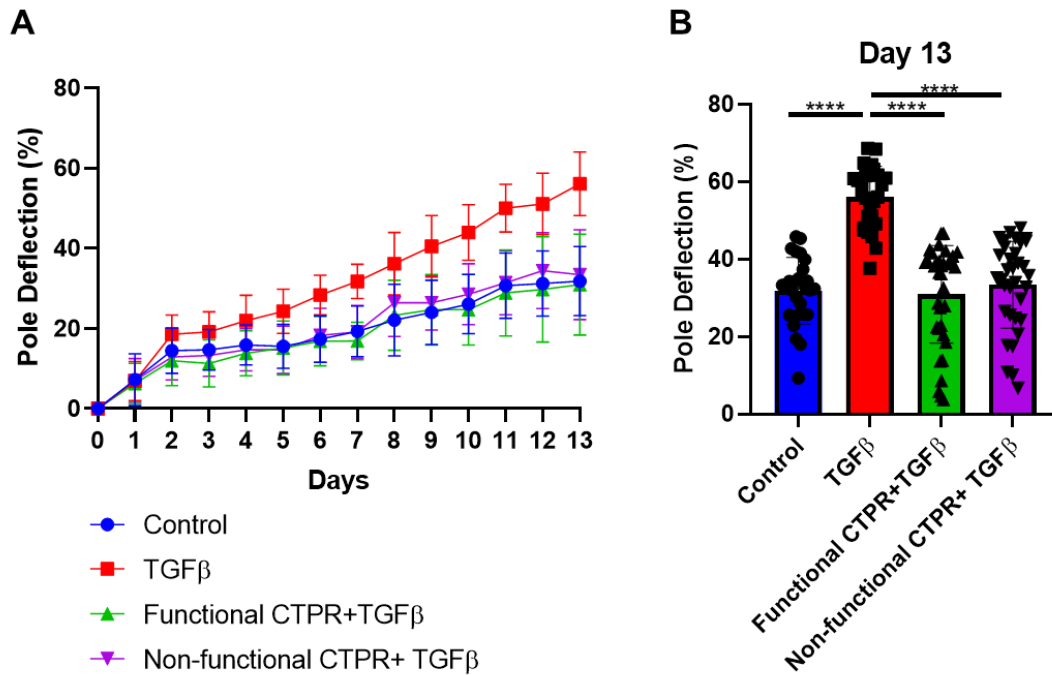


**Figure 29 Mechanical analysis of TGFβ-activated 3D cardiac organoids treated with CTPRs. (A)** Percentage deflection of the contracted poles that support the organoids, analysis of the control group without TGFβ in blue, in red the fibrotic group with TGFβ, in green the fibrotic group with functional CTPR390 and in purple the fibrotic group with non-functional CTPR390. **(B)** Quantitative visualization in a bar graph of the mechanical capacities of the 4 groups of human cardiac organoids under study. N= 12 organoids per group\*\*\*\*p<0,0001, t-test.

In the rheological analysis of the organoid, organoids offered significant differences among the four groups were observed. With regard to the Young's Modulus, inversely related to elasticity, the fibrotic "TGFβ" group offered higher significant values reaching average values of  $110.3 \pm 7.18$  kPa compared to the rest of groups (**Figure 30A**). The groups with the two variants of CTPR390 maintained values closer to the control, between  $50-70 \pm 5.7$  kPa of pressure (**Figure 30A**). In relation to resilience, (an index that indicates the total amount of energy that a system is capable of absorbing before suffering an irreversible deformation ( $\text{KJ/m}^3$ )), a deterioration was observed in the fibrotic TGFβ group compared to the control group (\*p<0.05). The average value in the TGFβ group was reduced to 4  $\text{KJ/m}^3$ , compared to the control group average of 13  $\text{KJ/m}^3$ . The groups treated with functional or non-functional CTPR390 maintained similar values to the control group (**Figure 30B**). Finally, in relation to the toughness, a parameter that refers to the amount of energy that can be absorbed prior to tissue rupture, no statistically significant differences have been found, with values in the range of  $30-75 \pm 4$   $\text{KJ/m}^3$  (**Figure 30C**).



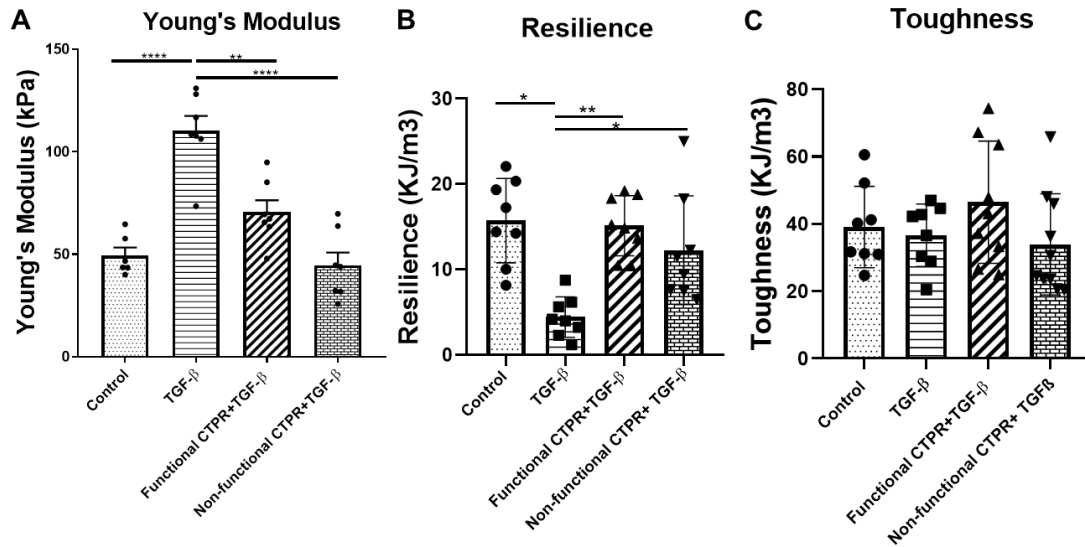


**Figure 30 Analysis of the human cardiac organoids hECT mechanical capabilities (A-C)** Mechanical capacities of the organoids, analysis of the 4 groups mentioned above, with reference to: **(A)** Young's Modulus (Elasticity), **(B)** Resilience (Resistance to deformation), **(C)** Toughness (total energy absorbed). N=4 organoids per group \* $p < 0.05$ , \*\* $p < 0.005$ , \*\*\*\* $p < 0.0001$ , t-test.

#### 4.1.3.2 CTPR390 distribution and gene regulation in cardiac organoids

The use of 3D organoids is becoming more and more widespread, and the possibility of working with a "human" model opens up new opportunities. As described above, the composition of the cardiac organoids used in this study is based on a mixture of a collagen matrix and human cardiac fibroblasts. In addition to studying the effects of CTPR390 mechanical capabilities, it is interesting to observe the presence of CTPR in this 3D model and evaluate the gene expression of profibrotic markers.

Fluorescent signal from CTPR390 molecules allow their detection at the end of the assay (day 13). The presence of functional and non-functional CTPR390 could be detected distributed homogeneously in the tissue (**Figure 31**), in these images the green signal coming from alexa-488 is clearly visible, while in the control and fibrotic group the fluorescent signal was not detected, presenting only a background signal (Figure 31 TGF $\beta$ -Alexa 488).

## RESULTS

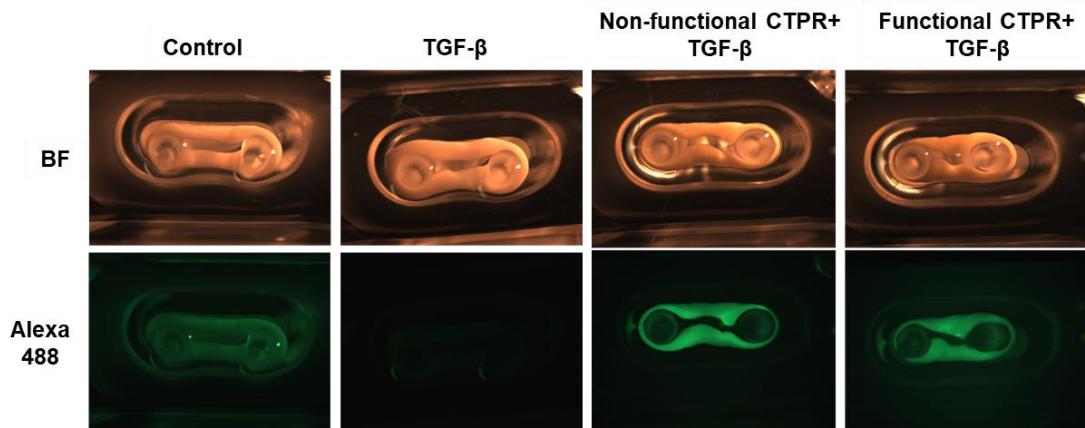


**Figure 31 CTPR390 visualization in human 3D organoids.** (BF) Brightfield microscopy images of the 4 groups of hECT organoids under study( control, TGF $\beta$  (fibrotic), TGF $\beta$  with non-functional CTPR and TGF $\beta$  with functional CTPR. Alexa488) Fluorescence detection of the CTPR390 added to TGF $\beta$  with non-functional CTPR and TGF $\beta$  with functional CTPR groups and the background observed in control group.

Another characteristic of these 3D organoids, concerns to the migration and orientation of the cells in the direction of the tensile forces into the periphery surface of the organoid. The observation of this phenomenon can be seen through multiphoton microscope images (¡Error! No se encuentra el origen de la referencia.). Thanks to the use of this technique we have been able to see in the preliminary data a very pronounced organoid surface orientation in the TGF $\beta$  group (¡Error! No se encuentra el origen de la referencia.A) which is not seen in the control group (¡Error! No se encuentra el origen de la referencia.B) at the same level.

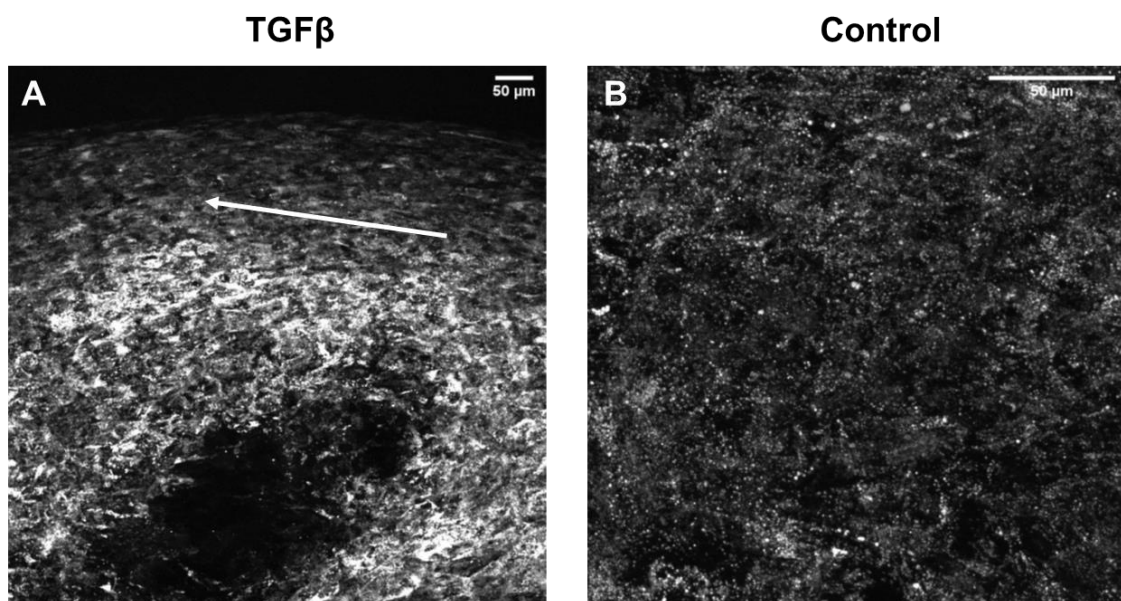


**Figure 32 Multiphoton imaging in organoids.** (A) Surface image of an organoid from the TGF group, where an orderly arrangement of the cells on the surface can be observed, following an orientation (marked with the arrow), (B) surface image of organoid from the control group, where the cells present in the organoid can be seen, with a degree of order not as high as in image A. Scale bar 50 $\mu$ M.

Direct observation of the fibroblasts inside the organoid (**Figure 33A**), or the observation of those fibroblasts once the organoid is disaggregated (**Figure 33B**) offered detection of the functional and non-functional CTPR390 inside fibroblasts. To ensure cell viability, at the end of the assay, part of the cells extracted from the organoids were plated and kept for 24 hours, and it was observed that the cells were able to adhere to the plate and continue to grow. As can be seen in **Figure 33B**

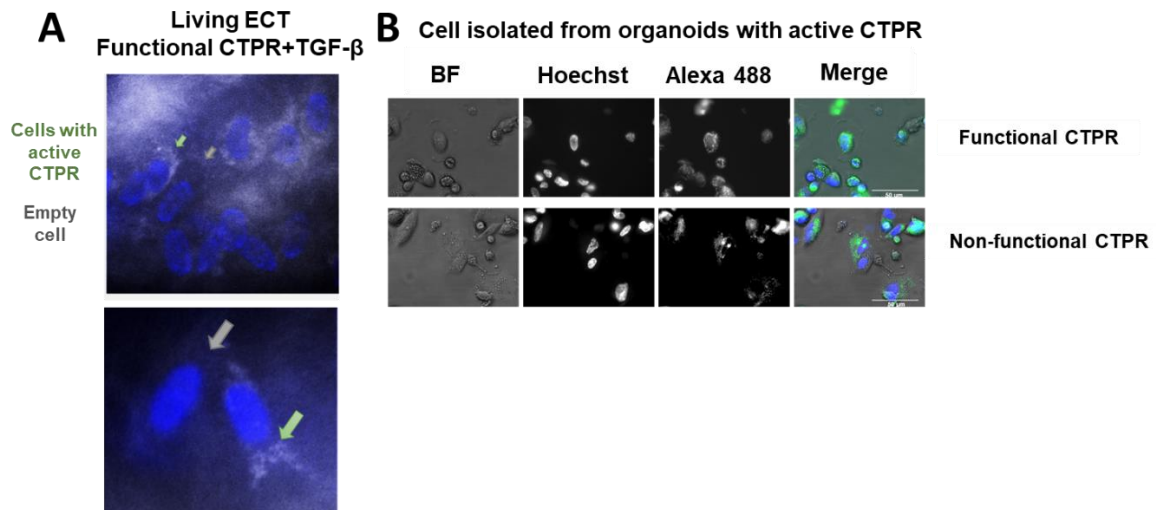


**Figure 33 CTPR390 accumulation in human cardiac fibroblasts of 3D organoids.** (A) Confocal live cell image of a representative TGFbeta-activated organoid with functional CTPR390, in white CTPR390 signal from Alexa488 and in blue Hoechst marker for nucleus. In the detail the grey arrow indicates ..... and the green arrow indicates the presence of CTPR390 (B) confocal microscopy images of cells extracted from organoids and cultured for 24 hours, (BF), brightfield view of the fibroblasts (Hoechst) cells stained with hoechst dye to mark their nuclei. (Alexa-488) autofluorescence detection of CTPR390 (Merge) in green Alexa488, in blue Hoechst dye and the BF composition.

Finally, an analysis of the regulation of the expression of several marker genes by the CTPR390 treatment was carried out. For this purpose, part of the organoids was disaggregated, and RNA was extracted from the fibroblasts located in them. The markers selected were COL1 as a structural fiber, Lysyl oxidase (LOX) an enzyme important for post translationally modifying collagens and elastin in the extracellular matrix [159], , and PDGFRA, a profibrotic-related tyrosine kinase receptor involved in cell proliferation, survival, differentiation, and cellular growth [160].

COLIII gene showed a clear overexpression in the TGFβ group (\*\*p<0.005) compared to the control group, while a significant reduction was observed in the groups treated with the two variants of the CTPR (functional CTPR \*\*\*p<0.001) and non-functional (\*p<0.05) (**Figure 34A**). LOX I gene expression presented a similar tendency as COL I gene expression but with no significant values in the case of the non-functional group (**Figure**

## RESULTS

34B). For PDGFRA, the non-functional CTPR390 group behaves as the TGF $\beta$  group and the control group as the functional CTPR390 group with significant reduction in its expression compared to TGF $\beta$  group (as it was desired) (**Figure 34C**).

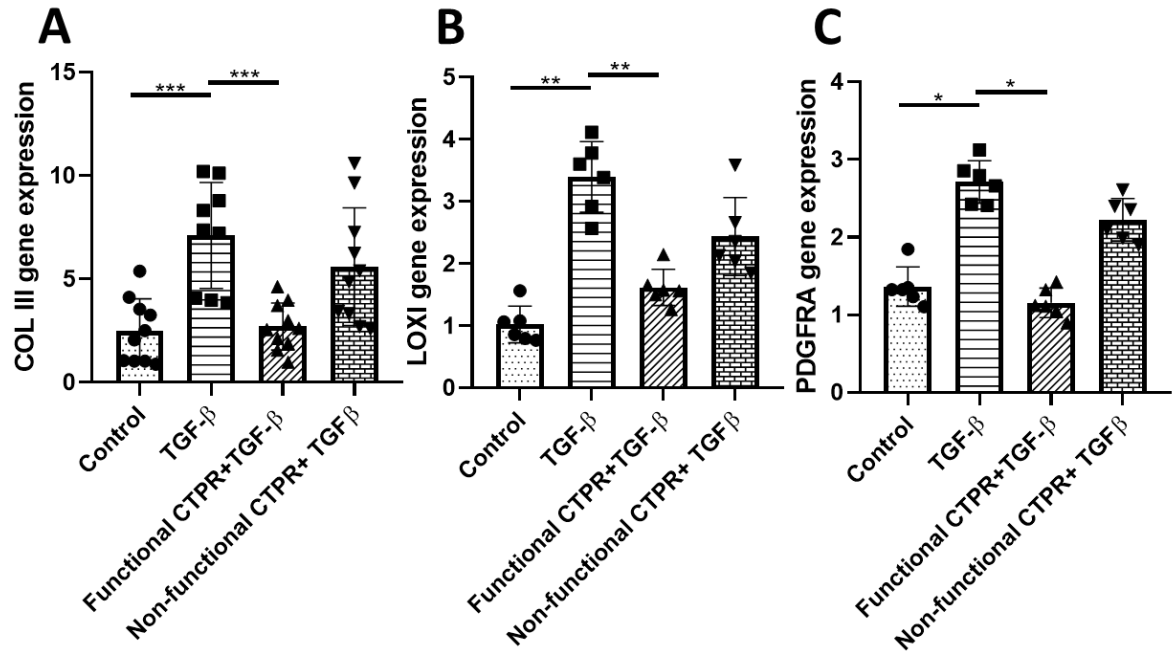


**Figure 34 Gene expression analysis of the fibrotic markers (A) COLIII. (B) LOXI and (C) PDGFRA** in the 4 experimental groups under study (“control” non-TGF $\beta$ -treated organoids, “TGF $\beta$ ”TGF $\beta$ -treated organoids. Functional CTPR+TGF $\beta$  Organoids treated with TGF $\beta$  and functional CTPR390 and Non-functional CTPR+TGF $\beta$  Organoids treated with TGF $\beta$  and non-functional CTPR390 \*p<0.05, \*\*p<0.005, \*\*\*p<0.001. Mann–Whitney test.

## 4.2 Genetic Alert System (GAS), construction and the evaluation of its activity

The construction and elaboration of the GAS system is based on the inclusion of a gene coding for the MMP2 protein responsible for the degradation of extracellular matrix elements, under the control of the periostin promoter (POSTN), following the protocols and techniques described in the material and methods section.

This kind of technology has been used before with different applications, but with the same objective, which is to enable expression in eukaryotic cells of target genes by means of plasmid systems that controls that expression [155, 161].

### 4.2.1 Construction and development of POSTN variant promoters for GAS.

For the elaboration and construction of the GAS system, we started from a previous clone obtained in the group. For the identification of the promoter and the design of the primers for its amplification, we relied on previous studies where this promoter had been identified, as well as the identification of regions of interest within it [138]. The high degree of conservation areas in the periostin promoter (POSTN) were identified, and the presence of enhancers and repressor sequences were located [138] (**Figure 35A**).

We proceeded to the amplification of the POSTN promoter and some other derived shorter promoter sequences whose functionality was previously checked (**Figure 35B**) [138]. From the variants present in the baseline study, a variant designated as **iii** (indicated in **Figure 35B** by an arrow) was selected because of its small size, as well as the high expression values. We also designed a new shorter region of interest inside POSTN with the aim of obtaining the minimum promoter necessary for its expression, (**pPOSTN AV**) preserving conserved regions (**Figure 35B**).

## RESULTS

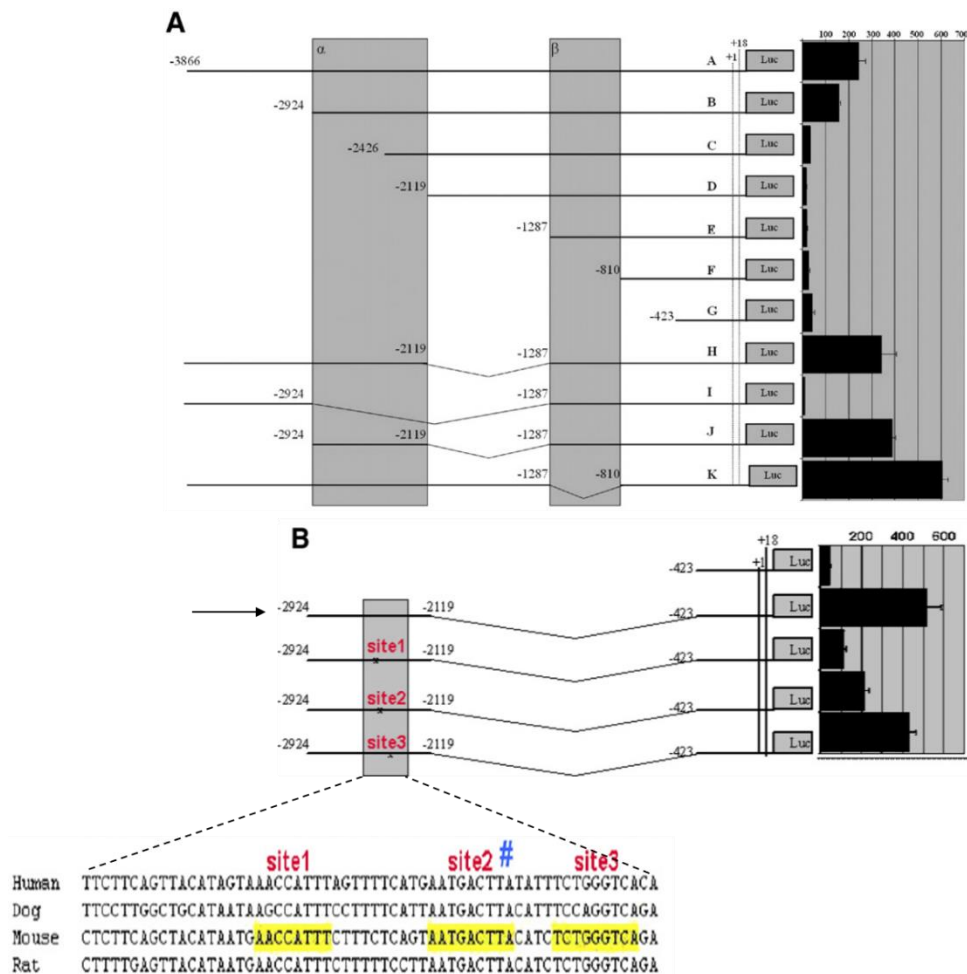


**Figure 35 Periostin promoter and variants, enhancer and repressor sequences.** (A) Representation of the sequence coding for the periostin promoter at the top, to successively find truncated variants of the promoter in regions of the same, for the study of the expression levels of each of them, with the aim of identifying controlling regions.  $\alpha$  represents a putative enhancer region identified in the promoter, while  $\beta$  represents a putative repressor region. (B) truncated variants of the promoter in which the repressor region has been deleted. Through alignments, 3 conserved sites in the enhancer region are identified and used for the design of new variants of the minimal promoter. (A and B) The different promoter sequences are controlling the expression of a reporter gene, luciferase. On the right, the level of expression of each of the sequences is represented graphically, as a result of luminometer measurements of the signal obtained in each case. Adapted from (Linsley, A. et al 2007).

After designating the sequence of the promoters, the different fragments were obtained. Obtaining the fragments for the minimum promoter designed in our laboratory, pPOSTNAV (Figure 36A), as well as the variant present in the selected baseline study pPOSTNiii (Figure 36B). The vector obtained previously in our group in which they will be cloned, was also amplified, removing the CMV promoter sequence present in the original construct (Tsectag-proMMP2, called proMMP2) (Figure 36C). The obtained fragments were analysed by gel migration, for their size (Figure 36).

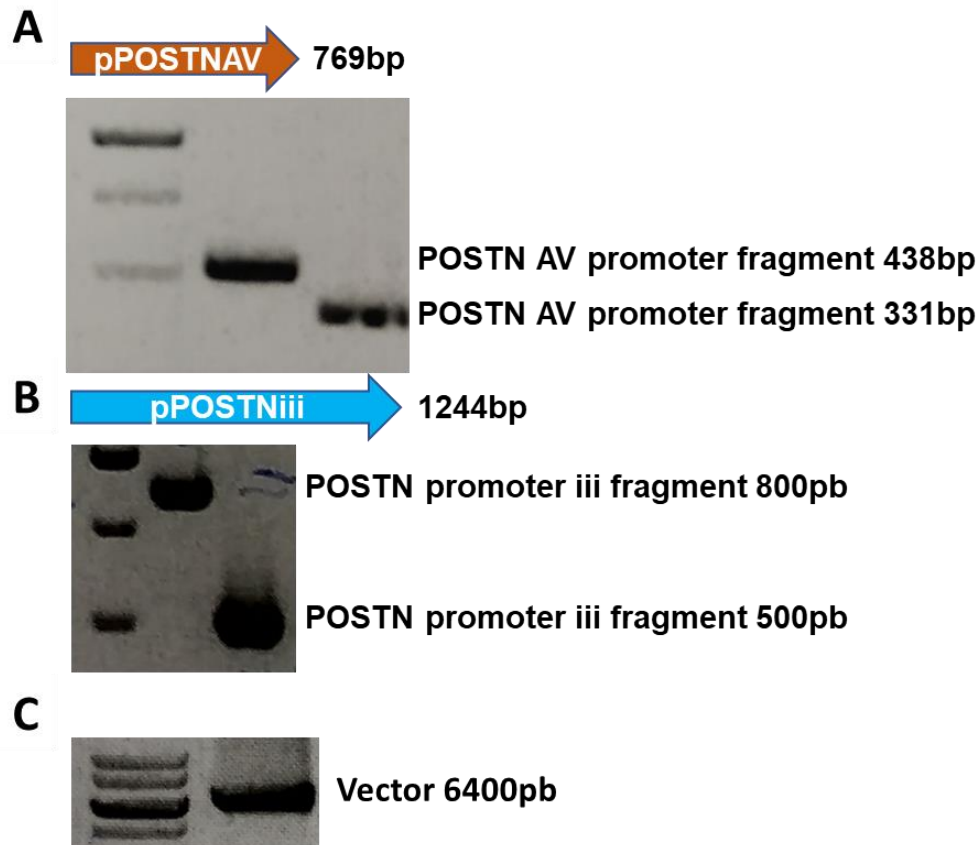


**Figure 36 Amplification of GAS system elements.** (A) Amplifications encoding for the minimal promoter of POSTNAV. **Lane 1** marker 1000, 750 and 500 bp band sizes. **Lane 2** 438 bp fragment detection. **Lane 3** 331 bp fragment detection of the POSTN AV promoter. (B) Amplification of variant iii of the POSTN promoter containing the three conserved sites. Lane 1 marker 1000, 750 and 500bp band sizes. **Lane 2** 800 bp fragment detection. **Lane 3** 500 bp fragment detection of the POSTN iii promoter. (C) Amplified sequence of the proMMP2 (psecTag-proMMP2) vector in which the promoters will be cloned. **Lane 1** marker 10000, 8000 and 6000 bp band sizes. **Lane 2** 6400 bp fragment detection of the proMMP2 vector.

#### 4.2.2 Evaluation of the activity of the constructs GAS AV and GAS iii

For the evaluation of the activity of the generated systems, zymography was used to assess the levels of proMMP2 production by the generated clones, as well as its activity.

The GAS AV and GAS iii constructs contain the gene coding for proMMP2 from the amplification of the proMMP2 vector (**Figure 36C**), under the control of the promoter variant in each case. In GAS iii, the 1244 bp promoter (pPOSTNiii) will be available, containing the three conserved sites of the enhancer region, as well as the entire unmodified enhancer sequence. GAS AV, on the other hand, will have the variant of the pPOSTNAV promoter that will maintain the same 3 conserved sites, but in which part of the sequence identified as enhancer will have been eliminated, obtaining a significant reduction in the size of the promoter to 769 bp. In relation to the proMMP2 gene present in the constructs, in addition to the sequence that encodes it, it has undergone a

## RESULTS

modification, adding a secretion signal sequence, to achieve greater extracellular secretion through its production, as this is where its activity will be required.

Once the constructs were obtained through the assembly of the fragments by isothermal assembly, and after sequencing the constructs to verify the correct integration of the different elements, they were transfected into NIH-3T3 cell cultures and then proceed to the collection of the different fractions to be analysed and their preparation, as described in the section **Analysis of MMP2 functionality and localisation by zymography assay**. The results obtained showed a higher presence of proMMP2 in the culture medium (**Figure 37B**) compared to the content in the cell lysate (**Figure 37A**), and of the constructs produced, the one containing the POSTNAV promoter (**Figure 37a and B**, in the graph it appears as **AV**) showed a significant increase in proMMP2 (\*\* $p < 0.005$ ) compared to the untransfected cell culture.

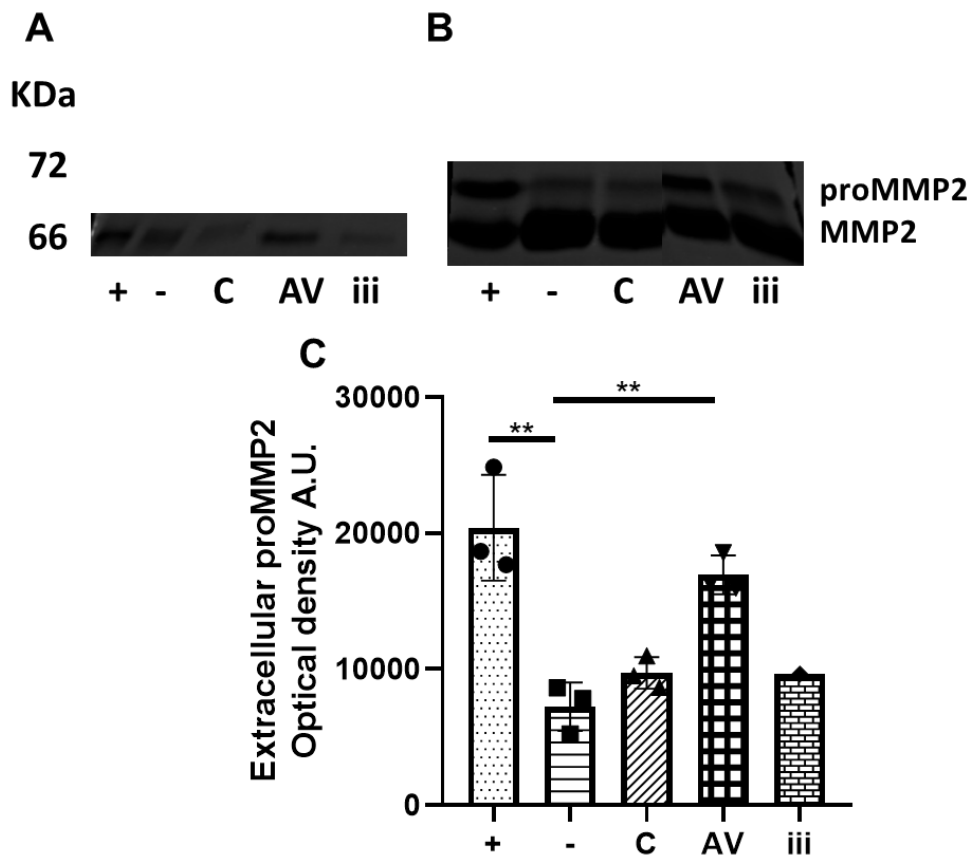


**Figure 37 proMMP2 activity in GAS systems.** (A-B) Transfection of the GAS systems was performed in NIH3T3 cells, control group untransfected (C), a positive control group transfected with the proMMP2 plasmid (+), a negative control containing the psectaq plasmid without the proMMP2 gene (-) and finally the groups with the POSTNAV (AV) and POSTNiii (iii) constructs. (A) zymography of lysates from the groups explained. (B) zymography of recovered culture media. (C) Quantification of the signal obtained in (B) from the different constructs under study. Three independent experiments were performed. \*\* $p < 0.005$  student t test.





### 5. Discussion

Cardiac fibrosis is a pathology with a high impact on the health of society. It is the subject of numerous investigations to describe the process that causes it, describing the different actors involved. Despite this, there is still a lack of effective treatment, which directly treats the pathology.

The complexity of the fibrotic process, with the different cellular agents involved and compensatory effects arising when inhibiting pro-fibrotic events, coupled with the divergence in the level of signalling pathways that may respond, makes it difficult to reach a complete understanding of the mechanism of action of the disease. The finding of effective therapeutic targets with a clear effect on the response, as well as the design of selective drugs that alleviate the damaging consequences of fibrosis need higher number of studies to reach the aim of treating affected patients.

The development and use of anti-fibrotic compounds, such as CTPR390, with a targeted action on effectors involved in the main profibrotic signaling cascade, is one of the solutions currently under investigation due to the importance of avoiding the inhibition of the main cytokine of the disease (TGF $\beta$ ), which is an ubiquitous cytokine and a key homeostatic regulator whose inhibition causes severe alterations in the tissue. CTPR390 was designed to interact with and affect Hsp90 (a protein involved in TGF $\beta$  signaling cascade) inhibiting in a selective manner, the interaction of Hsp90 with other TGF $\beta$  partners to effectively deactivate the profibrotic signaling [140]. Hsp90 has recently been described as a promising therapeutic target for diseases that overexpressed this chaperone. Hsp90 presents a wide variety of actions described in several studies [162], with a key function in the development of a pathology. Hsp90 is located at the cytoplasmic level [163, 164], nucleus [165] or at the extracellular level [166, 167]. In the present study, its extracellular presence led us to describe its capacity to act as a cofactor during the initiation of the activation of the TGF $\beta$  pathway at the plasma membrane level. The formation of a multiprotein complex with TGF $\beta$  receptors would allow reducing the intracellular response of the ligand activation facilitating the control over the profibrotic intracellular events, that would reduce the possible compensatory effects that could be generated downstream, by the branching of the cell signalling [140]. Through this strategy we would reduce the over expression of pathological fibers before their synthesis, secretion and accumulation in the extracellular matrix. This preventive strategy could be combined with a curative strategy based on reducing the already formed fibrosis.

The curative strategy that we have proposed in this thesis is based on the elimination of excess matrix components already deposited, by means of a plasmid named "genetic alert system" (GAS). GAS construction produces active MMP2 with the capacity to digest the matrix components, thus reducing fibrosis. Similar systems have already been used to control the expression of heterologous proteins in a specific manner [168, 169]. The logic behind this system, is based on its activation under profibrotic conditions. GAS does not express MMP2 during basal state in healthy environments but when the profibrotic protein periostin expresses the GAS system activates its capacity of synthesis and secrete MMP2 to degrade collagens.

The present work evaluates the antifibrotic behaviour of CTPR390 and GAS in different experimental models such as embryonic and primary fibroblast hypertensive mouse models and human cardiac organoids. Moreover, we evaluated the high potential of the molecules under study to be used as biomarkers of the disease. It is worth highlighting the migration and transition from traditional 2D models at the beginning of the study to models with greater complexity (3D models), always seeking a better adaptation of the experimental systems to the real human myocardial tissue.

The present work also evaluates the antifibrotic activity and responsiveness of the gene therapy named GAS analysing the first phases of its development and testing its enzymatic activity in collagenic environments.

## **5.1 CTPR390 is localized intra and extracellularly without affecting the fibroblasts homeostasis**

MEEVD motif of Hsp90 $\alpha$  and  $\beta$  isoforms is CTPR390 target and it is highly possible that of Hsp90 extra [143], intercellular presence allows the nanocluster to bind its target in both locations. Intracellular CTPR390 does not alter cell healthiness but in NIH3T3 fibroblasts seems to produce some stress that is not detected in cardiac primary fibroblasts revealing a very interesting aspect on the importance of choosing the adequate cell model to demonstrate the homeostatic alterations of a cardiac fibroblasts environment in the present of new biotechnological therapeutic strategies interacting with the key profibrotic cascade of TGF $\beta$ [140].

Due to the relevance of Hsp90 in the maintenance of cell homeostasis, partial or total inhibition of its activity has always been followed by side effects and may lead to cell death [170]. As an example of the above, the use of existing commercial inhibitors such as 17AAG or 17DAMG have demonstrate to be useful in cancer therapies due to the reduction in the cell homeostasis [147, 171]. Therefore, the described ability of

## DISCUSSION

CTPR390 to selectively inhibit the C-terminal end of Hsp90 without affecting its ATPase activity thus allowing its client proteins to correctly fold at the same time that affect the function related to TGF $\beta$  signaling cascade. Thus, the use of CTPR390 could be a biomedical opportunity to continue advancing toward the clinical trials with a potential treatment for myocardial fibrosis.

### 5.1.1 The intravesicle ultrastructural location of CTPR390 activates cell trafficking

The CTPR autofluorescent facilitates its tracking and detection. CTPR390 internalises into cells, although cytoplasmic CTPR390 represents a small percentage of the total CTPR390 added to fibroblasts (**Error! No se encuentra el origen de la referencia.**), because most of it is found extracellularly. So far, the mechanism of action through which this internalisation occurs has not been elucidated and more assays are needed to monitor the whole process more precisely. Despite this, and without ruling out the possibility of a passive or facilitated diffusion to get the cytoplasm, results obtained using cryo-3D-SIM and cryo-SXT techniques (**Figure 11**) show a homogeneous distribution and an elevated number of cellular vesicles (**Figure 12**). Protein markers, such as Alix, revealed that CTPR was incorporated to multivesicular bodies related to vesicle trafficking, [172]. Fibroblasts could transfer CTPR390 from one fibroblasts to another through extracellular vesicles (CTPR390 showed relation to CD9 marker), which would include CTPR390 among the intercellular signals that connect fibroblasts through exocytosis processes [173]. Importantly, the ability of CTPR390 to bind to extracellular Hsp90 may present an entry pathway associated with chaperone internalisation.

Despite the intracellular presence of CTPR390 in the majority of the nanocluster is located in the external environment of the cell (**Figure 7A**), which could be due to the extracellular presence of the CTPR target protein (Hsp90). This would be feasible if we take into account that profibrotic conditions favour the secretion of Hsp90 similar to other damages such as wounds that also favour the Hsp90 secretion[174, 175]. Another possibility for CTPR390 trafficking in the cell may be due to saturation that activates removal processes out of the cell.

### 5.1.2 Ultrastructural and cell signalling effects of CTPR390

The effects observed in cells with the administration of CTPR involve alterations at the ultrastructural level. The effects generated in different organellas related to CTPR390 presence in fibroblasts (**Figure 10**), can be located in the ER, the number of trafficking

vesicles (as we described above) and the size of mitochondria. Moreover the levels of collagen deposition in the intracellular regions are reduced. In TGF $\beta$  activated-fibroblasts, the increase in ER thickness indicating (active process of protein synthesis) and the presence of collagen deposition in intercellular spaces are related because collagen is the main protein generated by fibroblasts. CTPR390 treatment, avoids the ER enlargement and the collagen deposition [140]. Through the inhibition of key proteins in the profibrotic process. The modulation of the ER size can also be observed with other molecules showing similar effects to those obtained with CTPR390 [176-178].

The presence of the higher number of vesicles could also respond to normal endosomal cell traffic, independently of cell activation (**Figure 13**). Due to the increase was observed only in the groups treated with CTPR390 (**Figure 13**), which may be related to the internalisation processes of the CTPR into the cell [155, 179]. The analysis of the mitochondria, showed changes in the size and shape in the groups activated by TGF $\beta$ . Cell activating processes are energetically demanding, so an increase in the number of mitochondria is to be expected. This effect was suppressed by CTPR390 treatment ( ). (**Figure 10**).

At the molecular level, alterations in activation of TGF $\beta$  effectors in pathological conditions, such as fibrosis appears in both canonical and non-canonical TGF $\beta$  pathways [180-183]. A decrease in the phosphorylated fraction of the profibrotic proteins analysed in the presence of CTPR390 groups, (**Figure 15** and **Figure 16**) indicated that the antifibrotic effect of CTPR390 affected the secondary cytoplasmic messengers of the process. Those changes were not accompanied with a reduction of Hsp90 chaperone ATPase-dependent activity. As mentioned above, the analysis was performed on canonical and non-canonical TGF $\beta$  pathway components, so CTPR390 affected both, thus interfering at an upstream level, common to both signalling pathways. Which supports the idea of the relation of Hsp90 and TGF $\beta$  cascade at the plasma membrane level. This is further supported by the use of a mutated form of TGF $\beta$  receptor 1 (TGF $\beta$ R1), which was constitutively active. The constitutively active TGF $\beta$ R1 recovered the decrease of phosphorylated forms of TGF $\beta$  related effectors (**¡Error! No se encuentra el origen de la referencia.**). The desirable effect of CTPR390 would be the reduction of COL1 as one of the main fibres produced in the fibrotic pathology (**Figure 17**). Similar effects of collagen reduction have been observed using already available Hsp90 inhibitors such as 17AAG [164, 184].

Moreover, there was an increase in the expression of the Hsp90a inducible isoform, upon TGF $\beta$  addition, while the constitutive Hsp90 $\beta$  remained constant (**¡Error! No se**

## DISCUSSION

**encuentra el origen de la referencia.A).** This would indicate that while CTPR390 through its interaction with Hsp90 would affect TGF $\beta$  signalling, the effects of TGF $\beta$  on Hsp90 expression would not be through this pathway and could be controlled by different mechanisms [185].

### 5.1.3 Action model of the CTPR390-Hsp90 and Hsp90-TGF $\beta$ RI physical interactions

As described above, the approach to treat fibrosis that we have pursued in this work, is based on the Hsp90-TGF $\beta$ RI interaction, to reduce TGF $\beta$  profibrotic action, thus having a possible treatment that prevent the formation of an excess of fibers in the ECM. In the thermodynamically favourable interaction between Hsp90 and TGF $\beta$ RI *in silico* simulation was validated with molecular assays oriented to demonstrate direct protein-protein interactions, such as protein pull down or “proximity ligation assay” (PLA) assays. (**Figure 18**), in which the interaction of Hsp90 with the TGF $\beta$  receptor is observed. We showed (in silico representation and published ligand binding assays [157]) that the interaction of CTPR390 with the c-terminal end of Hsp90 affects the above interaction process. It was also possible to visualise *in vitro*, the interaction of the chaperone with the receptor with PLA (**Error! No se encuentra el origen de la referencia.**). We defend that the Hsp90-TGF $\beta$ RI physical interaction is part of the mechanism of action, of the decreased fibrosis obtained after the administration of CTPR390 [158]. Similarly, assays performed during this study, mentioned above, such as the experiments performed on cells transfected with constitutively active TGF $\beta$ RI (**Error! No se encuentra el origen de la referencia.B**), bypassed CTPR390 action, demonstrating the plasma membrane localization of the CTPR390 action in the profibrotic event (**Figure 15** and **Figure 16**). The logic behind this assay indicates that if the effect of CTPR390 would have been at the cytoplasmic level, no changes on the anti-fibrotic effect detected in the presence of CTPR390 will be observed, thus no difference should be observed between the two situations.

With these data and those presented above, the effectiveness and capabilities of this new CTPR390 molecule in traditional cell culture systems have been demonstrated, positioning it as an alternative therapeutic strategy that would need further research to reach clinical trials with a positive perspective. It is worth noting, as already discussed above, the variety of alternatives that are currently being studied, with different strategies corresponding to different therapeutic targets [186]. Compared to other approaches an advance in the field exhibited by the therapy proposed here would be the inhibition of the effect of crucial cytokines such as TGF $\beta$  in the absence of clear cellular adverse effects

[187, 188]. The use of innovative biomaterials with anti-immunogenic properties and addressing TGF $\beta$  partner proteins, as it is this case, have the aim of controlling the overproduction of fibers in fibroblasts but not replacing and repairing damaged tissue as in other strategies [189, 190] or even exploring the possibility of cell transplantation, which allows damaged tissue to be replaced [191, 192].

## 5.2 *In vivo* theragnostic capabilities of CTPR390

Experimentation in cell culture models in monolayer, although it is an accessible method that has demonstrated its advantages and uses, lack of the complexity of an organism, thus it is undoubtedly important to use *in vivo* models, which allow the assessment of the CTPR390's capabilities, getting results that could be closer to CTPR390 possible action in patients.

The use of animal models has been vitally useful, not only for translational purposes, but also for human health applications. In the case of mice, we have examples of different animal models generated for the study of different cardiac conditions [193]. The study in mice using the experimental groups shown in **¡Error! No se encuentra el origen de la referencia.** allowed us to assess not only the effect and behaviour of the molecule in a complex environment, but also its safety in unaffected healthy models [150]. The use of AngII in this model has proven to be a valid mechanism for the generation of the remodelling process we wish to initiate, the capabilities of which have been extensively described [194, 195].

### 5.2.1 CTPR interferes with cardiac remodelling in vivo

The cardiac remodelling initiated in the Ang II model, is a response of a chronic hypertension generated by the release of the hormone AngII via an osmotic release system. The remodeling process would include hypertrophic events, mainly caused by the increase in size of cardiac muscle cells and the fibrotic process involving cell proliferation and ECM greater extension, being the main component of which the uncontrolled production of matrix components, followed by the gradual replacement of healthy tissue by fibrotic connective tissue.

The effects observed with the administration of CTPR390 in the fibrotic groups varied greatly depending on the time of administration. In the case of the groups with the longest CTPR-mouse interaction time (4 and 8 days), clear recovery effects were observed. The hypertrophic processes analysed through the ratio between the weight of the heart (HW) and the weight of the individual (BW) (**¡Error! No se encuentra el origen de la**

## DISCUSSION

**referencia.** 8 Days) is reduced compared to the hypertensive mice, and the fibrotic remodelling decreased, based on the measurements of the areas of collagen present in sections of the cardiac organ (Masson's trichrome) (**Figure 22 4 and 8 Days**). The administration of CTPR390 for 3-hours (**¡Error! No se encuentra el origen de la referencia.** and **Figure 22 3 Hours**) revealed that it is not enough time to develop a detectable response, which is to be expected given the short action time of the assay. This result agrees with results obtained in other studies, in animal models [164, 184, 196], which showed a counter-effect on the remodelling processes, through the inhibition of Hsp90, by using inhibitors such as 17AAG, analysing the effect of the inhibition directly on the TGF $\beta$  pathway or accessory pathways [184, 196].

We demonstrate that 8 days of a single dose of CTPR390 was sufficient to reach the heart and exercise its therapeutic function. This is confirmed, by the effects on remodelling (as explained above), as well as with the data obtained with the analysis of the CTPR390 accumulation in the heart (XRF microscope images). XRF detection allowed us to detect and quantify the amount of CTPR in the target tissue through the gold signal (**Figure 24H and C and D**). Even so, it should be considered that in those groups with AngII administration, in which the administration of CTPR390 was carried out 4 days and 3 hours before slaughter, these were groups whose "treatment" was administered late, with respect to those that received it 8 days before slaughter, so that the pathological process generated had additional time for its development, which could rest efficacy. This observation indicate that an early prevention of fibrosis through the administration of CTPR390 could avoid the accumulation of excessive damaging ECM.

In addition, gene expression analysis of hypertensive markers such as Nppa and Nppb (**Figure 23A-B**) and matrix fibres such as COLIII and FN (**Figure 23C-F**), showed a trend towards recovery of physiological levels getting closer to the control groups. However, something worth noting is the ability of the CTPR molecule to continue to exert an effect 8 days after administration, showing signs of great stability in an organism that would avoid the administration of several doses to reach the desired effect; this would be a positive feature when administrate into patients.

### **5.2.2 CTPR testing, potential theranostic capacity through Hsp90 inhibition and fluorescence capacity**

So far, the therapeutic effects derived from the use of CTPR390 "*in vitro*" and "*in vivo*" showed beneficial anti-fibrotic features, such as reduction in collagen gene expression and deposition, the accumulation in the target area, as well as the absence of chaperone diminished activity to insured the maintenance of cell homeostasis. However, regarding



to its visualisation with fluorescent techniques, CTPR390 offers possibilities beyond its use as a therapy. As mentioned throughout this work, different variants of the CTPR390 molecule have been used in the study, all of them having in common the Hsp90 binding module, which would recognise the aforementioned MEEVD motif, present in the chaperone. The remainder of the molecule has been edited to give it specific stability and fluorescent characteristics. The use of the Alexa-488 fluorophore or the inclusion of gold nanoclusters [140, 150] open the possibility of the CTPR390 application as a diagnostic tool. Together with its therapeutic capabilities, this nanoparticle could be classified as a molecule with theragnostic capabilities. Compounds with these characteristics have been used in recent years, due to the interest they generate [197, 198], allowing in many cases the simultaneous monitoring of the pathology to check its evolution, and giving the opportunity to evaluate the effectiveness of the treatment administered to the patient, which can save adverse effects, time and money during the duration of the treatment [199].

The diagnostic capacity of CTPR390 lies in its selective accumulation in the affected areas, bigger than the CTPR390 accumulated in healthy tissues. This comparative could be observed in the heart of mice treated with CTPR390-Au at different times (3 hours, 4 days and 8 days before sacrifice), by XRF microscopy (**Figure 24A-F**, **Figure 24B**, **D** and **F**), reaching maximum values at 8 days (**Figure 24F**). In healthy hearts, the signal detected was identified as residual (**Figure 24A**, **C** and **E**). The relationship between the signal intensity obtained, directly proportional to the amount of CTPR390 in the area analysed correlated with the exposure time. However, what was also seen was a correlation between the percentage of fibrosis (fibrotic area) and the signal intensity in the fibrotic tissues treated with CTPR390 (**F**). Even though in the initial analyses comparing the different administration times of the CTPR shows that the 3-hour group, with the highest percentage of fibrotic tissue, has the lowest CTPR390 levels (**B**, **D** and **F**), the 8-day group has the highest concentrations and the lowest level of fibrosis. This would only imply the need of time to allow the arrival, accumulation, and action of the CTPR in the affected tissue.

The application of other assays only reinforced these data. The fluorescent signal of the CTPR390 combined with techniques that allowed the visualisation and quantification of the collagen present in the tissue, permitted the observation of CTPR390 in the areas where collagen is accumulated in the heart of the same myocardial sections **Figure 26** and **Figure 27**. The results showed in two of the CTPR390 variants ( the Alexa-488 CTPR390 molecule and the gold nanocluster CTPR390), indicated the selective accumulation of the CTPR in the affected areas of the fibrotic groups, and the collagen

## DISCUSSION

overexpressed in those areas(**Figure 26**) detected by staining the collagen fibres with a tungsten solution or by Masson's trichrome staining (**Figure 27** row of W). The accumulation of CTPR390 was only achieved in those fibrotic tissues treated with the CTPR390 (**Figure 26D** and **Figure 27K**), not being observed in healthy tissues of experimental groups to which CTPR390 had been administered in the same way (**Figure 26H** and **Figure 27H**), showing their capacity to discern between healthy and fibrotic tissues, diagnostic capacity. In the same way, it was also observed that those fibrotic tissues treated with CTPR390 showed a lower collagen signal than those that had not been treated (**Figure 26B-C**), therapeutic capacity.

Despite the theragnostic results obtained, one of the aspects that could not be studied for the moment, and which would provide a better understanding of the system, perfecting the system's therapeutic capabilities, would be to carry out an experiment in which not only the accumulation of the CTPR390 in a fibrotic area would be evaluated with respect to a healthy control, but also a follow-up over time would be carried out. This could provide information on the evolution of the concentration of CTPR in fibrotic tissue over time, and it may be the case that as the tissue recovers the characteristics of healthy tissue, the concentration of CTPR is reduced. This is to be expected, since in healthy groups, the signal coming from the CTPR is residual, so that if the fibrotic tissue with CTPR recovers similar characteristics to the healthy control, it is to be expected that this will progressively abandon the tissue. This would allow not only to differentiate between fibrotic and healthy tissue, but also to evaluate the degree of deterioration of the fibrotic tissue depending on the amount of CTPR390 present and the degree of recovery after the anti-fibrotic treatment.

### **5.2.3 CTPR390 acumulation in the cardiovascular system of fibrotic mice**

Among the characteristics that would affect the therapeutic and diagnostic capabilities of the CTPR390, we have described the specificity for the cardiovascular system. Specificity for the cardiovascular system, on which it must exert its therapeutic effect, guarantees that CTPR390 is able to distinguish between healthy and fibrotic tissue. The analysis of most of the key tissues of mice was carried out to check if CTPR390 selects the accumulating organ and exhibit different behaviour between healthy organs and the fibrotic ones.

Several organs were analyzed by ICP-MS in an attempt to screen as widely as possible. In this case, the presence of gold, CTPR390-Au, was detected in most of the tissues extracted from both healthy and fibrotic groups (**Figure 28**). It should be recalled that the

administration followed in all the trials was a systemic administration, which means that the molecule is expected to travel through the whole organism, which is why its arrival at the target tissue is not immediate, as evidenced by the gradual accumulation seen in (**Figure 24B**, D and F). It is also worth mentioning that the CTPR390 target Hsp90 chaperone, is widely distributed in all tissue cells, due to its role in the maintenance of cellular homeostasis [166, 185], so it is expected that the CTPR can interact with Hsp90 in the rest of the tissues. The extracellular presence of Hsp90 in pathological situations due to its secretion to the extracellular space would attract CTPR390. We have demonstrated that CTPR390 is located in greater amounts outside the cell and cardiac activated fibroblasts secrete Hsp90 as we showed. Thus, the accumulation observed in the cardiovascular system (ventricles, aorta and atria) would indicate fibrotic places.

In addition, most of the CTPR390 was found in organs related to the metabolism and elimination of drugs, such as the kidneys, liver and spleen and no differences were found between healthy and fibrotic mice in that respect (**¡Error! No se encuentra el origen de la referencia.**). Therefore, although it is true that the presence of CTPR could be distributed among most of the tissues analyzed, what is really important would be to identify whether the accumulation in these tissues shows differences between the healthy and fibrotic groups as we mentioned (**Figure 28** (ventricles, aorta and atria). As an interesting fact, the CTPR390, which already showed in previous assays its ability to penetrate at the cellular level and whose biodistribution has been made clear that at the systemic level is high, has not shown detectable levels of its presence at the level of the brain and cerebellum, which may imply its inability to cross the blood-brain barrier, interesting characteristic to avoid any undesirable accumulation in the. It would be interesting to design specific transport systems that could guide the CTPR390 to the target organ, maximizing the arrival and increasing the efficiency of the possible treatment. In vivo monitoring over time could help to clearly discern the of CTPR390 during time in those organs until it is eliminated [200].

### **5.3 Preservation of healthy mechanical behaviour in a fibrotic 3D human cardiac organoid in the presence of CTPR390**

During the first phases of the CTPR study, we focused on identifying the effects at the molecular level using 2D cell cultures and subsequently its behaviour and its capabilities were analyzed in an in vivo model. In this translational study, one further step to the final use of CTPR390 as an antifibrotic molecule in patients, is the analysis of its effects in human 3D cardiac models with mechanical characteristic that mimic the myocardium.

## DISCUSSION

Therefore, we proceeded to analyze the mechanical capacities in the presence of the CTPR390 in an in-vitro human 3D organoid. The complexity that the use of an in vivo model may entail for their measurements, could be simplified in this model, and in addition we would try getting a little closer to the native environment for which the CTPR390 would act in patients.

The 3D model used was fine-tuned and tested, in order to mimic the human cardiac connective tissue, providing an environment similar to that found in the native organ, with regard to conditions of mechanical stress. It must be understood that the conditions of rigidity and tension to which the cells are subjected do not correspond to natural conditions [201, 202] even though they are subjected to some rigidity and tensions absent in other models. This, together with the fact that fibroblasts, like any other cell type, are sensitive to mechanical stimuli, which generate a response in the cell, present an optimal model to observe a response to external stimuli [203-205], such as the presence of TGF $\beta$  and CTPR390. Those molecules would alter or distort to a greater or lesser extent the mechanical properties of the organoid and can affect the results obtained. Thanks to these 3D models, it is intended to perceive the real impact that the treatment of the CTPR390 could have on a native system.

### **5.3.1 Restoration of basal mechanical capabilities through the action of CTPR390**

In short, what we have been able to assess here is the evolution and adaptation of the mechanical capacities of the organoids used to the culture conditions, analysing the effect of the activity of the cells present in the organoid on the reorganisation of the matrix and the impact this has on its properties [206].

The results obtained in the 4 experimental conditions showed a clear difference between the fibrotic group, (group treated only with TGF $\beta$ ), and the rest of the groups. It was possible to clearly identify and differentiate the "properties" of a healthy state, as opposed to those affected by pathological remodelling, present in the TGF $\beta$  group that presents higher values of tension and different elasticity compared to controls or CTPR390-treated groups.

The design of the organoid allows to analyse the force of contraction produced by the fibroblasts that compose the system. Periodic measurements of the degree of deflection of the poles (**Figure 29**) during the contraction process, in addition to differences in the percentage of pole deflection, an alternation between stable periods of pole deflection followed by periods of sharp increase in deflection was observed in all groups (**Figure 29**) [207, 208]. However, in the case of the TGF $\beta$  group, observing the graph in **Figure**

**29**, the alternation between these two processes is barely perceptible, appearing at first glance to be a straight line with a constant slope (possibly due to the exacerbated remodelling process trigger by TGF $\beta$ ). The TGF $\beta$  group presented a clear increase in its expression, compared to the rest of the groups (**¡Error! No se encuentra el origen de la referencia.A** and **B**), which could indicate a transdifferentiation process [203] to myofibroblast, which could cause higher levels of extracellular matrix production in this group of organoids, followed by a greater traction force, exerted by this new cell population, given their capacities [203, 204].

One result that has been observed in part of the measured properties is the apparent effect that the control CTPR390, lacking the Hsp90 binding modulus, has on the recovery of these mechanical capabilities of the tissue, which is observed in the measurement of deflection (**Figure 29**). The organoids of this group seem to respond in the same way as the control group and the group treated with the functional CTPR390 and in two other measured mechanical parameters, Young's Modulus and Relisience (**¡Error! No se encuentra el origen de la referencia.A** and **B**). The non-functional CTPR390 presents lower affinity for Hsp90, [209], however seeing the results, one would expect non-specific interactions with proteins, or perhaps due to the negative charge of the molecule interaction with the ECM components mostly positive charged affecting the 3D structure of the organoid, in its polymerization and reorganization when supporting the fibroblasts Obviously, since it does not have the Hsp90 binding module, we would not expect a specific interaction, not being able to rule out some interference in the system. Reinforcing this possible interaction of the non-functional CTPR390, there are also genetic expression analyzes, which show, in the same way as in the previous models, a restorative effect on the expression levels of marker genes COL3 (**¡Error! No se encuentra el origen de la referencia.A**), LOX (**¡Error! No se encuentra el origen de la referencia.B**) and PDGFRA (**¡Error! No se encuentra el origen de la referencia.C**) (organoids treated with functional CTPR390) compared to TGF $\beta$  activated organoids. The unexpected result obtained was that the similar effects seen in organoids with the presence of functional CTPR390 were obtained in the organoids treated with non-functional CTPR. However, it should be noted that the degree of significance is lower (**¡Error! No se encuentra el origen de la referencia.A-C**), which could imply an interference at the level of the extracellular matrix that may cause distortions in the mechanical signals of the organoids [210, 211]. This phenomenon deserves further research to elucidate the mechanism of action of this CTPR390variant.

### 5.3.2 3D human culture model, under the action of the CTPR

As a final point in the work carried out with the CTPRs, we proceeded to analyze the behaviour of the organoids, as well as the cells present in them, in the presence of the functional and non-functional variants of CTPR390, analyzing both their distribution and cell viability. As in the animal model used previously, in this model, in addition to the cells, we will have a 3D framework, composed mostly of Collagen, which while acting as a support, can act as a possible reservoir of the CTPR administered to the organoids [212].

High concentrations of the CTPR390 molecules in the organoid at the end of the test are visualized as intense fluorescence signal with both variants of the CTPR390 (functional and non-functional) (**Figure 31**). The detection of the CTPR390 at the cellular level, allowed to assert again the internalization capacity, seen previously in monolayer cell cultures of cardiac primary fibroblasts of mouse (**Figure 7B**), although in this case we are observing a human model for the first time (**¡Error! No se encuentra el origen de la referencia.**). The observation of the organoid in vivo, as well as the visualization on the surface of cells in these organoids, also showed the presence of CTPR390s inside the cell (**¡Error! No se encuentra el origen de la referencia.A**), not being able to identify differences between functional and non-functional CTPR.

We are running assays on mouse fibroblasts, to define whether there are differences in the internalization capacity between the non-functional CTPR390 and the functional variant [155]. Observations of human fibroblasts from the organoids under study, showed cytoplasmic presence of CTPR390 and no differences between CTPR390 variants (**¡Error! No se encuentra el origen de la referencia.B**). Carrying out a cell count in the organoids, it was possible to verify very similar viability among the 4 experimental groups (control, TGF $\beta$ , functional CTPR390 and non-functional CTPR390). The data showed an increase in the size of cells from the organoids treated with TGF $\beta$ . This result could be related to the ultrastructural changes described above (**Figure 10A-B**).

### 5.4 First steps in the construction and assessment of the functioning of the Genetic Alert System

The implementation of a system based on the use of gene therapy has been studied for years [213, 214]. The provision of a system capable of acting on the components of the matrix already deposited provides an insight into the curative treatments for those people who have not been able to receive early anti-fibrotic treatments that would reduce the exacerbated accumulation of ECM structural components.

The development process is in its initial stages, with only the construction of the so-called "GAS<sub>AV</sub>" and "GAS<sub>iii</sub>" constructs having been successfully achieved. The isolation and obtaining of the fragments necessary for the construction of the GAS systems were obtained from the previous studies (**¡Error! No se encuentra el origen de la referencia.**) [138].

With regard to its function, as we have seen, a strong synthesis and secretion to the extracellular media of active MMP2 by GAS<sub>AV</sub> construct is obtained (**¡Error! No se encuentra el origen de la referencia.**B). One of the constructs, GAS<sub>iii</sub>, does not seem to stand out for its levels of MMP2 expression, despite being a system already tested previously by another research group [138], so we will proceed in the future to identify the ideal conditions for its activation. Both constructs have been sequenced and confirmed, so once these have been verified, the next step in future studies will be to identify the activation conditions that ensure strong and controlled activation.

## DISCUSSION





## 5. Conclusions

1. CTPR390 internalized into embryonic NIH/3T3 fibroblasts and cardiac primary fibroblasts from mouse being accumulated into vesicular bodies, belonging to the vesicular transit.
2. The use of CTPR390 has shown no detectable toxic effects in NIH/3T3 cells and cardiac primary fibroblasts from mouse.
3. The interaction of CTPR390 with the Hsp90 chaperone promotes inhibition of the Hsp90-TGF $\beta$ RI interaction, without affecting the ATPase refolding function of the chaperone.
4. CTPR390 presence in NIH/3T3 exhibited signs of cell stress such as increasing in mitochondria volume and sphericity, that are not detectable in cardiac primary fibroblasts from mouse maintaining their main ultrastructural characteristics increasing the number of trafficking vesicles and counteracting the effects of TGF $\beta$ .
5. The anti-fibrotic effects of CTPR390 treatment of TGF $\beta$ -activated NIH/3T3 cells or cardiac fibroblasts from mouse partially restores the expression levels of Col III, FN, Nppb, and Nppa indicating a regression remodeling at the molecular level.
6. The profibrotic canonical and non-canonical TGF $\beta$  effectors reduced the levels of active phosphorylated isoforms in the presence of CTPR390 in TGF $\beta$ -activated fibroblasts.
7. Hsp90 interacts physically with TGF $\beta$  receptor I to form a protein complex at the plasma membrane. This protein complex is involved in the pro-fibrotic signalling in cardiac fibroblasts.

- 8.** CTPR390 treatment prevents cardiac remodelling (hypertrophy and fibrosis) in hypertensive mice.
- 9.** Fibrotic mouse hearts accumulates CTPR390 that acts as a theragnostic nanocluster for cardiac fibrosis in vivo.
- 10.** Detection of Tungsten by XRF in fibrotic tissues treated with this reagent is a new method for the visualisation and quantification of collage by XRF microscopy.
- 11.** The CTPR390 is bio-distributed and accumulated in the cardiovascular system of fibrotic mice compared to control individuals. The presence of CTPR390 in other organs is related to its metabolization and elimination
- 12.** The CTPR390 recover the mechanical capabilities of the healthy 3D organoids composed by human fibroblasts and collagen.
- 13.** The presence of the non-functional CTPR appears to preserve the mechanical capabilities of the 3D model, but to a lesser degree compared to the functional CTPR390.
- 14.** None of the CTPR variants generate visible cellular toxicity effects in organoid cells.
- 15.** GAS system is secreted from fibroblasts and presents enzymatic activity in a model of collagen when fibroblasts mimic a fibrotic environment



## 7. Summary in Spanish

### 7.1 Introducción

Los últimos datos recogidos por la Organización Mundial de la Salud (OMS) que datan de 2019, muestran un escenario en el que las enfermedades cardiovasculares (ECV) representan la primera causa de muerte en el mundo, afectando en mayor medida a los países con un nivel de desarrollo medio/bajo [42]. Las ECV representan trastornos que afectan al corazón y a los vasos sanguíneos, afectando a su correcto funcionamiento, estos trastornos estarían asociados a, bloqueos parciales o totales del flujo sanguíneo a las zonas afectadas, disfunciones mecánicas o eléctricas [43-45].

Un factor subyacente en muchas de estas enfermedades, que no siempre se tiene en cuenta en el seguimiento de los pacientes, es la respuesta adaptativa que estos fenómenos inician en el tejido afectado. Y es que dentro de este grupo de patologías, podemos encontrar la isquemia, el infarto, las miocardiopatías, la hipertensión y la miocarditis, las cuales tendrían la capacidad de generar un daño o estrés tisular que provocaría esta respuesta adaptativa, dando lugar al fenómeno conocido como fibrosis cardíaca, patología que es el objetivo de este estudio [46, 47].

Sin embargo, no todas las afecciones en este caso cardíaca generarían una misma respuesta. Cabe diferenciarlas en función de las condiciones, pudiendo encontrarse aquellas como el infarto de miocardio (IM), que provocan un daño masivo en un periodo localizado, las cuales generaran una respuesta más rápida y enfocada a la sustitución/ reparación del tejido dañado de una manera más localizada. Por el otro lado, tendríamos las patologías como la estenosis aórtica o la hipertensión arterial, que someterían al tejido a una situación de estrés prolongada en el tiempo, que provocaría una respuesta más sostenida en el tiempo, y cuyo resultado no sería la sustitución de tejido sano por fibrótico de un área en especial, sino que sería un proceso que afectaría de manera difusa un área más extendida, provocando la invasión del tejido fibrótico de áreas sanas, siendo estas dos respuestas diferentes, ambas pueden conducir a un proceso fibrótico, a pesar de que el mecanismo y la respuesta serán diferentes [50, 51].

La Fibrosis Cardíaca es una patología que se asocia con la mayoría de las enfermedades cardíacas y que se caracteriza por la acumulación, principalmente de Colágeno I en la matriz extracelular, en el intersticio miocárdico. Esta patología en sus primeros estadios puede tener un efecto positivo en el paciente que la padece, ya que

## SUMMARY IN SPANISH

es una respuesta natural frente al daño en el tejido que sufre el órgano y cumple una función estructural. Sin embargo, en estadios más avanzados tiene un efecto contraproducente colonizando tejido sano, perjudicando la función cardíaca y en consecuencia produciendo un empeoramiento en la calidad de vida del paciente que la sufre, llegando a causar en algunos casos y junto a otros factores la muerte del paciente (**Figura 1**) [96, 215]. A pesar de ello en la actualidad no se dispone de ningún tratamiento efectivo, más allá de la administración de antihipertensores y finalmente la intervención quirúrgica para frenar el remodelado patológico del corazón que incluye hipertrofia y fibrosis. Un ejemplo de lo explicado es la cirugía de remplazamiento de la válvula aórtica cuyo mal funcionamiento promueve este tipo de alteraciones estructurales del corazón [96].

En gran medida la dificultad para el tratamiento de esta patología se debe a la gran cantidad de factores celulares, que intervienen y contribuyen a la generación de esta patología (**Figura 1**) [96, 216], ya que la producción, secreción y posterior deposición de las fibras de colágeno no se pueden asociar a un solo agente causal.

Sin embargo, los fibroblastos del corazón son las principales células responsables de la producción de colágeno, siendo la ruta celular inducida por del Factor de crecimiento transformante  $\beta$  (TGF $\beta$ ), la principal vía de estimulación de su producción [216, 217]. Por ello, muchos de los estudios centran sus esfuerzos en la identificación de posibles dianas farmacológicas que involucren la modulación de las cascadas de señalización de estas células para búsqueda una posible terapia [124].

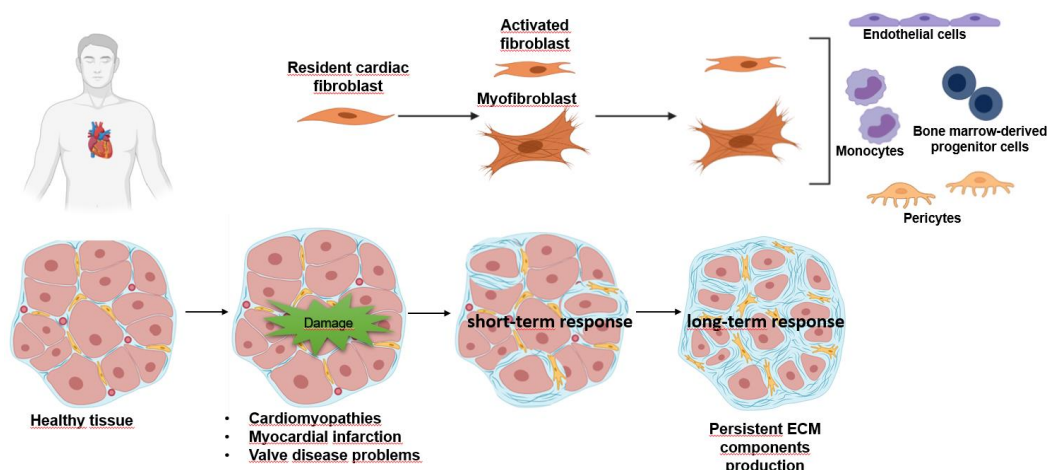


**Figura 1 Origen y agentes involucrados en la fibrosis cardíaca.** La patología tiene su origen en el tejido cardíaco tras sufrir un daño, con el objetivo de mantener la integridad estructural y funcionalidad del órgano. Se inicia una respuesta a nivel celular, que tiene como objetivo producir componentes de la matriz, para permitir al tejido aguantar las fuerzas de tracción del órgano. **Created with BioRender.com**

En relación a los fibroblastos y su funcionamiento, se han estudiado los efectos de muchas citoquinas y factores de crecimiento y su papel en la regulación de la activación de los fibroblastos, su diferenciación en miofibroblastos y sus efectos en la producción y remodelación, pero se ha demostrado que el TGF $\beta$  es uno de los principales agentes con un efecto más potente en todos estos fenómenos, encontrándose que es una citoquina versátil que puede desempeñar funciones tanto patológicas como fisiológicas. Al igual que la Angiotensina II, el TGF $\beta$  actúa a diferentes niveles y puede afectar a la proliferación celular, en la diferenciación celular, así como en la producción de componentes de la MEC, regula el fenotipo y la función de todas las células implicadas en la lesión tisular [104-106]. En los primeros momentos de su activación, durante una situación de estrés o daño en el tejido cardíaco, parece desempeñar un papel protector en el tejido, promoviendo la reparación de la zona dañada o promoviendo la proliferación o remodelación no patológica del órgano para mantener una función óptima del mismo, pero es en la respuesta sostenida cuando se generan problemas, promoviendo el depósito excesivo de MEC, afectando a la rigidez del tejido y afectando a su función [107].

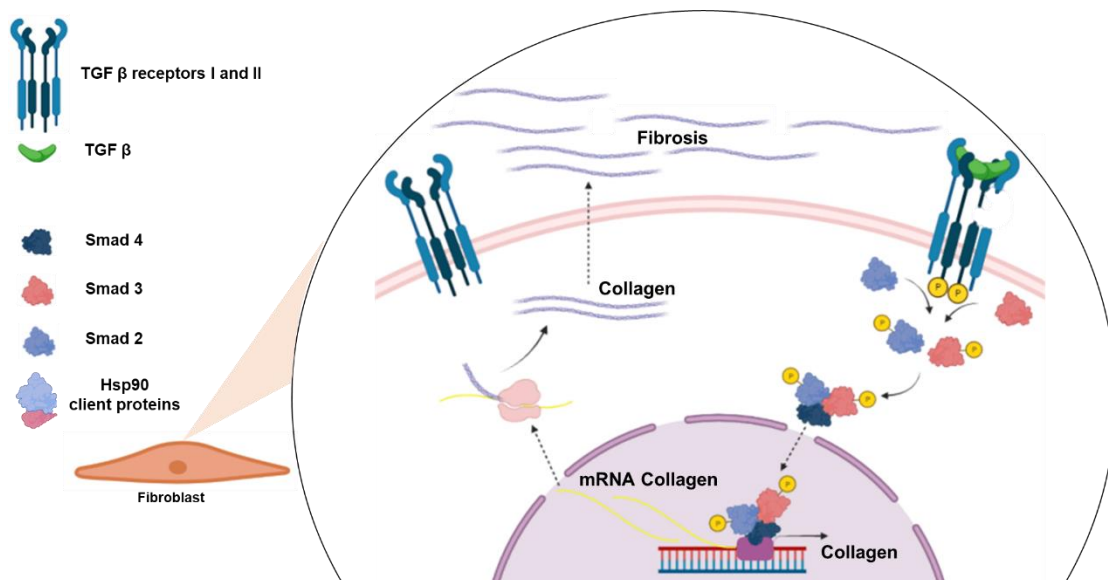


**Figura 2 Representación esquemática de la vía canónica del TGF $\beta$ .** Ruta canónica con los principales elementos descritos. A nivel de membrana en tonos azules se disponen los receptores de TGF $\beta$  tipo 1 y tipo 2. En verde tenemos una molécula de TGF $\beta$  que está siendo reconocida. Tras el proceso de reconocimiento tendremos los procesos de fosforilación, representados por las esferas amarillas (grupos fosfato) y que permitirían la transducción y transmisión de la señal desde la membrana hasta el núcleo, donde entraría el complejo constituido por los efectores Smad2/3/4, un complejo con capacidad de interactuar con factores de transcripción para exacerbar la expresión de los genes diana. Estos procesos terminarían en la transcripción de genes y su traducción a proteínas, en la imagen están presentes las fibras de colágeno como ejemplo de un gen afectado por la vía del TGF $\beta$ .

Analizando la ruta de señalización, varias son las proteínas, que han despertado el interés como posibles dianas terapéuticas, entre ellas, en los últimos años, se ha

## SUMMARY IN SPANISH

encontrado que la Hsp90 como posible objetivo de terapias, gracias a estudio en los que se ha conseguido detectar a nivel de la matriz extracelular, además de demostrarse que su presencia a dicho nivel no se debía a procesos de muerte celular que pudiesen provocar una liberación puntual de la misma [135]. Esta proteína tendría la capacidad de mediar en procesos celulares a través de interacciones proteína-proteína. Funcionando como cofactor junto con TGF $\beta$ RI durante el reconocimiento de citoquinas, afectando al inicio de la vía de señalización celular [135, 136].

### 7.2 Objetivos

Los objetivos planteados a lo largo del estudio en función de la línea de investigación fueron:

Línea de investigación: Herramientas nanobiotecnológicas modulares diseñadas para detectar e interferir en la vía de señalización clave de la fibrosis cardíaca in vitro e in vivo:

1. Caracterización de la localización de las nanopartículas CTPR en los fibroblastos. Estudio de la viabilidad celular y cambios ultraestructurales de los fibroblastos en presencia de CTPR.
2. Evaluación y cuantificación del impacto antifibrótico de la CTPR y la alteración de diferentes vías de señalización profibrótica en fibroblastos cardíacos embrionarios y primarios. Comparación del efecto antifibrótico de la CTPR y de algunos inhibidores comerciales de la Hsp90 como el 17AAG o el EGCG.
3. Desentrañar el mecanismo de acción antifibrótica de la CTPR centrándose en el estudio de la expresión de proteínas relacionadas con la señalización profibrótica.
4. Estudio del efecto in vivo de la CTPR sobre el remodelado cardíaco. Evaluación de los cambios de hipertrofia y fibrosis en un modelo de ratón hipertenso.
5. Evaluación de la CTPR como biomarcador y/o marcador de diagnóstico y su biodistribución en un modelo de ratón hipertenso.
6. Evaluación de las capacidades antifibróticas y los cambios biomecánicos de un organoide cardíaco humano tridimensional tratado con CTPR.

Línea de investigación: Sistema de Alerta Genética (GAS), terapia activa para la degradación del exceso de componentes de la matriz extracelular en situaciones patológicas.



1. Generación de la molécula del "sistema de alerta genética" (GAS).
2. Demostración de la latencia del GAS (MMP2-psecTag2-POSTN) en condiciones de salud y observación de su actividad gelatinosa en condiciones de remodelación cardíaca.

## 7.3 Resultados

### 7.3.1 Detección de CTPR y su interferencia en la vía de señalización clave de la fibrosis cardíaca in vitro e in vivo

Los primeros estudios relacionados con CTPR se realizan con CTPR conjugada con el fluoróforo Alexa 488 (CTPR390-488). Las principales características de todas las moléculas CTPR utilizadas en este estudio incluyen la capacidad de unión específica a Hsp90 mediante la unión al motivo MEEVD situado en el extremo carboxilo-terminal de Hsp90. CTPR390-488 presenta fluorescencia debido al fluoróforo Alexa488 conjugado a la partícula [140].

#### 7.3.1.1 Localización celular de CTPR390-488 en fibroblastos cardíacos primarios de cultivo celular y observación de los cambios ultraestructurales de los fibroblastos

El análisis de WB reveló que el anticuerpo CTPR390 generado específicamente para esta molécula no detectó ningún dominio TPR endógeno presente en una amplia variedad de proteínas citoplasmáticas (**Figura 3A**). También reveló que, aunque se produce la internalización, representa un pequeño porcentaje del total de CTPR390-488 (**Figura 3B**). La autofluorescencia de CTPR390-488 y la señal fluorescente del ensayo de inmunofluorescencia utilizando un anticuerpo específico contra CTPR390-488, presentaron colocalización (**Figura 3D**), mostrando no sólo que el fluoróforo Alexa-488 permanece asociado a la molécula de CTPR390 sino que también muestra la ausencia de inespecificidad procedente de los dominios endógenos de la TPR presentes en una amplia variedad de proteínas celulares [140], o de cualquier otra fuente cuando se detecta la CTPR390-488 tanto por autofluorescencia como por inmunofluorescencia (Figura 3D).

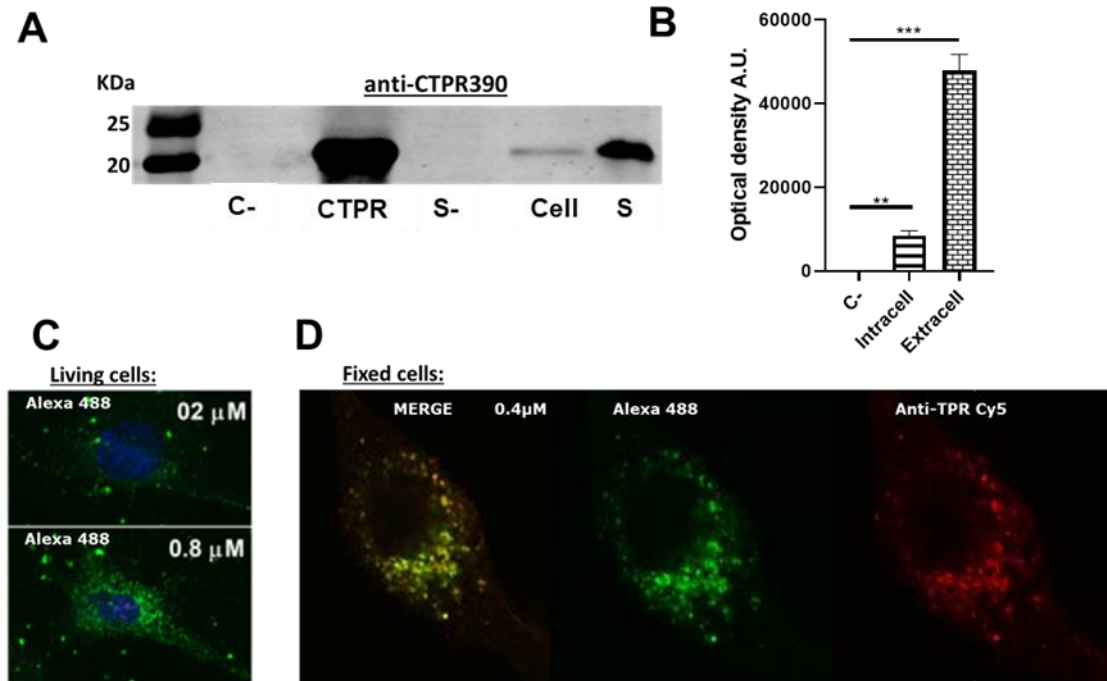


**Figura 3 Detección de CTPR en fibroblastos.** (A) WB de fibroblastos activados por TGF $\beta$  (0,3 ng/ml de TGF $\beta$ ) incubados en presencia de CTPR390-488. C- indica el lisado de control negativo utilizado de un cultivo celular sin la molécula CTPR. La CTPR muestra su señal en una solución pura. S- indica el sobrenadante recogido del cultivo utilizado como control negativo. Cell se referiría al lisado celular de las células incubadas con CTPR. S mostraría el sobrenadante de los cultivos celulares incubados en presencia del CTPR. (B) Medición de la intensidad de la señal mediante el software image J para definir las diferencias entre la señal de densidad óptica intra y extracelular de CTPR390-488, obtenida en el WB en unidades arbitrarias (U.A.). El valor medio corresponde a 3 experimentos independientes de WB (\*\* $p < 0,005$ , \*\*\* $p < 0,001$  Mann-Whitney (C,D) Observación por microscopía confocal de cultivos in vivo (C) y células fijadas (D) en presencia de CTPR390-488. (D) Las células fijadas no muestran CTPR390-488 extracelular, y se utilizó un anticuerpo específico contra la molécula sintética. Adaptado de (Cáceres, R. A. et al 2018).

Análisis realizados mediante técnicas de microscopía electrónica, realizados para analizar los efectos producidos por la exposición de las células activadas con TGF $\beta$  al CTPR, mostraron un retículo endoplasmático (RE) agrandado (marcado por la flecha 2 en la **Figura 4B**) observados en los fibroblastos activados por el TGF $\beta$ , indicaban una sobreexpresión general de la síntesis de proteínas que es un acontecimiento regular en los fibroblastos activados para sintetizar y secretar fibras ECM, principalmente colágeno (marcado por la flecha 1 en la **Figura 4B** y la flecha 3 en la **Figura 4C**) [140]. Las células tratadas con CTPT390 presentaron un tamaño basal del ER (**Figura 4D**) sin el engrosamiento observado en las células de control activadas por TGF $\beta$  (**Figura 4B**). Otra observación en este caso relacionada con el depósito de colágeno intercelular es la reducción de las moléculas de colágeno visualizadas entre los fibroblastos en las células tratadas con CTPR390 (marcadas con la flecha 4 y 5 en la **Figura 4E, F**) en comparación con las no tratadas (**Figura 4B, C**).

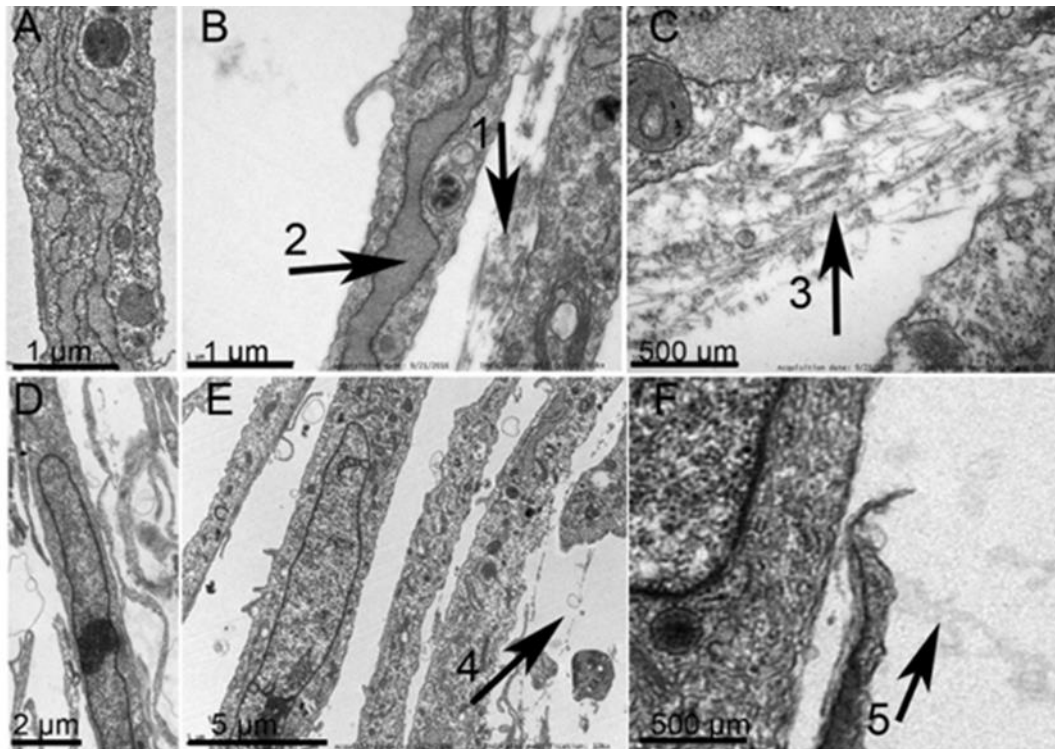


**Figura 4** Ensayos de microscopía electrónica para detectar los cambios ultraestructurales de los fibroblastos tratados con CTPR390 y la localización de CTPR390. (A) Fibroblastos tratados con TGF $\beta$  (0,3 ng/ml) con engrosamiento del RE. (B) Detalle del panel A en el que la flecha 1 marca la deposición de colágeno intercelular y la flecha 2 marca el RE engrosado. (C) La flecha 3 muestra un detalle del colágeno depositado mostrado en el panel B por la flecha 1. (D) Fibroblastos activados por TGF $\beta$  tratados con CTPR390. (E, F) Ausencia de colágeno depositado intercelularmente marcado por las flechas 4 y 5 en fibroblastos activados por TGF $\beta$  tratados con CTPR390 e incubados con CTPR390. La barra negra horizontal indica el aumento de microscopía electrónica utilizado (1 $\mu$ m-500 $\mu$ m). (Adaptado de (Cáceres, R. A. et al 2018).

Para describir la acción de CTPR390 sobre Hsp90 y, posteriormente, la participación de Hsp90 en las cascadas de señalización profibrótica de TGF $\beta$  canónicas y no canónicas, desarrollamos ensayos *in silico* y ensayos a nivel de proteínas. El análisis se centró en la cuantificación de las formas activas o fosforiladas de los diferentes actores, mostrando en el caso de efectores de las vías no canónicas del TGF $\beta$ , como p-AKT, una disminución progresiva de las formas fosforiladas de AKT (**Figura 5A**). Además, también se visualizó el complejo Smad2/3 de la vía canónica del TGF $\beta$ , mostrando una reducción significativa incluso a concentraciones más bajas (0,1 y 0,2 $\mu$ M) (**Figura 5B**), no alterándose ni la concentración de la forma no fosforilada, ni los niveles de expresión de SMAD2 (**Figura 5B y C**). Asimismo, el análisis de la expresión génica de uno de los efectores de la vía canónica, Smad2, no muestra alteraciones en las diferentes condiciones analizadas (**Figura 5C**).

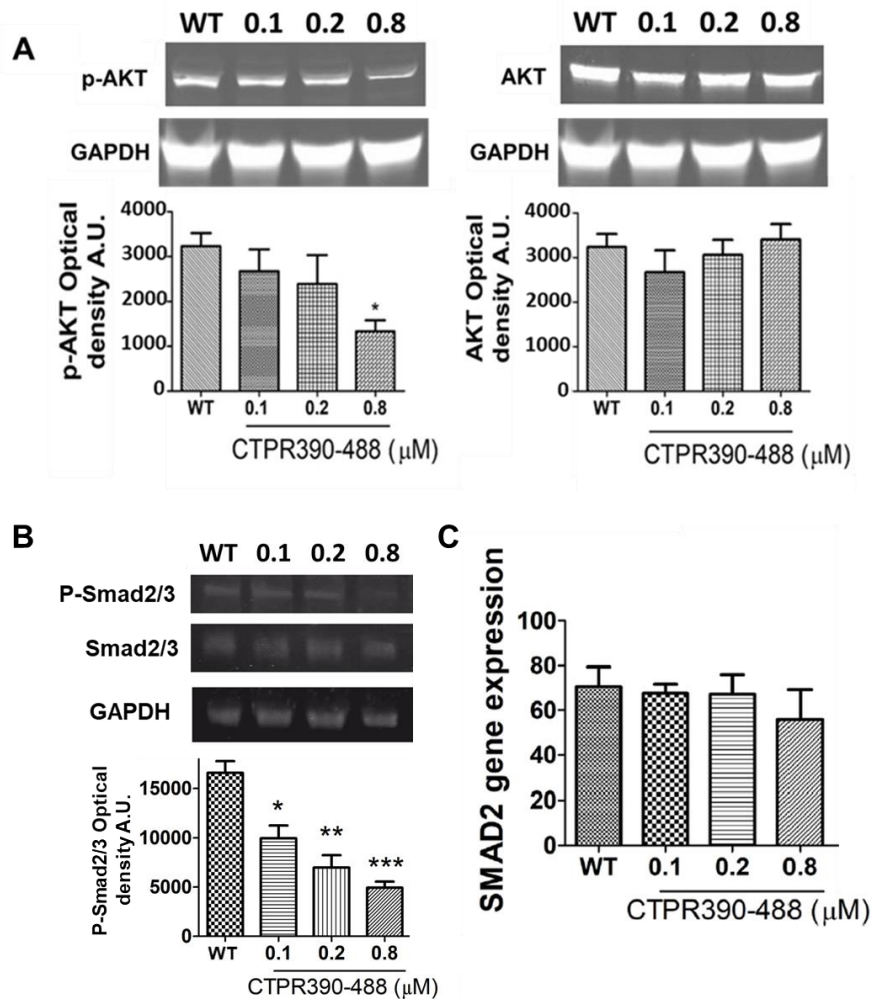


**Figura 5 Efectos de CTPR390 en los niveles proteicos de las proteínas vinculadas a la activación del TGFβ.** (A) Cuantificación y análisis del equilibrio entre las formas activas y no activas de los efectores de la vía no canónica del TGFβ, AKT. (B) Cuantificación de los niveles del complejo proteico pSmad2/3 y Smad2/3. (C) Niveles de expresión de Smad2 a diferentes concentraciones de CTPR390. \*p < .05, \*\*p < .005, \*\*\*p < .001; prueba de Mann-Whitney. Adaptado de (Cáceres, R. A. et al 2018).

### 7.3.2 Efecto antifibrótico in vivo del CTPR en el remodelado cardíaco. Evaluación del CTPR como biomarcador (molécula de diagnóstico)

Una vez descritos los resultados en los que se demuestra que la CTPR internaliza fibroblastos cardíacos primarios y reduce la sobreexpresión y deposición de colágeno de la MEC in vitro, procedimos a la utilización de la CTPR390 in vivo, con el objetivo de analizar sus capacidades en un organismo completo. Con este objetivo en mente, procedimos a generar un modelo in vivo de ratón hipertenso, que nos permitiera trabajar en un entorno fibrótico.

### 7.3.2.1 CTPR390 counteracts cardiac remodelling in hypertensive mice

Como hemos definido en la introducción, el proceso de remodelación puede iniciarse en el órgano cardíaco en situaciones patológicas. Las alteraciones sufridas en el órgano cardíaco debido a eventos perjudiciales promueven un remodelado adverso que incluye hipertrofia y fibrosis.

Para comprobar el incremento de la masa miocárdica, se procedió a medir el peso del corazón (HW) en relación con el peso corporal (BW) de cada ratón en estudio. Por otro lado, para el análisis de la remodelación fibrótica, se realizó por medio de la cuantificación de la expresión de las fibras, el análisis de la deposición de las fibras de los principales componentes de la matriz extracelular, más concretamente, la cuantificación del colágeno presente en el tejido, así como un estudio de los niveles de expresión de los marcadores profibróticos.

Sobre los resultados obtenidos en el remodelado hipertrófico, en la **Figura 6A** El grupo de 3 horas muestra un aumento significativo del factor HW/BW, para ambos grupos fibróticos, independientemente de la administración intraperitoneal de CTPR390 (**Figura 6A**), en comparación con sus controles, de forma que el grupo fibrótico+vehículo muestra un aumento del  $37,78 \pm 4,49\%$  en comparación con el grupo sano+vehículo, (\* $p < 0,05$ .) y el grupo fibrótico+CTPR390 muestra un aumento del  $25,25 \pm 5,3\%$  en comparación con el grupo sano+CTPR390. (\*\* $p < 0,005$ ). Los grupos de Sham muestran valores similares (**Figura 6A**). Con respecto a los grupos de 8 días, muestran un HW/BW similar en los grupos sanos (ratones tratados con vehículo o con CTPR390), (**Figura 6B**). Sin embargo, el análisis de los grupos fibróticos muestra una disminución significativa de los valores de HW/BW, en torno al  $13,89 \pm 2\%$  en el grupo tratado con CTPR390 en comparación con el grupo fibrótico+vehículo (\* $p < 0,05$ .), no se observaron diferencias estadísticamente significativas entre el grupo fibrótico tratado con CTPR390 y el grupo control tratado con CTPR390 mostrando valores similares (**Figura 6B**). Por otro lado, el grupo fibrótico no tratado mostró un incremento de valores significativamente mayor que los otros 3 grupos experimentales (\* $p < 0,05$ .) Ang II+CTPR390 vs Sham+CTPR390; y \*\* $p < 0,005$  Ang II +CTPR390 vs Sham+Vehicle. (**Figura 6B**).

Con respecto al remodelado fibrótico, los resultados sobre la cuantificación del colágeno en el tejido, mostraron valores similares en los grupos de control ( $7,3-9,2 \pm 1,4\%$ ), tanto en el grupo de control no tratado con CTPR390 como en los grupos tratados a las 3 horas, 4 y 8 días (**Figura 6C**). Por el contrario, se observan valores significativamente mayores en los grupos fibróticos sin administración de CTPR390 y en el grupo tratado

SUMMARY IN SPANISH

a 3 horas (**Figura 6C**). Por el contrario, los grupos fibróticos con administración de CTPR390 a los 4 y 8 días mostraron una reducción significativa del porcentaje de área de colágeno en las secciones con respecto a su control fibrótico sin CTPR390 (4 días:  $12,3\pm 0,4\%$  y 8 días:  $9,7\pm 0,3\%$  en comparación con Ang II+veh:  $14,9\pm 1,2\%$ , con  $p < 0,05^*$  y  $p < 0,005^{**}$  respectivamente) (**Figura 6C**).

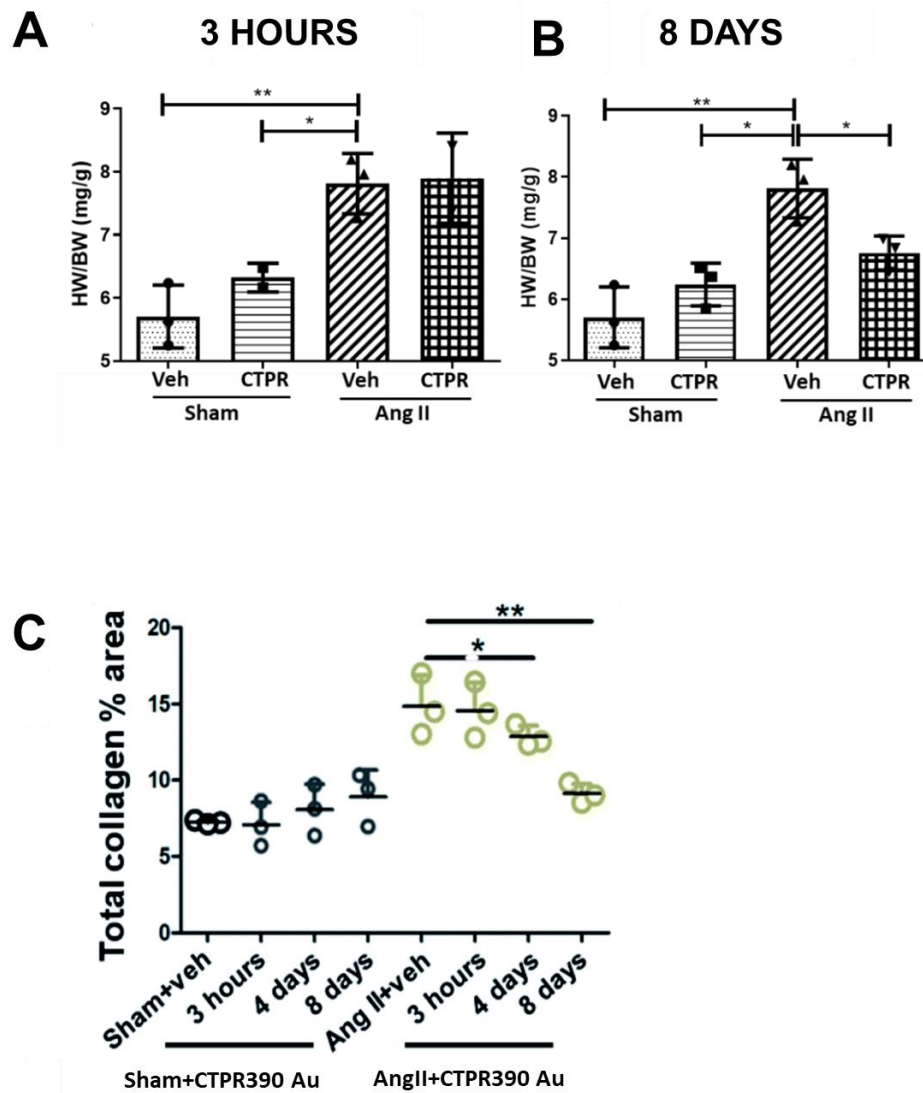


**Figura 6 Evaluación de la remodelación hipertrófica y Análisis de la remodelación fibrótica (A y B)** Evaluación y comparación del HW/BW en mg de corazón/g de unidades de ratón (mg/g). Todos los grupos se comparan con el grupo fibrótico sin CTPR390 (Veh/Ang II). (B) La cuantificación del porcentaje de colágeno en áreas aleatorias de las secciones transversales de A.  $*p < 0,05$ ,  $**p < 0,005$ . Prueba de Mann-Whitney. Adaptado de (Aires, A., Maestro, D. et al 2021).

### 7.3.2.2 Detección de CTPR390 entre los corazones fibróticos y los tratados con CTPR390 mediante microscopía SXRF capacidad de teragnóstica

Vistos los efectos del tratamiento mediante CTPR a nivel del remodelado, se procedió al análisis de las muestras mediante la técnica de microscopía de SXRF, la cual no permitió detectar los elementos inorgánicos presentes en los tejidos analizados. En la **Figura 7** se puede observar el análisis realizado en secciones de corazón analizadas por SXRF. En ellas se pudo detectar el oro presente en el CTPR390-Au utilizado en el tratamiento de algunos ratones, así como el Tungsteno utilizado para el marcaje del colágeno en los tejidos.

Los resultados obtenidos muestran una acumulación del CTPR390-Au en el tejido de los ratones fibróticos tratados con la molécula, a 8 días (**Figura 7K**), mientras que en el grupo control no se observa señal alguna (**Figura 7E**), mostrando su especificidad en la acumulación. Así mismo acumulaciones de Tungsteno son visualizadas en los tejidos fibróticos (**Figura 7F** y **L**), no observándose una señal clara en los grupos control (**Figura 7C** y **J**). Esto muestra da indicaciones sobre las capacidades no solo terapéuticas del CTPR390 ya observadas anteriormente, a través de sus efectos en la expresión de elementos de matriz, sino que también da una idea de las capacidades que puede tener a nivel diagnóstico, debido a su acumulación específica en áreas fibróticas, sin producirse acumulación en tejidos no afectados.

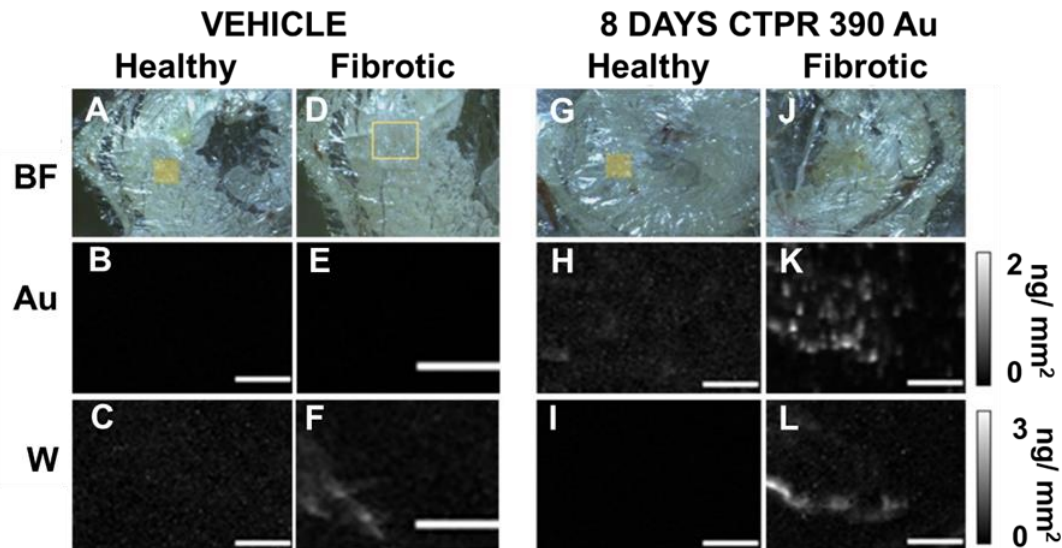


**Figura 7 Análisis presencia y capacidad terapéutica de CTPR390Au basado en una nueva detección de fibrosis mediante XRF. (A-J)** Visualización en campo brillante (BF) de áreas de sección transversal del corazón de modelos de ratón sanos (A,D) e hipertensos (G,J), para ser analizados por SXRF. Se analizan los grupos sanos y fibróticos, sin la administración de CTPR390 o con la administración de CTPR390 8 días antes del final del ensayo. Los cuadrados amarillos indican la representación del área bajo estudio Au) de la señal obtenida del oro CTPR390 presente en los ratones sanos (B) y fibróticos (E) sin CTPR390Au, y sanos (H) y fibróticos (K) con CTPR390Au. Imágenes de tungsteno (W) de ratones sanos (C) y fibróticos (F) no tratados con CTPR390Au, y de ratones sanos (I) y fibróticos (L) tratados con CTPR390Au, obtenidas de las mismas zonas, pero mostrando sólo la señal de tungsteno, asociada a las fibras de colágeno. La barra de escala horizontal blanca es de 100µm y la barra gris vertical indica la intensidad de la acumulación en ng/mm<sup>2</sup> del elemento inorgánico en estudio.

### 7.3.3 Efecto antifibrótico y cambios en los parámetros biomecánicos de un modelo cardíaco humano tridimensional tratado con CTPR

Con el fin de trasladar los estudios a modelos más cercanos al entorno humano que se genera durante el desarrollo de la fibrosis cardíaca, se procedió a la implementación de un modelo de organoide humano en 3D, que se asemeja a las condiciones mecánicas del tejido conectivo cardíaco humano, lo que permitirá recrear el entorno y las condiciones nativas con mayor precisión, avanzando así en el estudio.

#### 7.3.3.1 Comportamiento mecánico de CTPR390 y efecto antifibrótico en organoides de ingeniería humana

Una vez finalizada la exposición de los organoides al CTPR, se procedió al análisis reológico, en el que se observaron diferencias significativas entre los cuatro grupos. En cuanto al Módulo de Young, relacionado inversamente con la elasticidad. El grupo "TGFβ" fibrótico ofreció valores significativos más altos alcanzando valores medios de 110,3±7,18 kPa en comparación con el resto de grupos (**Figura 8A**). Los grupos con las dos variantes de CTPR390 mantuvieron valores más cercanos al control, entre 50-



$70 \pm 5,7$  kPa de presión (**Figura 8A**). En relación con la resiliencia, (índice que indica la cantidad total de energía que un sistema es capaz de absorber antes de sufrir una deformación irreversible (KJ/m<sup>3</sup>)), se observó un deterioro en el grupo TGF $\beta$  fibrótico en comparación con el grupo control (\* $p < 0,05$ ). El valor medio en el grupo TGF $\beta$  se redujo a 4 KJ/m<sup>3</sup>, en comparación con la media del grupo de control de 13KJ/m<sup>3</sup>. Los grupos tratados con CTPR390 funcional o no funcional mantuvieron valores similares al grupo control (**Figura 8B**). Finalmente, en relación a la tenacidad o Toughness, parámetro que se refiere a la cantidad de energía que puede ser absorbida antes de la ruptura del tejido, no se han encontrado diferencias estadísticamente significativas, con valores en el rango de 30-75 $\pm$ 4 KJ/m<sup>3</sup> (Figura 27C).

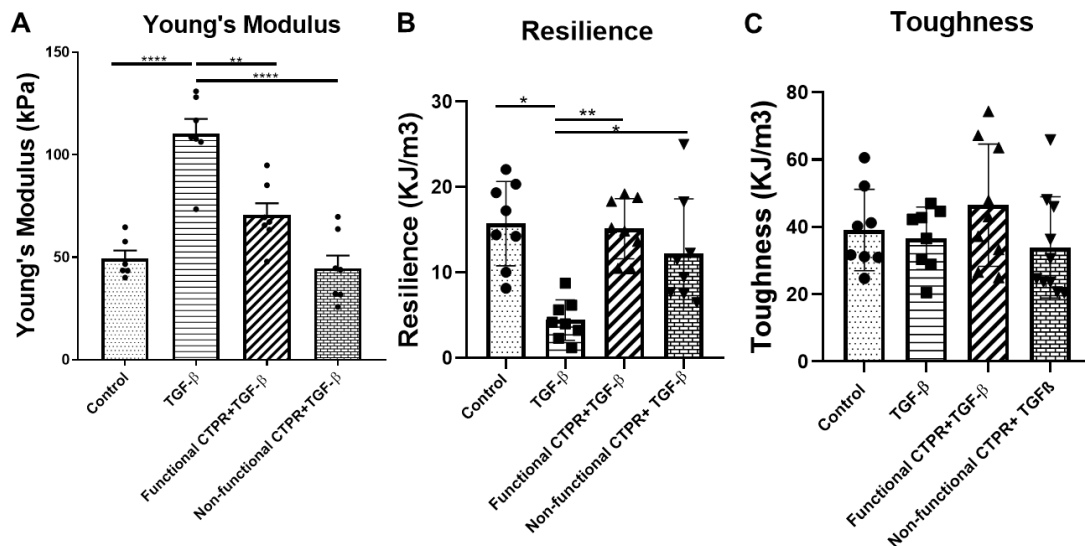


**Figura 8 Análisis de las capacidades mecánicas de los organoides cardíacos humanos hECT (A-C)** Capacidades mecánicas de los organoides, análisis de los 4 grupos mencionados anteriormente, con referencia a: (A) Módulo de Young (Elasticidad), (B) Resiliencia (Resistencia a la deformación), (C) Dureza (energía total absorbida). N=4 organoides por grupo \* $p < 0,05$ , \*\* $p < 0,005$ , \*\*\*\* $p < 0,0001$ , t-test

### 7.3.3.2 Distribución y regulación génica de CTPR390 en organoides cardíacos

Además de estudiar los efectos de las capacidades mecánicas de CTPR390, es interesante observar la presencia de CTPR en este modelo 3D y evaluar la expresión génica de los marcadores profibróticos. Observación directa de los fibroblastos dentro del organoide (**Figura 9A**)

Por último, se realizó un análisis de la regulación de la expresión de varios genes marcadores por el tratamiento con CTPR390.

Los marcadores seleccionados entre otros fueron el COL1 como fibra estructural y la lisil oxidasa (LOX) una enzima importante para la modificación postraduccional de los

## SUMMARY IN SPANISH

colágenos y la elastina en la matriz extracelular. El gen COLIII mostró una clara sobreexpresión en el grupo TGF $\beta$  (\*\*p<0,005) en comparación con el grupo control, mientras que se observó una reducción significativa en los grupos tratados con las dos variantes del CTPR (CTPR funcional \*\*\*p<0,001) y no funcional (\*p<0,05) (**Figura 9B**). La expresión del gen LOX I presentó una tendencia similar a la expresión del gen COL I, pero sin valores significativos en el caso del grupo no funcional (**Figura 9C**).

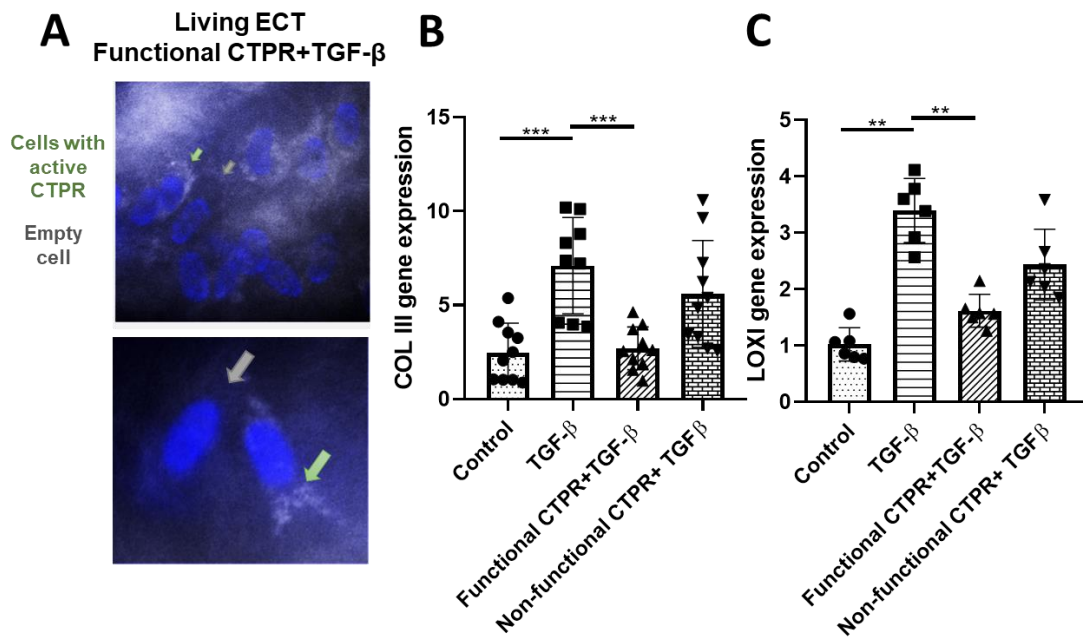


**Figura 9 Acumulación de CTPR390 en fibroblastos cardíacos humanos de organoides 3D y análisis de la expresión génica de los marcadores fibróticos. (A)** Imagen confocal de células vivas de un organoide representativo activado por TGF $\beta$  con CTPR390 funcional, en blanco la señal de CTPR390 de Alexa488 y en azul el marcador Hoechst para el núcleo. En el detalle la flecha gris indica células vacías si presencia de CTPR390 y la flecha verde indica la presencia de CTPR390. **(B)** COLIII. **(C)** LOXI en los 4 grupos experimentales en estudio ("control" no tratado con TGF $\beta$ , "TGF $\beta$ " tratado con TGF $\beta$ . Organoides CTPR+TGF $\beta$  funcionales tratados con TGF $\beta$  y CTPR390 funcional y Organoides CTPR+TGF $\beta$  no funcionales tratados con TGF $\beta$  y CTPR390 no funcional \*p<0,05, \*\*p<0,005, \*\*\*p<0,001. Prueba de Mann-Whitney.

### 7.3.4 Sistema de Alerta Genética (siglas en ingles "GAS"), construcción y evaluación de su actividad

La construcción y elaboración del sistema GAS se basa en la inclusión de un gen que codifica la proteína MMP2 responsable de la degradación de elementos de la matriz extracelular, bajo el control del promotor de la periostina (POSTN), siguiendo los protocolos y técnicas descritas en la sección de material y métodos

#### 7.3.4.1 Construcción y desarrollo de promotores de variantes de POSTN para GAS

Para la elaboración y construcción del sistema GAS, partimos de un clon previo obtenido en el grupo denominado proMMP2, y cuyos elementos de interés preentes en dicha

construcción, encontraríamos el gen que codifica para la proMMP2, bajo el control de expresión del promotor del citomegalovirus (pCVM).

Por otra parte se procedió a la identificación del promotor seleccionado y que servirá como control de expresión en el futuro GAS (pPOSTN) y el diseño de los cebadores para su amplificación, nos basamos en estudios previos en los que se había identificado este promotor, así como en la identificación de regiones de interés dentro del mismo **Figura 10** [138].

Las variantes seleccionadas para su generación en el laboratorio fueron la denominada como GASiii, cuyo promotor de periostina, proviene de un diseño previamente publicado [138] y el GAS AV, una construcción de diseño propio, cuyo objetivo era la de obtener el mínimo promotor funcional, que permitiera altos valores de expresión.

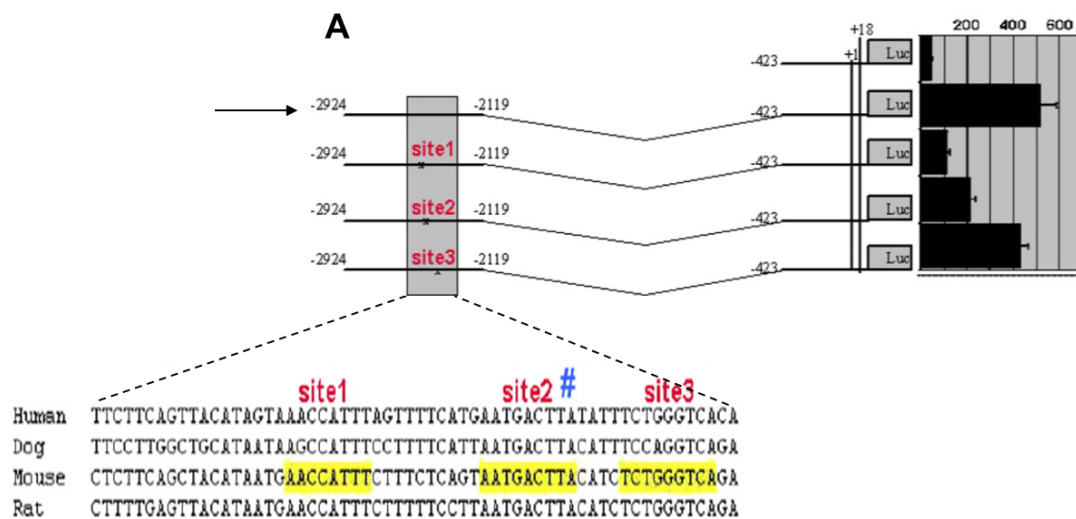


**Figura 10 Promotor de periostina y variantes, secuencias potenciadoras y represoras.** (A) Variantes truncadas del promotor en las que se ha eliminado la región represora. Mediante alineaciones, se identifican 3 sitios conservados en la región del potenciador y se utilizan para el diseño de nuevas variantes del promotor mínimo. (A y B) Las diferentes secuencias promotoras controlan la expresión de un gen reportero, la luciferasa. A la derecha, se representa gráficamente el nivel de expresión de cada una de las secuencias, como resultado de las mediciones con luminómetro de la señal obtenida en cada caso. Adaptado de (Linsdley, A. et al 2007).

### 7.3.4.2 Evaluation of the activity of the constructs GAS AV and GASiii

Para la evaluación de la actividad de los sistemas generados, se utilizó la zimografía para evaluar los niveles de producción de proMMP2 por los clones generados, así como su actividad.

El primer paso para realizar, fue la transfección de cultivos celulares NIH3T3 utilizando los constructos obtenidos previamente, mediante la amplificación de los fragmentos que codificaban para los diferentes elementos y su integración mediante la técnica de **Isothermal assembly**.

## SUMMARY IN SPANISH

De las fracciones recuperadas de los cultivos en el ensayo, por una parte el lisado celular, y por otra el medio de cultivo presente en cada uno de los cultivos, los resultados obtenidos mostraron una mayor presencia de proMMP2 en el medio de cultivo (**Figura 11B**) en comparación con el contenido en el lisado celular (**Figura 11A**), y de las construcciones producidas, la que contenía el promotor POSTNAV (Figura 34a y B, en el gráfico aparece como AV) mostró un aumento significativo de proMMP2 (\*\* $p < 0,005$ ) en comparación con el cultivo celular no transfectado

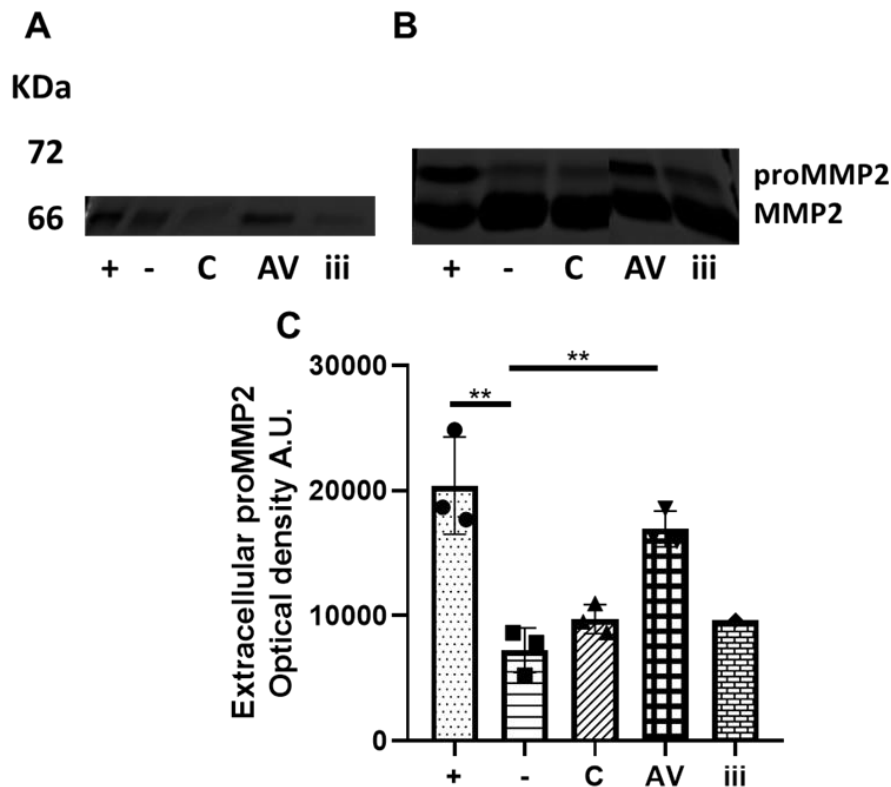


**Figura 11 Actividad de proMMP2 en los sistemas GAS.** (A-B) La transfección de los sistemas GAS se realizó en células NIH3T3, grupo de control no transfectado (C), un grupo de control positivo transfectado con el plásmido proMMP2 (+), un control negativo que contenía el plásmido psectaq sin el gen proMMP2 (-) y finalmente los grupos con las construcciones POSTNAV (AV) y POSTNiii (iii). (A) zimografía de los lisados de los grupos explicados. (B) zimografía de los medios de cultivo recuperados. (C) Cuantificación de la señal obtenida en (B) de las diferentes construcciones en estudio. Se realizaron tres experimentos independientes. \*\* $p < 0,005$  prueba t de student.

## 7.4 Discusión

La fibrosis cardíaca es una patología con un alto impacto en la salud de la sociedad. Es objeto de numerosas investigaciones para describir el proceso que la provoca, describiendo los diferentes actores implicados.

A pesar de ello, todavía se carece de un tratamiento eficaz, que trate directamente la patología. La complejidad del proceso fibrótico, con los diferentes agentes celulares

implicados y los efectos compensatorios que surgen al inhibir los eventos profibróticos, junto con la divergencia en el nivel de las vías de señalización que pueden responder, dificulta la comprensión completa del mecanismo de acción de la enfermedad. El hallazgo de dianas terapéuticas eficaces con un efecto claro en la respuesta, así como el diseño de fármacos selectivos que alivien las consecuencias perjudiciales de la fibrosis, necesitan un mayor número de estudios para alcanzar el objetivo de tratar a los pacientes afectados.

El desarrollo y uso de compuestos antifibróticos, como CTPR390, con una acción dirigida sobre los efectores implicados en la principal cascada de señalización profibrótica, es una de las soluciones que se están investigando actualmente debido a la importancia de evitar la inhibición de la principal citoquina de la enfermedad (TGF $\beta$ ), que es una citoquina ubicua y un regulador homeostático clave cuya inhibición provoca graves alteraciones en el tejido. CTPR390 fue diseñado para interactuar y afectar a Hsp90 (una proteína implicada en la cascada de señalización del TGF $\beta$ ) inhibiendo de forma selectiva, la interacción de Hsp90 con otros socios del TGF $\beta$  para desactivar eficazmente la señalización profibrótica [140]. La Hsp90 se ha descrito recientemente como una prometedor diana terapéutica para las enfermedades que sobreexpresan esta chaperona. En el presente estudio, su presencia extracelular nos llevó a describir su capacidad para actuar como cofactor durante el inicio de la activación de la vía del TGF $\beta$  a nivel de la membrana plasmática.

#### **7.4.1 CTPR390 se localiza intra y extracelularmente sin afectar a la homeostasis de los fibroblastos**

El motivo MEEVD de las isoformas Hsp90 $\alpha$  y  $\beta$  es el objetivo de CTPR390 [143]. La presencia intercelular permite que el nanocluster se una a su objetivo en ambas localizaciones. El CTPR390 intracelular no altera la salud celular pero en los fibroblastos NIH3T3 parece producir cierto estrés que no se detecta en los fibroblastos primarios cardíacos revelando un aspecto muy interesante sobre la importancia de elegir el modelo celular adecuado para demostrar las alteraciones homeostáticas de un entorno de fibroblastos cardíacos en la presentación de nuevas estrategias terapéuticas biotecnológicas que interactúen con la cascada profibrótica clave del TGF $\beta$  [140].

Debido a la relevancia de la Hsp90 en el mantenimiento de la homeostasis celular, la inhibición parcial o total de su actividad siempre ha ido seguida de efectos secundarios y puede conducir a la muerte celular [170]. Por lo tanto, la capacidad descrita de CTPR390 para inhibir selectivamente el extremo C-terminal de Hsp90 sin afectar a su actividad ATPasa permitiendo así que sus proteínas cliente se plieguen correctamente

al mismo tiempo que afectan a la función relacionada con la cascada de señalización del TGF $\beta$ .

#### **7.4.1.1 La localización ultraestructural intravesicular de CTPR390 activa el tráfico celular**

La autofluorescencia de la CTPR facilita su seguimiento y detección. El CTPR390 se internaliza en las células, aunque el CTPR390 citoplásmico representa un pequeño porcentaje del CTPR390 total añadido a los fibroblastos (**¡Error! No se encuentra el origen de la referencia.**), porque la mayor parte se encuentra extracelularmente. Los resultados obtenidos mediante técnicas de crio-3D-SIM y crio-SXT (**Figure 11**) muestran una distribución homogénea y un elevado número de vesículas celulares (**Figure 12**). Los marcadores de proteínas, como Alix, revelaron que la CTPR se incorporaba a cuerpos multivesiculares relacionados con el tráfico de vesículas [172]. Los fibroblastos podrían transferir CTPR390 de un fibroblasto a otro a través de vesículas extracelulares (CTPR390 mostró relación con el marcador CD9), lo que incluiría a CTPR390 entre las señales intercelulares que conectan a los fibroblastos mediante procesos de exocitosis [173].

A pesar de la presencia intracelular de CTPR390 en la mayor parte del nanocluster se encuentra en el entorno externo de la célula (**Figure 7A**). Esto sería factible si tenemos en cuenta que las condiciones profibróticas favorecen la secreción de Hsp90 de forma similar a otros daños como las heridas que también favorecen la secreción de Hsp90[174, 175]. Otra posibilidad para el tráfico de CTPR390 en la célula puede deberse a la saturación que activa los procesos de eliminación fuera de la célula.

#### **7.4.1.2 Ultrastructural and cell signalling effects of CTPR390**

Los efectos observados en las células con la administración de CTPR implican alteraciones a nivel ultraestructural. Los efectos generados en diferentes organelos relacionados con la presencia de CTPR390 en los fibroblastos (**Figure 10**), como en el RE, el número de vesículas de tráfico y el tamaño de las mitocondrias. Además, se reducen los niveles de deposición de colágeno en las regiones intracelulares. En los fibroblastos activados por TGF $\beta$ , el aumento del grosor del RE que indica (proceso activo de síntesis de proteínas) y la presencia de deposición de colágeno en los espacios intercelulares están relacionados porque el colágeno es la principal proteína generada por los fibroblastos. El tratamiento con CTPR390, evita el aumento del RE y la deposición de colágeno [140].

La presencia del mayor número de vesículas también podría responder al tráfico celular endosomal normal, independientemente de la activación celular (**Figure 13**). Debido a que el aumento se observó sólo en los grupos tratados con CTPR390 (**Figure 13**), que puede estar relacionado con los procesos de internalización del CTPR en la célula [155, 179]. El análisis de las mitocondrias, mostró cambios en el tamaño y la forma en los grupos activados por TGF $\beta$ . Los procesos de activación celular son energéticamente exigentes, por lo que es de esperar un aumento del número de mitocondrias. Este efecto fue suprimido por el tratamiento con CTPR390 ( ). (**Figure 10**).

A nivel molecular, las alteraciones en la activación de los efectores del TGF $\beta$  en condiciones patológicas, como la fibrosis aparecen tanto en las vías canónicas como en las no canónicas del TGF $\beta$  [180-183]. Una disminución de la fracción fosforilada de las proteínas profibróticas analizadas en presencia de grupos CTPR390, (**Figure 15 y Figure 16**) indicaron que el efecto antifibrótico de la CTPR390 afectaba a los mensajeros citoplasmáticos secundarios del proceso. Lo que apoya la idea de la relación de la cascada Hsp90 y TGF $\beta$  a nivel de la membrana plasmática. Esto se apoya además en el uso de una forma mutada del receptor 1 de TGF $\beta$  (TGF $\beta$ R1), que era constitutivamente activo. El TGF $\beta$ R1 constitutivamente activo recuperó la disminución de las formas fosforiladas de los efectores relacionados con el TGF $\beta$  (**¡Error! No se encuentra el origen de la referencia.**). El efecto deseable de CTPR390 sería la reducción de COL1 como una de las principales fibras producidas en la patología fibrótica (**Figure 17**). Se han observado efectos similares de reducción del colágeno utilizando inhibidores de Hsp90 ya disponibles, como el 17AAG [164, 184].

#### **7.4.1.3 Modelo de acción de las interacciones físicas CTPR390-Hsp90 y Hsp90-TGF $\beta$ RI**

Como se ha descrito anteriormente, el enfoque para tratar la fibrosis que hemos perseguido en este trabajo, se basa en la interacción Hsp90-TGF $\beta$ RI, para reducir la acción profibrótica del TGF $\beta$ . El modelo de interacción termodinámicamente favorable entre Hsp90 y TGF $\beta$ RI se validó primeramente mediante una simulación in silico, al que posteriormente se combino con ensayos moleculares orientados a demostrar las interacciones directas proteína-proteína, como los ensayos de pull down de proteínas o "proximity ligation assay" (PLA) (**Figure 18**). Defendemos que la interacción física Hsp90-TGF $\beta$ RI es parte del mecanismo de acción, de la disminución de la fibrosis obtenida tras la administración de CTPR390 [158]. Del mismo modo, los ensayos realizados durante este estudio, mencionados anteriormente, como los experimentos realizados en células transfectadas con TGF $\beta$ RI constitutivamente activo (**¡Error! No se encuentra el origen de la referencia.B**), de la acción de CTPR390, demostrando la

localización en la membrana plasmática de la acción de CTPR390 en el evento profibrótico (**Figure 15** and **Figure 16**). La lógica que subyace a este ensayo indica que si el efecto de CTPR390 se hubiera producido a nivel citoplasmático, no se observarían cambios en el efecto antifibrótico detectado en presencia de CTPR390, por lo que no debería observarse ninguna diferencia entre ambas situaciones.

Con estos datos y los presentados anteriormente, se ha demostrado la eficacia y las capacidades de esta nueva molécula CTPR390 en los sistemas tradicionales de cultivo celular, posicionándose como una estrategia terapéutica alternativa que necesitaría más investigación para llegar a los ensayos clínicos con una perspectiva positiva. En comparación con otros enfoques un avance en el campo exhibido por la terapia aquí propuesta sería la inhibición del efecto de citoquinas cruciales como el TGF $\beta$  en ausencia de efectos adversos celulares claros [187, 188].

### **7.4.2 Capacidades de diagnóstico in vivo de CTPR390**

La experimentación en modelos de cultivo celular en monocapa, si bien es un método accesible que ha demostrado sus ventajas y usos, carece de la complejidad de un organismo, por lo que es indudable la importancia de utilizar modelos in vivo, que permitan evaluar las capacidades del CTPR390, obteniendo resultados que podrían acercarse más a la posible acción del CTPR390 en los pacientes.

El estudio en ratones utilizando los grupos experimentales mostrados en **¡Error! No se encuentra el origen de la referencia.** nos permitió evaluar no sólo el efecto y el comportamiento de la molécula en un entorno complejo, sino también su seguridad en modelos sanos no afectados [150]. El uso de AngII en este modelo ha demostrado ser un mecanismo válido para la generación del proceso de remodelación que deseamos iniciar, cuyas capacidades han sido ampliamente descritas [194, 195].

#### **7.4.2.1 La CTPR interfiere en el remodelado cardíaco in vivo**

El remodelamiento cardíaco iniciado en el modelo de Ang II, es una respuesta de una hipertensión crónica generada por la liberación de la hormona AngII a través de un sistema de liberación osmótica. El proceso de remodelación incluiría eventos hipertróficos, causados principalmente por el aumento de tamaño de las células musculares cardíacas y el proceso fibrótico que implica la proliferación celular y la mayor extensión de la ECM.

Los efectos observados con la administración de CTPR390 en los grupos fibróticos variaron mucho en función del tiempo de administración. En el caso de los grupos con mayor tiempo de interacción CTPR-ratón (4 y 8 días), se observaron claros efectos de



recuperación. Los procesos hipertróficos analizados mediante la relación entre el peso del corazón (HW) y el peso del individuo (BW) (**¡Error! No se encuentra el origen de la referencia.** 8 Days), se reducen en comparación con los ratones hipertensos, y la remodelación fibrótica disminuye, según las mediciones de las áreas de colágeno presentes en las secciones del órgano cardíaco (Masson's trichrome) (**Figure 22 4 and 8 Days**).

Demostramos que 8 días de una dosis única de CTPR390 fueron suficientes para llegar al corazón y ejercer su función terapéutica. Esto se confirma, por los efectos sobre la remodelación (como se ha explicado anteriormente), así como con los datos obtenidos con el análisis de la acumulación de CTPR390 en el corazón (imágenes de microscopio XRF). La detección por XRF nos permitió detectar y cuantificar la cantidad de CTPR en el tejido objetivo a través de la señal de oro (**Figure 24H y C-D**). Aun así, hay que tener en cuenta que en los grupos con administración de AngII, en los que la administración de CTPR390 se realizó 4 días y 3 horas antes del sacrificio, se trataba de grupos cuyo "tratamiento" se administró de forma tardía, respecto a los que lo recibieron 8 días antes del sacrificio, por lo que el proceso patológico generado tuvo un tiempo adicional para su desarrollo, lo que pudo descansar la eficacia

#### **7.4.2.2 Pruebas de CTPR, capacidad teranóstica potencial mediante la inhibición de Hsp90 y capacidad de fluorescencia**

Como se ha mencionado a lo largo de este trabajo, en el estudio se han utilizado diferentes variantes de la molécula CTPR390, todas ellas con el módulo de unión a Hsp90 en común, que reconocería el citado motivo MEEVD, presente en la chaperona. El resto de la molécula se ha editado para dotarla de estabilidad y características fluorescentes específicas. El uso del fluoróforo Alexa-488 o la inclusión de nanoclusters de oro [140, 150] abren la posibilidad de la aplicación de la CTPR390 como herramienta de diagnóstico. Junto con sus capacidades terapéuticas, esta nanopartícula podría clasificarse como una molécula con capacidad teragnostica. Los compuestos con estas características han sido utilizados en los últimos años, debido al interés que generan [197, 198], permitiendo en muchos casos el seguimiento simultáneo de la patología para comprobar su evolución.

La capacidad diagnóstica de CTPR390 radica en su acumulación selectiva en las zonas afectadas, mayor que la de CTPR390 acumulada en los tejidos sanos. Esta comparativa se pudo observar en el corazón de los ratones tratados con CTPR390-Au en diferentes momentos (3 horas, 4 días y 8 días antes del sacrificio), mediante microscopía XRF

(**Figure 24A-F**, **Figure 24B**, D y F), alcanzando los valores máximos a los 8 días (**Figure 24F**).

La aplicación de otros ensayos no hizo sino reforzar estos datos. La señal fluorescente de la CTPR390 combinada con técnicas que permitían visualizar y cuantificar el colágeno presente en el tejido, permitió observar al CTPR390 en las zonas de acumulación de colágeno en el corazón de las mismas secciones miocárdicas **Figure 26** y **Figure 27**. Los resultados mostrados en dos de las variantes de CTPR390 (la molécula Alexa-488 CTPR390 y el nanocluster de oro CTPR390), indicaron la acumulación selectiva del CTPR en las áreas afectadas de los grupos fibróticos, y el colágeno sobreexpresado en esas áreas (**Figure 26**).

### **7.2.3 Preservation of healthy mechanical behaviour in a fibrotic 3D human cardiac organoid in the presence of CTPR390**

El modelo 3D utilizado se ha puesto a punto y se ha probado para imitar el tejido conectivo cardíaco humano, proporcionando un entorno similar al que se encuentra en el órgano nativo, en lo que respecta a las condiciones de tensión mecánica. Hay que entender que las condiciones de rigidez y tensión a las que se someten las células no se corresponden con las condiciones naturales [201, 202] aunque estén sometidos a cierta rigidez y tensiones ausentes en otros modelos. Esto, unido al hecho de que los fibroblastos, como cualquier otro tipo de célula, son sensibles a los estímulos mecánicos, que generan una respuesta en la célula, presentan un modelo óptimo para observar una respuesta a los estímulos externos [203-205], como la presencia de TGF $\beta$  y CTPR390.

Lo que hemos podido evaluar aquí es la evolución y adaptación de las capacidades mecánicas de los organoides utilizados a las condiciones de cultivo, analizando el efecto de la actividad de las células presentes en el organoide sobre la reorganización de la matriz y el impacto que ésta tiene sobre sus propiedades [206].

Los resultados obtenidos en las 4 condiciones experimentales mostraron una clara diferencia entre el grupo fibrótico, (grupo tratado sólo con TGF $\beta$ ), y el resto de los grupos. Fue posible identificar y diferenciar claramente las "propiedades" de un estado sano, frente a las afectadas por la remodelación patológica, presentes en el grupo TGF $\beta$  que presenta valores más altos de tensión y diferente elasticidad en comparación con los controles o los grupos tratados con CTPR390.

Un resultado que se ha observado en parte de las propiedades medidas es el aparente efecto que tiene el control CTPR390, carente del módulo de unión de Hsp90, en la

recuperación de estas capacidades mecánicas del tejido, lo que se observa en la medición de la deflexión (**Figure 29**). Los organoides de este grupo parecen responder de la misma manera que el grupo de control y el grupo tratado con el funcional CTPR390 y en otros dos parámetros mecánicos medidos, Módulo de Young y Relisancia (**¡Error! No se encuentra el origen de la referencia.**A y B). La CTPR390 no funcional presenta menor afinidad por la Hsp90 [209], sin embargo viendo los resultados, cabría esperar interacciones inespecíficas con las proteínas, o quizás debido a la carga negativa de la molécula la interacción con los componentes de la ECM mayoritariamente cargados positivamente afectando a la estructura 3D del organoide, en su polimerización y reorganización al soportar los fibroblastos. Obviamente, al no tener el módulo de unión a Hsp90, no cabría esperar una interacción específica, no pudiendo descartar alguna interferencia en el sistema. Reforzando esta posible interacción del CTPR390 no funcional, existen también análisis de expresión genética, que muestran, de la misma manera que en los modelos anteriores, un efecto restaurador en los niveles de expresión de los genes marcadores COL3 (**¡Error! No se encuentra el origen de la referencia.**A), L OX (**¡Error! No se encuentra el origen de la referencia.**B) en comparación con los organoides activados por TGF $\beta$ . El resultado inesperado obtenido fue que los efectos similares observados en los organoides con presencia de CTPR390 funcional se obtuvieron en los organoides tratados con CTPR no funcional. Sin embargo, cabe señalar que el grado de significación es menor (**¡Error! No se encuentra el origen de la referencia.**A-C), lo que podría implicar una interferencia a nivel de la matriz extracelular que podría causar distorsiones en las señales mecánicas de los organoides [210, 211].

#### **7.2.4 Primeros pasos en la construcción y evaluación del funcionamiento del Sistema de Alerta Genética**

La implantación de un sistema basado en el uso de la terapia génica se estudia desde hace años [213, 214].

El proceso de desarrollo se encuentra en sus fases iniciales, habiéndose logrado únicamente la construcción de los constructos denominados "GASAV" y "GASiii". El aislamiento y la obtención de los fragmentos necesarios para la construcción de los sistemas GAS se obtuvieron a partir de los estudios previos (**¡Error! No se encuentra el origen de la referencia.**) [138].

En cuanto a su función, como hemos visto, se obtiene una fuerte síntesis y secreción al medio extracelular de MMP2 activa por la construcción GASAV (**¡Error! No se encuentra el origen de la referencia.**B). Una de las construcciones, GASiii, no parece

## SUMMARY IN SPANISH

destacar por sus niveles de expresión de MMP2, a pesar de ser un sistema ya probado anteriormente por otro grupo de investigación [138], por lo que se procederá en el futuro a identificar las condiciones idóneas para su activación. Ambas construcciones han sido secuenciadas y confirmadas, por lo que una vez verificadas, el siguiente paso en futuros estudios será identificar las condiciones de activación que aseguren una activación fuerte y controlada.

## 7.5 Conclusiones

1. CTPR390 se internaliza en los fibroblastos embrionarios NIH/3T3 y en los fibroblastos primarios cardíacos de ratón acumulándose en cuerpos vesiculares, pertenecientes al tránsito vesicular.
2. El uso de CTPR390 no ha mostrado efectos tóxicos detectables en células NIH/3T3 y fibroblastos primarios cardíacos de ratón.
3. La interacción de CTPR390 con la chaperona Hsp90 promueve la inhibición de la interacción Hsp90-TGF $\beta$ RI, sin afectar a la función de refolding de la ATPasa de la chaperona.
4. La presencia de CTPR390 en NIH/3T3 exhibió signos de estrés celular como el aumento del volumen y la esfericidad de las mitocondrias, que no son detectables en los fibroblastos primarios cardíacos de ratón manteniendo sus principales características ultraestructurales aumentando el número de vesículas de tráfico y contrarrestando los efectos del TGF $\beta$ .
5. Los efectos antifibróticos del tratamiento con CTPR390 de las células NIH/3T3 activadas por TGF $\beta$  o de los fibroblastos cardíacos de ratón restablecen parcialmente los niveles de expresión de Col III, FN, Nppb y Nppa indicando una remodelación regresiva a nivel molecular.

6. Los efectores profibróticos canónicos y no canónicos del TGF $\beta$  redujeron los niveles de isoformas fosforiladas activas en presencia de CTPR390 en fibroblastos activados por el TGF $\beta$ .
7. Hsp90 interactúa físicamente con el receptor I del TGF $\beta$  para formar un complejo proteico en la membrana plasmática. Este complejo proteico está implicado en la señalización profibrótica en los fibroblastos cardíacos.
8. El tratamiento con CTPR390 previene el remodelado cardíaco (hipertrofia y fibrosis) en ratones hipertensos.
9. Los corazones fibróticos de los ratones acumulan CTPR390 que actúa como un nanocluster de diagnóstico de la fibrosis cardíaca in vivo.
10. La detección de tungsteno por XRF en tejidos fibróticos tratados con este reactivo es un nuevo método para la visualización y cuantificación del colágeno por microscopía XRF.
11. El CTPR390 está biodistribuido y acumulado en el sistema cardiovascular de los ratones fibróticos en comparación con los individuos de control. La presencia de CTPR390 en otros órganos está relacionada con su metabolización y eliminación.
12. El CTPR390 recupera las capacidades mecánicas de los organoides 3D sanos compuestos por fibroblastos humanos y colágeno.
13. La presencia del CTPR no funcional parece preservar las capacidades mecánicas del modelo 3D, pero en menor grado en comparación con el CTPR390 funcional.

## SUMMARY IN SPANISH

- 14.** Ninguna de las variantes de CTPR genera efectos visibles de toxicidad celular en las células del organoide.
- 15.** El sistema GAS es secretado por los fibroblastos y presenta actividad enzimática en un modelo de colágeno cuando los fibroblastos imitan un entorno fibrótico.



## 8. PUBLICATIONS

- Aires, A., Maestro, D., Ruiz Del Rio, J., Palanca, A. R., Lopez-Martinez, E., Llarena, I., Geraki, K., Sanchez-Cano, C., Villar, A. V., & Cortajarena, A. L. (2020). Engineering multifunctional metal/protein hybrid nanomaterials as tools for therapeutic intervention and high-sensitivity detection. *Chemical science*, 12(7), 2480–2487. <https://doi.org/10.1039/d0sc05215a>
- Cáceres, R. A., Chavez, T., Maestro, D., Palanca, A. R., Bolado, P., Madrazo, F., Aires, A., Cortajarena, A. L., & Villar, A. V. (2018). Reduction of cardiac TGF $\beta$ -mediated profibrotic events by inhibition of Hsp90 with engineered protein. *Journal of molecular and cellular cardiology*, 123, 75–87. <https://doi.org/10.1016/j.yjmcc.2018.08.016>
- Algeciras, L., Palanca, A., Maestro, D., RuizdelRio, J., & Villar, A. V. (2021). Epigenetic alterations of TGF $\beta$  and its main canonical signaling mediators in the context of cardiac fibrosis. *Journal of molecular and cellular cardiology*, 159, 38–47. <https://doi.org/10.1016/j.yjmcc.2021.06.003>
- Groen, J., Palanca, A., Aires, A., Conesa, J. J., Maestro, D., Rehbein, S., Harkiolaki, M., Villar, A. V., Cortajarena, A. L., & Pereiro, E. (2021). Correlative 3D cryo X-ray imaging reveals intracellular location and effect of designed antifibrotic protein-nanomaterial hybrids. *Chemical science*, 12(45), 15090–15103. <https://doi.org/10.1039/d1sc04183e>





## REFERENCES

1. Cao, J. and K.D.J.N.R.C. Poss, *The epicardium as a hub for heart regeneration*. 2018. **15**(10): p. 631-647.
2. Quijada, P., M.A. Trembley, and E.M.J.C.r. Small, *The role of the epicardium during heart development and repair*. 2020. **126**(3): p. 377-394.
3. Eisenberg, L.M. and R.R.J.D.b. Markwald, *Cellular recruitment and the development of the myocardium*. 2004. **274**(2): p. 225-232.
4. Pucéat, M.J.B.e.B.A.-M.C.R., *Embryological origin of the endocardium and derived valve progenitor cells: from developmental biology to stem cell-based valve repair*. 2013. **1833**(4): p. 917-922.
5. Jaworska-Wilczynska, M., et al., *Pericardium: structure and function in health and disease*. 2016. **54**(3): p. 121-125.
6. Weinhaus, A.J. and K.P. Roberts, *Anatomy of the human heart*, in *Handbook of cardiac anatomy, physiology, and devices*. 2005, Springer. p. 51-79.
7. Soliman, H. and F.M.J.M.B. Rossi, *Cardiac fibroblast diversity in health and disease*. 2020. **91**: p. 75-91.
8. Williams, B.J.J.o.t.A.C.o.C., *The aorta and resistant hypertension*. 2009, American College of Cardiology Foundation Washington, DC. p. 452-454.
9. Matthay, R.A., et al., *Pulmonary artery hypertension in chronic obstructive pulmonary disease: determination by chest radiography*. 1981. **16**(2): p. 95-100.
10. Nag, A.C. and R.J.J.o.a. Zak, *Dissociation of adult mammalian heart into single cell suspension: an ultrastructural study*. 1979. **129**(Pt 3): p. 541.
11. Brutsaert, D.L.J.P.r., *Cardiac endothelial-myocardial signaling: its role in cardiac growth, contractile performance, and rhythmicity*. 2003. **83**(1): p. 59-115.
12. Pinto, A.R., et al., *Revisiting cardiac cellular composition*. 2016. **118**(3): p. 400-409.
13. Hashmi, S. and H.J.C.R. Ahmad, *Molecular switch model for cardiomyocyte proliferation*. 2019. **8**(1): p. 12-20.
14. Senyo, S.E., et al., *Mammalian heart renewal by pre-existing cardiomyocytes*. 2013. **493**(7432): p. 433-436.
15. Segers, V.F., D.L. Brutsaert, and G.W.J.F.i.p. De Keulenaer, *Cardiac remodeling: endothelial cells have more to say than just NO*. 2018. **9**: p. 382.
16. Kamo, T., H. Akazawa, and I.J.C.r. Komuro, *Cardiac nonmyocytes in the hub of cardiac hypertrophy*. 2015. **117**(1): p. 89-98.
17. Segers, V.F. and R.T.J.N. Lee, *Stem-cell therapy for cardiac disease*. 2008. **451**(7181): p. 937-942.
18. Zeisberg, E.M., et al., *Endothelial-to-mesenchymal transition contributes to cardiac fibrosis*. 2007. **13**(8): p. 952-961.
19. Souders, C.A., S.L. Bowers, and T.A.J.C.r. Baudino, *Cardiac fibroblast: the renaissance cell*. 2009. **105**(12): p. 1164-1176.
20. Fan, D., et al., *Cardiac fibroblasts, fibrosis and extracellular matrix remodeling in heart disease*. 2012. **5**(1): p. 1-13.
21. Fries, K.M., et al., *Evidence of fibroblast heterogeneity and the role of fibroblast subpopulations in fibrosis*. 1994. **72**(3): p. 283-292.
22. Frangogiannis, N.G.J.C.r., *The extracellular matrix in ischemic and nonischemic heart failure*. 2019. **125**(1): p. 117-146.
23. Lockhart, M., et al., *Extracellular matrix and heart development*. 2011. **91**(6): p. 535-550.
24. Hynes, R.O.J.S., *The extracellular matrix: not just pretty fibrils*. 2009. **326**(5957): p. 1216-1219.
25. Rienks, M., et al., *Myocardial extracellular matrix: an ever-changing and diverse entity*. 2014. **114**(5): p. 872-888.
26. Valiente-Alandi, I., et al., *Extracellular matrix-mediated cellular communication in the heart*. 2016. **91**: p. 228-237.

27. Theocharis, A.D., et al., *Extracellular matrix structure*. 2016. **97**: p. 4-27.
28. Li, L., Q. Zhao, and W.J.M.b. Kong, *Extracellular matrix remodeling and cardiac fibrosis*. 2018. **68**: p. 490-506.
29. Kisling, A., R.M. Lust, and L.C. Katwa, *What is the role of peptide fragments of collagen I and IV in health and disease?* Life Sci, 2019. **228**: p. 30-34.
30. Marijjanowski, M.M., et al., *Dilated cardiomyopathy is associated with an increase in the type I/type III collagen ratio: a quantitative assessment*. 1995. **25**(6): p. 1263-1272.
31. Li, G., et al., *Matrix stiffness regulates  $\alpha$ -TAT1/Ac- $\alpha$ -Tub and promotes silica-induced epithelial-mesenchymal transition via DNA damage*. 2020.
32. Lenselink, E.A.J.I.w.j., *Role of fibronectin in normal wound healing*. 2015. **12**(3): p. 313-316.
33. Mosher, D., *Fibronectin*. 2012: Elsevier.
34. Rienks, M., A.-P.J.J.o.m. Papageorgiou, and c. cardiology, *Novel regulators of cardiac inflammation: Matricellular proteins expand their repertoire*. 2016. **91**: p. 172-178.
35. Conway, S.J. and J.D.J.C.g. Molkentin, *Periostin as a heterofunctional regulator of cardiac development and disease*. 2008. **9**(8): p. 548-555.
36. Conway, S.J., T. Doetschman, and M.J.T. Azhar, *The inter-relationship of periostin, TGF $\beta$ , and BMP in heart valve development and valvular heart diseases*. 2011. **11**: p. 1509-1524.
37. Zhao, S., et al., *Periostin expression is upregulated and associated with myocardial fibrosis in human failing hearts*. 2014. **63**(5): p. 373-378.
38. Oka, T., et al., *Genetic manipulation of periostin expression reveals a role in cardiac hypertrophy and ventricular remodeling*. 2007. **101**(3): p. 313-321.
39. Rozario, T. and D.W.J.D.b. DeSimone, *The extracellular matrix in development and morphogenesis: a dynamic view*. 2010. **341**(1): p. 126-140.
40. Kirkpatrick, C.A. and S.B.J.J.o.c.s. Selleck, *Heparan sulfate proteoglycans at a glance*. 2007. **120**(11): p. 1829-1832.
41. Robertson, I.B., et al., *Latent TGF- $\beta$ -binding proteins*. 2015. **47**: p. 44-53.
42. Organization, W.H. *Cardiovascular diseases*. 2019.
43. Heusch, G.J.N.R.C., *Myocardial ischaemia–reperfusion injury and cardioprotection in perspective*. 2020. **17**(12): p. 773-789.
44. Yildiz, M., et al., *Left ventricular hypertrophy and hypertension*. 2020. **63**(1): p. 10-21.
45. Tuncay, E. and B.J.B.t.e.r. Turan, *Intracellular Zn<sup>2+</sup> increase in cardiomyocytes induces both electrical and mechanical dysfunction in heart via endogenous generation of reactive nitrogen species*. 2016. **169**(2): p. 294-302.
46. Prabhu, S.D. and N.G.J.C.r. Frangogiannis, *The biological basis for cardiac repair after myocardial infarction: from inflammation to fibrosis*. 2016. **119**(1): p. 91-112.
47. Díez, J.J.T.J.o.C.H., *Mechanisms of cardiac fibrosis in hypertension*. 2007. **9**(7): p. 546-550.
48. Piccirillo, G., et al., *Age-Dependent Influence on Heart Rate Variability in Salt-sensitive Hypertensive Subjects*. 1996. **44**(5): p. 530-538.
49. Chen, S.T., et al., *The effect of dietary patterns on estimated coronary heart disease risk: results from the Dietary Approaches to Stop Hypertension (DASH) trial*. 2010. **3**(5): p. 484-489.
50. Wu, Q.-Q., et al., *Mechanisms contributing to cardiac remodelling*. 2017. **131**(18): p. 2319-2345.
51. Carabello, B.A. and W.J.J.T.I. Paulus, *Aortic stenosis*. 2009. **373**(9667): p. 956-966.
52. Majkut, S., P.D.P. Dingal, and D.E.J.C.B. Discher, *Stress sensitivity and mechanotransduction during heart development*. 2014. **24**(10): p. R495-R501.

## BIBLIOGRAPHY

53. Arts, T., et al., *Adaptation to mechanical load determines shape and properties of heart and circulation: the CircAdapt model*. 2005. **288**(4): p. H1943-H1954.
54. Göktepe, S., et al., *A generic approach towards finite growth with examples of athlete's heart, cardiac dilation, and cardiac wall thickening*. 2010. **58**(10): p. 1661-1680.
55. Eghbali, M., et al., *Molecular and functional signature of heart hypertrophy during pregnancy*. 2005. **96**(11): p. 1208-1216.
56. Weber, K., Y. Sun, and S.J.E.h.j. Campbell, *Structural remodelling of the heart by fibrous tissue: role of circulating hormones and locally produced peptides*. 1995. **16**(suppl\_N): p. 12-18.
57. Shimizu, I., T.J.J.o.m. Minamino, and c. cardiology, *Physiological and pathological cardiac hypertrophy*. 2016. **97**: p. 245-262.
58. Cohn, J.N., et al., *Cardiac remodeling—concepts and clinical implications: a consensus paper from an international forum on cardiac remodeling*. 2000. **35**(3): p. 569-582.
59. Hedman, K., et al., *Blood pressure in athletic preparticipation evaluation and the implication for cardiac remodeling*. 2019. **105**(16): p. 1223-1230.
60. Nakamura, M. and J.J.N.R.C. Sadoshima, *Mechanisms of physiological and pathological cardiac hypertrophy*. 2018. **15**(7): p. 387-407.
61. Spaich, S., H.A. Katus, and J.J.F.i.p. Backs, *Ongoing controversies surrounding cardiac remodeling: is it black and white—or rather fifty shades of gray?* 2015. **6**: p. 202.
62. Tham, Y.K., et al., *Pathophysiology of cardiac hypertrophy and heart failure: signaling pathways and novel therapeutic targets*. 2015. **89**(9): p. 1401-1438.
63. Swynghedauw, B.J.P.r., *Molecular mechanisms of myocardial remodeling*. 1999. **79**(1): p. 215-262.
64. Hill, J.A. and E.N.J.N.E.J.o.M. Olson, *Cardiac plasticity*. 2008. **358**(13): p. 1370-1380.
65. Mansell, D., et al., *Acute regional changes in myocardial strain may predict ventricular remodeling after myocardial infarction in a large animal model*. 2021. **11**(1): p. 1-10.
66. Bernardo, B.C., et al., *Molecular distinction between physiological and pathological cardiac hypertrophy: experimental findings and therapeutic strategies*. 2010. **128**(1): p. 191-227.
67. Grossman, W., D. Jones, and L.J.T.J.o.c.i. McLaurin, *Wall stress and patterns of hypertrophy in the human left ventricle*. 1975. **56**(1): p. 56-64.
68. Pluim, B.M., et al., *The athlete's heart: a meta-analysis of cardiac structure and function*. 2000. **101**(3): p. 336-344.
69. Oldfield, C.J., et al., *Mechanisms for the transition from physiological to pathological cardiac hypertrophy*. 2020. **98**(2): p. 74-84.
70. Müller, A.L. and N.S. Dhalla, *Differences in concentric cardiac hypertrophy and eccentric hypertrophy*, in *Cardiac Adaptations*. 2013, Springer. p. 147-166.
71. Azevedo, P.S., et al., *Cardiac remodeling: concepts, clinical impact, pathophysiological mechanisms and pharmacologic treatment*. 2015. **106**: p. 62-69.
72. Maillet, M., J.H. Van Berlo, and J.D.J.N.r.M.c.b. Molkentin, *Molecular basis of physiological heart growth: fundamental concepts and new players*. 2013. **14**(1): p. 38-48.
73. Weber, K.T., Y. Sun, and E.J.H. Guarda, *Structural remodeling in hypertensive heart disease and the role of hormones*. 1994. **23**(6\_pt\_2): p. 869-877.
74. Gallego Muñoz, C., C.I. Saldarriaga, and J.J.R.C.d.C. Díez Martínez, *Myocardial fibrosis: towards a new approach*. 2019. **26**(3): p. 142-151.
75. Nagai, T., et al., *Decreased myocardial dendritic cells is associated with impaired reparative fibrosis and development of cardiac rupture after myocardial infarction in humans*. *J Am Heart Assoc*, 2014. **3**(3): p. e000839.

76. Kai, H., et al., *Pressure overload-induced transient oxidative stress mediates perivascular inflammation and cardiac fibrosis through angiotensin II*. 2006. **29**(9): p. 711-718.
77. Kong, P., P. Christia, and N.G. Frangogiannis, *The pathogenesis of cardiac fibrosis*. Cell Mol Life Sci, 2014. **71**(4): p. 549-74.
78. Holmes, J.W., T.K. Borg, and J.W. Covell, *Structure and mechanics of healing myocardial infarcts*. Annu Rev Biomed Eng, 2005. **7**: p. 223-53.
79. Richardson, W.J., et al., *Physiological Implications of Myocardial Scar Structure*. Compr Physiol, 2015. **5**(4): p. 1877-909.
80. Hara, H., N. Takeda, and I. Komuro, *Pathophysiology and therapeutic potential of cardiac fibrosis*. Inflamm Regen, 2017. **37**: p. 13.
81. Hu, Y.F., et al., *Inflammation and the pathogenesis of atrial fibrillation*. Nat Rev Cardiol, 2015. **12**(4): p. 230-43.
82. Mouton, A.J., et al., *Obesity, hypertension, and cardiac dysfunction: novel roles of immunometabolism in macrophage activation and inflammation*. 2020. **126**(6): p. 789-806.
83. Bing, R., et al., *Imaging and impact of myocardial fibrosis in aortic stenosis*. 2019. **12**(2): p. 283-296.
84. Zeisberg, M. and R.J.A.J.o.P.-C.P. Kalluri, *Cellular mechanisms of tissue fibrosis. 1. Common and organ-specific mechanisms associated with tissue fibrosis*. 2013. **304**(3): p. C216-C225.
85. Weber, K.T., *Cardiac interstitium in health and disease: the fibrillar collagen network*. J Am Coll Cardiol, 1989. **13**(7): p. 1637-52.
86. Anderson, K., M. Sutton, and J.J.T.J.o.p. Lie, *Histopathological types of cardiac fibrosis in myocardial disease*. 1979. **128**(2): p. 79-85.
87. Maisch, B., *Ventricular remodeling*. Cardiology, 1996. **87 Suppl 1**: p. 2-10.
88. Anzai, T., *Inflammatory Mechanisms of Cardiovascular Remodeling*. Circ J, 2018. **82**(3): p. 629-635.
89. Chin, C.W.L., et al., *Myocardial Fibrosis and Cardiac Decompensation in Aortic Stenosis*. JACC Cardiovasc Imaging, 2017. **10**(11): p. 1320-1333.
90. Kehat, I. and J.D. Molkentin, *Molecular pathways underlying cardiac remodeling during pathophysiological stimulation*. Circulation, 2010. **122**(25): p. 2727-35.
91. Azevedo, P.S., et al., *Cardiac Remodeling: Concepts, Clinical Impact, Pathophysiological Mechanisms and Pharmacologic Treatment*. Arq Bras Cardiol, 2016. **106**(1): p. 62-9.
92. Thiedemann, K.U., et al., *Connective tissue content and myocardial stiffness in pressure overload hypertrophy. A combined study of morphologic, morphometric, biochemical, and mechanical parameters*. Basic Res Cardiol, 1983. **78**(2): p. 140-55.
93. Tallquist, M.D., *Cardiac Fibroblast Diversity*. Annu Rev Physiol, 2020. **82**: p. 63-78.
94. Snider, P., et al., *Origin of cardiac fibroblasts and the role of periostin*. Circ Res, 2009. **105**(10): p. 934-47.
95. de Lange, F.J., et al., *Lineage and morphogenetic analysis of the cardiac valves*. Circ Res, 2004. **95**(6): p. 645-54.
96. Travers, J.G., et al., *Cardiac Fibrosis: The Fibroblast Awakens*. Circ Res, 2016. **118**(6): p. 1021-40.
97. Le Bras, A., *Dynamics of fibroblast activation in the infarcted heart*. Nat Rev Cardiol, 2018. **15**(7): p. 379.
98. Moore-Morris, T., et al., *Resident fibroblast lineages mediate pressure overload-induced cardiac fibrosis*. J Clin Invest, 2014. **124**(7): p. 2921-34.
99. Fu, X., et al., *Cardiac Fibrosis and Cardiac Fibroblast Lineage-Tracing: Recent Advances*. Front Physiol, 2020. **11**: p. 416.

## BIBLIOGRAPHY

100. Shang, L.L., et al., *Human heart failure is associated with abnormal C-terminal splicing variants in the cardiac sodium channel*. *Circ Res*, 2007. **101**(11): p. 1146-54.
101. Kanisicak, O., et al., *Genetic lineage tracing defines myofibroblast origin and function in the injured heart*. *Nat Commun*, 2016. **7**: p. 12260.
102. Cao, L., et al., *Angiotensin II upregulates fibroblast-myofibroblast transition through Cx43-dependent CaMKII and TGF- $\beta$ 1 signaling in neonatal rat cardiac fibroblasts*. *Acta Biochim Biophys Sin (Shanghai)*, 2018. **50**(9): p. 843-852.
103. Cho, N., S.E. Razipour, and M.L. McCain, *Featured Article: TGF- $\beta$ 1 dominates extracellular matrix rigidity for inducing differentiation of human cardiac fibroblasts to myofibroblasts*. *Exp Biol Med (Maywood)*, 2018. **243**(7): p. 601-612.
104. Goumans, M.J. and P. Ten Dijke, *TGF- $\beta$  Signaling in Control of Cardiovascular Function*. *Cold Spring Harb Perspect Biol*, 2018. **10**(2).
105. Eghbali, M., et al., *Cardiac fibroblasts are predisposed to convert into myocyte phenotype: specific effect of transforming growth factor beta*. *Proc Natl Acad Sci U S A*, 1991. **88**(3): p. 795-9.
106. Dobaczewski, M., W. Chen, and N.G. Frangogiannis, *Transforming growth factor (TGF)- $\beta$  signaling in cardiac remodeling*. *J Mol Cell Cardiol*, 2011. **51**(4): p. 600-6.
107. Segura, A.M., O.H. Frazier, and L.M. Buja, *Fibrosis and heart failure*. *Heart Fail Rev*, 2014. **19**(2): p. 173-85.
108. Annes, J.P., J.S. Munger, and D.B. Rifkin, *Making sense of latent TGFbeta activation*. *J Cell Sci*, 2003. **116**(Pt 2): p. 217-24.
109. Leitlein, J., et al., *Processing of immunosuppressive pro-TGF-beta 1,2 by human glioblastoma cells involves cytoplasmic and secreted furin-like proteases*. *J Immunol*, 2001. **166**(12): p. 7238-43.
110. Morikawa, M., R. Derynck, and K. Miyazono, *TGF- $\beta$  and the TGF- $\beta$  Family: Context-Dependent Roles in Cell and Tissue Physiology*. *Cold Spring Harb Perspect Biol*, 2016. **8**(5).
111. Isogai, Z., et al., *Latent transforming growth factor beta-binding protein 1 interacts with fibrillin and is a microfibril-associated protein*. *J Biol Chem*, 2003. **278**(4): p. 2750-7.
112. Khan, S.A., J. Joyce, and T. Tsuda, *Quantification of active and total transforming growth factor- $\beta$  levels in serum and solid organ tissues by bioassay*. *BMC Res Notes*, 2012. **5**: p. 636.
113. Khan, S., et al., *Enhanced bioactive myocardial transforming growth factor- $\beta$  in advanced human heart failure*. *Circ J*, 2014. **78**(11): p. 2711-8.
114. Rifkin, D.B., *Latent transforming growth factor-beta (TGF-beta) binding proteins: orchestrators of TGF-beta availability*. *J Biol Chem*, 2005. **280**(9): p. 7409-12.
115. Yang, Z., et al., *Absence of integrin-mediated TGFbeta1 activation in vivo recapitulates the phenotype of TGFbeta1-null mice*. *J Cell Biol*, 2007. **176**(6): p. 787-93.
116. Jenkins, G., *The role of proteases in transforming growth factor-beta activation*. *Int J Biochem Cell Biol*, 2008. **40**(6-7): p. 1068-78.
117. Neuzillet, C., et al., *Targeting the TGF $\beta$  pathway for cancer therapy*. *Pharmacol Ther*, 2015. **147**: p. 22-31.
118. Chung, J.Y., et al., *TGF- $\beta$  Signaling: From Tissue Fibrosis to Tumor Microenvironment*. *Int J Mol Sci*, 2021. **22**(14).
119. Meng, X.M., D.J. Nikolic-Paterson, and H.Y. Lan, *TGF- $\beta$ : the master regulator of fibrosis*. *Nat Rev Nephrol*, 2016. **12**(6): p. 325-38.
120. Yan, X. and Y.G. Chen, *Smad7: not only a regulator, but also a cross-talk mediator of TGF- $\beta$  signalling*. *Biochem J*, 2011. **434**(1): p. 1-10.
121. Działo, E., K. Tkacz, and P. Błyszczuk, *Crosstalk between the TGF- $\beta$  and WNT signalling pathways during cardiac fibrogenesis*. *Acta Biochim Pol*, 2018. **65**(3): p. 341-349.

122. Kim, E.K. and E.J. Choi, *Compromised MAPK signaling in human diseases: an update*. Arch Toxicol, 2015. **89**(6): p. 867-82.
123. Yeh, C.C., et al., *Distinctive ERK and p38 signaling in remote and infarcted myocardium during post-MI remodeling in the mouse*. J Cell Biochem, 2010. **109**(6): p. 1185-91.
124. Choudhary, R., et al., *All-trans retinoic acid prevents development of cardiac remodeling in aortic banded rats by inhibiting the renin-angiotensin system*. Am J Physiol Heart Circ Physiol, 2008. **294**(2): p. H633-44.
125. Zhang, Y.E., *Non-Smad Signaling Pathways of the TGF- $\beta$  Family*. Cold Spring Harb Perspect Biol, 2017. **9**(2).
126. Shi, J., et al., *ROCK1 plays an essential role in the transition from cardiac hypertrophy to failure in mice*. J Mol Cell Cardiol, 2010. **49**(5): p. 819-28.
127. Haudek, S.B., et al., *Rho kinase-1 mediates cardiac fibrosis by regulating fibroblast precursor cell differentiation*. Cardiovasc Res, 2009. **83**(3): p. 511-8.
128. Hubchak, S.C., et al., *Rac1 promotes TGF-beta-stimulated mesangial cell type I collagen expression through a PI3K/Akt-dependent mechanism*. Am J Physiol Renal Physiol, 2009. **297**(5): p. F1316-23.
129. Oudit, G.Y., et al., *The role of phosphoinositide-3 kinase and PTEN in cardiovascular physiology and disease*. J Mol Cell Cardiol, 2004. **37**(2): p. 449-71.
130. Voloshenyuk, T.G., et al., *Induction of cardiac fibroblast lysyl oxidase by TGF- $\beta$ 1 requires PI3K/Akt, Smad3, and MAPK signaling*. Cytokine, 2011. **55**(1): p. 90-7.
131. Kim, S.K., M.A. Henen, and A.P. Hinck, *Structural biology of betaglycan and endoglin, membrane-bound co-receptors of the TGF-beta family*. Exp Biol Med (Maywood), 2019. **244**(17): p. 1547-1558.
132. Villar, A.V., et al., *BAMBI (BMP and activin membrane-bound inhibitor) protects the murine heart from pressure-overload biomechanical stress by restraining TGF- $\beta$  signaling*. Biochim Biophys Acta, 2013. **1832**(2): p. 323-35.
133. Shyu, K.G., *The Role of Endoglin in Myocardial Fibrosis*. Acta Cardiol Sin, 2017. **33**(5): p. 461-467.
134. Dorn, L.E., et al., *CTGF/CCN2 is an autocrine regulator of cardiac fibrosis*. J Mol Cell Cardiol, 2018. **121**: p. 205-211.
135. Cortes, S., et al., *Detection and Analysis of Extracellular Hsp90 (eHsp90)*. Methods Mol Biol, 2018. **1709**: p. 321-329.
136. Datta, R., et al., *Myocyte-Derived Hsp90 Modulates Collagen Upregulation via Biphasic Activation of STAT-3 in Fibroblasts during Cardiac Hypertrophy*. Mol Cell Biol, 2017. **37**(6).
137. Aires, A., et al., *A simple approach to design proteins for the sustainable synthesis of metal nanoclusters*. 2019. **58**(19): p. 6214-6219.
138. Lindsley, A., et al., *Identification and characterization of a novel Schwann and outflow tract endocardial cushion lineage-restricted periostin enhancer*. 2007. **307**(2): p. 340-355.
139. Santos, G.d.J.L.P.d., *Mechanical regulation of cardiac fibroblasts*, in *Institute of Pharmacology and Toxicology*. 2020, University Medical Center Göttingen.
140. Cáceres, R.A., et al., *Reduction of cardiac TGF $\beta$ -mediated profibrotic events by inhibition of Hsp90 with engineered protein*. J Mol Cell Cardiol, 2018. **123**: p. 75-87.
141. Biebl, M.M. and J. Buchner, *Structure, Function, and Regulation of the Hsp90 Machinery*. Cold Spring Harb Perspect Biol, 2019. **11**(9).
142. Pennisi, R., P. Ascenzi, and A. di Masi, *Hsp90: A New Player in DNA Repair?* Biomolecules, 2015. **5**(4): p. 2589-618.
143. García, R., et al., *Extracellular heat shock protein 90 binding to TGF $\beta$  receptor I participates in TGF $\beta$ -mediated collagen production in myocardial fibroblasts*. 2016. **28**(10): p. 1563-1579.

## BIBLIOGRAPHY

144. Bolado Desiré, P., *Papel de Hsp90 en la fibrosis patológica mediada por TGFβ:: Evaluación de un nuevo biomarcador*. 2017.
145. Felts, S.J., et al., *The hsp90-related protein TRAP1 is a mitochondrial protein with distinct functional properties*. 2000. **275**(5): p. 3305-3312.
146. Eletto, D., D. Dersh, and Y. Argon. *GRP94 in ER quality control and stress responses*. in *Seminars in cell & developmental biology*. 2010. Elsevier.
147. Glaze, E.R., et al., *Preclinical toxicity of a geldanamycin analog, 17-(dimethylaminoethylamino)-17-demethoxygeldanamycin (17-DMAG), in rats and dogs: potential clinical relevance*. 2005. **56**(6): p. 637-647.
148. Hollingshead, M., et al., *In vivo antitumor efficacy of 17-DMAG (17-dimethylaminoethylamino-17-demethoxygeldanamycin hydrochloride), a water-soluble geldanamycin derivative*. 2005. **56**(2): p. 115-125.
149. Couleaud, P., et al., *Designed modular proteins as scaffolds to stabilize fluorescent nanoclusters*. 2015. **16**(12): p. 3836-3844.
150. Aires, A., et al., *Engineering multifunctional metal/protein hybrid nanomaterials as tools for therapeutic intervention and high-sensitivity detection*. 2021. **12**(7): p. 2480-2487.
151. Miyata, Y.J.C.p.d., *Hsp90 inhibitor geldanamycin and its derivatives as novel cancer chemotherapeutic agents*. 2005. **11**(9): p. 1131-1138.
152. Iavello, A., et al., *Role of Alix in miRNA packaging during extracellular vesicle biogenesis*. 2016. **37**(4): p. 958-966.
153. Otto, G.P. and B.J.J.J.o.c.s. Nichols, *The roles of flotillin microdomains—endocytosis and beyond*. 2011. **124**(23): p. 3933-3940.
154. Suárez, H., et al., *CD9 inhibition reveals a functional connection of extracellular vesicle secretion with mitophagy in melanoma cells*. 2021. **10**(7): p. e12082.
155. Groen, J., et al., *Correlative 3D cryo X-ray imaging reveals intracellular location and effect of designed antifibrotic protein-nanomaterial hybrids*. 2021.
156. Petrov, V.V., R.H. Fagard, and P.J.J.H. Lijnen, *Stimulation of collagen production by transforming growth factor-β1 during differentiation of cardiac fibroblasts to myofibroblasts*. 2002. **39**(2): p. 258-263.
157. Tokuyama, T., et al., *Mitochondrial dynamics regulation in skin fibroblasts from mitochondrial disease patients*. 2020. **10**(3): p. 450.
158. Cortajarena, A.L., J. Wang, and L.J.T.F.j. Regan, *Crystal structure of a designed tetratricopeptide repeat module in complex with its peptide ligand*. 2010. **277**(4): p. 1058-1066.
159. Cox, T.R., et al., *LOX-mediated collagen crosslinking is responsible for fibrosis-enhanced metastasis*. 2013. **73**(6): p. 1721-1732.
160. Kikuchi, A. and S.P.J.G.e. Monga, *PDGFRα in liver pathophysiology: emerging roles in development, regeneration, fibrosis, and cancer*. 2015. **16**(3): p. 109.
161. Glover, D.J., H.J. Lipps, and D.A.J.N.R.G. Jans, *Towards safe, non-viral therapeutic gene expression in humans*. 2005. **6**(4): p. 299-310.
162. Roberts, R.J., L. Hallee, and C.K.J.J.o.P.M. Lam, *The Potential of Hsp90 in Targeting Pathological Pathways in Cardiac Diseases*. 2021. **11**(12): p. 1373.
163. Huang, G., et al., *Targeting HSP90 attenuates angiotensin II-induced adventitial remodelling via suppression of mitochondrial fission*. 2020. **116**(5): p. 1071-1084.
164. Tamura, S., et al., *Heat-shock protein 90 modulates cardiac ventricular hypertrophy via activation of MAPK pathway*. 2019. **127**: p. 134-142.
165. Lee, J., et al., *Heat shock protein 90 regulates subcellular localization of smads in Mv1Lu cells*. 2016. **117**(1): p. 230-238.
166. Chakraborty, A. and A.L.J.B.S.T. Ekins, *HSP90 as a regulator of extracellular matrix dynamics*. 2021. **49**(6): p. 2611-2625.
167. Gopal, U., et al., *A novel extracellular Hsp90 mediated co-receptor function for LRP1 regulates EphA2 dependent glioblastoma cell invasion*. 2011. **6**(3): p. e17649.



168. Manthorpe, M., et al., *Gene therapy by intramuscular injection of plasmid DNA: studies on firefly luciferase gene expression in mice*. 1993. **4**(4): p. 419-431.
169. van Gaal, E.V., et al., *Plasmid engineering for controlled and sustained gene expression for nonviral gene therapy*. *Pharm Res*, 2006. **23**(6): p. 1053-74.
170. Solit, D.B. and G.J.D.d.t. Chiosis, *Development and application of Hsp90 inhibitors*. 2008. **13**(1-2): p. 38-43.
171. Supko, J.G., et al., *Preclinical pharmacologic evaluation of geldanamycin as an antitumor agent*. 1995. **36**(4): p. 305-315.
172. Buratta, S., et al., *Extracellular vesicles released by fibroblasts undergoing H-Ras induced senescence show changes in lipid profile*. 2017. **12**(11): p. e0188840.
173. Peddibhotla, S.S., et al., *Tetraspanin CD9 links junctional adhesion molecule-A to  $\alpha\beta 3$  integrin to mediate basic fibroblast growth factor-specific angiogenic signaling*. 2013. **24**(7): p. 933-944.
174. Li, W., D. Sahu, and F.J.B.e.B.A.-M.C.R. Tsen, *Secreted heat shock protein-90 (Hsp90) in wound healing and cancer*. 2012. **1823**(3): p. 730-741.
175. Wong, M.Y., et al., *A high-throughput assay for collagen secretion suggests an unanticipated role for Hsp90 in collagen production*. 2018. **57**(19): p. 2814-2827.
176. Zimmerman, K.A., et al., *Calreticulin regulates neointima formation and collagen deposition following carotid artery ligation*. 2015. **52**(5): p. 306-320.
177. Kassan, M., et al., *Endoplasmic reticulum stress is involved in cardiac damage and vascular endothelial dysfunction in hypertensive mice*. 2012. **32**(7): p. 1652-1661.
178. Owusu, B.Y., et al., *The role of the endoplasmic reticulum protein calreticulin in mediating TGF- $\beta$ -stimulated extracellular matrix production in fibrotic disease*. 2018. **12**(1): p. 289-299.
179. Chen, X., et al., *Internalization pathways of nanoparticles and their interaction with a vesicle*. 2013. **9**(31): p. 7592-7600.
180. Wang, W., et al., *Anti-apoptotic effect of heat shock protein 90 on hypoxia-mediated cardiomyocyte damage is mediated via the phosphatidylinositol 3-kinase/AKT pathway*. 2009. **36**(9): p. 899-903.
181. Li, X., et al., *Aspirin reduces cardiac interstitial fibrosis by inhibiting Erk1/2-Serpine2 and P-Akt signalling pathways*. 2018. **45**(5): p. 1955-1965.
182. Dong, H., et al., *Blockade of extracellular heat shock protein 90 $\alpha$  by 1G6-D7 attenuates pulmonary fibrosis through inhibiting ERK signaling*. 2017. **313**(6): p. L1006-L1015.
183. Hough, C., M. Radu, and J.J. Doré, *Tgf-beta induced Erk phosphorylation of smad linker region regulates smad signaling*. 2012.
184. Marunouchi, T., et al., *Hsp90 inhibitor attenuates the development of pathophysiological cardiac fibrosis in mouse hypertrophy via suppression of the calcineurin-NFAT and c-Raf-Erk pathways*. 2021. **77**(6): p. 822-829.
185. Schopf, F.H., M.M. Biebl, and J.J.N.r.M.c.b. Buchner, *The HSP90 chaperone machinery*. 2017. **18**(6): p. 345-360.
186. Park, S., et al., *Cardiac fibrosis: potential therapeutic targets*. 2019. **209**: p. 121-137.
187. Ikeuchi, M., et al., *Inhibition of TGF- $\beta$  signaling exacerbates early cardiac dysfunction but prevents late remodeling after infarction*. 2004. **64**(3): p. 526-535.
188. Engebretsen, K.V., et al., *Attenuated development of cardiac fibrosis in left ventricular pressure overload by SM16, an orally active inhibitor of ALK5*. 2014. **76**: p. 148-157.
189. Segers, V.F. and R.T.J.C.r. Lee, *Biomaterials to enhance stem cell function in the heart*. 2011. **109**(8): p. 910-922.
190. Deng, B., et al., *Delivery of alginate-chitosan hydrogel promotes endogenous repair and preserves cardiac function in rats with myocardial infarction*. 2015. **103**(3): p. 907-918.

## BIBLIOGRAPHY

191. Menasché, P., et al., *Human embryonic stem cell-derived cardiac progenitors for severe heart failure treatment: first clinical case report*. 2015. **36**(30): p. 2011-2017.
192. Fernandes, S., et al., *Comparison of human embryonic stem cell-derived cardiomyocytes, cardiovascular progenitors, and bone marrow mononuclear cells for cardiac repair*. 2015. **5**(5): p. 753-762.
193. Rai, V., et al., *Relevance of mouse models of cardiac fibrosis and hypertrophy in cardiac research*. 2017. **424**(1-2): p. 123-145.
194. Dahlöf, B.J.J.o.h.h., *Effect of angiotensin II blockade on cardiac hypertrophy and remodelling: a review*. 1995. **9**: p. S37-44.
195. Kurdi, M. and G.W.J.H. Booz, *New take on the role of angiotensin II in cardiac hypertrophy and fibrosis*. 2011. **57**(6): p. 1034-1038.
196. Zhang, X., et al., *Inhibition of HSP90 S-nitrosylation alleviates cardiac fibrosis via TGF $\beta$ /SMAD3 signalling pathway*. 2021. **178**(23): p. 4608-4625.
197. Allegra, A., et al., *Nanoparticles in oncology: the new theragnostic molecules*. 2011. **11**(7): p. 669-686.
198. Kim, Y.-S., et al., *The potential theragnostic (diagnostic+ therapeutic) application of exosomes in diverse biomedical fields*. 2018. **22**(2): p. 113-125.
199. Weber, W.A., et al., *The Future of Nuclear Medicine, Molecular Imaging, and Theranostics*. 2020. **61**(Supplement 2): p. 263S-272S.
200. Kajander, T., et al., *Structure and stability of designed TPR protein superhelices: unusual crystal packing and implications for natural TPR proteins*. 2007. **63**(7): p. 800-811.
201. Pislaru, C., et al., *Viscoelastic properties of normal and infarcted myocardium measured by a multifrequency shear wave method: comparison with pressure-segment length method*. 2014. **40**(8): p. 1785-1795.
202. Ghista, D.N., et al., *Elastic modulus of the human intact left ventricle—determination and physiological interpretation*. 1975. **13**(2): p. 151-161.
203. Driesen, R.B., et al., *Reversible and irreversible differentiation of cardiac fibroblasts*. 2014. **101**(3): p. 411-422.
204. Shi, X., et al., *Elasticity of cardiac cells on the polymer substrates with different stiffness: an atomic force microscopy study*. 2011. **13**(16): p. 7540-7545.
205. Elson, E.L. and G.M.J.I.f. Genin, *Tissue constructs: platforms for basic research and drug discovery*. 2016. **6**(1): p. 20150095.
206. Wakatsuki, T., et al., *Cell mechanics studied by a reconstituted model tissue*. 2000. **79**(5): p. 2353-2368.
207. DeGrave, A., et al. *Cardiac fibroblasts follow their individual program in 3D cultures*. in *NAUNYN-SCHMIEDEBERGS ARCHIVES OF PHARMACOLOGY*. 2021. SPRINGER ONE NEW YORK PLAZA, SUITE 4600, NEW YORK, NY, UNITED STATES.
208. Kittana, N., et al., *Modulating the Biomechanical Properties of Engineered Connective Tissues by Chitosan-Coated Multiwall Carbon Nanotubes*. 2021. **16**: p. 989.
209. Groen, J., et al., *Correlative 3D cryo X-ray imaging reveals intracellular location and effect of designed antifibrotic protein–nanomaterial hybrids*. 2021. **12**(45): p. 15090-15103.
210. Boerma, M., et al., *Comparative gene expression profiling in three primary human cell lines after treatment with a novel inhibitor of Rho kinase or atorvastatin*. 2008. **19**(7): p. 709.
211. Smith, C.L., et al., *Epicardial-derived cell epithelial-to-mesenchymal transition and fate specification require PDGF receptor signaling*. 2011. **108**(12): p. e15-e26.
212. Silva, A.C., et al., *Bearing my heart: the role of extracellular matrix on cardiac development, homeostasis, and injury response*. 2021. **8**: p. 1705.

213. Acsadi, G., et al., *Direct gene transfer and expression into rat heart in vivo*. 1991. **3**(1): p. 71-81.
214. Ylä-Herttuala, S. and A.H. Baker, *Cardiovascular Gene Therapy: Past, Present, and Future*. *Mol Ther*, 2017. **25**(5): p. 1095-1106.
215. López, B., et al., *Diffuse myocardial fibrosis: mechanisms, diagnosis and therapeutic approaches*. 2021. **18**(7): p. 479-498.
216. Gourdie, R.G., S. Dimmeler, and P.J.N.r.D.d. Kohl, *Novel therapeutic strategies targeting fibroblasts and fibrosis in heart disease*. 2016. **15**(9): p. 620-638.
217. Krenning, G., E.M. Zeisberg, and R.J.J.o.c.p. Kalluri, *The origin of fibroblasts and mechanism of cardiac fibrosis*. 2010. **225**(3): p. 631-637.



## Original article

Reduction of cardiac TGF $\beta$ -mediated profibrotic events by inhibition of Hsp90 with engineered proteinCáceres R.A.<sup>a,f</sup>, Chavez T.<sup>a,f</sup>, Maestro D.<sup>a</sup>, Palanca A.R.<sup>a,b</sup>, Bolado P.<sup>a</sup>, Madrazo F.<sup>c</sup>, Aires A.<sup>d</sup>, Cortajarena A.L.<sup>d,e</sup>, Villar A.V.<sup>a,\*</sup><sup>a</sup> Instituto de Biomedicina y Biotecnología de Cantabria (IBBT), CSIC-Universidad de Cantabria, Santander, Spain<sup>b</sup> Departamento de Anatomía y Biología Celular, Universidad de Cantabria, Santander, Spain<sup>c</sup> Instituto de Investigación Marqués de Valdecilla (IDIVAL), Santander, Spain<sup>d</sup> CIC biomaGUNE, Parque Tecnológico de San Sebastián, 20014 Donostia-San Sebastián, Spain<sup>e</sup> Ikerbasque, Basque Foundation for Science, M<sup>o</sup> Díaz de Haro 3, 48013 Bilbao, Spain<sup>f</sup> Universidad Nacional de San Agustín de Arequipa, Perú

## ARTICLE INFO

## Keywords:

Consensus tetrapeptide repeat (CTPR)

Designed proteins

Hsp90/ Hsp90 protein inhibitor

Myocardial fibrosis

TGF $\beta$  signaling

## ABSTRACT

Myocardial fibroblast activation coupled with extracellular matrix production is a pathological signature of myocardial fibrosis and is governed mainly by transforming growth factor TGF $\beta$ -Smad2/3 signaling. Targeting the ubiquitous TGF $\beta$  leads to cellular homeostasis deregulation with adverse consequences. We previously showed the anti-fibrotic effects upon downregulation of 90-kDa heat shock protein (Hsp90), a chaperone that associates to the TGF $\beta$  signaling cascade. In the present study, we use a fluorescent-labeled Hsp90 protein inhibitor (CTPR390–488) with specific Hsp90 binding properties to reduce myocardial pro-fibrotic events *in vitro* and *in vivo*. The mechanism of action involves the disruption of TGF $\beta$ RI-Hsp90 complex, resulting in a decrease in TGF $\beta$  signaling and reduction in extracellular matrix collagen. *In vivo*, decreased myocardial collagen deposition was observed upon CTPR390–488 treatment in a pro-fibrotic mouse model. This is the first study demonstrating the ability of an engineered Hsp90 protein inhibitor to block collagen expression, reduce the motility of myocardial TGF $\beta$ -activated fibroblasts and ameliorate angiotensin-II induced cardiac myocardial fibrosis *in vivo*.

## 1. Introduction

Myocardial fibrosis is a common phenomenon in the late stages of diverse cardiac diseases and it is a predictive factor of poor cardiac recovery. The mechanical cues are known to activate cardiac fibroblasts resulting in their differentiation into myofibroblasts, proliferation and excessive extracellular matrix production and long-term matrix stiffening. These events result in structural and functional alterations of the heart. Myocardial fibrosis lacks an effective treatment; approaches to reduce fibrosis exploit the understanding of the fibroblasts' role in the fibrotic process. Fibroblasts are the main contributors in the production of myocardial collagen principally through the transforming growth factor  $\beta$  (TGF $\beta$ ) signaling pathway. TGF $\beta$  is the main pro-fibrotic cytokine. TGF $\beta$  exerts its effect by binding to a complex of TGF $\beta$  receptor I and II resulting in phosphorylation and translocation of Smad2/3 to the nucleus and increasing collagen production. Collagen protein deposition increases the extracellular matrix network [1–3]. The highly

conserved ATP-dependent chaperone heat shock protein 90 (Hsp90) has been described as a component of the TGF $\beta$  signaling cascade [4–7]. The Hsp90 family consists mainly of four members: Hsp90aa1 or Hsp90 $\alpha$ , Hsp90ab1 or Hsp90 $\beta$ , gp96 and TNF receptor associated protein 1 (TRAP1). The most important isoforms are the inducible Hsp90 $\alpha$ , expressed upon stress stimuli, and the constitutively expressed isoform Hsp90 $\beta$ . Apart from its classical role in protein folding, Hsp90 binds other proteins, like transcription factors. In regards to the TGF $\beta$  signaling cascade, Hsp90 inhibition was described to attenuate renal fibrosis through degradation of TGF $\beta$  type II receptor [4]. Hsp90 inhibition was found to reduce collagen I synthesis on hepatic stellate cells (HSCs) in liver fibrosis [8]. Interesting data described by different groups including ours, showed that pharmacological and biological inhibition of Hsp90 effectively blocks the pro-fibrotic effects of TGF $\beta$  in different preclinical models of skin fibrosis in systemic sclerosis [6], in cardiac hypertrophy [9] or in cardiac fibrosis [10]. Hsp90 was presented as a novel modulator of TGF $\beta$  signaling in lung adenocarcinoma

\* Corresponding author.

E-mail address: [villarav@unican.es](mailto:villarav@unican.es) (A.V. Villar).<https://doi.org/10.1016/j.yjmcc.2018.08.016>

Received 5 April 2018; Received in revised form 6 August 2018; Accepted 17 August 2018

Available online 05 September 2018

0022-2828/ © 2018 Elsevier Ltd. All rights reserved.

and bronchoalveolar carcinoma cells [5]. Various Hsp90 inhibitors such as geldanamycin, radicicol, 17-AAG, 17-DMAG, AUY-922, AT-13387, STA-9090, CNF-2024 are used to block Hsp90 activity in cancer with numerous side effects due to the inhibition of the ATPase domain, a key functional element in its Hsp90's protein folding activity [11].

A new class of small protein therapeutic agents have been described, derived from natural binding domains including ankyrin repeats, tetratricopeptide repeats, and other protein scaffolds [12–14]. Of particular interest is a previously designed Hsp90 binding module based on a tetratricopeptide repeat scaffold (CTPR390) that aims to inhibit Hsp90 minimizing the effects on cellular homeostasis [15] [16]. The engineered TPR scaffold is a protein generated by tandem repeats of a small structural motif (34 amino acids) with a simple architecture, stabilized by local interactions between the repeated modules [16]; its secondary and tertiary structures are characterized by the predominance of repeated and predictable local interactions. Therefore, there is a clear structural and functional delimitation between key residues encoding the stability and the functionality of the protein module [17]. These consensus TPRs (CTPRs) are scaffold proteins that can act as small antibody mimetics into which different ligand recognition properties can be encoded [18], thus opening the door to multiple biotechnological and biomedical applications. CTPR390 specifically binds the MEEVD sequence at the C-terminal region of the Hsp90 protein, which represents the recognition sequence for Hsp90 co-chaperones [19]. A fluorophore (Alexa 488) was incorporated to the final biomolecule (CTPR390–488) for both *in vitro* and *in vivo* tracking.

One of the most studied *in vivo* small animal models developing myocardial fibrosis is the angiotensin II treated-mouse. The renin/angiotensin/aldosterone system plays an important role in normal myocardial function. However, chronic elevation in angiotensin II (Ang II) levels is associated with fibrosis among other pathological remodeling adverse effects [20]. TGF $\beta$  activation occurs downstream Ang II activity and implicates TGF $\beta$ -dependent collagen synthesis [21]. Ang II deregulation results in pathological remodeling, especially myocardial fibrosis [22], and its administration in animal models commonly induces left ventricular remodeling, progressive deterioration of cardiac function, and finally clinical syndrome of heart failure [23]. This mouse model of myocardial fibrosis was used to determine the effects of selective Hsp90 inhibition by the engineered protein CTPR390–488 on myocardial collagen synthesis and accumulation. We have previously pointed out the role for Hsp90 in sustaining TGF $\beta$  signaling and collagen synthesis in cardiac fibroblasts and also Datta et al. suggested that Hsp90 participates in cardiac remodeling in an *in vivo* model of cardiac fibrosis [7,9,10]. The novelty of this paper resides in the use of an engineered protein that does not act by inhibiting the ATPase activity of Hsp90 but by mimicking co-chaperone binding to Hsp90. This binding results in the inhibition of collagen synthesis preserving cellular homeostasis.

## 2. Results

### 2.1. CTPR390-488 is internalized in primary myocardial fibroblasts and does not affect cellular viability

*In vivo* confocal imaging experiments revealed the presence of CTPR390–488 inside and outside primary cardiac fibroblasts treated with two different concentrations (0.2 and 0.8  $\mu$ M) of CTPR390–488 (Fig. 1A). Cell viability at increasing concentrations of CTPR390–488 was not affected (Fig. 1B). To assess the uptake efficiency of CTPR390–488 into primary cells, colorimetric and fluorometric assays were performed at 24 hours after CTPR390–488 addition. The average percentage of CTPR390–488 internalization at all concentrations tested (0.0, 0.1, 0.2, 0.4, 0.8, 1.5, and 3  $\mu$ M) was  $9.1 \pm 3.3\%$  measured by absorbance (Fig. 1C) or  $9.3 \pm 4.6\%$ , when detected by fluorescence (Fig. 1D). The percentage of cellular uptake of the CTPR390–488 protein at each concentration was determined (Table 1 source data).

Fig. 1E–1G show similar localization and distribution of the CTPR390–488 protein when detected by fluorometry and through immune-detection with the CTPR390-specific antibody in TGF $\beta$ -activated fibroblasts treated with 0.4  $\mu$ M of CTPR390–488. Fig. 1H–1J show the WB detection and quantification of intra and extracellular CTPR390–488 protein in treated fibroblasts. The densitometric analysis of CTPR390–488 indicated that 7.72% was inside the cell after 24 h (Fig. 1J). These results showed that CTPR390–488 is efficiently internalized in primary cardiac fibroblasts without affecting the viability of the cells.

### 2.2. CTPR390-488-Hsp90 interaction does not reduce Hsp90 chaperone activity

We utilized fluorescence anisotropy to monitor the interaction between CTPR390–488 protein and the Hsp90 C-terminal peptide and determine the corresponding binding affinity (Fig. 2A). The results demonstrate that the capability of the protein to recognize the Hsp90 C-terminal peptide was not affected by the cysteine modification. Furthermore, the  $K_D$  value obtained for the interaction was  $110 \pm 7 \mu$ M, comparable to the value obtained previously [15]. Refolding assays were used to determine Hsp90 ATPase activity in the presence of increasing concentrations of CTPR390–488 in myocardial fibroblasts (Fig. 2B). We did not observe reduction on Hsp90 chaperone activity in any of the groups (WT control, Hsp90aa1 KO, WT + CTPR390–488, KO + CTPR390–488) at increasing concentrations of the inhibitor (0.1, 0.2, 0.4, 0.8 1.5 and 3  $\mu$ M). We found significant increases in refolding activity when adding 0.4; 0.8 or 3  $\mu$ M of CTPR390–488 compared to control fibroblasts ( $*p < .05$ ). Rabbit reticulocyte lysate was used as positive control ( $**p < .005$ ) and denatured luciferase in the absence of Hsp90 as negative control ( $***p < .001$ ) (Fig. 2B). Gene expression of Hsp90aa1 slightly increased in WT fibroblasts with the CTPR390–488 treatment and Hsp90aa1 was not detected in Hsp90aa1 KO fibroblasts as expected (Fig. 2C). Gene expression of Hsp90ab1 was reduced in KO cells compared to WT fibroblasts ( $***p < .001$ ) (Fig. 2D). The significant variations of Hsp90 chaperone activity were not due to changes in Hsp90 protein levels (Fig. 2E–2F). We did not find any Hsp90 overexpression in Hsp90aa1 KO cells treated with CTPR390–488 either (Fig. 2E–2F). Thus, the presence of CTPR390–488 did not alter the Hsp90 mRNA or protein expression, and the cellular effects observed in the presence of CTPR390–488 were not due to changes in Hsp90 expression. Activation of fibroblasts is ligand-dependent and TGF $\beta$  triggered Hsp90 mRNA and protein expression (Fig. S1) and collagen synthesis [10] in myocardial fibroblasts.

### 2.3. Co-localization of Hsp90 and CTPR390-488

CTPR390–488 is an engineered TPR-based protein domain with Hsp90 binding properties [15,24,25]. We previously reported, that the extracellular domain of TGF $\beta$ RI seems to interact with the Hsp90 dimer, and both Hsp90 isoforms ( $\alpha$  and  $\beta$ ) can be secreted extracellularly and be part of the Hsp90 dimer [10]. Here, we observed the co-localization of Hsp90 and TGF $\beta$ RI in primary fibroblasts extracted from the myocardium of WT mice cultured in the presence of TGF $\beta$  (0.3 ng/ml) (Fig. 3A–3D), and the co-localization of Hsp90 and CTPR390–488 (Fig. 3E–3I). We did not detect the triple co-localization (Hsp90/ TGF $\beta$ RI/ CTPR390–488). We included in the Discussion a possible mechanism of action that disrupts Hsp90-TGF $\beta$ RI complex due to the presence of CTPR390–488.

### 2.4. Collagen and p-Smad2/3 expressions were reduced in CTPR390-488-treated fibroblasts and fibroblasts from Hsp90aa1 KO mice

To explore the collagen production and TGF $\beta$  signaling activity in the presence of CTPR390–488, primary cardiac fibroblasts from WT mice were treated with CTPR390–488 (0, 0.1, 0.2 and 0.8  $\mu$ M) and

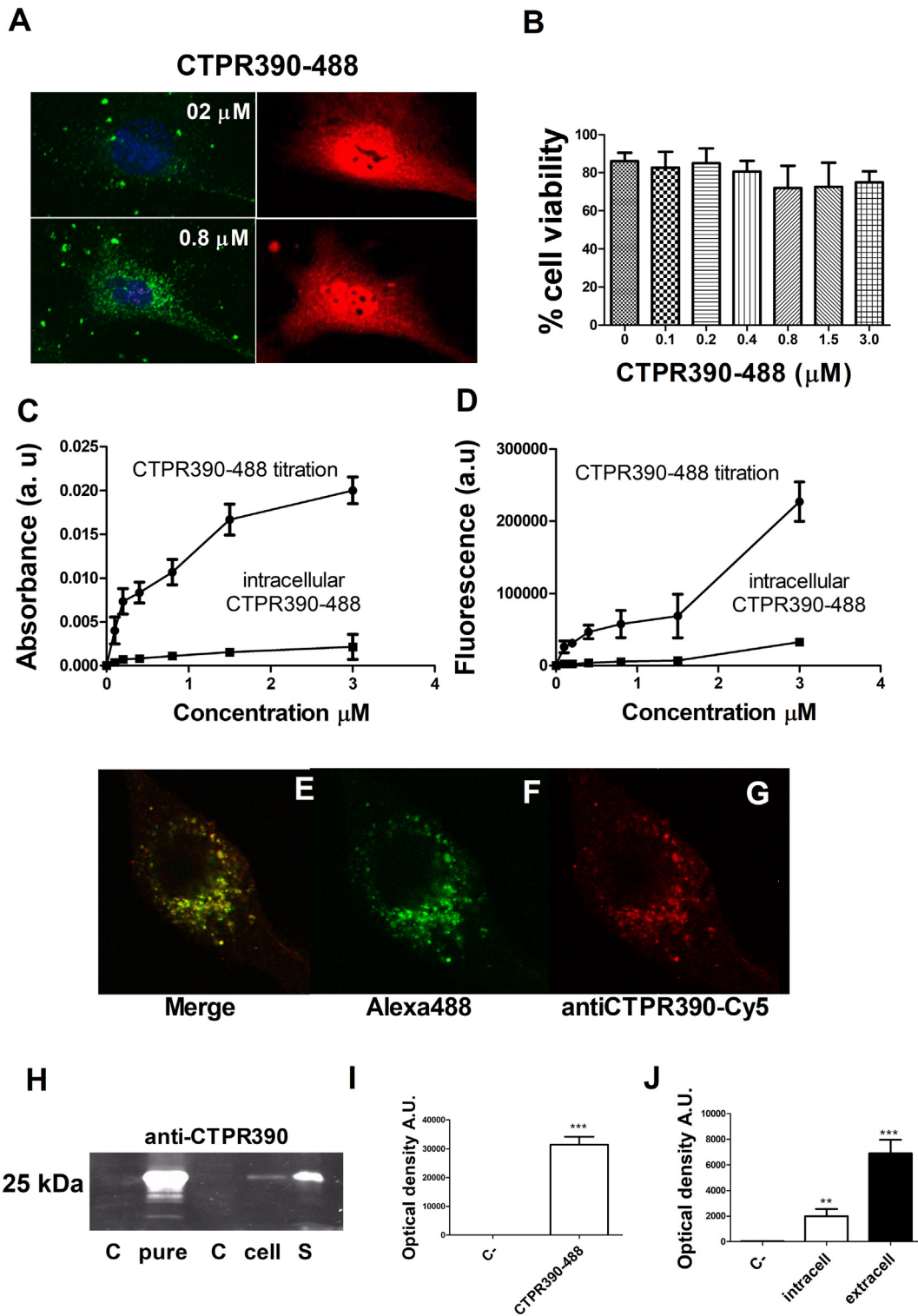


**Fig. 1.** CTPR390–488 detection in primary fibroblasts from WT mice myocardial tissue. **A:** Confocal microscopy showing the intrinsic fluorescence (green) of CTPR390–488 both intra and extracellularly at two different concentrations (0.2 and 0.8  $\mu\text{M}$ ) in living cells (not fixed). Right panels show the shape of the fibroblast in red. **B:** Cell viability at increasing concentrations of CTPR390–488. **C, D:** Absorbance and fluorescence values of a titration curve (pure CTPR390–488) and the correspondent CTPR390–488 signal at each concentration of intracellular samples. In all cases three independent experiments were performed. **E, F, G:** Co-localization of the two possible detection for CTPR390–488: its intrinsic Alexa 488 fluorescence and the CTPR390 immunodetection. **E:** merge images of **F** and **G**. **F:** Confocal microscopy of the CTPR390–488 intrinsic fluorescence. **G:** the immunofluorescence detection of CTPR390–488 using anti-CTPR390 antibody and Cy5 secondary antibody. **H:** WB of the CTPR390–488 pure molecule (C), and CTPR390–488 from the fibroblasts lysate and the supernatant (S). **I, J:** quantification of CTPR390–488 WBs from (H). Significant variations of three independent experiments assayed were expressed vs. control (C), \* $p < .05$ , \*\* $p < .005$ , \*\*\* $p < .001$ ; Mann–Whitney test. (For interpretation of the references to colour in this figure legend, the reader is referred to the web version of this article.)



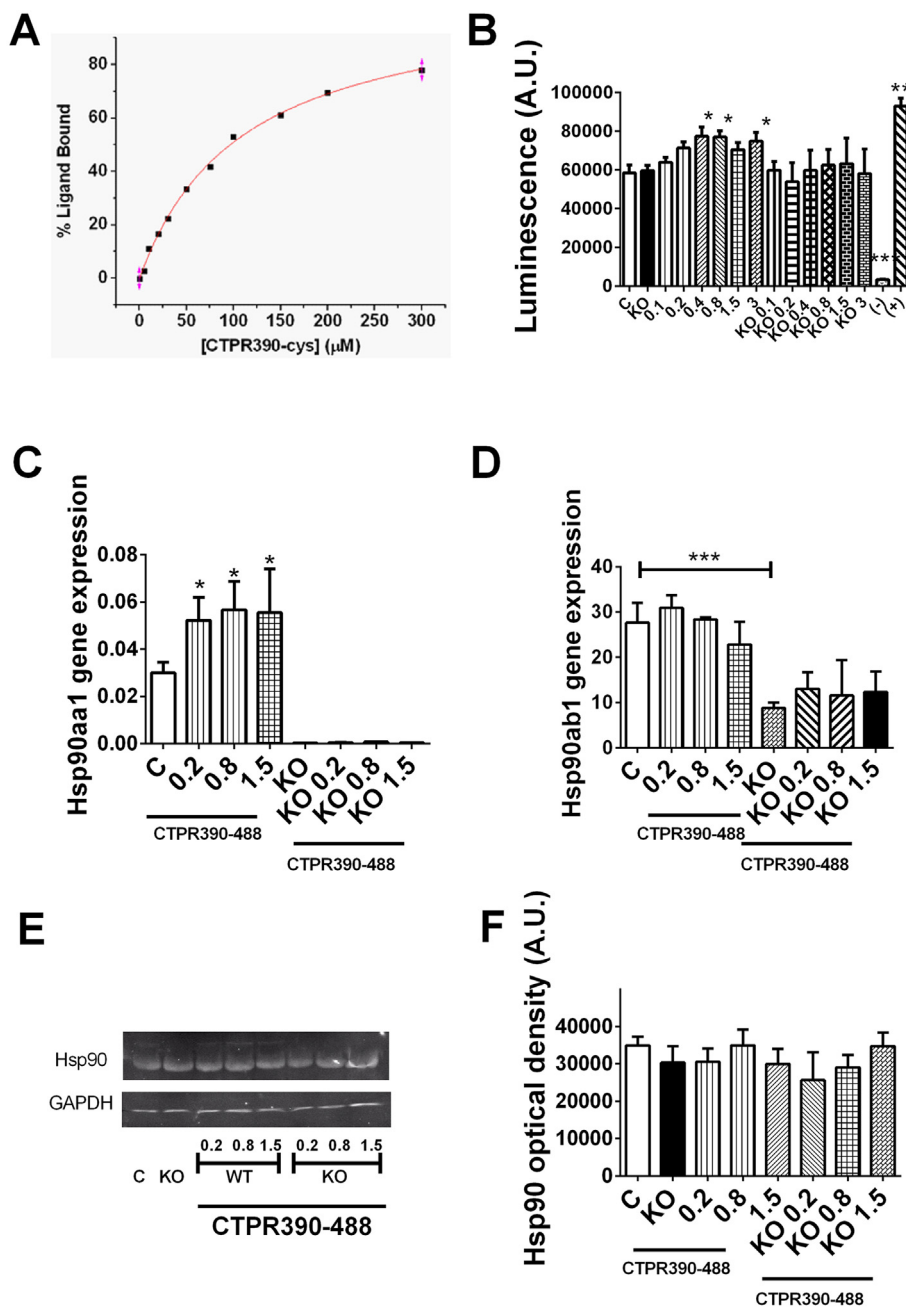


**Fig. 2.** Hsp90 binding and effect on Hsp90 chaperone activity of CTPR390–488. **A:** Fluorescein anisotropy assay showing Hsp90 binding activity of CTPR390–488 ( $K_D = 110 \pm 7 \mu\text{M}$ ). **B:** Hsp90-dependent refolding activity of lysates from WT and KO, myocardial fibroblasts adding CTPR390–488 different concentrations; the negative control (-) was denatured luciferase and the positive control (+) corresponded to rabbit reticulocyte lysate (RRL). **C, D:** Hsp90aa1 and Hsp90ab1 gene expressions in WT and Hsp90aa1 KO fibroblasts under increasing concentrations of CTPR390–488. **E:** Representative Western blot (WB) of Hsp90 expression in primary myocardial fibroblast of WT mice (C), Hsp90aa1 KO mice (KO) and WT and KO fibroblasts in the presence of different concentrations of CTPR390–488 (0.2; 0.8; 1.5  $\mu\text{M}$ ), GAPDH was used as control. **F:** Densitogram quantifying three independent experiments; data were expressed as mean  $\pm$  SD of optical density in arbitrary units (A.U.). Significant variations of three independent experiments assayed were expressed vs. control (C), \* $p < .05$ , \*\* $p < .005$ , \*\*\* $p < .001$ ; Mann–Whitney.

compared to primary cardiac fibroblasts from Hsp90aa1 KO mice (Fig. 4). The results showed significant reduction in gene and protein expression for collagen I and collagen III upon treatment with increasing concentrations of CTPR390–488 (Fig. 4A–4D). The quantification of collagens from Hsp90aa1 KO cells also exhibited lower gene and protein expressions compared to WT control (Fig. 4A–4D). Collagen levels of Hsp90aa1 KO fibroblasts were also reduced upon treatment with CTPR390–488 compared to control KO cells (Fig. S2A–S2C). COL I deposition is lower in CTPR390–488-treated WT fibroblasts compared to control cells (Fig. 4E–4H). Immunofluorescence studies showed a higher area of collagen deposition in WT cells (Fig. 4F) than in CTPR390–488-treated cells (Fig. 4H). Quantification of the immunofluorescence results concluded that the collagen area (COL I) in WT cells ( $67.4\% \pm 6.5$ ) was higher than in CTPR390–488 treated cells ( $36.9\% \pm 13.7$  (\*\* $p < .005$ )) (Fig. 4I). The reduction of in vivo COL I deposition from Hsp90aa1 KO myocardial fibroblasts was previously described by our group [10]. Furthermore, TGF $\beta$ -induced Smad2/3

phosphorylation was reduced by the addition of CTPR390–488 (Fig. 4J–4K). TGF $\beta$ RI was found to be a Hsp90 interacting protein [27] and Hsp90 inhibition can affect TGF $\beta$ RI protein levels. Thus, we also analyzed the expression of TGF $\beta$ RI and other Hsp90 well known interactors not directly related to the canonical Smad TGF $\beta$  signaling cascade (Akt, Erk and Hsp70) by Western blot analysis. Cardiac fibroblasts were treated with different doses of CTPR390–488, including doses effective in reducing collagen production. We did not observe differences in protein expression (Fig. S2D–S2J) of any of the tested Hsp90 interactors.

This result would sustain the ability of CTPR390–488 to maintain Hsp90 chaperone activity thus avoiding cellular homeostasis disruption. It has been shown that higher concentrations of CTPR390 (40  $\mu\text{M}$ ) induces a substantial decrease in the phosphorylation of Hsp90 client protein Her2 (p-Her2) in cancer cells [16]. Similar to those observations, the levels of the p-Smad2/3 was also diminished (Fig. 4K) as it were the phosphorylation levels of Akt and Erk (Fig. S2D, S2E, S2G). Akt and Erk activation are TGF $\beta$ RI dependent in fibrotic processes, so

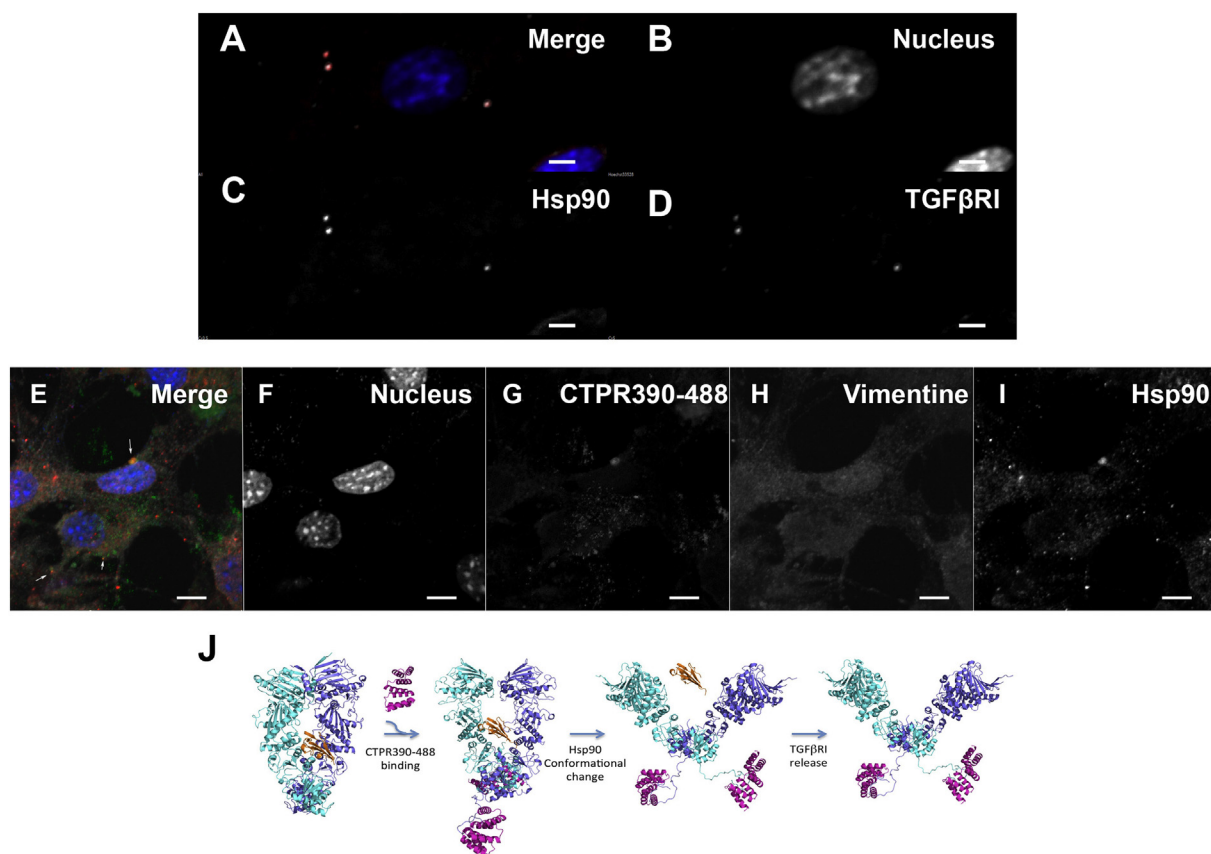


**Fig. 3.** Confocal microscopy assays showing protein co-localization in myocardial fibroblasts and in silico prediction of CTPR390–488 mechanism of action. A: merge-image showing co-localization of Hsp90 and TGFβRI. B: Hoechst was used as nuclear staining. C, D: Hsp90 is visualized with Cy3 and TGFβRI with Cy5 secondary antibodies. E: Co-localization of CTPR390–488 (green) and Hsp90 (red) in myocardial fibroblasts was detected in yellow and it was marked by white arrows. F: Hoechst was used as nuclear staining. G: intrinsic fluorescence of CTPR390–488 (green). H: vimentin marks the cellular shape (vimentin-Cy3 was placed in channel grey to merge the final image 3E with Image J software). I: Hsp90 is visualized with Cy5 secondary antibody and included in channel red of the Image J software to merge the final image 3E. Bar indicates 10 μm. J: From left to right: Molecular model of the interaction between the TGFβRI extracellular domain and Hsp90 dimer; Interaction of CTPR390–488 protein with the C-terminal end of Hsp90 domain; Hsp90 conformational change from the close to the open state upon CTPR390–488 interaction; disruption of the interaction between Hsp90 dimer (cyan and dark blue) and TGFβRI (orange). (For interpretation of the references to colour in this figure legend, the reader is referred to the web version of this article.)

its activation could be diminished by a reduction in TGFβRI effectiveness upon Hsp90 inhibition as it was shown for pulmonary fibrosis [28]. To show that CTPR390–488 indeed promoted inactivation of the TGFβ receptor complex, we transfected a constitutive active TGFβRI (TGFβRI-CA, kindly sent by Dr. Bartholin, TGFβ and Pancreatic Cancer – Lab Centre de Recherche en Cancérologie de LYON (CRCL)) and observed that CTPR390–488 was not able to influence pSmad2/3 or pErk expression (Fig. S2K, S2L, S2M).

#### 2.5. CTPR390-488-treated fibroblasts and fibroblasts from Hsp90aa1 KO mice showed significant reduction of collagen extracellular deposition

The differences among the ultrastructural features of myocardial primary fibroblasts from WT mice, CTPR390–488-treated WT mice and from Hsp90aa1 KO mice were analyzed using electron microscopy technique. Fig 5A and B shows engrossed endoplasmic reticulum because of activated WT fibroblasts synthesizing proteins. WT fibroblasts also exhibited abundant deposition of extracellular collagen fibers (Fig. 5B (1 μm) Fig. 5C (500 μm) pointed with arrows). CTPR390–488-treated fibroblasts showed much thinner endoplasmic reticulum and unstructured collagen fibers extracellularly deposited (Fig. 5D–5F). We did not find CTPR390–488 associated to any cellular organelle (Fig. S3). In the case of myocardial fibroblasts from Hsp90aa1 KO mice, more longitudinal shaped cells (Fig. 5G–5H) with thinner endoplasmic reticulum (Fig. 5I) and the absence of collagen deposition were observed.

#### 2.6. Cell motility is diminished in CTPR390–488-treated fibroblasts and fibroblasts from Hsp90aa1 KO mice

Type I collagen is the major protein component of fibrous connective tissues, and fibroblasts are the cell type primarily responsible for collagen biosynthesis. Cells interacting with collagen network form an arrangement through local matrix. This patterning allows the establishment of tracks for fibroblasts migration and colonization [29–31]. WT myocardial primary fibroblasts were tracked to observe their migration during 20 h after activation with TGFβ (0.3 ng/ml). The average path length per WT cell was  $273 \pm 24 \mu\text{m}$  (Fig 6A, G). When cells were treated with  $0.2 \mu\text{M}$  of CTPR390–488 the path length travelled decreased significantly ( $147 \pm 19 \mu\text{m}$ ,  $***p < .001$ ) (Fig 6C, G); similar to the Hsp90aa1 KO fibroblasts ( $143 \pm 9 \mu\text{m}$ ,  $***p < .001$ ) (Fig 6E, G). The collagen secreted to the extracellular media is the main component of the extracellular matrix and the extracellular matrix is the key biological system involved in the progression of disease [32]. The reduction in motility of the CTPR390–488-treated cells can be recovered to initial values culturing the cells on synthetic extracellular matrix (Matrigel) ( $241 \pm 10 \mu\text{m}$ ,  $***p < .001$ ) (Fig 6D, G). The Hsp90aa1 KO cells on Matrigel also exhibited a certain recovery in their motility but they did not reach the path length values of WT cells ( $182 \pm 24 \mu\text{m}$ ,  $*p < .05$ ) (Fig. 6F, G). The motility of WT control cells was unaltered on the synthetic matrix ( $242 \pm 20 \mu\text{m}$ ) (Fig. 6B, G). Fig. S4 shows the individual cell paths of each assay.



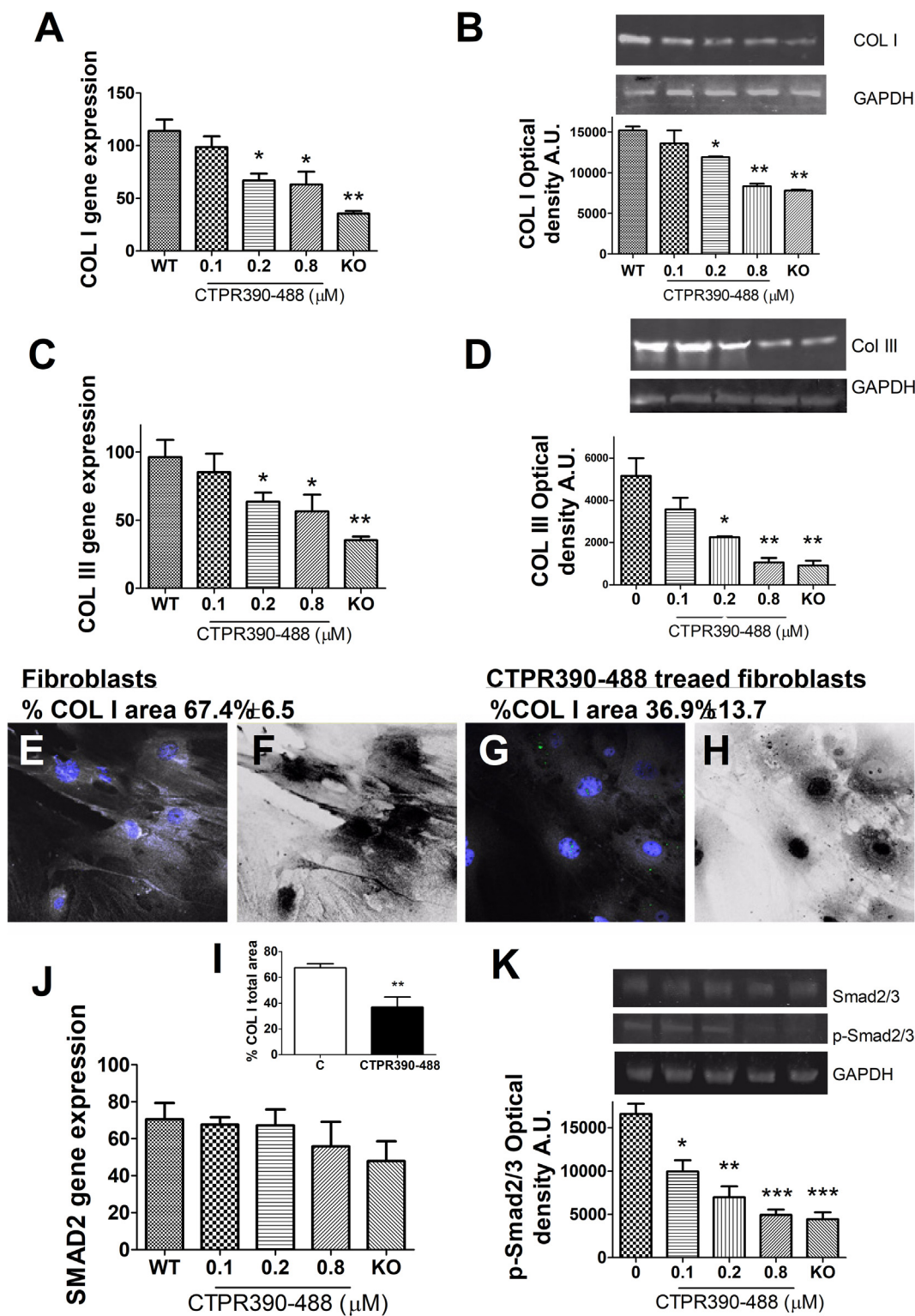


**Fig. 4.** Gene and protein expression of collagens and Smad2/3 from primary myocardial fibroblasts of WT mice (WT), Hsp90aa1 KO mice (KO) and WT with CTPR390-488. A, C, J: Gene expression of collagen I (COL I), collagen III (COL III) and Smad2 presented as relative expression versus 18S ribosomal RNA. B, D, K: Representative Western blots (WB) of COL I, COL III, Smad2/3 and p-Smad2/3 and densitograms of three independent experiments. GAPDH was used as loading control. E, G: Confocal microscopy showing the immunofluorescence detection of collagen I in TGFβ-treated (0.3 ng/ml) primary fibroblasts from WT mice (E), and WT + CTPR390-488-treated fibroblasts (G). Hoechst (blue) was used as a nuclear staining. Anti-rabbit secondary antibody conjugated with Cy5 detected COL I. F, H: Black and white images corresponding to E and G panels respectively. The calculated percentage of collagen I area was the sum of the values in square pixels of the collagen-detected correspondent to graphs F and H (I). The calculated area percentage of the selected pixels was given in calibrated units using ImageJ 1.52e software (Fig. 4I). Data were expressed as mean ± SD of optical density in arbitrary units (A.U.). (\**p* < .05, \*\**p* < .005, \*\*\**p* < .001; Mann–Whitney test). (For interpretation of the references to colour in this figure legend, the reader is referred to the web version of this article.)

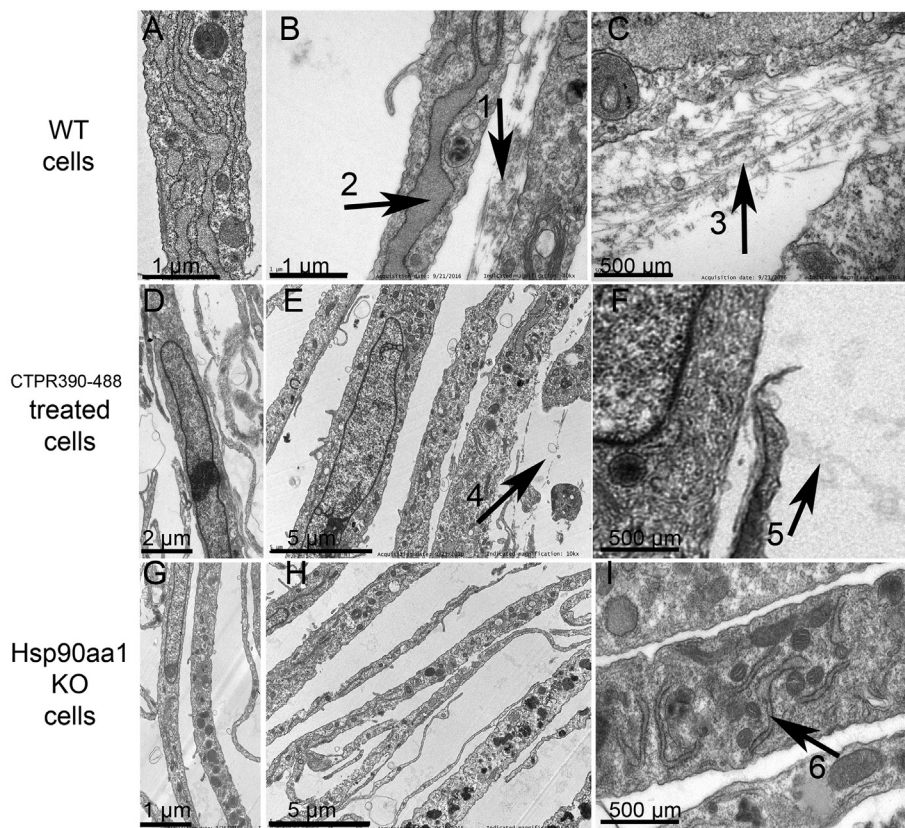


**Fig. 5.** Representative electron microscopy images of primary myocardial fibroblasts activated with TGF $\beta$  (0.3 ng/ml) from control WT mice, WT + CTPR390–488 treated mice and Hsp90aa1 KO mice. A, B: WT cells with engorged endoplasmic reticulum (ER) (a detail is marked with arrow 2 in panel B). B, C: WT cells with intercellular collagen deposition (arrows 1 panel B and arrow 3 panel C). D, E, F: CTPR390–488 treated WT cells showing normal ER and no structured collagens fibers (arrow 4 panel E, and arrow 5 panel F) and no signs collagen accumulation. G, H, I: cells from Hsp90aa1 KO mice showing thinner morphology, no active ER (arrow 6 panel I) and absence of collagen deposition.

### 2.7. In vivo administration of CTPR390–488 reduced myocardial fibrosis in Angiotensin II-treated mice

We administrated Ang II to promote the activation of the TGF $\beta$ -dependent pro-fibrotic process in the heart of WT and Hsp90 KO mice (see Fig. S5A to check in vivo experimental design). Myocardial Hsp90 chemical inhibition reduces TGF $\beta$  signaling cascade [10,33–35]. Mice received a constant infusion of Ang II (0.25  $\mu$ l per hour, 14 days); and one dose (1 mM) of CTPR390–488 was administrated intraperitoneally. The administration of CTPR390–488 did not alter mice behavior and no sign of discomfort was observed. We measured CTPR390–488 plasma concentrations at different time points for a duration of 2 weeks after its administration, (Fig. S5B–S5C). After 7 days of CTPR390–488 administration collagen I and III reached the lowest levels of gene expression (Fig. S5D–S5E). One week later, the presence of CTPR390–488 was not detected in plasma and the collagen expression increased (Fig. S5D–S5E). Thus, 7 days after CTPR390–488 injection and 14 days after Ang II minipump implantation was a good time-point to determine the effects on gene and protein expression.

TGF $\beta$  gene expression in WT + Ang II mice compared to Sham littermates was increased ( $458.2 \pm 39.4$  vs  $277.3 \pm 31.2$   $^{**}p < .005$ ). Furthermore, TGF $\beta$  gene expression in WT + Ang II mice treated with CTPR390–488 was also elevated, while Hsp90aa1 KO mice showed lower levels of TGF $\beta$  ( $^{**}p < .005$ ) (Fig. 7A). We also evaluated the activation of the canonical signaling mediator of TGF $\beta$ , Smad2/3, in heart samples from WT mice treated with Ang II, and we observed significant higher levels of protein phosphorylation compared to control mice ( $16,470.7 \pm 880.3$  vs  $5380.1 \pm 1238.5$  a.u.  $^{***}p < .001$ ) and a significant reduction when those mice were treated with CTPR390–488 ( $^{**}p < .005$ ) (Fig. 7B). In vivo, collagen I and III expression increased upon Ang II treatment ( $p < .05^*$ ) and they both were reduced in WT + Ang II + CTPR390–488 mice ( $p < .05^*$ ) compared to Ang II-treated mice (Fig 7C and D). The Hsp90aa1 KO mice did not exhibited changes in TGF $\beta$ , COL I, COL III gene expression nor

Smad2/3 phosphorylation with Ang II, or Ang II + CTPR390–488 treatment compared to Hsp90aa1 KO sham mice. TGF $\beta$  ( $^{**}p < .005$ ), COL I ( $^{**}p < .005$ ), COL III ( $^*p < .05$ ) gene expression and Smad2/3 phosphorylation ( $^*p < .05$ ) were significantly reduced in Hsp90 KO compared to WT + Ang II mice, (Fig. 7A–7D).

### 2.8. Systemic CTPR390–488 levels increased in Angiotensin II-treated mice

The endogenous fluorescence of CTPR390–488 allowed its detection in plasma. To obtain the calibration curve of the assay a serial dilution of CTPR390–488 (83.3; 41.7; 20.8; 10.4; 5.2 and 0  $\mu$ M) was added to plasma of WT mice, and the fluorescence signal obtained for each concentration was adjusted to a second order polynomial (quadratic) curve (Fig. 7E). We checked the CTPR390–488 signal at different time-points (1 h, 5 days, 7 days and 14 days) after CTPR390–488 administration to the different groups of mice in the study (see Fig. S5C); we also generated the calibration curve for each time point (Fig. S5B). Mice subjected to Ang II osmotic infusion for 14 days and CTPR390–488 treatment for 7 days were chosen for the in vivo measurements. The control groups without Ang II showed significant lower levels of CTPR390–488 compared to the Ang II counterparts ( $0.02 \mu\text{M} \pm 0.01$  vs  $0.80 \mu\text{M} \pm 0.10$ ,  $^{**}p < .005$ ;  $0.007 \mu\text{M} \pm 0.004$  vs  $0.05 \mu\text{M} \pm 0.01$ ,  $^{**}p < .005$ ) (Fig. 7F). In contrast, we observed that the CTPR390–488 plasma levels were higher in the WT + Ang II + CTPR390–488 group compared to KO + Ang II + CTPR390–488 ( $0.80 \mu\text{M} \pm 0.10$  vs  $0.02 \mu\text{M} \pm 0.01$ ,  $^{**}p < .005$ ) (Fig. 7F).

### 2.9. CTPR390–488 myocardial accumulation

The histological assessment (Fig. 8), showed that CTPR390–488 is accumulated at the left ventricle of WT + Ang II mice treated with CTPR390–488 (Fig. 8D) to a higher extent than their correspondent WT + CTPR390–488 control group (Fig. 8H) or KO + Ang II + CTPR390–488 mice (Fig. 8L) ( $10.5\% \pm 1.5$ ,  $1.3\% \pm 0.4$ ,



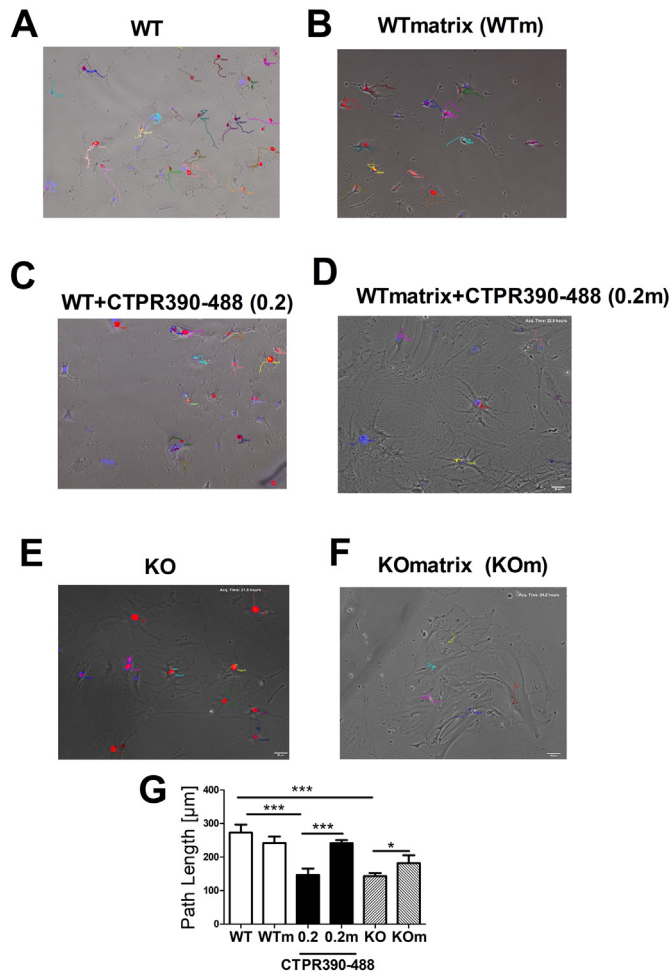


**Fig. 6.** Path length and cell tracking analysis of myocardial primary fibroblasts followed for 20 h. A, C, E: Representative cell tracks in different colors showing the motility of WT controls (A), WT + CTPR390–488 treated (0.2 µM) cells (C) and Hsp90aa1 KO cells respectively (E). Nuclei marked in red. B, D, F: Path length measurements of cells soaked in matrigel (m) (3 mg/ml) under the same conditions of A, C and E respectively. Nuclei marked in red. G: The path length data obtained from 15 to 32 different areas per assay in triplicate and in three independent experiments. (See S5 Fig for the analysis of the path length travelled (µm) versus time (h:min)). (\*p < .05, \*\*\*p < .001; Mann–Whitney test). (For interpretation of the references to colour in this figure legend, the reader is referred to the web version of this article.)

0.3% ± 0.2, \*\*\*p < .001 see measurements in Fig. S6A–S6D). We checked that both myofibroblasts took up CTPR390–488 in vivo as well as cardiomyocytes (Fig. S6E–S6F). WT + Ang II mice treated with CTPR390–488 presented reduced fibrosis compared to the non-treated mice (Fig. 8B compared to 8C). Fig. 8A showed the combinatory image of myocardial tissue section showing collagen fibers (blue) and the CTPR390–488 detection (green). In the WT + CTPR390–488 mice (Fig. 8E–8H) or the Hsp90aa1 KO + Ang II mice (Fig. 8I–8L) the fibrotic areas were barely detectable in both groups presenting similar appearance.

### 3. Discussion

The data presented here suggest that the blockade of Hsp90 with an engineered Hsp90 protein inhibitor (CTPR390–488) in myocardial fibroblasts effectively attenuated the canonical TGFβ signaling cascade. The consequences of this modulation promoted lower levels of collagen production and collagen deposition in vitro and in vivo.

We confirmed that the phosphorylation of Smad2/3 signaling

effector and the phosphorylation of the non-Smad TGFβ downstream signaling molecules (Akt and Erk) [36] was decreased in the presence of CTPR390–488, while their protein expression is not affected. The preserved folding activity and the unaltered protein expression of Hsp90 client proteins (Akt, Erk, Hsp70 and luciferase) indicated that Hsp90 inhibition by CTPR390–488 was affecting downstream effectors of TGFβRI without altering Hsp90 client proteins. TPR binding domain of the Hsp90 co-chaperones is crucial for the Hsp90 protein-protein interactions and functional complexes formation. CTPR390–488 is an engineered protein presenting an active Hsp90 TPR binding domain that can disrupt the TGFβRI–Hsp90 complex by mimicking the co-chaperone Hsp90-binding domain. Considering the interaction interface observed in the Hsp90–TGFβRI model the conformational change to the open state will disrupt the Hsp90 surface interaction in which the two monomers participate, thus destabilizing Hsp90–TGFβRI complex [7,10]. We hypothesized that CTPR390–488 binding promotes conformational change to open the close Hsp90 dimeric conformation and expulse TGFβRI (Fig. 3J). The crystal structure of the CTPR390–488 domain in complex with the Hsp90 peptide confirmed the mechanism of recognition, mimicking the natural TPR domains that bind the C-terminal sequence of Hsp90 [25]. The specificity of the interaction has been tested by biophysical characterization [15] and in cell culture [16]. The interaction of the extracellular domain of TGFβRI with Hsp90 homodimers occurs when Hsp90 is in a closed conformation [10]. The binding of TPR domain to the C-terminal end of Hsp90 has been shown to promote a conformational change of Hsp90 from the closed state to the open state [26]. Therefore, it is expected that the binding of CTPR390–488 protein to Hsp90 shift its conformational equilibrium toward the open state.

In our previous work [10], we demonstrated that both, Hsp90aa1 and Hsp90ab1 isoforms can be secreted into the extracellular medium and could be part of the Hsp90 dimer bound to TGFβRI. Moreover, CTPR390–488 does not distinguish between Hsp90 isoforms as shown by the reduction in collagens I and III in Hsp90aa1 KO and WT cells. We assume that it also acts on the inducible isoform Hsp90aa1 whose deletion also promotes lowering of TGFβ pro-fibrotic related signaling through phospho-Smad2/3, as well as collagen I and collagen III production. In any of these cases, Hsp90 lost its chaperon activity. The specific binding of CTPR390–488 to the C-terminal end of Hsp90 displayed binding affinity similar to the endogenous TPR domains and allowed the maintenance of the ATPase dependent Hsp90 chaperon activity.

Cardiac fibroblasts together with cardiomyocytes are the most prevalent cell types in the myocardium [37,38]. Under pathological conditions, cardiac fibroblasts proliferate and increase their motility. The remodeling process includes the colonization of new areas with increase of the total interstitial fibrosis, which in the long term enhances intrinsic myocardial stiffness and results in diastolic dysfunction [39]. The interstitial fibrosis is facilitated by the increased extracellular matrix deposition [36] reduced in Hsp90aa1 KO primary fibroblasts or in the cells treated with the CTPR390–488 protein. Both CTPR390–488 treated-primary fibroblasts and fibroblasts from Hsp90aa1 KO mice exhibited lowered cell motility compared to WT cells. The motility was recovered when cells were cultured on a collagen matrix surface. Thus, the CTPR390–488 protein, likely through its disruption of the Hsp90/TGFβRI complex, promotes a reduction of collagen accumulation in the extracellular matrix, which influences cell motility.

Persistent fibroblast activation is considered responsible for excessive extracellular matrix production and involves tight regulation of the main pro-fibrotic TGFβ signaling cascade. The deletion of Hsp90 affects cell response in myocardial remodeling [9]. Ultrastructural studies of CTPR390–488 treated-fibroblasts interestingly showed intercellular unstructured collagen fibers. We also observed thinner endoplasmic reticulum in the CTPR390–488 treated fibroblasts (as it is the case also for the Hsp90aa1 KO fibroblasts), while the WT fibroblasts presented engorged endoplasmic reticulum as it would be expected in

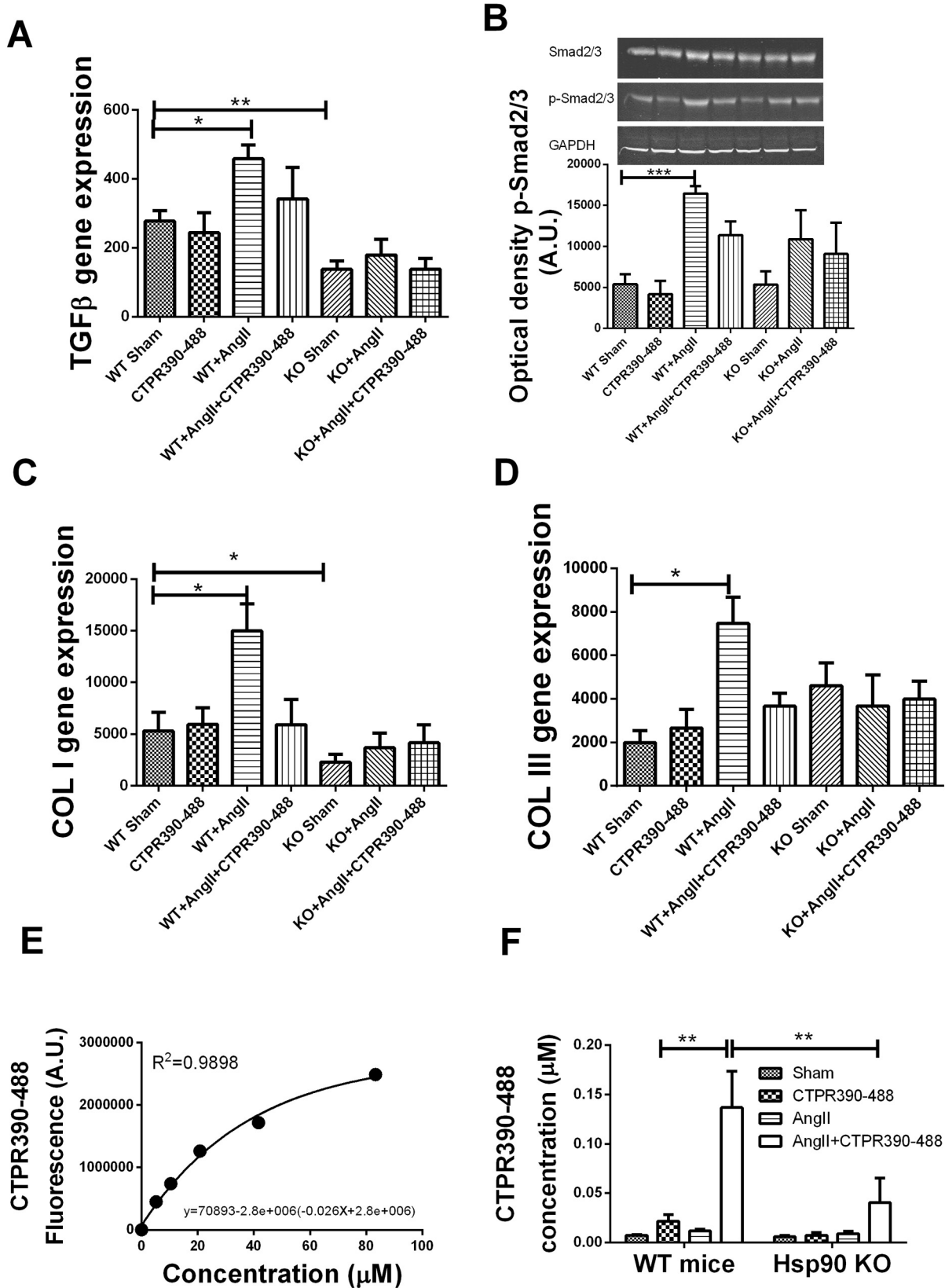
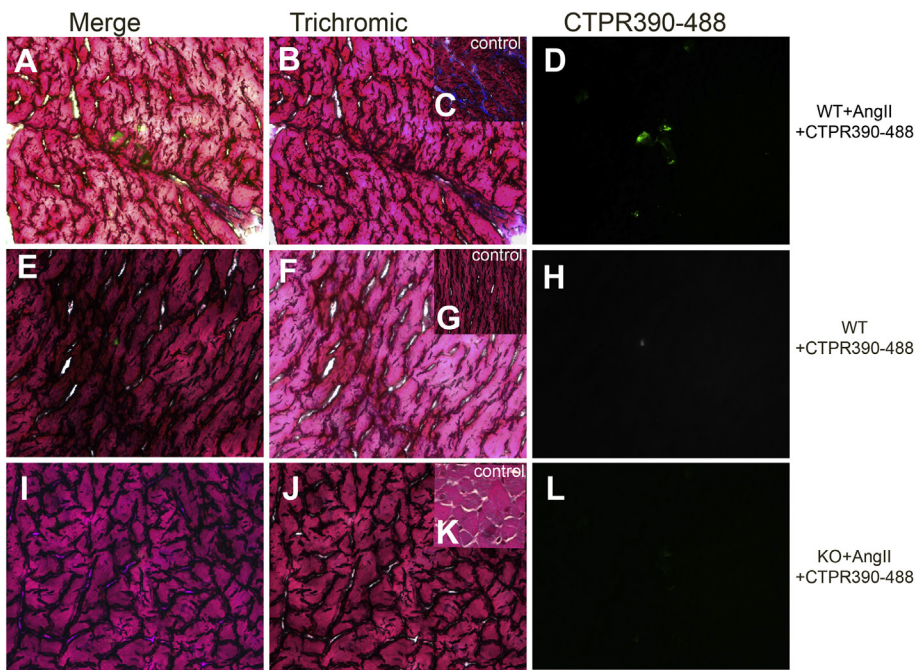


Fig. 7. Gene and protein expressions related to the pro-fibrotic process in the myocardium of WT and KO mice, treated with or without Ang II and CTPR390-488. The samples from left ventricle were extracted from the mice under study: WT, WT + CTPR390-488, WT + Ang II, WT + AngII+CTPR390-488, KO, KO + CTPR390-488, KO + Ang II, KO + AngII + CTPR390-488. (n = 4 per group). A, B, C, D: These panels showed TGFβ gene expression (A), Smad2/3, p-Smad2/3 protein expression and p-Smad2/3 quantification (in arbitrary units A.U.) (B), COL I gene expression (C), and COL III gene expression (D). E: Graph showing the fluorescent signal of CTPR390-488 titration in plasma. F: Graph showing the plasma concentration of CTPR390-488 in the groups of mice under study, n = 4 per group. (\*p < .05, \*\*\*p < .001; Mann-Whitney test).



**Fig. 8.** Representative histological fibrosis of left ventricles transversal sections of Ang II + CTPR390–488 WT mice, CTPR390–488 treated WT mice, and Ang II + CTPR390–488 Hsp90aa1 KO mice. A, E, I: merge of Masson's trichrome staining and confocal images showing accumulation of collagen in blue and detection of CTPR390–488 in green. B, C, F, G, J, K: Collagen staining in blue by Masson's trichrome. D, H, L: Confocal microscopy showing CTPR390–488 in green. C, G and K are the correspondent controls of B, F, and J in the absence of CTPR390–488. (For interpretation of the references to colour in this figure legend, the reader is referred to the web version of this article.)

TGF $\beta$ -activated fibroblasts synthesizing collagens.

The rapid advances in understanding the pathophysiology of fibrosis have generated intense interest in developing effective anti-fibrotic therapies for patients with chronic myocardial diseases. With no agents yet approved for this indication, considerable efforts are being invested in developing therapies and novel markers for myocardial fibrosis. These studies using an engineered protein inhibitor, CTPR390–488, is proof of concept to focus our scientific efforts by exploiting the Hsp90 biology. The ability of fluorescently tracking the protein is of special interest in the field of the biomedical use but most importantly is the lack of toxicity when it is internalized by human ductal breast cancer cells [16] or myocardial fibroblasts as we showed herein.

We investigated the *in vivo* reduction of myocardial fibrosis with the use of the CTPR390–488 protein in WT and Hsp90aa1 KO mice subject to angiotensin II (Ang II) infusion. The systemic administration of Ang II induces cardiac fibroblasts activation including the production and release of the pro-fibrotic cytokine TGF $\beta$  [40,41]. TGF $\beta$  expression is induced by angiotensin II in kidney, vascular smooth muscle cells, and in cardiac fibroblasts [35]. We utilized the Ang II fibrotic mouse model since angiotensin II receptor blockade were mainly attributed to a reduction in extracellular protein accumulation, most likely mediated through inhibition of TGF $\beta$  and its downstream signals [42]. Blockade of the Ang II-TGF $\beta$  signaling pathway has consistently been demonstrated to be effective for the prevention of cardiac fibrosis in experimental animals [43–45]. In this study, we show reduction in the accumulation of collagen in the heart of the Ang II treated-mice upon the CTPR390–488 peptide administration or by Hsp90aa1 deletion. This observation suggests that a role of Hsp90 in this fibrotic process and that the inhibition of its TPR binding domain (linked to TGF $\beta$ RI) is enough to diminish collagen deposition, collagen expression and TGF $\beta$  signaling cascade activation.

Moreover, the higher presence of CTPR390–488 protein in the left ventricle and plasma of fibrotic mice compared to control mice indicated its accumulation in fibrotic areas. These observations open the possibility of studying the CTP390–488 protein as a new anti-fibrotic therapy that could also be utilized as a biomarker of the disease. The inhibition of Hsp90 with small molecules produces important side effects in the clinic due to the ATPase activity annulment [46]. We presented here a trackable and potentially safe biomolecule, CTPR390–488, as the first *in vivo* myocardial anti-fibrotic bio-therapy.

#### 4. Conclusions

Hsp90 inhibition is reached using an engineered protein CTPR390–488, this inhibition likely affects the Hsp90-TGF $\beta$ RI interaction and it promoted the reduction of key myocardial pro-fibrotic events both *in vitro* and *in vivo*. We give an insight into the mechanism of action that would support the hypothesis of Hsp90 and TGF $\beta$ RI partnership regarding the myocardial fibrotic process. Hsp90 inhibition implies TGF $\beta$  signaling deregulation and collagen synthesis reduction. Preservation of Hsp90 folding activity by inhibiting the chaperon with CTPR390–488 offers a new way of targeting left ventricle remodeling without damaging cell homeostasis.

#### 5. Materials and methods

##### 5.1. Protein expression and purification

CTPR390-Cys protein was produced by the introduction of a single C-terminal cysteine in CTPR390 [15] by quick change mutagenesis. CTPR390-cys was expressed as previously described [15,47]. Briefly, CTPR390-Cys gene cloned in pProEx-HTA vector, coding for N-terminal (His)6 tag and ampicillin resistance, was transformed into *Escherichia coli* C41 (DE3). Overnight bacteria culture in 50 ml of Luria–Bertani (LB) media containing 100  $\mu\text{g ml}^{-1}$  of ampicillin was grown to saturation. 10 ml of the saturated culture were diluted into 1 l of LB media supplemented with 100  $\mu\text{g ml}^{-1}$  ampicillin. The cells were grown in an incubator-shaker (250 rpm) at 37  $^{\circ}\text{C}$  to an optical density ( $\text{OD}_{600}$ ) of 0.6–0.8. Expression of CTPR390 was induced with 0.6 mM isopropyl  $\beta$ -D-thiogalactoside (IPTG) followed by 5 h expression at 37  $^{\circ}\text{C}$ . The cells were harvested by centrifugation at 5000 rpm for 20 min. The cell pellets were resuspended in lysis buffer consisting of 300 mM sodium chloride, 50 mM Tris pH 8.0. After 2 min sonication at 30% power using a microtip and Mison sonicator, lysed cells were centrifuged at 16000 rpm for 30 min and the protein supernatant was purified using standard Ni-NTA affinity purification protocol. The N-terminal hexahistidine tag was then cleaved using TEV protease. As a final step, the CTPR390-Cys was dialyzed against 150 mM NaCl, 50 mM phosphate buffer pH 7.4. Protein concentration was measured by UV absorbance at 280 nm, using extinction coefficients at 280 nm calculated from amino acid composition.



## 5.2. Ligand binding experiments

CTPR390-Cys protein binding affinity to Hsp90 C-terminal peptide was determined by fluorescence anisotropy titrating with increasing amounts of protein into a 50 nM fluorescein-labeled Hsp90 peptide solution [47–49]. Fluorescence anisotropy was recorded exciting at 492 nm with a 5 nm slit width and recording the emission at 516 nm with slit widths of 5 nm. G-factor corrections to account the difference in transmission efficiencies of the two emission channels were applied to calculate anisotropy using PBS buffer as blank solution and a 50 nM fluorescein as a standard solution. Anisotropy values are automatically calculated. The fraction of peptide bound at each point in the binding curve was calculated by the Eq. [15]:

$$\%Bound = \frac{r - r_f}{r_b - r_f}$$

where  $r$  is the observed anisotropy of the peptide at any protein concentration,  $r_f$  is the anisotropy of the free peptide and  $r_b$  is the anisotropy of the peptide bound to the protein in the plateau region of the binding curve. The percentage of peptide bound is plotted versus the protein concentration. The data were fit to a 1:1 binding model using Origin to calculate the dissociation constant.

## 5.3. CTPR390 labeling with Alexa 488 to obtain CTPR390–488

CTPR390-Cys protein was labeled with the cysteine-reactive maleimide form of Alexa Fluor 488 (Molecular Probes, Inc.) dye through the cysteine at the C-terminal following previously described protocols [24]. Briefly, CTPR390-Cys protein at 100  $\mu$ M concentration was reduced by incubation with 10 mM 1,4-dithio-DL-treitol (DTT) for 15 min. DTT was removed by gel filtration over a PD-10 column against 150 mM NaCl and 50 mM phosphate (pH 7.0). A solution of Alexa Fluor 488 maleimide in water was added dropwise into the freshly reduced protein in the presence of 1 mM tris(2-carboxyethyl)phosphine to a final 1:5 protein:dye molar ratio. The reactions were allowed to proceed for 4 h at room temperature under a non-reducing atmosphere of  $N_2$  in the dark. The free dye was removed from the reaction mixtures by two consecutive buffer exchange steps over PD-10 columns, followed by concentration and extensive washing using Amicon ultrafiltration tubes with a MWCO of 10-kDa. The extent of labeling was calculated from the absorption spectra of the conjugate and using the extinction coefficient for Alexa Fluor 488  $\epsilon_{493} = 72,000 \text{ M}^{-1} \text{ cm}^{-1}$  and the protein extinction coefficient at 280 nm calculated from the amino acid composition.

## 5.4. Cultured primary cardiac fibroblasts

Adult cardiac fibroblasts from mice C57BL6 strain (wild type) and the transgenic Hsp90aa1 KO were originally isolated directly from enzymatically digested hearts (collagenase, trypsin and DNase) followed by centrifugation and filtration. They were maintained in Dulbecco's Modified Eagle's Medium (DMEM) containing 10% FBS, 10% DBS and 100 U/ml penicillin-streptomycin. The cells ( $2 \times 10^5$ ) were plated in 35 mm tissue culture dishes and, 4 h later, recombinant TGF $\beta$ 1 (0.3 ng/ml) (R&D Systems) was added with or without CTPR390–488 (0.2  $\mu$ M) 24 h later cells were lysed and stored at  $-80^\circ\text{C}$ . Results included triplicate of three independent assays. Vimentin marked for positive fibroblasts. For experimental procedures, low passage cells (p2) were seeded onto 35 mm cell culture dishes and incubated at  $37^\circ\text{C}$  in 5%  $\text{CO}_2$  for 15–20 h.

## 5.5. Fluorescence and immunofluorescence assays

The immunofluorescence assays of Hsp90 were performed using TGF $\beta$ -treated (0.3 ng/ml for 24 h) primary myocardial fibroblasts and adding 0.2–0.8  $\mu$ M of CTPR390–488. Paraformaldehyde fixed cells were incubated with mouse primary antibody against Hsp90 (Abcam). We

utilized anti-mouse secondary antibody conjugated with Cy3 to detect Hsp90, (Jackson ImmunoResearch, USA). CTPR390–488 was detected with FITC filters and PureBlu Hoechst 33342 (Bio-Rad) was used as nuclear staining dye. LSM-510 laser scanning microscope (Carl Zeiss Inc., Germany) was utilized for these experiments using an objective Plan Apo VC 60  $\times$  Oil DIC N2.

## 5.6. Cell viability assay

Cell viability was assessed in TGF $\beta$ -treated cells (0.3 ng/ml for 24 h) in the presence or absence of CTPR390–488. Cells samples were diluted in DMEM medium, PBS 1  $\times$ , pH 7.4 and 0.4% trypan blue solution (Gibco®-Life technologies) and viability measured by the utilizing Countess®Automated Cell Counter and following the manufacturer's protocol (Countess®Automated, Invitrogen).

## 5.7. Absorption and fluorescence spectroscopy

The absorbance of the CTPR390–488 treated cells was measured at 488 nm with a NanoDrop instrument (Thermo Scientific) including a calibration curve (3.0, 1.5, 0.8, 0.4, 0.2, 0.1 and 0  $\mu$ M of CTPR390–488).

Fluorescence measurements of CTPR390–488 signal were performed with 96 well black/clear plates in a Berthold Mithras LB 940 spectrofluorometer. The excitation/emission wavelengths were 485/535 nm. Fluorescence was measured from primary cell lysates and plasma samples containing CTPR390–488.

## 5.8. Functional refolding assay

To determine Hsp90 chaperone activity we measured the ability of Hsp90 to refold denatured luciferase, which will ultimately catalyze the luciferin reaction. The luciferase renaturation assay was performed in 96-well clear bottom plates containing 25  $\mu$ g of protein lysate from TGF $\beta$ -treated (0.3 ng/ml for 24 h) cells isolated from the left ventricle mice. The refolding reaction was initiated by the addition of the denatured luciferase (1.5  $\mu$ g/ml, denatured at  $46^\circ\text{C}$  for 10 min, in presence of TGF $\beta$  (0.3 ng/ml) to the lysate containing Hsp90 or Hsp90 + CTPR390–488. Once luciferase is renatured after 2 h incubation at room temperature, it will catalyze the luminescent reaction with luciferin. The luciferase activity was measured by addition of Luciferase Assay Reagent (E1501, Promega). The source of Hsp90 was WT primary myocardial fibroblasts and primary myocardial fibroblasts of Hsp90aa1 KO mice. The negative control utilized corresponded to the substrate (heat-denatured luciferase) in the absence of Hsp90 and the positive control corresponded to rabbit reticulocyte lysate (RRL) with high content of Hsp90. Light emission from each micro well was recorded with a 1 s integration time using a Berthold Centro LB 960 plate reader 3 min after addition of the luminescent reagent. Results included triplicate of three independent assays. Buffers and reagents were previously described more in detail by Eachkoti et al. [50].

## 5.9. Determination of mRNA expressions by Q-PCR

Total mRNA from cells and tissue samples were assayed by Q-PCR; Cell samples were cultured with recombinant TGF $\beta$ 1 (0.3 ng/ml) with CTPR390–488 and TGF $\beta$  for 24 h were obtained by TRIzol extraction (Invitrogen). The mRNA was reverse transcribed using random primers. The quantitative PCR (Q-PCR) were performed with specific TaqMan primers: Hsp90aa1, Hsp90ab1, COL I, COL III, TGF $\beta$ 1, Smad2 and  $\alpha$ SMA. The housekeeping gene was 18S in all cases. The values represented the average of three independent experiments.

## 5.10. Protein detection by Western Blot

Protein expression was detected by Western blot analysis and

densitogram quantification. Tissue samples were disrupted and lysated. Cell samples were treated with recombinant TGF $\beta$ 1 (0.3 ng/ml) (Abcam) for 24 h collected, the lysate was resolved on 10% sodium dodecyl sulfate-polyacrylamide (SDS-PAGE) gel and transferred onto polyvinylidene difluoride (PVDF) membranes (Bio-Rad Lab., California, USA). The primary antibodies used were: polyclonal anti Smad2/3 and p-Smad2/3 (Santa Cruz); polyclonal anti GAPDH (Santa Cruz); and polyclonal anti COL I and COL III (Santa Cruz), monoclonal Hsp90 (Abcam). Secondary antibodies conjugated with IRDye 800CW and IRDye 680RD were used for immunodetection. CTPR390–488 protein detection was performed using anti-CTPR390 rabbit antibody purified from the serum from a rabbit immunized with CTPR390 (Unidad de Ensayos Biotecnológicos y Biomédicos, Servicios Científico Técnicos, Universidad de Oviedo).

### 5.11. Transmission electronic microscopy

Wild type, CTPR390–488 treated, and Hsp90aa1 KO primary cardiac fibroblasts were examined for conventional ultrastructural analysis. Cells were rinsed in 0.1 M phosphate buffer, fixed in 2% osmium tetroxide, dehydrated in acetone, and embedded in araldite (Durcupan, Fluka, Switzerland). For immunogold electron microscopy, myocardial primary fibroblasts were fixed with 4% paraformaldehyde in 0.1 M cacodylate buffer for 30 min at room temperature. Cells were scraped from the dishes, transferred to an Eppendorf tube, and centrifuged for 1 min in a microfuge to obtain cell pellets. The pellets were washed with 0.1 M cacodylate buffer, dehydrated in increasing concentrations of methanol at  $-20^{\circ}\text{C}$ , embedded in Lowicryl K4M at  $-20^{\circ}\text{C}$ , and polymerized with ultraviolet irradiation. Ultrathin sections were mounted on nickel grids and sequentially incubated with 0.1 M glycine in PBS for 15 min, 5% BSA in PBS for 1 h, and the rabbit polyclonal anti-CTPR390–488 antibody diluted 1:50 in PBS containing 1% BSA and 0.1 M glycine for 1 h. After washing, the sections were incubated with goat anti-rabbit IgG coupled to 15 nm gold particles (diluted 1:50 in PBS containing 1% BSA; BioCell, UK). After immunogold labeling. All grids were stained with lead citrate and uranyl acetate and examined with an 80KV electron microscope with Camara Orius SC 100 CCD and Software Gatan. For control, ultrathin sections were treated as described above, but without the primary antibody.

### 5.12. Cell tracking

Cell track assays were conducted with or without matrigel (3 mg/ml) and activated with TGF $\beta$  (0.3 ng/ml). Images were captured overnight every 10 min following cell nuclei (marked with NucBlue Live ReadyProbes Reagent). The distance travelled by cells was obtained by quantification of segmented nuclei. The measurements of the distance travelled by the fibroblasts for 20 h were done on cells plated on tissue culture plates with or without matrigel (3 mg/ml) (Sigma-Aldrich) and activated with TGF $\beta$ 1 (0.3 ng/ml). The data were obtained from 15 to 32 different areas per assay in triplicate and in three independent experiments. Cell track was captured with an epifluorescence microscope Nikon Ti, objective 10 $\times$  plan fluor 0.30 NA. Phase contrast / DAPI (387/25 exc-440/25 emis)/ FITC (485/20 exc-521/25 emis). The camera installed was Hamamatsu ORCA R2 and the Software Nis elements with the cell-tracking module was utilized. 0.2  $\mu\text{g}/\text{ml}$  of CTPR390–488 was utilized in three independent experiments.

### 5.13. Simulations of protein-protein interactions

In silico prediction of the interaction between the Hsp90 dimer in close conformation (PDB ID: 2CG9) and the extracellular domain of TGF $\beta$ RI PDB: 3KFD was described previously [10]. The CTPR390 structure was previously solved in complex with the C-terminal peptide of Hsp90 (PDB ID: 3KD7) [25]. In order to model the ternary complexes including Hsp90-TGF $\beta$ RI-CTPR390 proteins the flexible C-terminal

region of Hsp90 proteins that is recognized by the TPR domain and does not appear in the crystal structure was modeled using UCSF Chimera interface with MODELLER [49].

### 5.14. Animal studies

Adult (16–20 weeks old) C57BL6 wild type (WT) mice or Hsp90aa1 KO mice were housed in a 22  $^{\circ}\text{C}$  room with 12:12 h light/dark cycle and provided with food and water ad libitum. Mice were divided into 7 groups of  $n = 4$  mice per group: WT, WT + CTPR390–488, WT + Ang II, WT + Ang II + CTPR390–488, Hsp90aa1 KO, Hsp90aa1 KO + Ang II and Hsp90aa1 KO + Ang II + CTPR390–488. Live animals' studies were approved by the University of Cantabria Institutional Laboratory Animal Care and Use Committee in compliance with the Guide for the Care and Use of Laboratory Animals (ILAR, 1985) and were conducted in accordance with the “European Directive for the Protection of Vertebrate Animals Used for Experimental and Other Scientific Purposes” (European Communities Council Directive 86/606/EEC).

### 5.15. Mice handling

In vivo experimental design is shown in Fig. S5A. The experimental time points indicated Ang II time of implantation, CTPR390–488 time of injection and samples collection time-points. Mice were placed on preheated pad set to prevent hypothermia and were anesthetized by inhaled isoflurane in oxygen/nitrous oxide mixtures at 2.0%. Under this anesthesia conditions we performed the following actions:

#### 5.15.1. Subcutaneous implantation of osmotic minipumps

A mid-scapular incision is made, and a subcutaneous pocket is created for the micro-osmotic pump (0.25  $\mu\text{l}$  per hour, 14 days, alzet) to be inserted. The pump was previously filled with an aqueous solution of angiotensin II (0.70 mg). The wound was closed with a suture. Mice were monitored daily for any discomfort and they were euthanized 2 weeks after surgery.

#### 5.15.2. CTPR390–488 intraperitoneal administration

CTPR390–488 (200  $\mu\text{l}$  of 1 mM) intraperitoneal (IP) administration. For the CTPR390–488 intraperitoneal administration mice were anesthetized by 1.0–2.0% inhaled isoflurane in oxygen/nitrous oxide mixtures for 1 min and injected 200  $\mu\text{l}$  of 1 mM of CTPR390–488. Mice did not present any sign of discomfort.

#### 5.15.3. Plasma extraction

Retro-orbital blood collection in mice was performed with animals fully anesthetized. Within 5 min of blood collection plasma was separated by centrifugation at 1000  $\times g$  and store at  $-20^{\circ}\text{C}$  for posterior use.

### 5.16. Histological assessment of myocardial fibrosis and CTPR390–488 detection

The hearts from the mice under study described in the section “animal studies” were isolated and fresh frozen after incubation in sucrose 30% for 24 h. The degree of fibrosis was detected in 6  $\mu\text{m}$  sections stained with Masson's trichrome assay. After trichromic staining, bright field images were acquired on an upright fluorescence microscope (Eclipse 80i, Nikon) using a 20  $\times$  0.5 NA or 40  $\times$  0.57 NA objective, a DS-Ri1 colour camera (1280  $\times$  1024 pixels; 0.46  $\mu\text{m}$  & 0.23  $\mu\text{m}$  pixel size). Next, wide field-fluorescence images of the same fields were acquired using excitation (472/30 nm) and emission (520/35) filters. Finally, to reconstitute a RGB colour image we added the green channel from the corresponding fluorescence image to the green channel of the trichrome staining image. The merged images of fluorescence and trichromic staining were obtained with ImageJ after splitting the trichromic RBG colour images in 8bits individual channels (R: red, G:

green, B: blue).

### 5.17. Statistics and graphics program

The data sets were assessed for normality using the Kolmogorov–Smirnov test. Continuous variables were compared using two-tailed Student's *t*-test or Mann–Whitney *U* test. GraphPad Prism 5.03 was utilized as the statistical package and graphics program.

Supplementary data to this article can be found online at <https://doi.org/10.1016/j.yjmcc.2018.08.016>.

### Acknowledgments

We thank Dr. Miguel Lafarga and Dr. Victor Campa for their valuable help.

### Funding sources

This work was supported by the Spanish Ministerio de Economía, Industria y Competitividad [BIO2015-72124-EXP] and [BIO2016-77367-R], and the European Research CouncilERC-2014-CoG-648071-ProNANO. The Instituto de Formación e Investigación Marqués de Valdecilla IDIVAL [InnVal 15/31] and [InnVal 17/22], and the FEDER European Union, SODERCAN “Proyecto Puente 2017”.


### Disclosures

None declared.

### References

- X.H. Feng, R. Derynck, Specificity and versatility in *tgf*-beta signaling through Smads, *Annu. Rev. Cell Dev. Biol.* 21 (2005) 659–693.
- J. La, et al., Downregulation of TGF-beta Receptor-2 Expression and Signaling through Inhibition of Na/K-ATPase, *PLoS One* (2016) 11(12).
- M.M. Villarreal, et al., Binding Properties of the Transforming Growth Factor-beta Coreceptor Betaglycan: Proposed Mechanism for Potentiation of Receptor complex Assembly and Signaling, *Biochemistry* 55 (49) (2016) 6880–6896.
- H. Noh, et al., Heat shock protein 90 inhibitor attenuates renal fibrosis through degradation of transforming growth factor-beta type II receptor, *Lab. Investig.* 92 (11) (2012) 1583–1596.
- A.K. Reka, et al., Identifying inhibitors of epithelial-mesenchymal transition by connectivity map-based systems approach, *J. Thorac. Oncol.* 6 (11) (2011) 1784–1792.
- M. Tomcik, et al., Heat shock protein 90 (Hsp90) inhibition targets canonical TGF-beta signalling to prevent fibrosis, *Ann. Rheum. Dis.* 73 (6) (2014) 1215–1222.
- R. Datta, et al., Hsp90/Cdc37 assembly modulates TGFbeta receptor-II to act as a profibrotic regulator of TGFbeta signaling during cardiac hypertrophy, *Cell. Signal.* 27 (12) (2015) 2410–2424.
- S.J. Myung, et al., Heat shock protein 90 inhibitor induces apoptosis and attenuates activation of hepatic stellate cells, *J. Pharmacol. Exp. Ther.* 330 (1) (2009) 276–282.
- R. Datta, et al., Myocyte-Derived Hsp90 Modulates Collagen Upregulation via Biphasic Activation of STAT-3 in Fibroblasts during Cardiac Hypertrophy, *Mol. Cell Biol.* 37 (6) (2017) 00611–00616.
- R. Garcia, et al., Extracellular heat shock protein 90 binding to TGFbeta receptor I participates in TGFbeta-mediated collagen production in myocardial fibroblasts, *Cell. Signal.* 28 (10) (2016) 1563–1579.
- C. Vancheri, et al., Idiopathic pulmonary fibrosis: a disease with similarities and links to cancer biology, *Eur Respir J.* 35 (3) (2010) 496–504, <https://doi.org/10.1183/09031936.00077309> Mar.
- Y.L. Boersma, A. Pluckthun, DARPins and other repeat protein scaffolds: advances in engineering and applications, *Curr. Opin. Biotechnol.* 22 (6) (2011) 849–857.
- A. Pluckthun, Designed ankyrin repeat proteins (DARPins): binding proteins for research, diagnostics, and therapy, *Annu. Rev. Pharmacol. Toxicol.* 55 (2015) 489–511.
- L. Regan, M.R. Hinrichsen, C. Oi, Protein engineering strategies with potential applications for altering clinically relevant cellular pathways at the protein level, *Expert Rev. Proteomics* 13 (5) (2016) 481–493.
- A.L. Cortajarena, et al., Protein design to understand peptide ligand recognition by tetratricopeptide repeat proteins, *Protein Eng Des Sel* 17 (4) (2004) 399–409.
- A.L. Cortajarena, F. Yi, L. Regan, Designed TPR modules as novel anticancer agents, *ACS Chem. Biol.* 3 (3) (2008) 161–166.
- A.L. Cortajarena, S.G. Mochrie, L. Regan, Modulating repeat protein stability: the effect of individual helix stability on the collective behavior of the ensemble, *Protein Sci.* 20 (6) (2011) 1042–1047.
- A.L. Cortajarena, et al., Designed proteins to modulate cellular networks, *ACS Chem. Biol.* 5 (6) (2010) 545–552.
- M.E. Jackrel, et al., Screening libraries to identify proteins with desired binding activities using a split-GFP reassembly assay, *ACS Chem. Biol.* 5 (6) (2010) 553–562.
- D. Bai, et al., Cytoplasmic translocation of HuR contributes to angiotensin II induced cardiac fibrosis, *Biochem. Biophys. Res. Commun.* 463 (4) (2015) 1273–1277.
- Y. Sun, et al., Angiotensin II, transforming growth factor-beta1 and repair in the infarcted heart, *J. Mol. Cell. Cardiol.* 30 (8) (1998) 1559–1569.
- K.T. Weber, Extracellular matrix remodeling in heart failure: a role for de novo angiotensin II generation, *Circulation* 96 (11) (1997) 4065–4082.
- Y. Zhang, et al., Overexpressed connective tissue growth factor in cardiomyocytes attenuates left ventricular remodeling induced by angiotensin II perfusion, *Clin. Exp. Hypertens.* 39 (2) (2017) 168–174.
- A.L. Cortajarena, et al., Non-random-coil behavior as a consequence of extensive PPII structure in the denatured state, *J. Mol. Biol.* 382 (1) (2008) 203–212.
- A.L. Cortajarena, J. Wang, L. Regan, Crystal structure of a designed tetratricopeptide repeat module in complex with its peptide ligand, *FEBS J.* 277 (4) (2010) 1058–1066.
- J. Li, J. Soroka, J. Buchner, The Hsp90 chaperone machinery: conformational dynamics and regulation by co-chaperones, *Biochim. Biophys. Acta* 3 (2012) 624–635.
- K.H. Wrighton, X. Lin, X.H. Feng, Critical regulation of TGFbeta signaling by Hsp90, *Proc. Natl. Acad. Sci. U. S. A.* 105 (27) (2008) 9244–9249.
- H. Dong, et al., Blockade of extracellular heat shock protein 90alpha by 1G6-D7 attenuates pulmonary fibrosis through inhibiting ERK signaling, *Am J Physiol Lung Cell Mol Physiol* 313 (6) (2017) L1006–L1015.
- P. Friedl, et al., Migration of highly aggressive MV3 melanoma cells in 3-dimensional collagen lattices results in local matrix reorganization and shedding of alpha2 and beta1 integrins and CD44, *Cancer Res.* 57 (10) (1997) 2061–2070.
- P.P. Provenzano, et al., Collagen reorganization at the tumor-stromal interface facilitates local invasion, *BMC Med.* 4 (1) (2006) 38.
- R.T. Tranquillo, Self-organization of tissue-equivalents: the nature and role of contact guidance, *Biochem. Soc. Symp.* 65 (1999) 27–42.
- T. Ishimoto, et al., Activation of Transforming Growth factor Beta 1 Signaling in Gastric Cancer-associated Fibroblasts increases their Motility, via Expression of Rhomboid 5 Homolog 2, and Ability to Induce Invasiveness of Gastric Cancer Cells, *Gastroenterology* 5 (17) (2017) (35398–2).
- J.A. de la Mare, T. Jurgens, A.L. Edkins, Extracellular Hsp90 and TGFbeta regulate adhesion, migration and anchorage independent growth in a paired colon cancer cell line model, *BMC Cancer* 17 (1) (2017) 017–3190.
- Z. Sibinska, et al., Amplified canonical transforming growth factor-beta signalling via heat shock protein 90 in pulmonary fibrosis, *Eur. Respir. J.* 49 (2) (2017) 01941–02015.
- S.B. Lee, et al., Modulation of heat shock protein 90 affects TGF-beta-induced collagen synthesis in human dermal fibroblast cells, *Tissue Cell* 48 (6) (2016) 616–623.
- C. Bonnans, J. Chou, Z. Werb, Remodelling the extracellular matrix in development and disease, *Nat Rev Mol Cell Biol* 15 (12) (2014) 786–801.
- P. Camelliti, T.K. Borg, P. Kohl, Structural and functional characterisation of cardiac fibroblasts, *Cardiovasc. Res.* 65 (1) (2005) 40–51.
- I. Banerjee, et al., Determination of cell types and numbers during cardiac development in the neonatal and adult rat and mouse, *Am. J. Physiol. Heart Circ. Physiol.* 293 (3) (2007) 29.
- J. Diez, et al., Clinical aspects of hypertensive myocardial fibrosis, *Curr. Opin. Cardiol.* 16 (6) (2001) 328–335.
- I. Manabe, T. Shindo, R. Nagai, Gene expression in fibroblasts and fibrosis: involvement in cardiac hypertrophy, *Circ. Res.* 91 (12) (2002) 1103–1113.
- S. Rosenkranz, TGF-beta1 and angiotensin networking in cardiac remodeling, *Cardiovasc. Res.* 63 (3) (2004) 423–432.
- A.E. El-Agroudy, et al., Effect of donor/recipient body weight mismatch on patient and graft outcome in living-donor kidney transplantation, *Am J Nephrol* 23 (5) (2003) 294–299.
- D.S. Lim, et al., Angiotensin II blockade reverses myocardial fibrosis in a transgenic mouse model of human hypertrophic cardiomyopathy, *Circulation* 103 (6) (2001) 789–791.
- C.M. Yu, et al., Effects of combination of angiotensin-converting enzyme inhibitor and angiotensin receptor antagonist on inflammatory cellular infiltration and myocardial interstitial fibrosis after acute myocardial infarction, *J. Am. Coll. Cardiol.* 38 (4) (2001) 1207–1215.
- P. Teekakirikul, et al., Cardiac fibrosis in mice with hypertrophic cardiomyopathy is mediated by non-myocyte proliferation and requires Tgf-beta, *J. Clin. Invest.* 120 (10) (2010) 3520–3529.
- D.S. Hong, et al., Targeting the molecular chaperone heat shock protein 90 (HSP90): lessons learned and future directions, *Cancer Treat. Rev.* 39 (4) (2013) 375–387.
- P. Couleaud, et al., Designed Modular Proteins as Scaffolds to Stabilize Fluorescent Nanoclusters, *Biomacromolecules* 16 (12) (2015) 3836–3844.
- A.L. Cortajarena, L. Regan, Ligand binding by TPR domains, *Protein Sci.* 15 (5) (2006) 1193–1198.
- T.Z. Grove, L. Regan, A.L. Cortajarena, Nanostructured functional films from engineered repeat proteins, *J. R. Soc. Interface* 10 (83) (2013) 6.
- R. Eachkoti, et al., Identification and characterisation of a novel heat shock protein 90 inhibitor ONO4140, *Eur. J. Cancer* 50 (11) (2014) 1982–1992.



Cite this: *Chem. Sci.*, 2021, 12, 2480 All publication charges for this article have been paid for by the Royal Society of Chemistry

# Engineering multifunctional metal/protein hybrid nanomaterials as tools for therapeutic intervention and high-sensitivity detection†

Antonio Aires,<sup>‡a</sup> David Maestro,<sup>‡b</sup> Jorge Ruiz del Rio,<sup>b</sup> Ana R. Palanca,<sup>bc</sup> Elena Lopez-Martinez,<sup>id a</sup> Irantzu Llarena,<sup>a</sup> Kalotina Geraki,<sup>id d</sup> Carlos Sanchez-Cano,<sup>id \*a</sup> Ana V. Villar,<sup>\*be</sup> and Aitziber L. Cortajarena<sup>id \*af</sup>

Protein-based hybrid nanomaterials have recently emerged as promising platforms to fabricate tailored multifunctional biologics for biotechnological and biomedical applications. This work shows a simple, modular, and versatile strategy to design custom protein hybrid nanomaterials. This approach combines for the first time the engineering of a therapeutic protein module with the engineering of a nanomaterial-stabilizing module within the same molecule, resulting in a multifunctional hybrid nanocomposite unachievable through conventional material synthesis methodologies. As the first proof of concept, a multifunctional system was designed *ad hoc* for the therapeutic intervention and monitoring of myocardial fibrosis. This hybrid nanomaterial combines a designed Hsp90 inhibitory domain and a metal nanocluster stabilizing module resulting in a biologic drug labelled with a metal nanocluster. The engineered nanomaterial actively reduced myocardial fibrosis and heart hypertrophy in an animal model of cardiac remodeling. In addition to the therapeutic effect, the metal nanocluster allowed for *in vitro*, *ex vivo*, and *in vivo* detection and imaging of the fibrotic disease under study. This study evidences the potential of combining protein engineering and protein-directed nanomaterial engineering approaches to design custom nanomaterials as theranostic tools, opening up unexplored routes to date for the next generation of advanced nanomaterials in medicine.

Received 21st September 2020  
Accepted 12th December 2020

DOI: 10.1039/d0sc05215a

rsc.li/chemical-science

## Introduction

Despite tremendous advancement in diagnosis, treatment, and prevention procedures, highly prevalent diseases such as cancer and neurodegenerative and cardiovascular diseases are still a leading cause of death worldwide.<sup>3</sup> Therefore, the development of new nanotechnological tools for relevant application in biomedicine is still an ongoing research goal addressed by

different methodological approaches. In this context, the specific targeting of disease-related pathways and molecules, mostly proteins, is a promising strategy.

Current techniques for tracking, imaging, and inhibiting proteins rely mostly on antibodies. These highly specific proteins are extremely useful tools for different applications, but present some limitations that hamper their use in some cases, including high toxicity, the immunogenicity observed in patients, and inefficient access to cytoplasmic targets.<sup>4</sup> The aforementioned challenges could be overcome by the use of recombinantly produced alternatives, for example, molecules based on simpler protein recognition modules. Engineered proteins can go beyond what is possible with antibodies, as their sequence and structure can be easily modified to modulate their targeting capacities or intracellular localization. Furthermore, modular design strategies can be used to combine recognition units with other functionalities, thus generating powerful new tools for therapeutic intervention and diagnosis.

In this context, small engineered protein domains, inspired by natural binding domains, such as tetratricopeptide repeats, ankyrin repeats, and other repeat protein scaffolds, show great promise as the next generation of therapeutic biologics.<sup>5–8</sup> For example, the engineered consensus tetratricopeptide repeat (CTPR) scaffold is a domain comprising the repetition of 34

<sup>a</sup>Center for Cooperative Research in Biomaterials (CIC biomagUNE), Basque Research and Technology Alliance (BRTA), Paseo de Miramón 194, 20014, Donostia-San Sebastián, Spain. E-mail: alcortajarena@cicbiomagune.es; csanchez@cicbiomagune.es

<sup>b</sup>Instituto de Biomedicina y Biotecnología de Cantabria (IBBTec), CSIC-Universidad de Cantabria, Albert Einstein 22, 39011, Santander, Spain. E-mail: anavictoria.villar@unican.es

<sup>c</sup>Departamento de Anatomía y Biología Celular, Universidad de Cantabria, Avd. Herrera Oria s/n, 39011, Santander, Spain

<sup>d</sup>Diamond Light Source, Harwell Science and Innovation Campus, RG20 6RE, UK, England

<sup>e</sup>Departamento de Fisiología y Farmacología, Universidad de Cantabria, Avd. Herrera Oria s/n, 39011, Santander, Spain

<sup>f</sup>Ikerbasque, Basque Foundation for Science, Ma Díaz de Haro 3, 48013 Bilbao, Spain

† Electronic supplementary information (ESI) available. See DOI: 10.1039/d0sc05215a

‡ These authors contributed equally to this work.



amino acid structural modules, which are stabilized by predictable inter-repeat local interactions.<sup>9</sup> These interactions determine the CTPR protein structure, with a clear distinction between residues that encode their stability or their functionality.<sup>10</sup> CTPR proteins can be engineered to display different ligand recognition properties, as antibody mimics.<sup>11</sup> In addition to their binding capabilities, CTPR domains can also be engineered to synthesize metal nanoclusters (NCs) by introducing metal binding sites within protein scaffolds.<sup>12–15</sup> Of particular interest for biomedical applications are small noble metal nanoclusters, such as silver and gold, stabilized within biomolecules.<sup>16</sup> The resulting CTPR-stabilized metal nanoclusters (Prot-NC) are highly photoluminescent, photo-stable, and biocompatible. Furthermore, these Prot-NCs are readily internalized by living cells, without compromising the NC integrity and their luminescence properties.<sup>14</sup> Therefore, CTPR protein hybrid nanomaterials show great promise as the basis to construct tailored multifunctional nanomaterials for biotechnological and biomedical applications.

This work presents, as the first proof of concept, the fusion of a CTPR390 module [1] (as the protein recognition module)<sup>10,17</sup> to target and inhibit Hsp90,<sup>18</sup> and a fluorescent metal nanocluster stabilizing module, for *in vitro*, *ex vivo*, and *in vivo* detection and imaging (or tracking). The main goal is to explore the development and application of multifunctional hybrid nanomaterials based on the rational assembly of engineered protein modules with specified properties as building blocks. Remarkably, since the modules used are based on the same structural scaffold, the CTPR protein, they can be easily fused into single proteins to form new molecular tools for therapeutic intervention and high-sensitivity detection technologies. This multifunctional molecule is validated for therapeutic intervention and for monitoring replacement myocardial fibrosis secondary to heart damage. Replacement myocardial fibrosis has prognostic value usually associated with risk factors of poor cardiac recovery,<sup>19–21</sup> that strongly affects heart function by overexpression and deposition of extracellular matrix pro-fibrotic components, mainly collagen I. However, therapies to directly target excessive fibrosis remain limited.<sup>20,22</sup> The main target cytokine that triggers the overexpression of collagen fibers is transforming growth factor beta (TGF $\beta$ ),<sup>23,24</sup> and the blockade of its cascade through the inhibition of the chaperone Hsp90 reduces collagen synthesis and deposition in damaged hearts.<sup>25,26</sup> In this sense, the correlation between the inhibition of Hsp90 and the reduction of the pro-fibrotic effects of TGF $\beta$  in cardiac fibrosis opened a new route for the development of anti-fibrotic therapies.<sup>8,25</sup> As such, the designed Hsp90-binding module (CTPR390; [1]) inhibited Hsp90 preserving its chaperone activity and thus the cellular homeostasis,<sup>8,10,17</sup> resulting in TGF $\beta$  signaling deregulation and collagen synthesis reduction.<sup>8</sup> The added value of labelling the biologic drug 1 with gold nanoclusters (AuNCs) is demonstrated in this work by using Au as a unique tracing signal of the molecule when imaging the heart tissue obtained from treated animals by synchrotron X-ray fluorescence (SXRF). SXRF is a powerful technique that allows simultaneous mapping of the distribution of different elements in cells and tissues.<sup>27,28</sup> The approach shown here enables the

specific labelling of the protein-based biologic drug of interest, generating a theranostic tool that reduces the effects of the disease and can be unequivocally traced and quantified in tissue. This strategy permits assessment of the correlation between the tissue localization and the therapeutic effect of the biologic drug. Overall, this work reveals the first design of a hybrid protein-nanocluster biologic drug and the potential of this nanocomposite as a theranostic tool, opening up unexplored routes to date for the next generation of advanced biocompatible multimodal nanomaterials.

## Results and discussion

To explore the development of multifunctional nanomaterials based on engineered proteins as new tools for therapeutic intervention and high-sensitivity monitoring of pathological myocardial fibrosis, fusion between the CTPR390 module [1], designed as a protein recognition moiety to target and inhibit the Hsp90 protein, and a fluorescent metal nanocluster stabilizing module [2], for *ex vivo*, *in vitro*, and *in vivo* detection and imaging, was performed (Fig. 1). The 1 module was previously developed and tested for fibrosis inhibition,<sup>8,17</sup> and the nanocluster stabilizing module [2] was previously designed based on the crystal structure of CTPR protein (PDB ID: 2HYZ)<sup>2</sup> for the synthesis and stabilization of iron–sulfur nanoclusters.<sup>12</sup> Since thiols are known to bind strongly to metals, such as gold,<sup>29,30</sup> a metal coordination site carrying four cysteine residues (Cys) was modelled on the CTPR concave surface.<sup>12</sup> This site is expected to result in a stronger nanocluster coordination compared to previously reported sites comprising histidines.<sup>14</sup> The initial design gave rise to the nanocluster stabilization module C2<sub>NC</sub> [2], which was the module intended to generate the final hybrid system. This module was first tested for its ability to stabilize gold nanoclusters, using a slightly modified green biocompatible chemistry method that had been previously described,<sup>14</sup> in the context of a protein with two flanking wild type CTPR repeats [3] (Fig. S1†), since a CTPR with two repeats is marginally stable.<sup>31</sup> The 3-AuNC complex was purified by size-exclusion chromatography, and the NC growth was followed by the appearance of a single peak fluorescence emission with a maximum at 440 nm (excitation at the maximum absorbance wavelength, 374 nm; Fig. 2A). Extensive control experiments confirmed the fluorescence emission of 3-AuNCs after reduction with sodium ascorbate, as the fluorescence was observed only when all the reagents were present (Fig. S1†).

Upon demonstrating the capability of 2 to allow the synthesis/stabilization of blue-emitting AuNCs, 1 and 2 were fused using a modular cloning strategy (Fig. 1A).<sup>9</sup> The resulting protein 4 was used for the synthesis/stabilization of AuNCs (Fig. 1A). After synthesizing the multifunctional 4-AuNC hybrid nanomaterial, the fluorescence emission and structural integrity of the protein scaffold were verified. Remarkably, excitation of 4-AuNCs with UV light caused a fluorescence emission with comparable efficiency to that of the NC obtained from 3 under the same experimental conditions (Fig. 2A). In addition, the circular dichroism (CD) spectra of 4-AuNCs revealed that the  $\alpha$ -helical structure of the protein scaffold was not affected by the





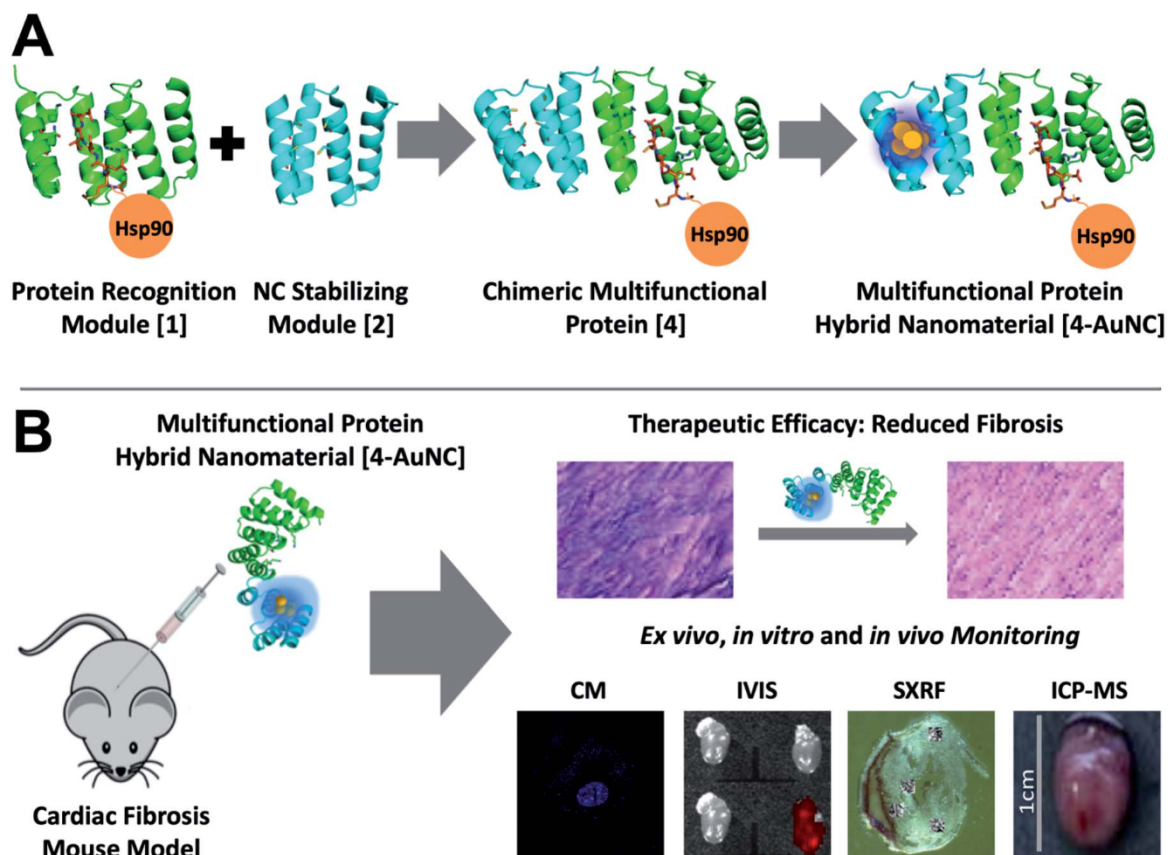


**Fig. 1** Multifunctional proteins designed for the treatment and monitoring of myocardial fibrosis. (A) General scheme of the chimeric multifunctional protein scaffold design and the synthesis and stabilization of fluorescent AuNCs. The crystal structure of the designed CTPR390 [1] recognition module (green) in complex with the C-terminal Hsp90 peptide (orange) (PDB ID: 3KD7) (center).<sup>1</sup> A nanocluster stabilization site is introduced on a modified CTPR module in which four cysteines have been introduced [2] (cyan) on the structure of the CTPR (PDB ID: 2HYZ).<sup>2</sup> Chimeric bifunctional protein [4] made by the fusion of the 1 and 2 modules. Synthesis and stabilization of fluorescent 4-AuNCs. (B) Schematic representation of the general approach for the treatment and monitoring of myocardial fibrosis. Representation of therapeutic 4-AuNC intraperitoneal injection into a fibrotic mouse. Representative examples of the therapeutic efficacy in the reduction of myocardial fibrosis. *In vitro*, *ex vivo*, and *in vivo* monitoring of the myocardial fibrosis. *In vitro* imaging of 4-AuNC treated primary myocardial fibroblasts by confocal microscopy (CM). *Ex vivo* 4-AuNC fluorescence detection with an *in vivo* imaging system (IVIS) by excitation at 440 nm of 3 controls and one 4-AuNC treated heart. 4-AuNC detection by synchrotron X-ray fluorescence (SXRF) and inductively coupled plasma mass spectrometry ICP-MS techniques of *in vivo* 4-AuNC treated mice.

AuNC formation, which is critical for their application as a biologic drug (Fig. 2B). Then, the binding of the protein to Hsp90 (ref. 18) was verified by fluorescence anisotropy using a fluorescein labelled 24-mer Hsp90 peptide (Fig. 2C). The  $K_D$  value obtained for the interaction between 4-AuNCs and the Hsp90 peptide was  $160 \pm 15 \mu\text{M}$ , similar to the value determined for the protein 4 alone ( $155 \pm 11 \mu\text{M}$ ) and to the value described for 1 ( $200 \mu\text{M}$ ).<sup>17</sup> These results confirmed that the binding domain module 1 present in 4 was not affected by the AuNC formation, which is key for using this novel methodology to develop new theranostic tools.

The multifunctional 4-AuNC hybrid nanomaterial was fully characterized, showing a fluorescence quantum yield (QY) of 10.05%, significantly higher than the QY reported for other protein-stabilized AuNCs (3.5–6.0%).<sup>13,32–34</sup> The origin of this high QY is probably associated with the characteristics of the protein scaffold, since the QY of the AuNCs is strongly affected by the capping agents.<sup>35,36</sup> The cysteine residues that compose

the gold binding site were placed onto the protein concave surface and, thus the resulting AuNC should be shielded and rigidified by the protein scaffold. This decreases the non-radiative deactivation process and improves the stability of the AuNCs, leading to high QY values.<sup>37</sup> In addition, the presence of electron-rich cysteine residues on the concave surface of the protein scaffold can largely promote the photoluminescence of the protein-stabilized AuNCs.<sup>36,38</sup> The excited-state dynamics of the 4-AuNC was analyzed with time-resolved photoluminescence measurements (Fig. S2†). Multi-exponential fits of the photoluminescence decay curves, provided 2.53 ns amplitude-weighted average lifetimes that correspond to transitions between singlet states in AuNCs.<sup>39–41</sup> XPS indicated that the Au cores of the 4-AuNC were mainly composed of Au<sup>1+</sup> and Au<sup>0</sup> species with a ratio 2 : 1 (Fig. S3†). In order to use the Au atoms as a specific tracer of the multifunctional molecule for SXRF a precise quantification of the NC size and the number of Au atoms per protein was performed. MALDI-TOF and ICP-MS



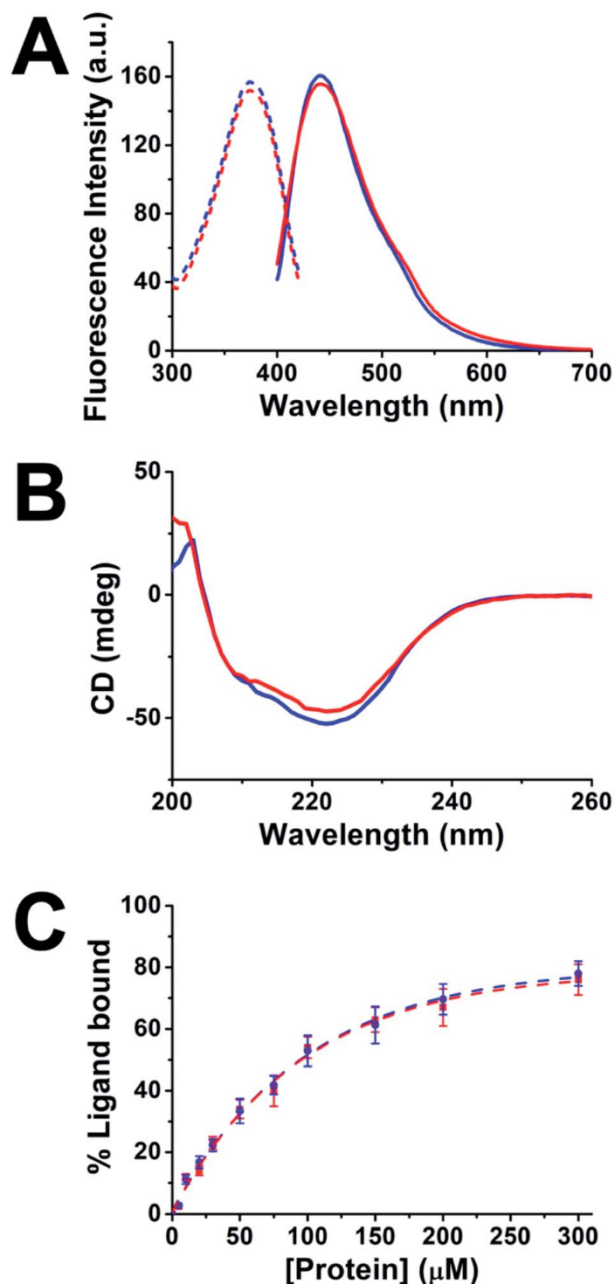


Fig. 2 (A) Fluorescence spectra of 3-AuNCs (blue) and 4-AuNCs (red). The excitation spectra are shown in dashed lines and the emission spectra in solid lines. (B) CD spectra of 4 (solid blue line) and 4-AuNCs (solid red line) recorded at 10  $\mu\text{M}$  protein concentration at 25  $^{\circ}\text{C}$ . (C) Ligand binding activity of 4 (blue circles) and 4-AuNC (red squares). Fluorescence anisotropy of the fluorescein-labelled 24-mer C-terminal peptide of Hsp90. Dashed lines show the fit to a 1 : 1 binding model to calculate the binding affinity. The dissociation constant ( $K_D$ ) was  $K_D = 155 \pm 11 \mu\text{M}$  for 4, and  $K_D = 160 \pm 15 \mu\text{M}$  for 4-AuNCs.

were employed to define the number of Au atoms in the multifunctional 4-AuNC hybrid nanomaterial. The MALDI-TOF mass spectrum of 4-AuNC showed a broad peak at a larger molecular weight than that of the protein 4, which proved the stabilization of AuNCs by the protein and revealed certain polydispersity in size for the AuNC (Fig. S4 and Table S1<sup>†</sup>). An

average of  $8 \pm 4$  gold atoms per protein were estimated for the multifunctional 4-AuNC hybrid nanomaterial. Accordingly, ICP-MS determination of Au from 4-AuNCs indicated  $8 \pm 1$  Au atoms per protein (Table S2<sup>†</sup>). This size is in concordance with that of previously described blue fluorescent AuNCs.<sup>33,42,43</sup> Finally, the homogeneity in the morphology and size of the 4-AuNC was evaluated by scanning transmission electron microscopy (STEM) (Fig. S5<sup>†</sup>). The STEM images showed homogeneous NCs with diameters of  $1.0 \pm 0.2$  nm (Fig. S5<sup>†</sup>).

The multifunctional 4-AuNC hybrid nanomaterial also showed good stability and biocompatibility, which are required for any biomedical application. 4-AuNCs were stable over a month in PBS at 4  $^{\circ}\text{C}$  (Fig. S6A<sup>†</sup>) and over a week under physiological conditions (PBS, and human plasma at 37  $^{\circ}\text{C}$ ) (Fig. S6B<sup>†</sup>). In addition, the biocompatibility of the 4-AuNC was evaluated in cell cultures. NIH-3T3 fibroblast cells and primary cardiac fibroblasts extracted from adult mice were incubated with different concentrations of 4-AuNCs under standard cell culture conditions. Following 5 days of incubation, 4-AuNCs did not present any evident cytotoxicity even at the highest concentration tested (Fig. S7<sup>†</sup>). Furthermore, functional validation of 4-AuNCs as a biologic anti-fibrotic drug was also performed *in vitro* using primary cardiac fibroblasts extracted from adult mice. Fibroblasts treated with 4-AuNCs showed a significant reduction in gene expression of key pro-fibrotic markers, including collagen I and III, and fibronectin in Fig. S8.<sup>†</sup> Moreover, 4-AuNCs exhibited an efficient internalization (Fig. S9 and Movies S1 and S2<sup>†</sup>) while did not inhibit the Hsp90 chaperone activity (Fig. S10<sup>†</sup>) after 24 h of incubation in primary cardiac fibroblasts extracted from adult mice. These results are in agreement with previous observations for the 1 protein without AuNCs.<sup>8</sup>

Hereafter, the use of 4-AuNCs as a biologic anti-fibrotic drug to reduce myocardial fibrosis *in vivo* was evaluated in an angiotensin II (Ang II) mice model. It has been widely demonstrated that Ang II administration induces cardiovascular damage through pathological remodelling including hypertrophy and fibrosis.<sup>44</sup> To induce fibrosis, mice were continuously infused with Ang II for 15 days through a subcutaneous osmotic mini-pump. The hypertension promoted by Ang II generates mechanical damage in the heart and in addition to mechanical stress, it activates pathological remodelling (hypertrophy and fibrosis) to end-organ damage in the short term. These reparative mechanisms, mainly fibrosis, in the long term lead to cardiac dysfunction and in the worst scenario cardiac failure.<sup>45</sup> Consistent with previous reports, significant and widespread fibrosis was observed throughout the myocardium 15 days after Ang II administration.<sup>46</sup> However, a reduction of the collagen area was observed in the hearts of mice treated with 4-AuNCs (Fig. 3A and B). With only one single dose of 4-AuNCs (200  $\mu\text{l}$  at 1 mM), fibrosis remained limited 4 days after the treatment and it showed a more significant reduction 8 days after the 4-AuNC administration (Fig. 3A and B). At a shorter time after the administration (3 hours) reduction of the Ang II-enhanced fibrosis (Fig. 3A and B) and reversion of the hypertrophy (Fig. S11<sup>†</sup>) were not observed. These results were in accordance with previously described data for the 1 protein without AuNCs.<sup>8</sup>





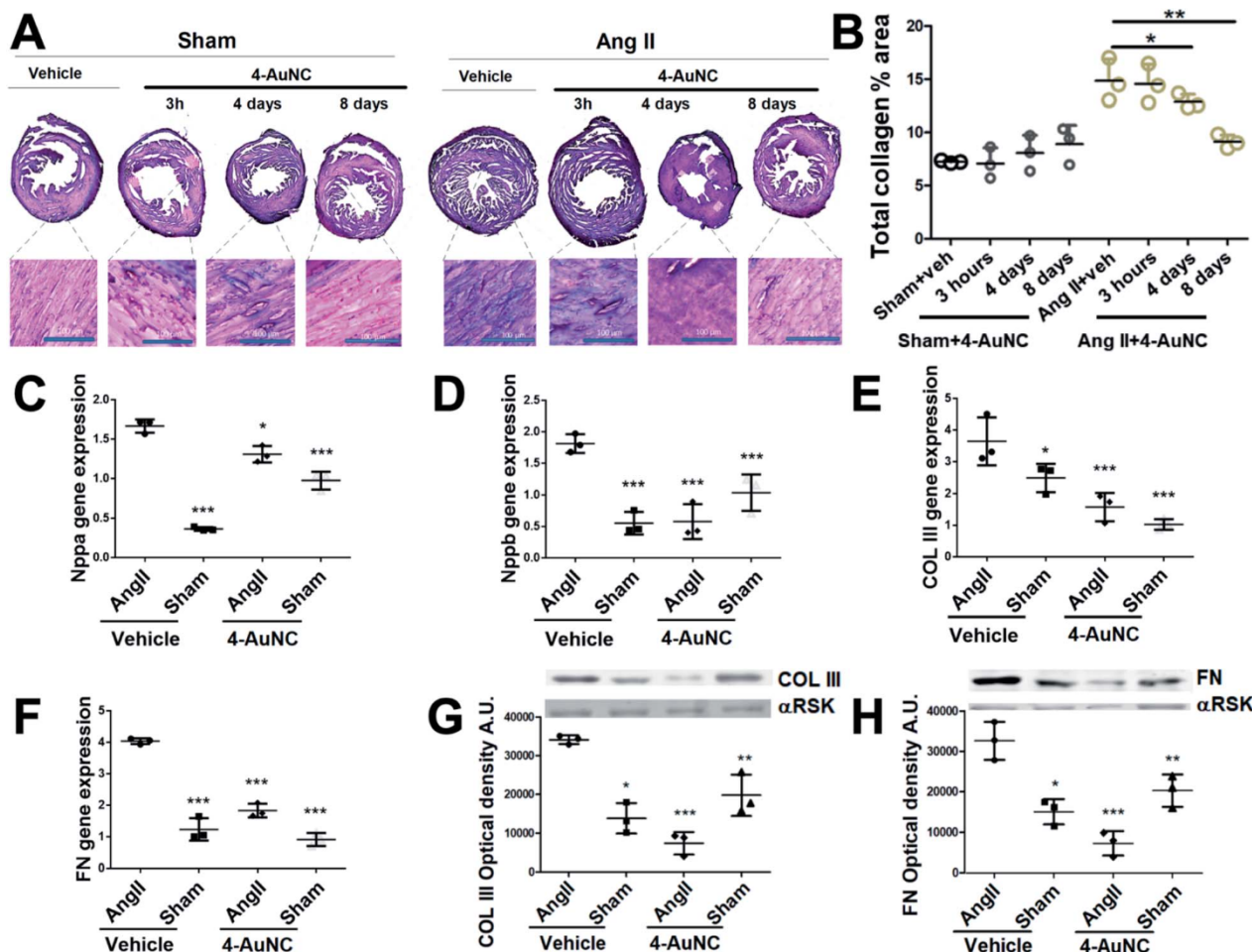


**Fig. 3** *In vivo* 4-AuNC effect on cardiac fibrosis. Histology, gene, and protein expression of cardiac markers related to fibrosis in the Ang II mouse model treated with 4-AuNCs. (A) Masson's trichrome staining of heart cross sections to evaluate fibrosis (mainly collagen I) and details of these sections. Muscle visualization in pink and fibrotic areas in purple. Groups of mice under study: Sham control mice with vehicle or with 4-AuNC administration at 3 hours, 4 and 8 days after the treatment (left panel); Ang II fibrotic mice with vehicle or with 4-AuNC administration at 3 hours, 4 and 8 days after the treatment (right panel). (B) Total collagen I area measured in the heart cross sections from the mice under study at 3 hours, 4 days or 8 days after the anti-fibrotic 4-AuNC administration. (C and D) Expression of the cardiac stress inducible genes encoding atrial natriuretic peptides Nppa and Nppb 8 days after the biologic 4-AuNC anti-fibrotic drug administration. (E and F) Gene-expression changes for COL III (D) and FN (E) in 4-AuNC treated mice (8 days). (G and H) Expression and quantification of COL III and FN proteins of 4-AuNC treated mice (8 days) in arbitrary units (A.U.). (\* $p < 0.05$ , \*\* $p < 0.005$ , \*\*\* $p < 0.001$ ; Mann-Whitney test).

The greatest reduction of myocardial fibrotic areas was observed 8 days after the 4-AuNC treatment. Thus, the study at the molecular level was focused on this time point showing the reduction in gene expression of myocardial stress biomarkers (Nppa and Nppb) (Fig. 3C and D), and the reduction in gene and protein expression of the structural pro-fibrotic proteins (COL III, and FN) in 4-AuNC treated mice, compared to vehicle-treated mice (Fig. 3E–H). In addition to the reduced cardiac fibrosis by 4-AuNC treatment, a study of cardiac hypertrophy (heart weight to body weight ratio) was performed. Fig. S11† shows that the myocardial hypertrophy was notably reduced 8 days after 4-AuNC treatment.

Remarkably, the presence of Au made possible the detection of the multifunctional 4-AuNC hybrid nanomaterial, in organs, tissues, and fluids using a number of different techniques. As such, imaging of *ex vivo* hearts injected with 4-AuNCs showed

a uniform distribution of the 4-AuNC within the organ (Fig. 1B). ICP-MS allowed the assessment of the biodistribution of 4-AuNC in mice (Fig. S12†), showing that 8 days after injection 4-AuNCs were accumulated mostly in the kidneys, liver, and spleen of both healthy and fibrotic individuals. These results suggest the presence of a regular activity of the hepatic metabolism and a desirable renal clearance in treated mice with or without fibrosis, as was expected considering the hydrodynamic size of the multifunctional 4-AuNC hybrid nanomaterial ( $8 \pm 1$  nm). In contrast, Au was found in low quantities in the stomach, lungs, intestines, urine, and blood, and was not detected in the brain and cerebellum, indicating that 4-AuNCs do not cross the brain blood barrier. Interestingly, significant differences were observed in the accumulation of Au in the cardiovascular areas of fibrotic individuals, such as atria, right and left ventricles, and the aorta, compared to healthy controls



(Fig. S12†). These cardiovascular areas have been consistently reported as damaged areas in an Ang II murine model.<sup>47,48</sup>

SXRF using microfocused synchrotron radiation also permitted quantification of the accumulation of Au in tissue samples, while providing lateral resolution not available from ICP-MS. This technique allows the assessment of the localization of 4-AuNCs within the hearts of Ang II and healthy mice with a  $\mu\text{m}$  resolution (Fig. 4A–E and S13–21, and Table S3†). Three different time-points, 3 hours, 4 days and 8 days, were selected to evaluate the accumulation of 4-AuNC by SXRF in the hearts of the mice after the administration of 4-AuNCs (Fig. S15–S21†). Au elemental maps acquired using SXRF showed a higher accumulation of 4-AuNC in the hearts of fibrotic mice in comparison with the hearts of healthy mice. Furthermore, this accumulation was time dependent, and could be correlated with the antifibrotic response of 4-AuNCs (Fig. S23 and S24†). The two time-points that presented the maximal difference in the anti-fibrotic response (according to the collagen reduction and fibrotic biomarker quantification – Fig. 3) compared to that of the vehicle treated mice, 3 hours (lack of response) and 8 days (highest anti-fibrotic response) were analysed more in detail by SXRF. Initially, Au elemental maps acquired using SXRF confirmed the absence of 4-AuNCs in the hearts of vehicle treated mice, and the presence of low quantities of Au in those heart sections extracted from healthy mice treated with the 4-AuNCs, independent of the time after the treatment ( $1.66 \pm 0.11$  and  $0.8 \pm 0.02$  ng  $\text{mg}^{-1}$ , respectively 3 hours or 8 days after the treatment). In contrast, the hearts of Ang II mice treated with 4-AuNCs seemed to accumulate high quantities of Au ( $5.62 \pm 0.22$  and  $27.22 \pm 6.27$  ng  $\text{mg}^{-1}$ , respectively 3 hours or 8 days after the treatment) in a time dependent manner (4-fold increase between 3 hours and 8 days

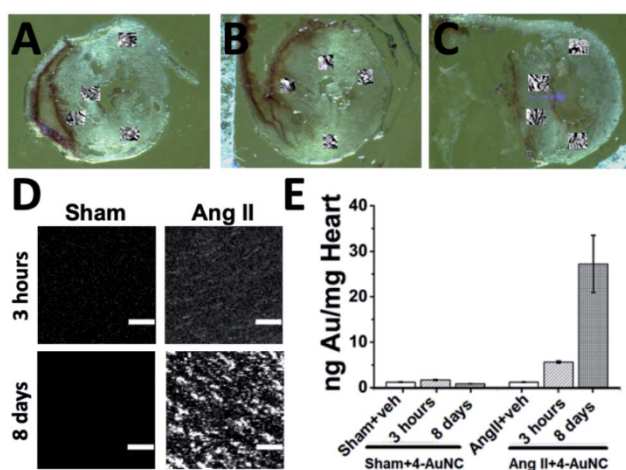


Fig. 4 (A–C) Heart sections from mice showing the areas studied with SXRF. (A) Ang II fibrotic mouse treated with 4-AuNCs; (B) vehicle treated Ang II fibrotic mouse; (C) Sham healthy mouse treated with 4-AuNCs. (D) Au SXRF elemental maps showing localization of the Au element from 4-AuNCs in healthy (Sham) or fibrotic (Ang II) hearts of mice 3 hours and 8 days after 4-AuNC treatment; Raster scan:  $5 \times 5 \mu\text{m}^2$  step size, 1 s dwell time. Scale bar  $100 \mu\text{m}$ . Concentration range in images:  $0\text{--}2$  ng  $\text{mm}^{-2}$  Au. (E) Quantity of Au accumulated in hearts of healthy (Sham) or fibrotic (Ang II) mice 3 hours and 8 days after 4-AuNC treatment.

after the treatment; Fig. 4E). Remarkably, Au accumulation was independent of the area of the hearts studied (*i.e.* septum and posterior wall, top or bottom; Fig. 4A–C and S14–S20†). But, while the distribution of 4-AuNCs within these areas was homogeneous in healthy mice or Ang II mice 3 hours after the treatment with 4-AuNCs, Au maps acquired from the hearts of Ang II mice 8 days after the treatment showed a distinct punctuated pattern (with hot-spots containing over 50 times more gold than the average found in the whole area studied; Fig. 4D and S14–S21†). Such accumulation patterns are similar to the ones obtained from Ang II hearts when they are stained with the Masson's trichrome staining, which highlights fibrotic areas with a high concentration of collagen (Fig. 3A). Therefore, it might be possible that 4-AuNCs respond to distinct collagen deposit-domains within specific myocardial areas, thus tracking the damage. To confirm the accumulation of the multifunctional 4-AuNC hybrid nanomaterial in the fibrotic areas and explore its potential as a bio-marker of the myocardial fibrosis disease, partial Masson's trichrome staining was applied to specifically stain, with tungsten (W), the collagen-rich fibrotic regions. The experimental design was based on the first steps of the Masson's trichrome assay in which phosphotungstic acid (PTA) binds to collagen and fibres of connective tissues at low pH. Once the tungsten–collagen interaction was fixed on the fresh tissue, the co-localization of Au and W was assessed using SXRF maps obtained from PTA-stained heart sections. PTA is widely used as a contrast agent for X-ray based techniques, and is currently being tested as a possible contrast agent to study collagen distribution in cartilage using contrast-enhanced micro-computed tomography.<sup>49–51</sup> High levels of tungsten were found in the hearts of Ang II mice when compared with those from the healthy mice ( $0.192 \pm 0.003$  and  $0.079 \pm 0.001$  ng W per ng Zn, respectively; normalized to Zn levels as it indicates cellular areas due to high levels in nuclear regions; Fig. S22 and S24†). These results were expected, as increased collagen levels in fibrotic hearts were already observed (Fig. 3A). However, when fibrotic (Ang II) and healthy (Sham) mice were analyzed 8 days after 4-AuNC treatment, the hearts showed similar levels of W to the hearts of vehicle treated healthy (Sham) mice ( $0.096 \pm 0.001$  and  $0.083 \pm 0.001$  ng W per ng Zn, respectively; Fig. S24†). Furthermore, only fibrotic (Ang II) mice accumulated high amounts of Au (as expected; Fig. S23†), and the correlation between the W and Au signals was much higher in the fibrotic heart samples treated with 4-AuNCs when compared with the healthy analogues (*R*-Pearson's coefficients 0.35 and  $-0.2$  respectively; Fig. S24†). These results suggest that the reduced fibrosis levels observed upon treatment with 4-AuNCs might be related to the accumulation of the multifunctional 4-AuNC hybrid nanomaterial in fibrotic areas. Such accumulation could be due to the presence of high levels of Hsp90 (the target of 4-AuNCs) related to collagen production, as the expression of Hsp90 $\alpha$  (inducible isoform under pathological conditions) was significantly augmented in the heart of AngII-fibrotic mice, while there was no variation in Hsp90 $\beta$  (constitutively expressed isoform) (Fig. S25†).<sup>8</sup>

## Conclusions

In summary, a simple protein engineering-based versatile approach to generate custom protein–metal hybrid





nanomaterials for biomedical applications has been demonstrated. The main goal in this work was to explore the development and application of synthetic strategies to obtain multifunctional hybrid nanomaterials based on the rational assembly of engineered protein modules with specified properties as building blocks. As the sequence and structure of these engineered protein modules can be easily modified to modulate their targeting capacities and to introduce other functionalities, this modular design strategy can be used to combine recognition units and other functionalities, depending on the specific application, thus generating powerful tailored multifunctional nanomaterials for therapeutic intervention and diagnosis.

Here, as the first proof of concept, an engineered multifunctional system was constructed, by combination of two designed modules, a recognition module, and a metal nanocluster stabilizing module, in a chimeric protein. In particular, a new tool for the therapeutic intervention and monitoring of myocardial fibrosis was generated, by the fusion of the CTPR390 module [1], a protein recognition moiety that targets and inhibits the TGF $\beta$  pro-fibrotic cascade protein, Hsp90, and a fluorescent metal nanocluster stabilizing module, for *ex vivo*, *in vitro*, and *in vivo* detection and imaging. The resulting protein-based hybrid nanomaterial (4-AuNC) was evaluated as a biologic anti-fibrotic drug to reduce myocardial fibrosis *in vivo* in an angiotensin II (Ang II) mouse model. A single dose administration of 4-AuNCs caused a significant reduction in the myocardial fibrosis and heart hypertrophy 8 days after treatment, due to the Hsp90 inhibition function. This inhibition preserved the Hsp90 chaperone function, thus minimizing the effects on cellular homeostasis, which opens a new route for the development of anti-fibrotic therapies. In addition, 4-AuNCs allowed *ex vivo*, *in vitro*, and *in vivo* detection and imaging of the fibrosis disease, due to the selective labelling of the biological molecule with a biocompatible metal nanocluster. Overall, the strategy presented here shows great promise of engineered protein-based hybrid nanomaterials and their potential use as theranostic tools, opening up unexplored routes to date for the synthesis of the next generation of advanced nanocomposites and their application in medicine.

## Ethical statement

Live animal studies were approved by the University of Cantabria Institutional Laboratory Animal Care and Use Committee in compliance with the Guide for the Care and Use of Laboratory Animals (ILAR, 1985) and were conducted in accordance with the "European Directive for the Protection of Vertebrate Animals Used for Experimental and Other Scientific Purposes" (European Communities Council Directive 86/606/EEC).

## Author contributions

Conceptualization, A. L. C., and A. V. V.; methodology, A. A., D. M., JRdR., A. R. P., E. L.-M., I. L. L., K. G., and C. S.-C.; formal analysis, A. A., D. M., C. S.-C., A. V. V., and A. L. C.; investigation: protein hybrid synthesis and characterization and analytical studies A. A.; investigation: *in vitro* and *in vivo* studies, D. M.,

JRdR., A. R. P., and A. V. V.; investigation: XRF studies, C. S.-C., E. L.-M., K. G., A. V. V., and A. L. C.; writing-original draft preparation, A. A., D. M., C. S.-C., A. V. V., and A. L. C.; funding acquisition, A. V. V. and A. L. C. All the authors have read and agreed to the published version of the manuscript.

## Conflicts of interest

There are no conflicts to declare.

## Acknowledgements

This work was partially supported by the European Research Council ERC-CoG-648071-ProNANO and ERC-PoC-841063-NIMM; Agencia Estatal de Investigación, Spain (PID2019-111649RB-I00; RTI2018-095214-B-I00; BIO2016-77367-C2-1-R; and BIO2015-72124-EXP); the Basque Government (Elkartek KK-2017/00008; RIS3-2019222005); and IDIVAL InnVal 17/22. C. S. C. thanks Gipuzkoa Foru Aldundia (Gipuzkoa Fellows program; grant number 2019-FELL-000018-01/62/2019) for financial support. E.L.-M. thanks the Spanish Ministry of Science and Innovation for the FPI grant (BES-2017-079646). This work was performed under the Maria de Maeztu Units of Excellence Program from the Spanish State Research Agency – Grant No. MDM-2017-0720 (CIC biomaGUNE). SXRF maps were acquired at the I18 beamline in the frame of the Diamond proposals SP20603. We thank Dr Marco Moller, Dr J. Calvo, Dr Otaegui, and Dr Desire Di Silvio at CIC biomaGUNE for support with the acquisition of electron microscopy images, mass spectrometry, and X-ray photoelectron spectroscopy measurements.

## Notes and references

- 1 A. L. Cortajarena, J. Wang and L. Regan, *FEBS J.*, 2010, **277**, 1058–1066.
- 2 T. Kajander, A. L. Cortajarena, S. Mochrie and L. Regan, *Acta Crystallogr., Sect. D: Biol. Crystallogr.*, 2007, **63**, 800–811.
- 3 A. Becker, M. Leskau, B. L. Schlingmann-Molina, S. C. Hohmeier, S. Alnajjar, H. Murua Escobar and A. Ngezahayo, *Sci. Rep.*, 2018, **8**, 14963.
- 4 A. Bradbury and A. Plückthun, *Nature*, 2015, **518**, 27–29.
- 5 Y. L. Boersma and A. Plückthun, *Curr. Opin. Biotechnol.*, 2011, **22**, 849–857.
- 6 A. Plückthun, *Annu. Rev. Pharmacol. Toxicol.*, 2015, **55**, 489–511.
- 7 L. Regan, M. R. Hinrichsen and C. Oi, *Expert Rev. Proteomics*, 2016, **13**, 481–493.
- 8 R. A. Caceres, T. Chavez, D. Maestro, A. R. Palanca, P. Bolado, F. Madrazo, A. Aires, A. L. Cortajarena and A. V. Villar, *J. Mol. Cell. Cardiol.*, 2018, **123**, 75–87.
- 9 A. L. Cortajarena, S. G. J. Mochrie and L. Regan, *Protein Sci.*, 2011, **20**, 1042–1047.
- 10 A. L. Cortajarena, F. Yi and L. Regan, *ACS Chem. Biol.*, 2008, **3**, 161–166.
- 11 A. L. Cortajarena, T. Y. Liu, M. Hochstrasser and L. Regan, *ACS Chem. Biol.*, 2010, **5**, 545–552.



- 12 S. H. Mejias, Z. Bahrami-Dizicheh, M. Liutkus, D. J. Sommer, A. Astashkin, G. Kodis, G. Ghirlanda and A. L. Cortajarena, *Chem. Commun.*, 2019, **55**, 3319–3322.
- 13 P. Couleaud, S. Adan-Bermudez, A. Aires, S. H. Mejías, B. Sot, A. Somoza and A. L. Cortajarena, *Biomacromolecules*, 2015, **16**, 3836–3844.
- 14 A. Aires, I. Llarena, M. Moller, J. Castro-Smirnov, J. Cabanillas-Gonzalez and A. L. Cortajarena, *Angew. Chem., Int. Ed.*, 2019, **58**, 6214–6219.
- 15 A. Aires, V. Fernández-Luna, J. Fernández-Cestau, R. D. Costa and A. L. Cortajarena, *Nano Lett.*, 2020, **20**, 2710–2716.
- 16 Y. Tao, M. Li, J. Ren and X. Qu, *Chem. Soc. Rev.*, 2015, **44**, 8636–8663.
- 17 A. L. Cortajarena, T. Kajander, W. Pan, M. J. Cocco and L. Regan, *Protein Eng., Des. Sel.*, 2004, **17**, 399–409.
- 18 C. Scheufler, A. Brinker, G. Bourenkov, S. Pegoraro, L. Moroder, H. Bartunik, F. U. Hartl and I. Moarefi, *Cell*, 2000, **101**, 199–210.
- 19 G. Balčiūnaitė, D. Palionis, E. Žurauskas, V. Skorniakov, V. Janušauskas, A. Zorinas, T. Zaremba, N. Valevičienė, A. Aidietis, P. Šerpytis, K. Ručinskas, P. Sogaard and S. Glaveckaitė, *BMC Cardiovasc. Disord.*, 2020, **20**, 275.
- 20 J. G. Travers, F. A. Kamal, J. Robbins, K. E. Yutzey and B. C. Blaxall, *Circ. Res.*, 2016, **118**, 1021–1040.
- 21 P. Kong, P. Christia and N. G. Frangogiannis, *Cell. Mol. Life Sci.*, 2014, **71**, 549–574.
- 22 Z. Fan and J. Guan, *Biomater. Res.*, 2016, **20**, 016–0060.
- 23 M. Dobaczewski, W. Chen and N. G. Frangogiannis, *J. Mol. Cell. Cardiol.*, 2011, **51**, 600–606.
- 24 H. Khalil, O. Kanisicak, V. Prasad, R. N. Correll, X. Fu, T. Schips, R. J. Vagnozzi, R. Liu, T. Huynh, S. J. Lee, J. Karch and J. D. Molckentin, *J. Clin. Invest.*, 2017, **127**, 3770–3783.
- 25 R. Garcia, D. Merino, J. M. Gomez, J. F. Nistal, M. A. Hurle, A. L. Cortajarena and A. V. Villar, *Cell. Signalling*, 2016, **28**, 1563–1579.
- 26 R. Datta, T. Bansal, S. Rana, K. Datta, S. Chattopadhyay, M. Chawla-Sarkar and S. Sarkar, *Cell. Signalling*, 2015, **27**, 2410–2424.
- 27 M. J. Pushie, I. J. Pickering, M. Korbas, M. J. Hackett and G. N. George, *Chem. Rev.*, 2014, **114**, 8499–8541.
- 28 R. Zhang, L. Li, Y. Sultanbawa and Z. P. Xu, *Am. J. Nucl. Med. Mol. Imaging*, 2018, **8**, 169–188.
- 29 Y. Ding, G. Gu, X.-H. Xia and Q. Huo, *J. Mater. Chem.*, 2009, **19**, 795–799.
- 30 B. Maity, S. Abe and T. Ueno, *Nat. Commun.*, 2017, **8**, 14820.
- 31 T. Kajander, A. L. Cortajarena, E. R. G. Main, S. G. J. Mochrie and L. Regan, *J. Am. Chem. Soc.*, 2005, **127**, 10188–10190.
- 32 H. Wei, Z. Wang, L. Yang, S. Tian, C. Hou and Y. Lu, *Analyst*, 2010, **135**, 1406–1410.
- 33 H. Kawasaki, K. Hamaguchi, I. Osaka and R. Arakawa, *Adv. Funct. Mater.*, 2011, **21**, 3508–3515.
- 34 J. Xie, Y. Zheng and J. Y. Ying, *J. Am. Chem. Soc.*, 2009, **131**, 888–889.
- 35 S. E. Crawford, C. M. Andolina, A. M. Smith, L. E. Marbella, K. A. Johnston, P. J. Straney, M. J. Hartmann and J. E. Millstone, *J. Am. Chem. Soc.*, 2015, **137**, 14423–14429.
- 36 Z. Wu and R. Jin, *Nano Lett.*, 2010, **10**, 2568–2573.
- 37 A. Cantelli, G. Guidetti, J. Manzi, V. Caponetti and M. Montalti, *Eur. J. Inorg. Chem.*, 2017, **2017**, 5068–5084.
- 38 R. Jin, H. Qian, Z. Wu, Y. Zhu, M. Zhu, A. Mohanty and N. Garg, *J. Phys. Chem. Lett.*, 2010, **1**, 2903–2910.
- 39 C. C. Huang, Z. Yang, K. H. Lee and H. T. Chang, *Angew. Chem.*, 2007, **46**, 6824–6828.
- 40 M. A. Muhammed, P. K. Verma, S. K. Pal, R. C. Kumar, S. Paul, R. V. Omkumar and T. Pradeep, *Chemistry*, 2009, **15**, 10110–10120.
- 41 A. M. Hussain, S. N. Sarangi, J. A. Kesarwani and S. N. Sahu, *Biosens. Bioelectron.*, 2011, **29**, 60–65.
- 42 P. Khandelwal, D. K. Singh, S. Sadhu and P. Poddar, *Nanoscale*, 2015, **7**, 19985–20002.
- 43 H. Ding, H. Li, X. Wang, Y. Zhou, Z. Li, J. K. Hiltunen, J. Shen and Z. Chen, *Chem. Mater.*, 2017, **29**, 8440–8448.
- 44 J. M. Schnee and W. A. Hsueh, *Cardiovasc. Res.*, 2000, **46**, 264–268.
- 45 N. Munoz-Durango, C. A. Fuentes, A. E. Castillo, L. M. Gonzalez-Gomez, A. Vecchiola, C. E. Fardella and A. M. Kalergis, *Int. J. Mol. Sci.*, 2016, **17**, 797.
- 46 D. J. Glenn, M. C. Cardema, W. Ni, Y. Zhang, Y. Yeghiazarians, D. Grapov, O. Fiehn and D. G. Gardner, *Am. J. Physiol.: Heart Circ. Physiol.*, 2015, **308**, 5.
- 47 W. J. Li, Y. Liu, J. J. Wang, Y. L. Zhang, S. Lai, Y. L. Xia, H. X. Wang and H. H. Li, *Life Sci.*, 2016, **149**, 18–24.
- 48 Q. Wang, Y. Yu, P. Zhang, Y. Chen, C. Li, J. Chen, Y. Wang and Y. Li, *Basic Res. Cardiol.*, 2017, **112**, 47.
- 49 H. J. Nieminen, T. Ylitalo, S. Karhula, J. P. Suuronen, S. Kauppinen, R. Serimaa, E. Hæggrström, K. P. H. Pritzker, M. Valkealahti, P. Lehenkari, M. Finnilä and S. Saarakkala, *Osteoarthr. Cartil.*, 2015, **23**, 1613–1621.
- 50 C. M. Disney, K. Madi, A. J. Bodey, P. D. Lee, J. A. Hoyland and M. J. Sherratt, *Sci. Rep.*, 2017, **7**, 16279.
- 51 L. Han, S. S. Karhula, M. A. Finnilä, M. J. Lammi, J. H. Ylärinne, S. Kauppinen, L. Rieppo, K. P. H. Pritzker, H. J. Nieminen and S. Saarakkala, *PLoS One*, 2017, **12**, e0171075.







Cite this: DOI: 10.1039/d1sc04183e

All publication charges for this article have been paid for by the Royal Society of Chemistry

# Correlative 3D cryo X-ray imaging reveals intracellular location and effect of designed antifibrotic protein–nanomaterial hybrids†

J. Groen,<sup>a</sup> A. Palanca,<sup>bc</sup> A. Aires,<sup>d</sup> J. J. Conesa,<sup>ae</sup> D. Maestro,<sup>b</sup> S. Rehbein,<sup>f</sup> M. Harkiolaki,<sup>g</sup> A. V. Villar,<sup>gh</sup> A. L. Cortajarena<sup>idi</sup> and E. Pereiro<sup>ja</sup>

Revealing the intracellular location of novel therapeutic agents is paramount for the understanding of their effect at the cell ultrastructure level. Here, we apply a novel correlative cryo 3D imaging approach to determine the intracellular fate of a designed protein–nanomaterial hybrid with antifibrotic properties that shows great promise in mitigating myocardial fibrosis. Cryo 3D structured illumination microscopy (cryo-3D-SIM) pinpoints the location and cryo soft X-ray tomography (cryo-SXT) reveals the ultrastructural environment and subcellular localization of this nanomaterial with spatial correlation accuracy down to 70 nm in whole cells. This novel high resolution 3D cryo correlative approach unambiguously locates the nanomaterial after overnight treatment within multivesicular bodies which have been associated with endosomal trafficking events by confocal microscopy. Moreover, this approach allows assessing the cellular response towards the treatment by evaluating the morphological changes induced. This is especially relevant for the future usage of nanoformulations in clinical practices. This correlative super-resolution and X-ray imaging strategy joins high specificity, by the use of fluorescence, with high spatial resolution at 30 nm (half pitch) provided by cryo-SXT in whole cells, without the need of staining or fixation, and can be of particular benefit to locate specific molecules in the native cellular environment in bio-nanomedicine.

Received 30th July 2021  
Accepted 17th October 2021

DOI: 10.1039/d1sc04183e

rsc.li/chemical-science

## Introduction

The intracellular localization of specific therapeutic agents is a mandatory step towards understanding their mechanisms of action and effects at the cellular level. To this aim, a correlative imaging approach, which delivers information on the cellular

ultrastructure and the molecular localization in whole cells under close-to-native conditions, is compulsory. An unambiguous molecular localization will allow, firstly, an understanding of the possible routes used to enter the cell, secondly, how the cell deals with a specific agent, and finally what are the effects induced by the treatment on the ultrastructural morphology, which is a direct reflection of the cellular homeostasis.<sup>1</sup> Here we use a novel 3D cryo correlative light and X-ray tomography (CLXT) imaging approach, the protocol of which is described elsewhere,<sup>2</sup> towards the investigation of a promising antifibrotic treatment for myocardial fibrosis as a model system. CLXT utilizes the gold standard for sample preparation of cryo-preserved cells, and combines 3D structured illumination microscopy (cryo-3D-SIM) to locate the therapeutic agent through its fluorescence signal, followed by soft X-ray tomography (cryo-SXT) to visualize this specific fluorescence signal in the cell ultrastructural context pinpointing its fate in the whole 3D cellular environment. This novel methodology is not only high-throughput, allowing imaging of cell populations under different conditions and time points, but it also benefits from the broad range of existing fluorescent dyes and proteins, opening its use to a wide range of biological studies.

This work focuses on the particular example of cardiac fibrosis, a health condition that negatively influences the progression of many heart diseases and affects millions of

<sup>a</sup>MISTRAL Beamline, Experiments Division, ALBA Synchrotron Light Source, Cerdanyola del Valles, 08290 Barcelona, Spain. E-mail: epereiro@cells.es

<sup>b</sup>Instituto de Biomedicina y Biotecnología de Cantabria (IBBT), University of Cantabria, CSIC, 39011 Santander, Spain

<sup>c</sup>Department of Anatomy and Cell Biology, University of Cantabria, 39011 Santander, Spain

<sup>d</sup>Center for Cooperative Research in Biomaterials (CIC biomAGUNE), Basque Research and Technology Alliance (BRTA), Paseo de Miramón 194, 20014, Donostia San Sebastian, Spain. E-mail: alcortajarena@cicbiomagune.es

<sup>e</sup>National Center for Biotechnology CSIC (CNB-CSIC), Department of Macromolecular Structures, Cantoblanco, 28049 Madrid, Spain

<sup>f</sup>Helmholtz-Zentrum Berlin für Materialien und Energie, Bessy II, D-12489 Berlin, Germany

<sup>g</sup>Beamline B24, Diamond Light Source, Harwell Science and Innovation Campus, Didcot, Oxfordshire, OX11 0DE, UK

<sup>h</sup>Department of Physiology and Pharmacology, University of Cantabria, Avd. Herrera Oria s/n, Santander, Spain

<sup>i</sup>Ikerbasque, Basque Foundation for Science, 48009 Bilbao, Spain

† Electronic supplementary information (ESI) available. See DOI: 10.1039/d1sc04183e



people worldwide.<sup>3</sup> Regardless of the etiology of the cardiac injury, cardiac fibrosis promotes the pathological increase of collagen deposition leading to heightened myocardial stiffness and dampened cardiac function, which are common features in patients with advanced cardiac failure.<sup>4</sup> There is no preventive or curative treatment for cardiac fibrosis, due to the elusive mechanism of fibrosis and the lack of specific targets.<sup>5</sup> Although a number of therapeutic agents prescribed for specific cardiovascular disorders have been shown to exert beneficial effects on myocardial fibrosis, in most cases an invasive surgery to save the patients life is needed.<sup>3</sup> The transforming growth factor  $\beta$  (TGF- $\beta$ ) is a cytokine that triggers the activation of myocardial fibroblasts, regulating collagen production and deposition in the extracellular matrix.<sup>6</sup> Together with the heat shock protein 90 (Hsp90), they participate in the pro-fibrotic signaling cascade promoting cardiac fibrosis.<sup>7</sup> Transforming growth factor  $\beta$  (TGF- $\beta$ ) is a cytokine that triggers fibroblast activation, regulating collagen production and deposition in the extracellular matrix. Heat shock protein 90 (Hsp90) participates in the pro-fibrotic signaling cascade triggered by TGF- $\beta$  promoting cardiac fibrosis.<sup>7</sup> TGF- $\beta$  is an essential cytokine excreted by many cell-types and involved in many important functional processes such as regulation of immune reaction, control of differentiation, regulation of proliferation and participation in inflammation among others.<sup>8</sup> Due to these pleiotropic effects, *in vivo* TGF- $\beta$  targeting to reduce fibrosis is always accompanied by a large number of side effects. As a result, a possible strategy to reduce fibrosis while avoiding side effects is the inhibition of a key factor involved in its pro-fibrotic signaling cascade, such as Hsp90, which has been shown to play an essential role in TGF- $\beta$ -mediated collagen production.<sup>9</sup>

The development of an engineered Hsp90 inhibiting module (CTPR390) based on a tetratricopeptide repeat (TPR) domain has shown great potential inhibiting Hsp90.<sup>10–12</sup> In particular, previous studies have demonstrated its effectiveness to reduce myocardial pro-fibrotic events *in vitro* and *in vivo*.<sup>12</sup> Further studies focused on re-engineering the Hsp90 inhibitory domain by its fusion to a related TPR domain that enables the stabilization of a metallic nanocluster, in this case a gold nanocluster (AuNC).<sup>13</sup> This engineered protein–nanomaterial hybrid (Prot-NM) also showed efficient therapeutic activity by reducing the myocardial fibrosis and heart hypertrophy in an animal model of cardiac remodeling.<sup>14</sup> In addition, the AuNC has shown to exhibit fluorescence ( $\lambda_{\text{exc}} = 370/\lambda_{\text{em}} = 445 \text{ nm}$ ),<sup>13</sup> which can be used for localization, and it has shown to have a positive effect on the internalization of the Prot-NM.<sup>14</sup> Herein, we have further investigated its *in vitro* localization and effect by looking at the cellular response at the ultrastructural level, testing both primary cardiac mouse fibroblast and the NIH-3T3 immortalized embryonic fibroblasts. We aim at unravelling the cellular effects of this promising therapeutic agent, and expect to directly correlate those effects with the Hsp90 inhibition. For this aim, we treated the fibroblasts with two protein hybrid systems, with and without the engineered Hsp90 inhibitory domain (TPR-Hsp90-AuNC and TPR-AuNC, respectively). Then, the treated fibroblasts were cryopreserved and imaged using

CLXT.<sup>2</sup> Furthermore, these results were complemented by confocal microscopy.

Cryo-3D-SIM at B24 beamline (Diamond Synchrotron, UK)<sup>15</sup> was used to locate the Prot-NM in the cellular environment. Due to a sub-optimal laser excitation wavelength (405 nm) for the AuNC, resulting in low fluorescence emission, the Prot-NM was tagged with the fluorophore Alexa-488 (see S1†). Furthermore, to position the fluorescence signal in the context of the full cellular structure, cryo-SXT<sup>16,17</sup> in the water window energy range was subsequently used<sup>18–26</sup> at the Mistral beamline (Alba Synchrotron, Spain).<sup>27,28</sup> The data collected with cryo-SXT was in addition used to obtain valuable information about specific organelle morphology and number which are an indication of cellular homeostasis.<sup>1</sup> Indeed, the mitochondrial homeostasis in healthy cells is maintained through dynamic and tightly regulated fission and fusion events. Therefore, a change in the mitochondrial morphology and number gives insights into the overall health of the cell.<sup>29</sup>

The combination of cryo-3D-SIM and cryo-SXT is a novel and powerful correlative imaging approach<sup>15,30</sup> which enables linking cellular function and structure with high spatial resolution under close-to-native conditions. Both techniques are high throughput and easy to use (*e.g.* same sample support and no intensive sample preparation needed) although 3D data correlation requires an appropriate fiducialisation strategy.<sup>2</sup> Note that a full workflow under cryogenic conditions maximizes efficiency by maintaining sample integrity and quality between the microscopy modalities.

Herein, we investigated the intracellular fate of these two Prot-NM, with and without the Hsp90 binding domain, accurately locating them within specific cellular organelles while describing related clear morphological effects which have been found to be cell type-dependent, concluding that primary mouse fibroblasts are more resilient to treatment with Prot-NM than NIH-3T3 cells.

## Results

### Cryo-3D-SIM confirms the presence of the protein–nanomaterial hybrid in treated cells

CLXT was used to image four groups of both primary cardiac mouse fibroblasts and NIH-3T3 cells: the control group, TGF- $\beta$  activated group, TGF- $\beta$  activated and TPR-Hsp90-AuNC treated group (TPR-Hsp90-AuNC group), and finally TGF- $\beta$  activated and TPR-AuNC treated group lacking the Hsp90 inhibitory domain (TPR-AuNC group). Comparing previous studies, it became apparent that the presence of the metal cluster on the Prot-NM has a positive effect on the internalization and the final therapeutic effect of the Hsp90 inhibitory activity.<sup>12–14</sup> Considering this, only hybrid formulations with AuNCs were selected for evaluation.

In the case of the TPR-Hsp90-AuNC group, the Alexa-488 specific signal was intense and well-defined in specific intracellular locations, confirming that the observed fluorescence signal corresponded indeed to the internalized TPR-Hsp90-AuNC as no equivalent signal was found in the other groups. Nonetheless, some low intensity auto-fluorescence signal was



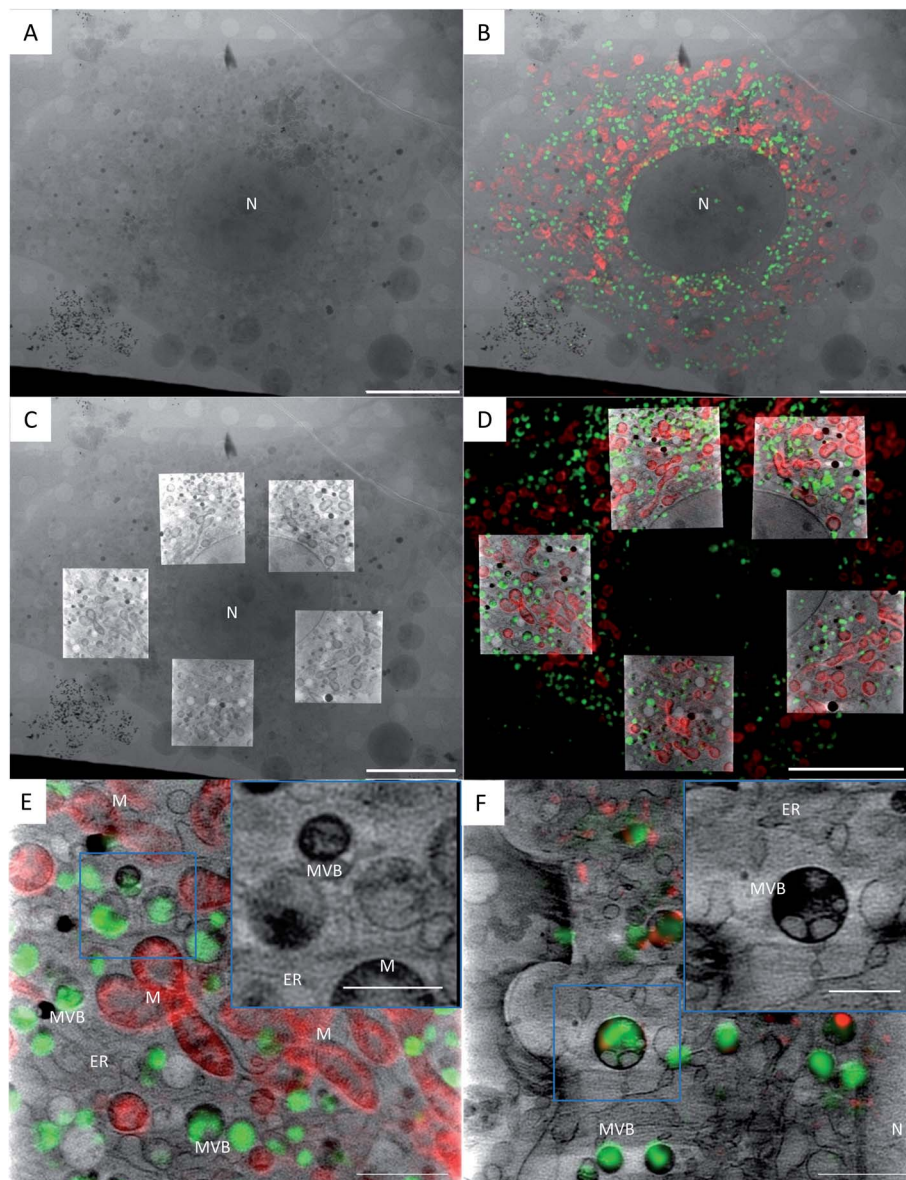


**Fig. 1** Correlation of a TPR-Hsp90-AuNC treated NIH-3T3 cell using cryo-3D-SIM showing the mitochondria in red (cmxros mitotracker) and the TPR-Hsp90-AuNC in green (alexa-488), and cryo-SXT showing the reconstructed linear absorption coefficient. (a) X-ray projection mosaic; (b) cryo-SIM signal projection overlaid on X-ray mosaic; (c) single slice of the tomographic reconstructions of 5 areas overlaid on the X-ray mosaic; (d) single slice of the tomographic reconstruction overlaid with a single slice of the cryo-3D-SIM, see S5† for the correlation accuracy map. Scale bar: (a–d) 10  $\mu\text{m}$ ; bottom row: single slice from a single tomographic reconstruction showing the reconstructed absorbance from SXT overlaid with the cryo-SIM signal from TPR-Hsp90-AuNC (green) coming from MVBs and from the mitochondria (red) in NIH-3T3 (E) and cardiac primary mice fibroblasts (F). Scale bar: 2  $\mu\text{m}$ ; inset 1  $\mu\text{m}$ . N = nucleus, M = mitochondria, MVB = multivesicular bodies, ER = endoplasmic reticulum.

observed in the control and the TGF- $\beta$  groups at both excitation wavelengths (405 nm and 488 nm) (see S1, S2 and S3†). In the case of the TPR-AuNC group a low but distinct signal was found (S2 and S3†) indicating the presence of TPR-AuNC at significantly lower concentrations than TPR-Hsp90-AuNC in the cell. The comparison of the maximum fluorescence signal value collected between the treatment groups showed a slight increase of the TPR-AuNC signal compared to the auto-fluorescence signal of the control (2-fold) and TGF- $\beta$  (1.5-fold), and a 6-fold increase in value for the TPR-Hsp90-AuNC

compared to the TPR-AuNC (see S3†). After cryo-3D-SIM imaging, cryo-SXT was performed on the same cells at the Mistral beamline (Fig. 1).

#### **Cryo-SXT provides ultrastructural information of the cell and places the fluorescence signal unambiguously within multivesicular bodies**

Fig. 1 presents the correlated data of a TPR-Hsp90-AuNC treated NIH-3T3 cell. Fig. 1A shows the 2D X-ray projection mosaic (*i.e.* tile-scanned projections covering a grid square) of the full cell





## TPR-Hsp90-AuNC

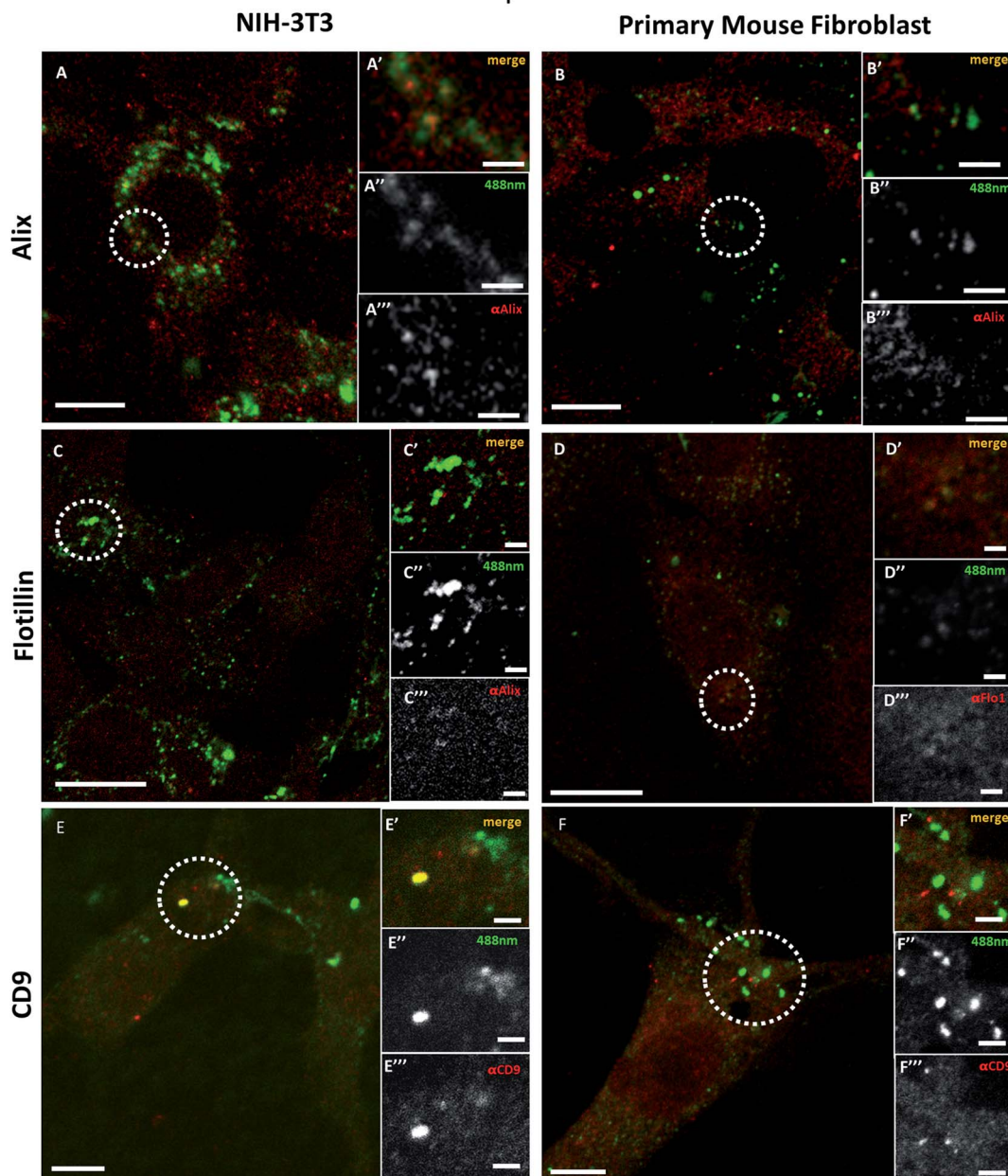


Fig. 2 TPR-Hsp90-AuNC co-localization study on NIH-3T3 and primary mice fibroblasts, respectively, of anti-alix (a and b), anti-flotillin (c and d) and anti-cd9 (e and f) using confocal microscopy. The inset shows the merged ('), green (alexa488, ") and red (from the respective antibody, ""') signals. Scale bars: (a; b; e; and f) 5  $\mu\text{m}$ ; (c and d) 3  $\mu\text{m}$ ; insets for (a; b; c and d), 1  $\mu\text{m}$ ; insets for (e and f) 2  $\mu\text{m}$ .

and Fig. 1B its overlay with the 2D SIM data projection. The red fluorescence signal corresponds to the mitotracker Red CMXRos (ThermoFisher) and the green to the Alexa488-labelled TPR-Hsp90-AuNC. For this cell, five areas within the cytoplasm surrounding the nucleus were chosen for tomography collection, and a single slice of the resulting combined reconstructions is shown in Fig. 1C, superimposed on top of the X-ray 2D mosaic. In Fig. 1D a single slice from the correlated 3D datasets is shown (see S4† for the correlation accuracy map and for a video of the whole 3D stack). No laser damage was noticed at the achievable resolution of cryo-SXT (30 nm half pitch

according to the FSCe/o criterion, see S5†)<sup>19,31–33</sup> after cryo-3D-SIM. Correlating both 3D datasets, the TPR-Hsp90-AuNC signal was unambiguously located in multivesicular bodies (MVBs) which were homogeneous in size (0.5–1  $\mu\text{m}$  in diameter) and distributed throughout the cytoplasm (Fig. 1B, D and 2). The calculated correlation accuracy map shows an accuracy down to 70 nm although this will vary within the volume region and depends directly on the fiducialisation strategy chosen<sup>14</sup> as shown in S4.† These MVBs showed vesicle-like compartments with different morphologies and higher linear absorption coefficient in the case of primary mouse fibroblasts, which



might indicate a different mechanism of processing this TPR-Hsp90-AuNC accumulation by the cell (see Fig. 1 bottom and S6† for additional information on MVB morphologies in both cell types). Note that cryo-SXT directly reconstructs the linear absorption coefficient value of the elemental composition within each voxel, hence being quantitative and therefore allowing direct comparison.<sup>24</sup>

In order to evaluate the number and size of MVBs observed upon the different treatments, we segmented the volumes using Amira software<sup>34</sup> (see Fig. 4). Even though no direct comparison can be made between cell types due to the larger size of the primary cells compared to NIH-3T3, the appearance and tendencies observed in the two can be compared. When evaluating the TGF- $\beta$ -treated groups, both cell types seem very similar to the control group, having an almost identical average and slightly decreased median MVB volume, the latter being more evident in NIH-3T3 than in primary fibroblasts. This result suggests that these MVBs are part of a normal cell function and not related or affected by stress-induction. In the case of cells treated with TPR-Hsp90-AuNC, a large increase in MVB number was found with respect to the control group (85% increase for NIH-3T3 and 74% for primary mouse fibroblasts, see Fig. 4). When focusing on the primary fibroblasts a non-significant decreased volume was observed. Together with the increase in MVB number, these results suggest the recent formation of new vesicles upon the treatments. Regarding the NIH-3T3 cells, the vesicles present an increase in volume, although non-significant, suggesting that these vesicles were formed early after incorporation of the therapeutic agent and matured by the time of vitrification. Finally, the samples treated with TPR-AuNC showed a slight increase in the number of MVBs compared to the untreated control (29% for NIH-3T3 and 11% for primary fibroblasts) and TGF- $\beta$  treated cells, although not significant as overall numbers are very low. However, in both cell types this group presented the smallest average and median volume for the MVBs ( $t \leq 0.05$  for NIH-3T3 and  $t \leq 0.01$  for primary fibroblasts). Ultimately, with the exception of the TPR-Hsp90-AuNC samples, the MVBs evaluated in both cell types were very similar when the same treatment is compared.

### Confocal microscopy reveals the nature of the organelle containing the therapeutic agent

To determine which type of vesicles contains the TPR-Hsp90-AuNCs and understand their role, different biomarkers were tested to evaluate their spatial association with the Alexa488 signal. The selected targets were: Alix, Flotillin-1, CD9 and LC3-II, all associated with different types of cellular vesicles as explained below. All assays were performed on cells fixed with paraformaldehyde (PFA) and imaged by confocal microscopy.

Fig. 3 shows the comparison of the co-localization of Alix (Fig. 2A and B), Flotillin-1 (Fig. 2C and D), and CD-9 (Fig. 2E and F) with TPR-Hsp90-AuNC in NIH-3T3 and primary fibroblasts. Both anti-Alix and anti-Flotillin-1 are markers for MVB biogenesis while anti-CD9 (anti-tetraspanin CD9) is associated with adhesion, motility, membrane fusion, signal trafficking vesicles and cargo transfer from cellular vesicles.<sup>35,36</sup> In NIH-3T3

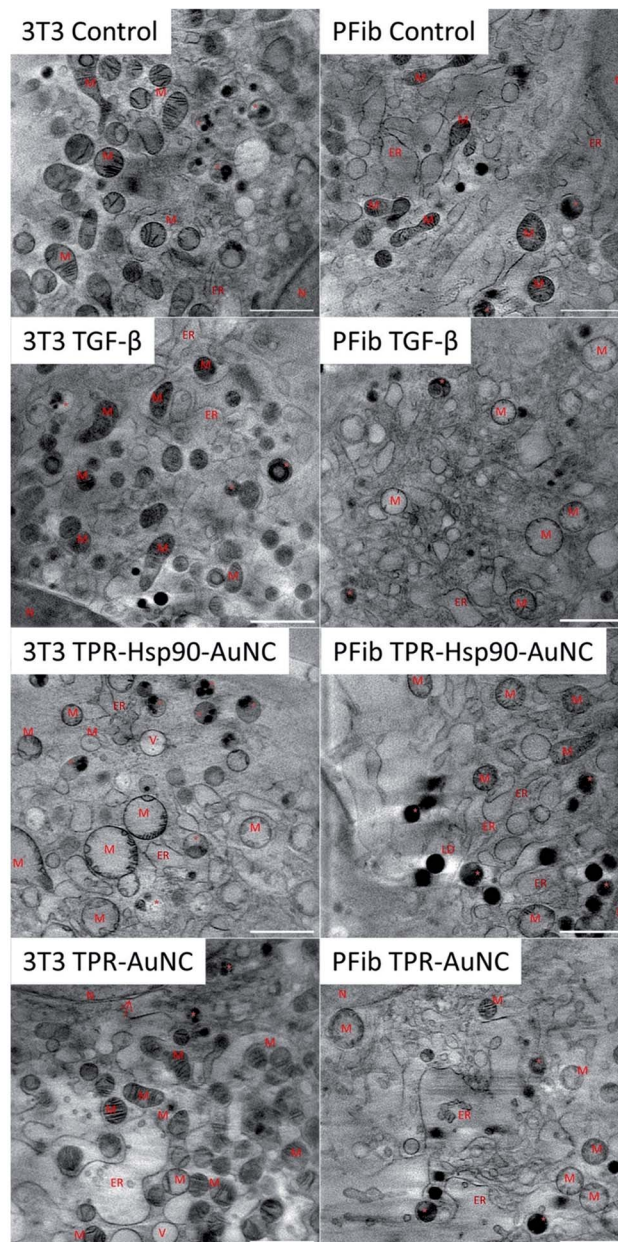


Fig. 3 Snapshot of a representative tomographic reconstruction for each sample showing the reconstructed absorbance value to compare the morphology of the cell after treatment. \* = MVB; M = mitochondria; N = nucleus, ER = endoplasmic reticulum, V = vacuole, LD = lipid droplet, arrow = nuclear double membrane. Scale bar: 2  $\mu\text{m}$ .

cells a spatial co-localization (at the achievable confocal resolution) of TPR-Hsp90-AuNC with anti-Alix and anti-CD9 was observed. In addition, a low anti-Flotillin-1 signal was detected and there was no spatial association with the therapeutic molecule. In the case of primary mouse fibroblasts, some spatial association was observed with anti-Alix, although the signal was lower compared to the NIH-3T3 cells. Similar to NIH-3T3, some signal was detected from anti-Flotillin-1, although it appeared diffused. Finally, some foci were observed from anti-CD9, but there was no association with the TPR-Hsp90-AuNC.





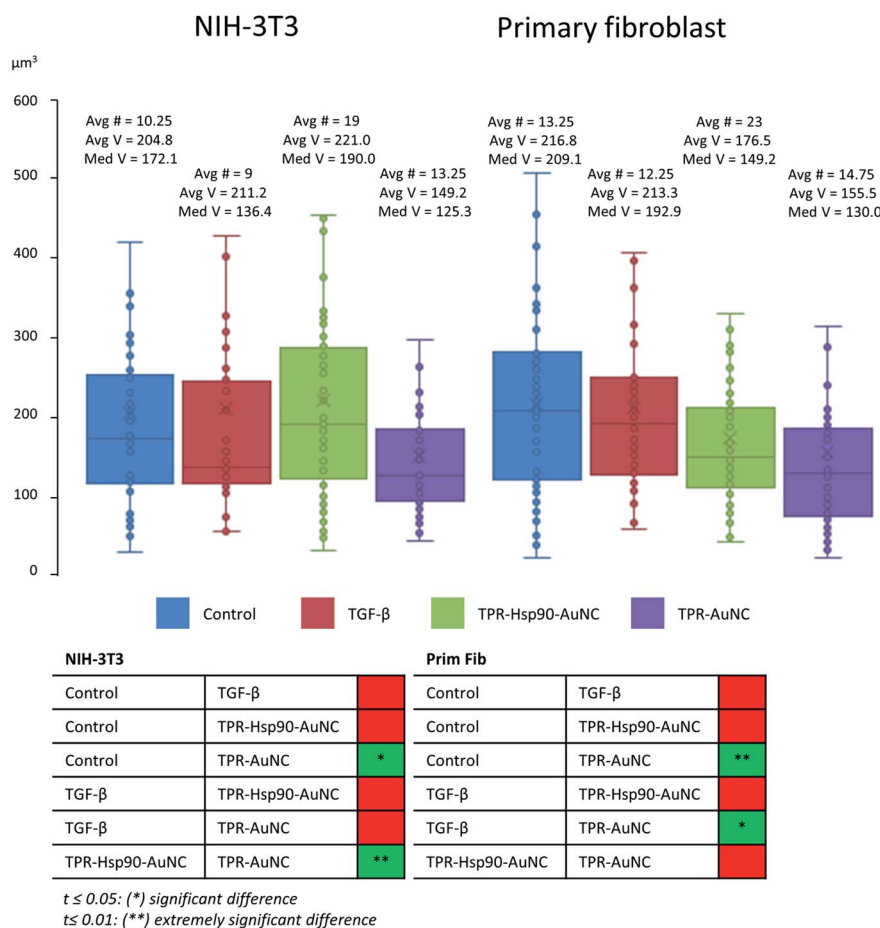


Fig. 4 Comparison of MVB volumes of both NIH-3T3 and primary fibroblast cells measured after segmentation using Amira.<sup>34</sup> Avg # represents the average number of segmented MVBs in a tomogram, Avg V stands for average volume and Med V stands for median volume (both in μm<sup>3</sup>). The measured data were tested for variance and the corresponding t-test was used to determine statistically relevant differences between groups, the results of which are shown in the table below.

With the above observations, the two cell types appear to show the same tendency with the exception of the CD9 biomarker that showed co-localization with TPR-Hsp90-AuNC in NIH-3T3 and not in primary fibroblasts.

These biomarkers were also tested upon TPR-AuNC treatment (S7†). The TPR-AuNC group showed the same associations with anti-Alix for both cell types and a co-localization with anti-CD9 in NIH-3T3, however none in primary fibroblasts similar to TPR-Hsp90-AuNC. Moreover, and in contrast to TPR-Hsp90-AuNC, a clear spatial association between Flotillin-1 and TPR-AuNC was observed, especially in primary fibroblasts. Few foci were also observed in NIH-3T3 cells.

The last biomarker, anti-LC3-II, was chosen to test for autophagy and degradation *via* autophagosomes (S8†). A small number of foci were detected in both cell types for both treatments; however, only in NIH-3T3 cells treated with TPR-AuNC an association was observed. Overall, these results ruled out the conjecture that TPR-Hsp90-AuNC-containing MVBs were involved in the autophagosome pathway. The possibility of an enhancement of programmed cell-death apoptotic events caused by stress upon treatment was also tested using the

activated caspase-3 (cleaved caspase-3 Asp175).<sup>37</sup> No increments were seen for TPR-AuNC, TPR-Hsp90-AuNC, or TGF-β treated cells, which indicates that TGF-β did not induce apoptosis at the concentration used in this study. Moreover, the control cells were also labelled and imaged and showed no foci with any of the tested biomarkers (S9†).

### Cryo-SXT enables a statistical analysis of the observed morphological differences upon treatment

In addition to elucidating the intracellular fate of Prot-NM, cryo-SXT allowed evaluating possible changes in the cellular ultrastructure upon treatment (Fig. 3). Of special interest was the mitochondrial morphology as their appearance is directly related to the cellular health, as already mentioned. In order to obtain statistical information about morphological changes of the different cell groups and to understand the effect of the treatment, the mitochondria were also segmented using Amira software.<sup>34</sup> This segmentation allowed evaluating the number, volume and shape dependence of these organelles for each treatment with respect to the control cells.



In the case of the NIH-3T3 cells, the TGF- $\beta$  group presented an increased number of mitochondria (78% more compared to the control) with smaller volume and increased elongation (see Fig. 3 and 5). This indicates that the cells are both increasing

their mitochondria surface area and are producing more mitochondria for upcoming changes. Previous work showed that treatment with TGF- $\beta$  leads to differentiation or activation of the cell to increase collagen production,<sup>38</sup> both being highly

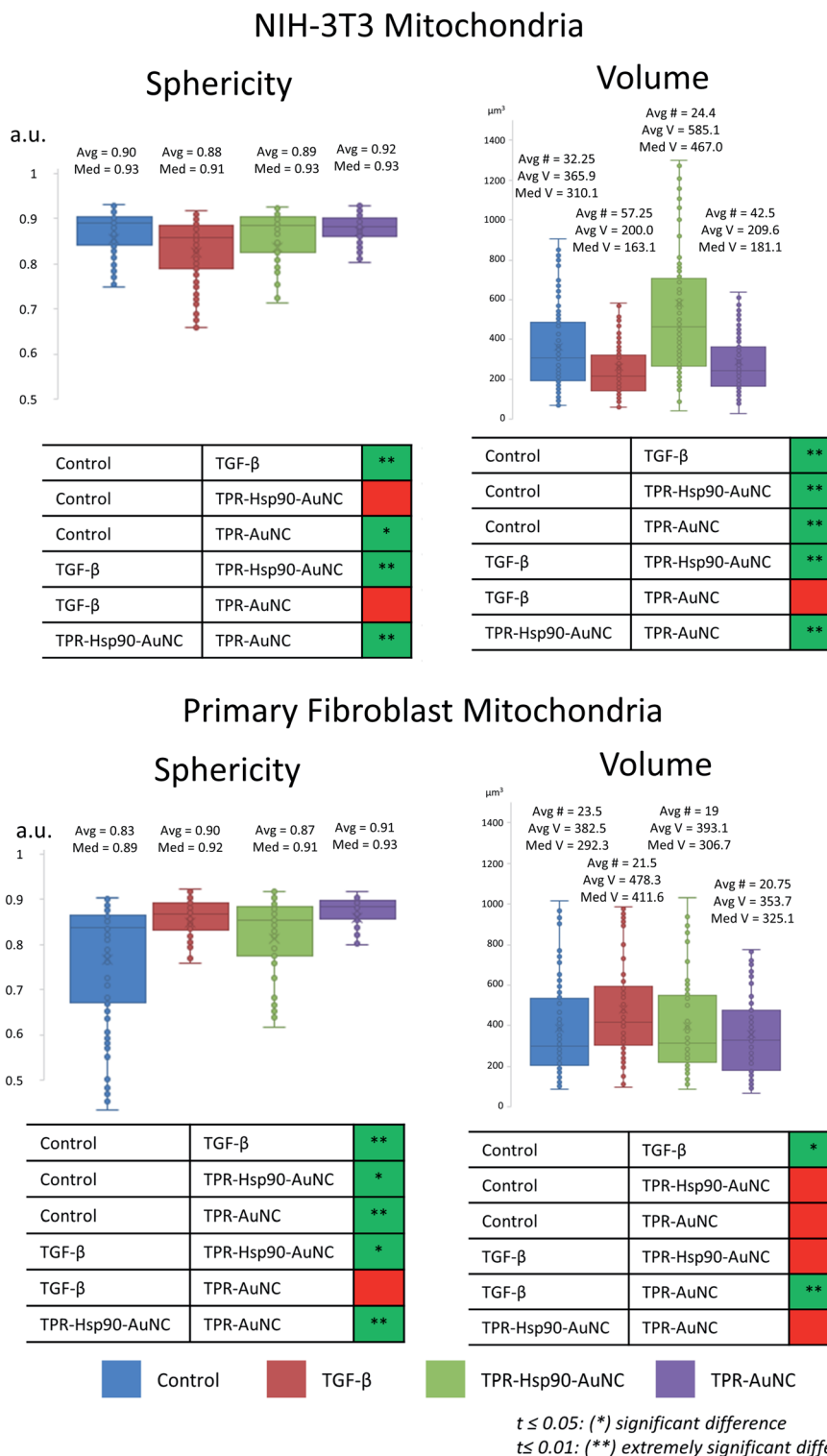


Fig. 5 Comparison of mitochondrial volumes of both NIH-3T3 and primary mouse fibroblast cells, measured after segmentation using Amira.<sup>34</sup> Avg # represents the average number of segmented mitochondria in a tomogram, Avg V stands for average volume and Med V stands for median volume (both in  $\mu\text{m}^3$ ). The measured data were tested for variance and the corresponding *t*-test was used to determine statistically relevant differences, the results of which are shown in the table below.



energy consuming processes. This confirms that the TGF- $\beta$  treatment promotes the desired cellular pro-fibrotic events and that the changed mitochondrial morphology is a natural reaction to the activation with TGF- $\beta$ . The TPR-Hsp90-AuNC group showed a smaller number of mitochondria (44% less compared to the control) with increased volume. This type of mitochondrial swelling is usually associated with cellular stress.<sup>39</sup> In the case of TPR-AuNC, a similar effect on the cells to that of the TGF- $\beta$  group was expected. Indeed, similar mitochondrial volume but with a slight increase in the number of mitochondria (20%) was observed. However, the mitochondrial elongation present in the TGF- $\beta$  group was not observed.

When analyzing the cardiac primary mouse fibroblast, significant differences compared to the NIH-3T3 cells were observed (see Fig. 3 and 5). First, the number of mitochondria was similar in all four groups (see Fig. 5), although a decrease of 20% compared to the control is found in the TPR-Hsp90-AuNC group, following the same tendency as that for NIH-3T3. Second, the mitochondrial volume was also similar for all the groups except the TGF- $\beta$  one which showed a significantly higher mean volume compared to the control. This can be explained by the increased energy demand, similar to the observed effect in NIH-3T3 cells. In terms of sphericity, there were significant differences between most of the groups. In contrast to what was seen in the NIH-3T3 cells, the control group had the most diverse shapes consistent with the expected continuous fission and fusion of mitochondria.<sup>29</sup> For both TGF- $\beta$  and the TPR-AuNC groups, mitochondria appeared rather spherical, while the TPR-Hsp90-AuNC group showed slightly greater variety of shapes, but still leaning towards spherical mitochondria. Mitochondria morphological changes due to fission and fusion are beneficial under conditions of high-energy demand<sup>40</sup> as in the case of TGF- $\beta$  induced collagen production in fibroblasts. Note that apart from the control, all groups have been 'activated' with TGF- $\beta$  and therefore higher mitochondrial activity demand was expected.

Even though no direct comparison of the numbers between cell types can be done, as primary mouse fibroblasts are larger than NIH-3T3 cells, tendencies and the mitochondria appearance can be compared. Primary mouse fibroblasts seemed overall more stable, as no large divergence from the control was measured, although a significant reaction towards the activation with TGF- $\beta$  was observed. In contrast, each treatment in NIH-3T3 cells causes a unique and seemingly extreme reaction. A significant reduction in mitochondrial size combined with increased number suggests mitochondrial fission events, which play a critical role in the attenuation of mitochondrial damage.<sup>41</sup> In addition, the presence of many small, rounded mitochondria points to a stationary phase of the cell with low activity.<sup>42</sup> These findings already suggest that the NIH-3T3 cells experience more difficulties when dealing with a sudden change in cellular homeostasis, as in the case of TGF- $\beta$  activation. Furthermore, the mitochondrial swelling observed in the TPR-Hsp90-AuNC groups, which is a clear indicator of oxidative stress,<sup>43</sup> supports this hypothesis. These results demonstrate that primary mouse fibroblasts are more resilient to an altered cellular homeostasis which is in this case induced by both TGF-

$\beta$  and the nanomaterial treatment compared to the immortalized embryonic NIH-3T3 fibroblasts.

It is worth mentioning that no structural changes have been observed in the cell nuclei, lipid droplets or vacuole numbers whereas in the case of the ER, some opening was observed in the groups treated with Prot-NM for both cell types with respect to their control cells. This type of ER enlargement is normal in cardiac fibroblasts in which fibrosis events have been triggered, as is also stimulated with the TGF- $\beta$  treatment. This effect was already shown previously<sup>12</sup> and was here confirmed. However, in the NIH-3T3 TPR-AuNC group this effect appeared even larger than for the TGF- $\beta$  group (Fig. 3).

Finally, in order to confirm the findings of previous studies<sup>12</sup> that this Prot-NM can indeed inhibit collagen production, NIH-3T3 cells were incubated for 48 h applying the same treatment groups and imaged. Note that, to this aim, tomograms were collected in extracellular areas between cells, where collagen bundles are expected. As was previously described for a similar Hsp90 inhibitory molecule (CTPR390-488),<sup>12</sup> some collagen fibers were found in the TPR-Hsp90-AuNC group. However, these fibers seemed less structured and in lower quantity than for the TGF- $\beta$  group, which presented clearly defined collagen bundles as expected (see S10<sup>†</sup>). Therefore, a complete inhibition of extracellular collagen production in NIH-3T3 cells was not achieved upon treatment, but a substantial reduction was indeed visible.

## Discussion

Alix is an accessory protein of the endosomal sorting complex required for transport and has been related to the biogenesis of trafficking vesicles, such as extracellular vesicles.<sup>44</sup> The cellular trafficking-related protein Flotillin-1<sup>45</sup> has been related to endocytosis and endosomal trafficking events. In addition, lipid raft-dependent endocytosis can be mediated by Flotillin-1 that would be recruited to the surface forming pre-endocytic clusters.<sup>45</sup> TPR-Hsp90-AuNC did not show co-localization with Flotillin-1, while TPR-AuNC did. The lack of association for the first could suggest that the protein hybrid does not enter *via* endocytosis. The ability of TPR-Hsp90-AuNC to bind to extracellular Hsp90<sup>12</sup> (may allow it to enter the cell bound to this chaperone through a different route than TPR-AuNC. This mechanism would also explain the lower intracellular concentration of TPR-AuNC as an active transport *via* Hsp90 naturally results in higher intracellular concentrations compared to a passive, endocytosis-dependent incorporation. After uptake of the nanomaterials, trafficking vesicles presenting Alix, which showed association with both Prot-NM, could then be the main transport route. The difference concerning the association with CD9 for both nanomaterials, observed only in NIH-3T3 cells, can be related to exocytosis events and may suggest a different cell-dependent way of dealing with the Prot-NM. This hypothesis is in line with our observation of an increased absorbance of the MVBs in primary fibroblasts compared to NIH-3T3 cells (Fig. 1 bottom and S6<sup>†</sup>) by cryo-SXT. Overall, these results suggest that the MVBs are mainly related to endosomal trafficking events, however the origin of the endosomal trafficking





seems to differ depending, not only on cell type, but also on the presence of the Hsp90 binding module.

Cryo-SXT allowed us to draw conclusions regarding the reaction of the cell towards the treatment. The immortalized NIH-3T3 fibroblasts showed clear signs of stress in the form of mitochondrial swelling, likely due to the TPR-Hsp90-AuNC treatment. This swelling event was not observed for TPR-AuNC, which suggests a direct link between the molecular changes promoted by the binding of the hybrid functional protein to the C-terminal end of Hsp90,<sup>14</sup> although the lower uptake could also explain this lack of visible swelling. Other studies have already reported that stress, especially oxidative stress, induces mitochondrial swelling, which would support our first hypothesis.<sup>43</sup> Whether the stress is induced only by the Hsp90 inhibition<sup>46,47</sup> or also because of the presence of the AuNC<sup>48,49</sup> is therefore still to be answered.

Both cell types were affected by a low intracellular TPR-AuNC concentration, as shown by the morphological differences in mitochondria shape and number, as well as in the extra ER enlargement, especially in NIH-3T3 cells. This type of ER enlargement is normal in cardiac fibroblasts in which fibrosis events have been triggered as shown previously<sup>12</sup> and confirmed here. Nonetheless, the fact that TPR-AuNC treatment has a noticeable effect on the cells, while missing the Hsp90 inhibitory domain suggests that the observed effect for the NIH-3T3 TPR-Hsp90-AuNC group is probably not entirely due to the Hsp90 inhibition. These effects could stem from the AuNC, the metallic component of the Prot-NM as was suggested before. Note that the increased Hsp90 production is not the only effect induced by the TGF- $\beta$  activation. Another possibility could therefore be related to a different signaling cascade induced by the TGF- $\beta$ . This hypothesis is supported by our observation in the TGF- $\beta$  group, which showed a drastic morphological change compared to the control group. Ultimately, more research will be needed to investigate these observations and to determine which aspect of the treatment is causing the morphological changes observed. Finally, it is worth mentioning that these results reinforce the need of evaluating systematically the cellular structure upon application of specific treatments with adequate imaging techniques to be able to assess the cellular response.

Primary mouse fibroblasts, on the other hand, do not exhibit these symptoms of stress after overnight TPR-Hsp90-AuNC treatment, indicating that the cells had time to recover or adapt to the new conditions. The fact that the number of mitochondria is similar in every group, is in line with other work that related organelle size to cellular homeostasis,<sup>1</sup> arguing that every cell type has an optimum number of organelles and a deviation from this number suggests a change in gene expression. While previous studies<sup>12-14</sup> already highlighted the lack of negative effects, we now confirm that at the ultrastructural level TPR-Hsp90-AuNC is a viable option to inhibit the Hsp90 protein in primary mouse fibroblasts while also ensuring its ATPase activity and thereby keeping the cell in homeostasis. Despite the side effects in NIH-3T3 cells, we confirm here that Hsp90 inhibition at the C-terminal end reduces collagen overproduction in both cell types.

## Methods

### TPR preparation

The TPR variants used in this work have been previously described.<sup>11,14</sup> The His-tagged proteins have been purified by affinity chromatography following standard protocols. C41 (DE3) cells transfected with the pProEx-HTA plasmid encoding the desired TPR gene, were grown in an orbital shaker at 37 °C to an optical density of 0.6–0.8. Then the protein expression was induced with 1 mM isopropyl  $\beta$ -D-thiogalactoside (IPTG) and the cells were left for 16 hours at 20 °C. The cells were centrifuged and lysed by sonication in 50 mM Tris, 500 mM NaCl, pH 8.0. Proteins were purified from the supernatant using a 5 ml HisTrap Q column (GE Healthcare). Then, the his-tag was removed by TEV protease cleavage and purified by gel filtration chromatography (HiLoad 16/60 Superdex 200 column).

### AuNC formation

AuNCs were synthesized and stabilized in the protein scaffolds using a protocol based on previously reported procedures.<sup>13,14</sup> A protein at 20  $\mu$ M was incubated with HAuCl<sub>4</sub> (30 eq. with respect to protein) for 1 hour at 20 °C. Afterwards, a reduction step was applied by adding 100 eq. with respect to the Au concentration of sodium ascorbate and left to incubate at 50 °C for 72 h. Finally, the Prot-NM was purified by gel filtration (Sephadex G-25 column).

### Alexa labeling

Alexa Fluor 488 NHS ester was used to label the TPR-Hsp90-AuNC and TPR-AuNC proteins through their primary amines at a 1 : 2 stoichiometry to avoid over-labeling and potential disruption of the protein recognition activity.

### Primary mouse fibroblast isolation

Live animal studies were approved by the University of Cantabria (Spain) Institutional Laboratory Animal Care and Use Committee in compliance with the Guide for the Care and Use of Laboratory Animals (ILAR, 1985) and were conducted in accordance with the “European Directive for the Protection of Vertebrate Animals Used for Experimental and Other Scientific Purposes” (European Communities Council Directive 86/606/EEC).

Adult cardiac fibroblasts from mice C57BL6 strain (wildtype) were isolated directly from enzymatically digested hearts (collagenase, trypsin and DNase) followed by centrifugation and filtration. They were maintained in Dulbecco's Modified Eagle's Medium (DMEM) containing 10% FBS and 100 U/ml penicillin-streptomycin. The cells ( $2 \times 10^5$ ) were plated in 35 mm cell culture dishes incubated at 37 °C in 5% CO<sub>2</sub>. For experimental procedures, low passage cells (p2) were seeded onto 60 mm cell culture dishes.

### Sample preparation for CLXT

The sample preparation protocol is based on a previously published procedure<sup>2,50</sup> and involves cryogenic liquids. Both



NIH-3T3 and primary myocardial mouse fibroblasts were grown in complete culture medium (DMEM with 10% FBS and 1% Penicillin/Streptomycin) at 37 °C and 5% CO<sub>2</sub> until a confluence of 70–80% was reached. At this point the cells are ready for subculture, or for sample preparation. As the sample support, gold quantifoil R 2/2 holey carbon-film microscopy grids (Au-G200F1) were used. Before cell deposition, grids were placed in P60 Petri-dishes, already separated by the type of treatment, and UV-sterilized. Spreading the grids at this stage minimizes grid handling and possible damaging. Cells are washed in PBS and seeded on top of the grids at a concentration of around  $2\text{--}3 \times 10^5$  cells per ml (3 ml total in the case of a P60 Petri dish). After allowing the cells to settle and get accustomed to the surface for around 24 hours, they were treated. Both the NIH-3T3 and primary fibroblasts were divided into 4 groups: control, TGF- $\beta$  activated, TGF- $\beta$  activated and treated with TPR-Hsp90-AuNC, and finally TGF  $\beta$  activated and treated with TPR-AuNC lacking the Hsp90 inhibitory domain. Cells were activated with 1 ng ml<sup>-1</sup> TGF- $\beta$  final concentration and for the TPR-Hsp90-AuNC, as well as TPR-AuNC groups, the activated cells were treated with their respective Prot-NM at a final concentration of 0.8  $\mu$ M. Note that the concentration of TGF- $\beta$  to activate the cells was increased compared to the previous study (by 3 times).<sup>12</sup> This increase provided a more consistent response of the cell population without affecting the gene-expression on a single cell basis (data not shown). After overnight incubation, Mitotracker Red CMXRos (ThermoFisher) was added to the grids, following manufacturer recommendations. After the incubation time of the fluorescent dye passed, a mix of 100 nm gold fiducial markers (BBI Solutions; 10 $\times$  concentrated) and 200 nm Tetraspecks (ThermoFisher; 5 $\times$  diluted) was prepared and 3  $\mu$ l thereof was deposited on the grid followed by blotting of 2 s using a Whatman #1 filterpaper and vitrification through plunge freezing in liquid ethane precooled by liquid nitrogen in a Leica EM-CPC. Care has to be taken as grids have to be kept at cryogenic temperatures from this point on at all times. Pre-screening of the vitrified grids was done using a Linkam CMS196 cryo-stage on a Zeiss Axio Scope fluorescence microscope to determine the integrity of the grid as well as pin-pointing cells of interest. A selection of grids is made at this point for correlative workflow.

### Cryo-3D-SIM

The selected grids, at least two per cell and condition, were sent to B24 at the Diamond Synchrotron (UK). The grids were imaged with a home-built cryo-3D-SIM<sup>31</sup> to collect the green signal coming from the Alexa488 on the TPR proteins ( $\lambda_{\text{exc}}$  488/ $\lambda_{\text{em}}$  525, 40 mW, 100 ms), and red signal coming from mitotracker Red CMXRos ( $\lambda_{\text{exc}}$  561/ $\lambda_{\text{em}}$  605, 40 mW, 50–100 ms depending on staining efficiency) using a 100 $\times$  0.9 NA objective lens achieving a lateral resolution of roughly 210 nm full width at half maximum (FWHM) at an emission wavelength of 488 nm.<sup>15</sup> For each sample-type three to six cells, preferably from different grids, were imaged and the collected data were processed on site.

### Cryo soft X-ray tomography

The grids were then sent back to Mistral at ALBA (Spain) for data collection using soft X-ray microscopy.<sup>27,28,50</sup> The grids were loaded into the transmission X-ray microscope (TXM) chamber and the cells imaged prior with the cryo-3D-SIM were identified using the on-line visible light fluorescence microscope inside the TXM vacuum vessel with a long distance 20 $\times$  objective. Once the areas were found again, tilt series were collected at a photon energy of 520 eV in areas showing interesting fluorescence signals in the cryo-3D-SIM data. In addition, other cells were imaged for morphological data evaluation, comparison and statistics. All data were collected using a Ni Fresnel zone plate lens with an outermost zone width of 25 nm (courtesy of S. Rebhein, HZB-Bessy II), giving an effective voxel size of 10 nm<sup>3</sup>. Depending on the sample and the position of the cell on the grid, images were collected covering a maximum angular range of  $-65^\circ$  to  $+65^\circ$  (or less) with a constant step size of  $1^\circ$ . While for the lower tilt angles an exposure time of 1–2 seconds was used, at higher tilt angles the exposure time was increased up to 4 seconds, to increase the signal-to-noise ratio while taking care to not oversaturate the CCD camera. The data were then pre-processed by normalization with the collected flatfield signal (flux impinging the sample) and the corresponding machine current, followed by deconvolution of the measured PSF of the TXM at the corresponding energy.<sup>31</sup>

### Fluorescence and immunofluorescence assays

The immunofluorescence assays of Hsp90 were performed using the aforementioned treatments. Then samples were fixed (4% paraformaldehyde), permeabilized (20–30 min 0.05% Triton-X in PBS 1 $\times$ ) and incubated overnight at 4°C with different primary antibodies anti-Alix (1 : 100, sc53540), anti-Flotillin-1 (1 : 100, sc74566), antiCD9 (1 : 100, donation from Sanchez-Madrid), anti-LC3-II (Cell Signaling #2775) and anti-caspase-2 (ab182657). The samples were washed with 0.05% Tween 20 in PBS, incubated for 30 min in the specific secondary antibody conjugated with Alexa-568 (ThermoFisher), washed in PBS and mounted with the Vectashield antifade mounting medium (Vector).

Confocal images were obtained in the microscopy facility (IDIVAL, Santander, Spain) with a confocal microscope NIKON A1R spectral (405 nm, 488 nm, 514 nm, 561 nm, 638 nm) and Fiji<sup>52</sup> was used for data visualization.

### Data processing

The tilt-series were aligned using the 100 nm Au fiducials and the IMOD software.<sup>53</sup> The reconstruction was performed using the SIRT algorithm<sup>54</sup> with tomo3d with long object compensation<sup>55</sup> for a fast reconstruction, which is for visualization purposes only, or using the ART algorithm<sup>56</sup> with tomoj<sup>57</sup> for linear absorption coefficient recovery. The tomographic reconstruction of each of the cells (several tomograms per cell collected) imaged before using the cryo-3D-SIM were then post-processed using Fiji<sup>52</sup> to ensure they are aligned to each other by flattening and cropping in the z-direction to adjust the height,



based on the carbon quantifoil support layer. The correlation was done using the ICY<sup>58</sup> plugin in ecCLEM.<sup>59</sup> First, the cryo-SXT reconstructions were 2D transformed to the X-ray mosaic to place them in the context of the whole cell as each tomogram covers a volume of 10  $\mu\text{m}^3$  of the cell. To prevent excessively large files, cropping of the X-ray mosaic to the area containing the reconstructions is performed. The transformed files could then be combined into one for subsequent 3D correlation. Because of the chromatic shift of the 3D-SIM, the fluorescent channels were first aligned to each other using the 200 nm Tetraspecks. After this, the now aligned fluorescent channels were roughly transformed in 2D to the X-ray mosaic using large features, like, for example, the holes in the quantifoil film or using large organelles, like mitochondria. After this the fluorescent data were transformed in 3D using more fine features such as Tetraspecks or recognizable organelle shapes.

### Statistical analysis of organelles

The tomographic reconstructions were segmented using Amira software.<sup>34</sup> Measurements of the segmentation were performed using the Amira module Label Analysis. For the volume, the native measure is used but for the sphericity a custom measure had to be created using the formula:

$$\text{Sphericity} = \frac{\pi^{\frac{1}{3}} \times (6V)^{\frac{2}{3}}}{A}$$

with  $V$  being the volume of the label and  $A$  being the surface area. For each condition four tomographic reconstructions belonging to four different cells were segmented and measured. The statistical analysis was performed using Excel 2016s Data Analysis add-in. First, the datasets were tested for equal or unequal variance, followed by the corresponding two-tailed  $t$ -test using a cut-off value of 0.05 to test for significance between the groups.

## Conclusions

Herein, CLXT has allowed locating unambiguously and in the 3D cellular environment, a designed therapeutic agent inhibiting Hsp90 after being internalized by two different types of fibroblasts. Furthermore, this novel methodology enables evaluating the effects of the different treatments at the cellular level which is essential for a future practical usage at the clinical level. Cryo-3D-SIM provides excellent specificity using a wide range of common dyes and fluorescent proteins and adequate 3D resolution for correlative purposes, although higher sensitivity at the single molecule level and resolution would be desirable. Cryo-SXT in turn reveals the environmental context and the ultrastructural details, which allow identifying the designed protein–nanomaterial hybrid (Prot-NM) containing organelles and describing the morphological differences accompanying the different treatments. In both cases, the TPR-AuNC with and without the Hsp90 binding module were found in specific multivesicular bodies (MVBs), although in higher numbers in the first case. These MVBs likely play a functional role in cell homeostasis. Furthermore, we found substantial

differences between NIH-3T3 and primary mouse fibroblast cells, which led us to conclude that the immortalized version of a cell type may not always be a good functional alternative when studying molecular processes as deviations from primary cells can occur.

This detailed study, using correlatively cryo-3D-SIM and cryo-SXT to obtain specific intracellular location and ultrastructural information, highlights the relevance of a mechanistic understanding of the molecular process triggered by novel engineered Prot-NM with potential therapeutic applications. Here, a protein engineering-based biological drug (TPR-Hsp90-AuNC) with a demonstrated effect as an antifibrotic molecule has been evaluated. The results of this study reveal the effect of the Hsp90 inhibitory domain and its correlation with its antifibrotic function and mechanism. But at the same time, they show that the presence of a small metallic nanocluster of 4 to 12 atoms, in addition to its function as a stabilizing and tagging module, possibly has an effect on the cellular morphology, which still needs to be investigated further for a complete understanding. It is important to note that, considering the modularity of the engineered system, the inhibitory domain is interchangeable. This opens up possibilities for a wide variety of treatments that could benefit from the design of alternative Prot-NM. As has been shown here, CLXT is able to track the fate of the specific therapeutic agent with high correlation accuracy, as well as monitor with statistical significance the morphological changes due to the treatment, allowing shedding light on the cellular processes triggered. The methodology utilized is applicable to other disease models and systems and will always provide excellent specificity and spatial resolution. These latest results put the focus on the need to study the effects of nanomaterials at the cellular level under close-to-native conditions in order to be able to further propel nanomaterial-based drugs and nanomedicine into the clinic.

## Data availability

The data of the main correlation figure was deposited at the BioImage Archive (<https://www.ebi.ac.uk/biostudies/BioImages>) and EMPIAR (<https://www.ebi.ac.uk/pdbe/emdb/empiar/>). The accession numbers for the data deposited at EMPIAR is EMPIAR-10839, and the accession numbers for the data deposited at the BioImage Archive is S-BSST728.

## Author contributions

J. G. performed all the experiments, with the exception of the confocal microscopy part, which was done by A. P. and A. V. V. Primary fibroblasts were isolated and shipped to Alba by D. M. Prot-NM was prepared and sent to Alba by A. A. Access to the SIM was provided by M. H. and the 25 nm Fresnel zone plate lens was built by S. R. Assistance with the X-ray microscope data collection was provided by E. P., and J. J. C. assisted and guided the data processing and correlation process. E. P. and A. L. C. directed the research and together with J. G. wrote the paper. The manuscript was written through contributions of all





authors. All authors have given approval to the final version of the manuscript.

## Conflicts of interest

There are no conflicts to declare.

## Acknowledgements

We acknowledge the help of R. Oliete (Alba) for his help with the sample preparation and C. Okolo for the cryo-3D-SIM data collected at B24 at Diamond Synchrotron during experimental session BI25162. Cryo-SXT data were collected at Mistral beamline at Alba Synchrotron during experimental sessions 2019093739 and 2020034355. The authors wish to thank F. Madrazo for his time and expertise at the IDIVAL image facility. This project has received funding from the European Union's Horizon 2020 research and innovation programme under the Marie Skłodowska-Curie grant agreement No 754397. This work was partially supported by the European Research Council ERC-CoG-648071-ProNANO, ERC-PoC-841063-NIMM; Spanish State Research Agency, Spain; (BIO2015-72124-EXP), (MDM-2017-0720), (PID2019-111649RB-I00) and (RTI2018-095214-B-I00); the Basque Government (Elkartek KK-2017/00008; RIS3-2019222005); and the Next Generation and Innovation Valdecilla (PREVAL19/05), (IDIVAL INIVAL17/22), (INIVAL20/34), (NVAL18/11) and (NextVal 18/14). This work was performed under the Maria de Maeztu Units of Excellence Program from the Spanish State Research Agency – Grant No. MDM-2017-0720 (CIC biomaGUNE).

## Notes and references

- 1 L. W. Cole, The Evolution of Per-cell Organelle Number, *Front. Cell Dev. Biol.*, 2016, **4**, 85.
- 2 C. A. Okolo, I. Kounatidis, J. Groen, K. L. Nahas, S. Balint, T. M. Fish, *et al.*, Sample preparation strategies for efficient correlation of 3D SIM and soft X-ray tomography data at cryogenic temperatures, *Nat. Protoc.*, 2021, **16**(6), 2851–2885.
- 3 K. E. Porter and N. A. Turner, Cardiac fibroblasts: At the heart of myocardial remodeling, *Pharmacol. Ther.*, 2009, **123**(2), 255–278.
- 4 S. Hinderer and K. Schenke-Layland, Cardiac fibrosis – A short review of causes and therapeutic strategies, *Adv. Drug Delivery Rev.*, 2019, **146**, 77–82.
- 5 M. Liu, B. López de Juan Abad and K. Cheng, Cardiac fibrosis: Myofibroblast-mediated pathological regulation and drug delivery strategies, *Adv. Drug Delivery Rev.*, 2021, **173**, 504–519.
- 6 T. Doetschman, J. v. Barnett, R. B. Runyan, T. D. Camenisch, R. L. Heimark, H. L. Granzier, *et al.*, Transforming growth factor beta signaling in adult cardiovascular diseases and repair, *Cell Tissue Res.*, 2012, **347**(1), 203–223.
- 7 R. Datta, T. Bansal, S. Rana, K. Datta, S. Chattopadhyay, M. Chawla-Sarkar, *et al.*, Hsp90/Cdc37 assembly modulates TGF $\beta$  receptor-II to act as a profibrotic regulator of TGF $\beta$  signaling during cardiac hypertrophy, *Cell. Signalling*, 2015, **27**(12), 2410–2424.
- 8 M. Morikawa, R. Derynck and K. Miyazono, TGF- $\beta$  and the TGF- $\beta$  Family: Context-Dependent Roles in Cell and Tissue Physiology, *Cold Spring Harbor Perspect. Biol.*, 2016, **8**(5), a021873.
- 9 R. García, D. Merino, J. M. Gómez, J. F. Nistal, M. A. Hurlé, A. L. Cortajarena, *et al.*, Extracellular heat shock protein 90 binding to TGF $\beta$  receptor I participates in TGF $\beta$ -mediated collagen production in myocardial fibroblasts, *Cell. Signalling*, 2016, **28**(10), 1563–1579.
- 10 A. L. Cortajarena, T. Kajander, W. Pan, M. J. Cocco and L. Regan, Protein design to understand peptide ligand recognition by tetratricopeptide repeat proteins, *Protein Eng., Des. Sel.*, 2004, **17**(4), 399–409.
- 11 A. L. Cortajarena, F. Yi and L. Regan, Designed TPR Modules as Novel Anticancer Agents, *ACS Chem. Biol.*, 2008, **3**(3), 161–166.
- 12 R. A. Cáceres, T. Chavez, D. Maestro, A. R. Palanca, P. Bolado, F. Madrazo, *et al.*, Reduction of cardiac TGF $\beta$ -mediated profibrotic events by inhibition of Hsp90 with engineered protein, *J. Mol. Cell. Cardiol.*, 2018, **123**, 75–87.
- 13 A. Aires, I. Llarena, M. Moller, J. Castro-Smirnov, J. Cabanillas-Gonzalez and A. L. Cortajarena, A Simple Approach to Design Proteins for the Sustainable Synthesis of Metal Nanoclusters, *Angew. Chem., Int. Ed.*, 2019, **58**(19), 6214–6219.
- 14 A. Aires, D. Maestro, J. Ruiz del Rio, A. R. Palanca, E. Lopez-Martinez, I. Llarena, *et al.*, Engineering multifunctional metal/protein hybrid nanomaterials as tools for therapeutic intervention and high-sensitivity detection, *Chem. Sci.*, 2021, **12**(7), 2480–2487.
- 15 M. A. Phillips, M. Harkiolaki, D. M. Susano Pinto, R. M. Parton, A. Palanca, M. Garcia-Moreno, *et al.*, CryoSIM: super-resolution 3D structured illumination cryogenic fluorescence microscopy for correlated ultrastructural imaging, *Optica*, 2020, **7**(7), 802.
- 16 D. Weiß, G. Schneider, B. Niemann, P. Guttmann, D. Rudolph and G. Schmahl, Computed tomography of cryogenic biological specimens based on X-ray microscopic images, *Ultramicroscopy*, 2000, **84**(3–4), 185–197.
- 17 G. Schneider, P. Guttmann, S. Heim, S. Rehbein, F. Mueller, K. Nagashima, *et al.*, Three-dimensional cellular ultrastructure resolved by X-ray microscopy, *Nat. Methods*, 2010, **7**(12), 985–987.
- 18 J. L. Carrascosa, F. J. Chichón, E. Pereiro, M. J. Rodríguez, J. J. Fernández, M. Esteban, *et al.*, Cryo-X-ray tomography of vaccinia virus membranes and inner compartments, *J. Struct. Biol.*, 2009, **168**(2), 234–239.
- 19 F. J. Chichón, M. J. Rodríguez, E. Pereiro, M. Chiappi, B. Perdiguero, P. Guttmann, *et al.*, Cryo X-ray nanotomography of vaccinia virus infected cells, *J. Struct. Biol.*, 2012, **177**(2), 202–211.
- 20 C. Hagen, P. Guttmann, B. Klupp, S. Werner, S. Rehbein, T. C. Mettenleiter, *et al.*, Correlative VIS-fluorescence and soft X-ray cryo-microscopy/tomography of adherent cells, *J. Struct. Biol.*, 2012, **177**(2), 193–201.

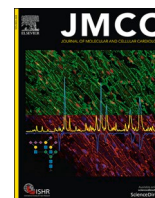


- 21 E. M. H. Duke, M. Razi, A. Weston, P. Guttman, S. Werner, K. Henzler, *et al.*, Imaging endosomes and autophagosomes in whole mammalian cells using correlative cryo-fluorescence and cryo-soft X-ray microscopy (cryo-CLXM), *Ultramicroscopy*, 2014, **143**, 77–87.
- 22 M. Chiappi, J. J. Conesa, E. Pereiro, C. O. S. Sorzano, M. J. Rodríguez, K. Henzler, *et al.*, Cryo-soft X-ray tomography as a quantitative three-dimensional tool to model nanoparticle:cell interaction, *J. Nanobiotechnol.*, 2016, **14**(1), 15.
- 23 A. J. Pérez-Berná, M. J. Rodríguez, F. J. Chichón, M. F. Friesland, A. Sorrentino, J. L. Carrascosa, *et al.*, Structural Changes In Cells Imaged by Soft X-ray Cryo-Tomography During Hepatitis C Virus Infection, *ACS Nano*, 2016, **10**(7), 6597–6611.
- 24 J. Groen, J. J. Conesa, R. Valcárcel and E. Pereiro, The cellular landscape by cryo soft X-ray tomography, *Biophys. Rev.*, 2019, **11**(4), 611–619.
- 25 B. Kepsutlu, V. Wycisk, K. Achazi, S. Kaphishnikov, A. J. Pérez-Berná, P. Guttman, *et al.*, Cells Undergo Major Changes in the Quantity of Cytoplasmic Organelles after Uptake of Gold Nanoparticles with Biologically Relevant Surface Coatings, *ACS Nano*, 2020, **14**(2), 2248–2264.
- 26 V. Weinhardt, J.-H. Chen, A. A. Ekman, J. Guo, S. G. Remesh, M. Hammel, *et al.*, Switchable resolution in soft x-ray tomography of single cells, *PLoS One*, 2020, **15**(1), e0227601.
- 27 E. Pereiro, J. Nicolás, S. Ferrer and M. R. Howells, A soft X-ray beamline for transmission X-ray microscopy at ALBA, *J. Synchrotron Radiat.*, 2009, **16**(4), 505–512.
- 28 A. Sorrentino, J. Nicolás, R. Valcárcel, F. J. Chichón, M. Rosanes, J. Avila, *et al.*, MISTRAL: a transmission soft X-ray microscopy beamline for cryo nano-tomography of biological samples and magnetic domains imaging, *J. Synchrotron Radiat.*, 2015, **22**(4), 1112–1117.
- 29 R. J. Youle and A. M. van der Bliek, Mitochondrial Fission, Fusion, and Stress, *Science*, 2012, **337**(6098), 1062–1065.
- 30 I. Kounatidis, M. L. Stanifer, M. A. Phillips, P. Paul-Gilloteaux, X. Heiligenstein, H. Wang, *et al.*, 3D Correlative Cryo-Structured Illumination Fluorescence and Soft X-ray Microscopy Elucidates Reovirus Intracellular Release Pathway, *Cell*, 2020, **182**(2), 515–530.
- 31 J. Otón, E. Pereiro, A. J. Pérez-Berná, L. Millach, C. O. S. Sorzano, R. Marabini, *et al.*, Characterization of transfer function, resolution and depth of field of a soft X-ray microscope applied to tomography enhancement by Wiener deconvolution, *Biomed. Opt. Express*, 2016, **7**(12), 5092.
- 32 G. Cardone, K. Grünwald and A. C. Steven, A resolution criterion for electron tomography based on cross-validation, *J. Struct. Biol.*, 2005, **151**(2), 117–129.
- 33 P. Reineck, A. N. Abraham, A. Poddar, R. Shukla, H. Abe, T. Ohshima, *et al.*, Multimodal Imaging and Soft X-Ray Tomography of Fluorescent Nanodiamonds in Cancer Cells, *Biotechnol. J.*, 2021, **16**(3), 2000289.
- 34 ThermoFisher Scientific, *Amira for Life & Biomedical Sciences*, Mar, 8, 2021, Retrieved from: <https://www.thermofisher.com/es/es/home/industrial/electron-microscopy/electron-microscopy-instruments-workflow-solutions/3d-visualization-analysis-software/amira-life-sciences-biomedical.html>.
- 35 Z. Andreu and M. Yáñez-Mó, Tetraspanins in Extracellular Vesicle Formation and Function, *Front. Immunol.*, 2014, **5**, 442.
- 36 M. F. Santos, G. Rappa, J. Karbanová, C. Vanier, C. Morimoto, D. Corbeil, *et al.*, Anti-human CD 9 antibody Fab fragment impairs the internalization of extracellular vesicles and the nuclear transfer of their cargo proteins, *J. Cell. Mol. Med.*, 2019, **23**(6), 4408–4421.
- 37 R. H. Chen and T. Y. Chang, Involvement of caspase family proteases in transforming growth factor-beta-induced apoptosis, *Cell Growth Differ.*, 1997, **8**(7), 821–827.
- 38 V. v. Petrov, R. H. Fagard and P. J. Lijnen, Stimulation of Collagen Production by Transforming Growth Factor- $\beta$ 1 During Differentiation of Cardiac Fibroblasts to Myofibroblasts, *Hypertension*, 2002, **39**(2), 258–263.
- 39 T. Farmer, N. Naslavsky and S. Caplan, Tying trafficking to fusion and fission at the mighty mitochondria, *Traffic*, 2018, **19**(8), 569–577.
- 40 B. Westermann, Bioenergetic role of mitochondrial fusion and fission, *Biochim. Biophys. Acta, Bioenerg.*, 2012, **1817**(10), 1833–1838.
- 41 T. Tokuyama, A. Hirai, I. Shiiba, N. Ito, K. Matsuno, K. Takeda, *et al.*, Mitochondrial Dynamics Regulation in Skin Fibroblasts from Mitochondrial Disease Patients, *Biomolecules*, 2020, **10**(3), 450.
- 42 K. J. de Vos, V. J. Allan, A. J. Grierson and M. P. Sheetz, Mitochondrial Function and Actin Regulate Dynamin-Related Protein 1-Dependent Mitochondrial Fission, *Curr. Biol.*, 2005, **15**(7), 678–683.
- 43 R. Rossignol, R. Gilkerson, R. Aggeler, K. Yamagata, S. J. Remington and R. A. Capaldi, Energy Substrate Modulates Mitochondrial Structure and Oxidative Capacity in Cancer Cells, *Cancer Res.*, 2004, **64**(3), 985–993.
- 44 A. Iavello, V. S. L. Frech, C. Gai, M. C. Deregibus, P. J. Quesenberry and G. Camussi, Role of Alix in miRNA packaging during extracellular vesicle biogenesis, *Int. J. Mol. Med.*, 2016, **37**(4), 958–966.
- 45 G. P. Otto and B. J. Nichols, The roles of flotillin microdomains – endocytosis and beyond, *J. Cell Sci.*, 2011, **124**(23), 3933–3940.
- 46 A. Sable, K. M. Rai, A. Choudhary, V. K. Yadav, S. K. Agarwal and S. v Sawant, Inhibition of Heat Shock proteins HSP90 and HSP70 induce oxidative stress, suppressing cotton fiber development, *Sci. Rep.*, 2018, **8**(1), 3620.
- 47 J. Li, A. Csibi, S. Yang, G. R. Hoffman, C. Li, E. Zhang, *et al.*, Synthetic lethality of combined glutaminase and Hsp90 inhibition in mTORC1-driven tumor cells, *Proc. Natl. Acad. Sci. U. S. A.*, 2015, **112**(1), E21–E29.
- 48 C. Y. Tay, Y. Yu, M. I. Setyawati, J. Xie and D. T. Leong, Presentation matters: Identity of gold nanocluster capping agent governs intracellular uptake and cell metabolism, *Nano Res.*, 2014, **7**(6), 805–815.
- 49 P. Jawaid, M. U. Rehman, Q.-L. Zhao, M. Misawa, K. Ishikawa, M. Hori, *et al.*, Small size gold nanoparticles



- enhance apoptosis-induced by cold atmospheric plasma via depletion of intracellular GSH and modification of oxidative stress, *Cell Death Discovery*, 2020, **6**(1), 83.
- 50 J. Groen, A. Sorrentino, L. Aballe, R. Oliete, R. Valcárcel, C. Okolo, *et al.*, A 3D Cartographic Description of the Cell by Cryo Soft X-ray Tomography, *J. Visualized Exp.*, 2021, **2021**(169), e62190.
- 51 N. Vyas, N. Perry, C. A. Okolo, I. Kounatidis, T. M. Fish and K. L. Nahas, *et al.*, Cryo-Structured Illumination Microscopic Data Collection from Cryogenically Preserved Cells, *J. Visualized Exp.*, 2021, **2021**(171), e62274.
- 52 J. Schindelin, I. Arganda-Carreras, E. Frise, V. Kaynig, M. Longair, T. Pietzsch, *et al.*, Fiji: an open-source platform for biological-image analysis, *Nat. Methods*, 2012, **9**(7), 676–682.
- 53 J. R. Kremer, D. N. Mastronarde and J. R. McIntosh, Computer Visualization of Three-Dimensional Image Data Using IMOD, *J. Struct. Biol.*, 1996, **116**(1), 71–76.
- 54 P. Gilbert, Iterative methods for the three-dimensional reconstruction of an object from projections, *J. Theor. Biol.*, 1972, **36**(1), 105–117.
- 55 J. I. Agulleiro and J. J. Fernandez, Fast tomographic reconstruction on multicore computers, *Bioinformatics*, 2011, **27**(4), 582–583.
- 56 R. Gordon, R. Bender and G. T. Herman, Algebraic Reconstruction Techniques (ART) for three-dimensional electron microscopy and X-ray photography, *J. Theor. Biol.*, 1970, **29**(3), 471–481.
- 57 C. Messaoudi, T. Boudier, C. Sorzano and S. Marco, TomoJ: tomography software for three-dimensional reconstruction in transmission electron microscopy, *BMC Bioinf.*, 2007, **8**(1), 288.
- 58 F. de Chaumont, S. Dallongeville, N. Chenouard, N. Hervé, S. Pop, T. Provoost, *et al.*, Icy: an open bioimage informatics platform for extended reproducible research, *Nat. Methods*, 2012, **9**(7), 690–696.
- 59 P. Paul-Gilloteaux, X. Heiligenstein, M. Belle, M.-C. Domart, B. Larijani, L. Collinson, *et al.*, eC-CLEM: flexible multidimensional registration software for correlative microscopies, *Nat. Methods*, 2017, **14**(2), 102–103.





## Epigenetic alterations of TGF $\beta$ and its main canonical signaling mediators in the context of cardiac fibrosis

Luis Algeciras<sup>a,d</sup>, Ana Palanca<sup>a,b,d</sup>, David Maestro<sup>a,d</sup>, Jorge RuizdelRio<sup>a,d</sup>, Ana V. Villar<sup>a,c,d,\*</sup>

<sup>a</sup> Instituto de Biomedicina y Biotecnología de Cantabria (IBBTEC), CSIC-Universidad de Cantabria, Santander, Spain

<sup>b</sup> Departamento de Anatomía y Biología Celular, Universidad de Cantabria, Santander, Spain

<sup>c</sup> Departamento de Fisiología y Farmacología, Universidad de Cantabria, Santander, Spain

<sup>d</sup> Instituto de Investigación Marqués de Valdecilla (IDIVAL), Santander, Spain

### ARTICLE INFO

#### Keywords:

Epigenetic regulation  
cardiac fibrosis  
fibroblasts  
canonical TGF $\beta$  signaling

### ABSTRACT

Cardiac fibrosis is a pathological process that presents a continuous overproduction of extracellular matrix (ECM) components in the myocardium, which negatively influences the progression of many cardiac diseases. Transforming growth factor  $\beta$  (TGF $\beta$ ) is the main ligand that triggers the production of pro-fibrotic ECM proteins. In the cardiac fibrotic process, TGF $\beta$  and its canonical signaling mediators are tightly regulated at different levels as well as epigenetically. Cardiac fibroblasts are one of the most important TGF $\beta$  target cells activated after cardiac injury. TGF $\beta$ -driven fibroblast activation is subject to epigenetic modulation and contributes to the progression of cardiac fibrosis, mainly through the expression of pro-fibrotic molecules implicated in the disease. In this review, we describe epigenetic regulation related to canonical TGF $\beta$  signaling in cardiac fibroblasts.

### 1. Introduction

Cardiac fibrosis is characterized by increased collagen deposition and/or its altered composition in the myocardium. These changes lead to increased myocardial stiffness and dampening of systolic ejection, which are common features in patients with advanced heart failure, regardless of the etiology of cardiomyopathy [1]. Although fibrosis is one of the major biological factors of mortality in cardiovascular disease, there is currently no established treatment for patients [1]. Transforming Growth factor  $\beta$  (TGF $\beta$ ) is a central *trigger* of myocardial fibroblast activation that regulates a wide variety of biological processes such as the extracellular matrix (ECM) production, cell growth, differentiation, cell homeostasis and migration [2–4]. TGF $\beta$  function is controlled through well-characterized and tightly regulated pathways that include extracellular access to transmembrane serine-threonine kinase receptors and signaling through intracellular mediators [5–7]. In recent years, epigenetic regulation of these pro-fibrotic molecules has been highlighted as essential during fibrosis development [8,9]. The central role of TGF $\beta$  regulatory actions involves its canonical effectors that mainly regulate the biological activity of TGF $\beta$ . These mediators undergo epigenetic modulation that promotes deleterious cardiac consequences such as epithelial-mesenchymal transition (EMT), endothelial-mesenchymal transition (EndMT) [10,11] fibroblast proliferation [12],

fibroblast-to-myofibroblast transdifferentiation [13–15], fibroblast senescence [16], and ECM restructuring [2,17]. These are the main relevant modifications that promote pathological myocardial remodeling. Since cardiac fibroblasts are the main fiber production machinery in the fibrotic pathological process, we will focus mainly on epigenetic studies performed in this cell type. In the context of cardiac fibrosis, we consider a broad definition of epigenetics that includes post-transcriptional non-coding RNA-mediated regulation and the more traditional epigenetics of DNA and histones (Hs) modifications. Here, we sought to review the epigenetics of TGF $\beta$  and the epigenetics of the major canonical signaling mediators involved in TGF $\beta$ -triggered activation of cardiac fibroblasts. The main canonical signaling mediators are named Mothers Against Decapentaplegic homolog 2, 3, and 4 (SMAD2, SMAD3, and SMAD 4). (See Fig. 1).

### 2. TGF $\beta$ epigenetic modifications

#### 2.1. DNA methylation related to TGF $\beta$

DNA methylation is an epigenetic mechanism that commonly indicates the transfer of a methyl group onto the C5 position of the cytosine to form 5-methylcytosine. 5-methylcytosine residues are mainly located in cytosine-phosphate-Guanine (CpG) dinucleotides. Genomic

\* Corresponding author at: Instituto de Biomedicina y Biotecnología de Cantabria (IBBTEC), CSIC-Universidad de Cantabria, Santander, Spain.

E-mail address: [villarav@unican.es](mailto:villarav@unican.es) (A.V. Villar).

<https://doi.org/10.1016/j.yjmcc.2021.06.003>

Received 3 July 2020; Received in revised form 26 May 2021; Accepted 7 June 2021

Available online 10 June 2021

0022-2828/© 2021 Elsevier Ltd. All rights reserved.



regions with high CpG density (GpC islands) have non-uniform distribution, although are usually associated with the promoters of most housekeeping genes and many tissue-specific genes [18]. DNA methylation at gene promoters, driven by DNA methyltransferases (DNMTs), reduces the access of transcription factors to DNA and therefore often associated with transcription silencing [19].

In rat cardiac fibroblasts, TGFβ inhibits the action of DNMT1 and DNMT3 during fibroblast to myofibroblast differentiation and fibroblast-mediated matrix contraction and remodeling (Table 1) [20,21]. Consistent with these results, pharmacological inhibition of DNMTs with an isoform-non-specific compound named RG-108 appears to prevent dysregulation of pro-fibrotic gene expression and cardiac fibrosis in the rat TAC model [22]. It has been demonstrated that in the TAC mouse model, deletion of DNMT3b results in exaggerated cardiac fibrosis, but surprisingly prevents hypertrophy (Table 1) [23]. These findings support the importance of DNA methylation in preventing the progression of cardiac fibrosis. Therefore, further studies in TGFβ-activated fibroblasts are needed to clarify the potential of this epigenetic regulation to control the disease.

### 2.2. Histone methylation related to TGFβ

In cardiac fibrosis, epigenetic modification of histones (methylation/demethylation and acetylation) appears as a mechanism of transduction of environmental stimuli by controlling gene expression [24]. In general, histone methyltransferases (HMTs) are a class of enzymes that

mediate the methylation of histone lysine or arginine residues. Specific methylation of histone lysine residues is regulated by lysine methyltransferases (KMTs) and lysine demethylases (KDMs). Trimethylation of histone H3 at lysine 4 (H3K4me3) and H3K36me3 are usually associated with transcription activation, whereas H3K9 and H3K27 methylations are associated with transcription repression [25]. H3K4me is driven by a KMT named Suv, Ez, and Trithorax domain 1 (SET1). Endothelial-SET1-specific depletion promotes in vivo reduction of cardiac fibrosis in a mouse model of hypertension via chronic angiotensin-II (Ang-II) administration [26]. However, the role of SET1 remains un-elucidated in cardiac fibroblasts. H3K9me is normally associated with transcriptional silencing; accordingly, the H3K9me2-specific demethylase, KDM3a, has been found to promote fibrosis in response to pressure overload. Likewise, pressure overload-associated fibrosis is diminished in the KDM3a knockout TAC transgenic mouse or after administration of the pan-KDM inhibitor JIB-04 [27]. The H3K27 HMT enhancer of zeste homolog 2 (EZH2) is a SET domain-containing KMT responsible for H3K27me3 in embryonic progenitor cells whose dysregulation is a predisposing factor for adult cardiac pathological remodeling that alters the expression of TGFβ-related proteins. Deletion of EZH2 in cardiac progenitors causes postnatal myocardial pathology and destabilizes cardiac gene expression (Table 1) [28].

### 2.3. Histone acetylation related to TGFβ

The addition of an acetyl group to histones (histone acetylation) is

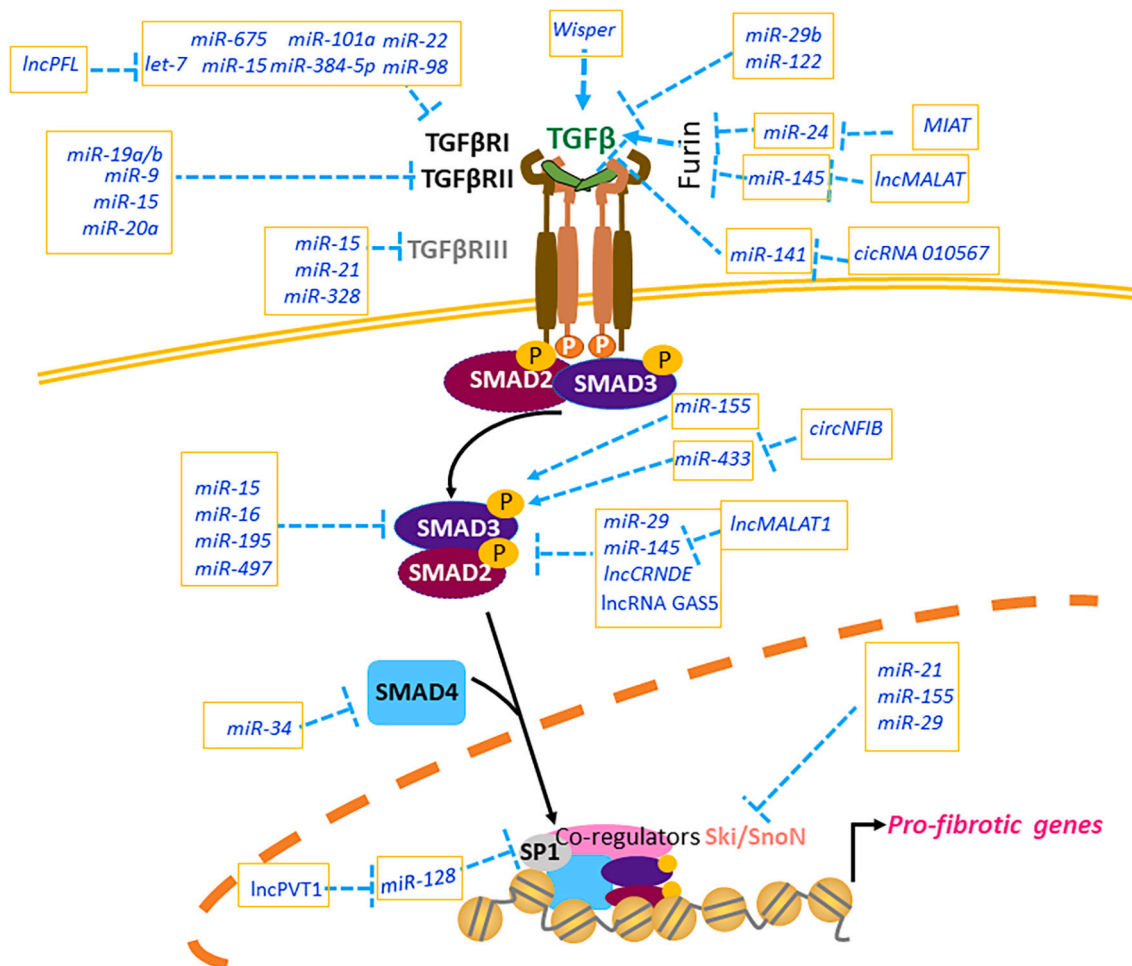


**Fig. 1.** Summary of post-transcriptional epigenetic modifications that modulate the TGFβ-related fibrotic response in cardiac fibroblasts. Representation of the canonical TGFβ signaling pathway. The lncRNAs, miRNAs and circRNAs involved in the post-transcriptional epigenetic regulation of the canonical TGFβ cascade (TGFβ, TGFβRI, II, III, and SMAD2/3/4) are indicated.



**Table 1**Summary of the regulators involved in DNA methylation and histone methylation related to TGF $\beta$  canonical signaling in the context of cardiac fibrosis.

	Regulator	Expression level of the regulator	Function	Experimental model	Refs
DNA methylation	DNMT1	Inhibition	Differentiation of fibroblasts to myofibroblasts.	Rat cardiac fibroblasts	[20,21]
	DNMT3	Inhibition	ECM remodeling Collagen expression	Rat cardiac fibroblasts	[21]
	DNM3b	Knock out	Exaggerated cardiac fibrosis	DNMT3b Knock out TAC mouse	[23]
	DNMT SET1 responsible for H3K4me H3K36me	non-isoform-specific DNMT inhibition Endothelial depletion of SET1	Reduced fibrosis Reduction of myocardial fibrosis	TAC rat Ang-II-mediated hypertensive mouse.  TAC mouse. Mouse model of myocardial infarction	[22] [26,96]
Histone methylation	KDM3a responsible for H3K9me2	pan-KDM inhibition. KDM3a knock out	Reduction of myocardial fibrosis	TAC mouse.	[27]
	EZH2 responsible for H3K27me3 H3K4me3 H3K36me3	Deletion	postnatal myocardial pathology	KDM3a knock out TAC mouse Embryonic progenitor cells	[28]
	H3K4me3 H3K36me3	Inhibition with <i>Salvia miltiorrhiza</i> and <i>Carthamus tinctorius</i> plant extract	Reduction of myocardial fibrosis	Cardiac fibroblasts. Mouse model of myocardial infarction	[91]
	ASC (MLL3)co-activator of H3K4me H3K36me	Upregulated	Myocardial fibrosis Myocardial remodeling	TAC mouse.  Human dilated cardiomyopathy	[92]

one of the possible histone modifications that help coordinate transcription factors. Histone proteins that associate with DNA to form nucleosomes, the basic units of chromatin, are H2A, H2B, H3 and H4. In cardiac fibrosis, histone acetylation represents an epigenetic signature associated with active transcription [24]. This post-translational modification promotes changes in the interaction between histones and the DNA promotes changes in the interaction between histones and DNA in nucleosomes. Histone acetylation is balanced by the activity of histone acetyltransferases (HATs) and histone deacetylases (HDACs) [29].

Chromatin modifiers like HAT and HDAC help coordinate the activity of transcription factors in cardiovascular diseases [30]. The HDAC superfamily is divided into four classes (class I, (HDAC1,2,3,8,11), class II (HDAC4,5,6,7,9,10), class III and class IV) and most of the HDAC proteins in each class are expressed in the heart. Class I, II, and IV HDACs are zinc-dependent, and class III HDACs/Sirtuins (SIRT) are NAD<sup>+</sup> dependent proteins [31]. HDACs promote pro- and anti-fibrotic effects in cardiac fibrosis, and these effects have been demonstrated by inhibition of HDACs. The inhibitor of class I and class II HDAC, 2-

**Table 2**Summary of the regulators involved in histone acetylation related to TGF $\beta$  canonical signaling in the context of cardiac fibrosis.

	Regulator	Expression level of the regulator	Function	Experimental model	Refs
Histone acetylation	HDAC2 HDAC8	Inhibition with VPA	Cardiac fibrosis reduction ameliorated cardiac fibrosis,	Renovascular hypertensive rat model	[33]
	HDAC1	Inhibition with curcumin	TGF $\beta$ downregulation. Myofibroblasts transdifferentiation. Increase of cardiac fibrosis	Ang-II-mediated hypertensive rat.	[34]
	HDAC class I	Inhibition with Mocetinostat, apicidin	Blockage of cell cycle	Cardiac fibroblasts	[35]
	HDAC4	Inhibition with VPA	Pericyte-myofibroblast trans-differentiation	Ang-II-mediated hypertensive rat.	[36]
	HDAC classes I, II,VI	Inhibition with MPTOE014	Less cardiac fibroblast proliferation migration, improvement of cardiac function.	Heart failure rats	[38]
	SIRT1	Activation with SRT1720	Cardioprotection	TAC mouse	[93]
	SIRT3	Activation with RSV	Reduction of cardiac fibrosis. Fibroblast-to-myofibroblast transformation	TAC mouse.	[97]
	SIRT6	Deletion	Increase cardiac fibrosis	Cardiac fibroblasts SIRT6 knock out mice	[94]
	BRD4	Inhibition	Reduction of cardiac fibrosis. Reduction of EndMT	Rat model of heart failure. TAC mouse	[39,61]
	MBNL1	Deletion	Weakening of the heart wall	Isoproterenol-induced cardiac hypertrophy	[77]
	P300	Inhibition with L002	Reduce cardiac fibrosis. Recover cardiac function	Ang-II and Renovascular hypertensive mouse model. Human and rat cardiac fibroblasts	[113,116]
	HDACs	Inhibition with Ski/SnoN	Reduction of expression of ECM proteins. Reduction of myofibroblast contractility	cardiac fibroblasts	[117,118,120]

Propylpentanoic acid sodium, termed Valproic Acid sodium (VPA) [32], is of particular interest in the control of cardiac fibrosis. *In vivo* administration of VPA results in inhibition of HDAC2, HDAC8 and TGF $\beta$  in a renovascular hypertensive rat model (obtained by clipping left and right renal arteries). Cardiac fibrosis and cardiac hypertrophy were markedly attenuated by VPA treatment in this fibrotic rat model [33]. Indirectly, these results indicate that TGF $\beta$ -mediated pro-fibrotic signaling decreases in an environment where HDAC is inhibited; which correlates with the observed inhibitory action of the natural polyphenol curcumin on HDAC1 and the consequent downregulation of TGF $\beta$  obtained in hypertensive rats (Table 2) [34].

Other studies indicate that the cardiac fibroblast cycle progression can be potently blocked by *in vitro* administration of HDAC class I inhibitors such as Mocetinostat or apicidin [35]. Specifically apicidin promoted the expression of a subset of fibrosis-associated and related TGF $\beta$  genes in cardiac fibroblasts, opening the question of its role as an HDAC inhibitor in fibrosis [35]. Inhibition of class II HDAC4 by VPA action promotes the induction of pericyte-myofibroblast trans-differentiation by eliciting ERK1/2 phosphorylation in an Ang-II-induced rat cardiac fibrosis model (Table 2) [36]. These results indicate that specific HDAC isoform inhibitors would be necessary to understand the overall HDACs related-epigenetic regulatory network.

The NAD<sup>+</sup> dependent class III HDAC family termed SIRT has been shown to act directly on TGF $\beta$  signaling. The protection of SIRT2 was demonstrated by the observation of spontaneous cardiac fibrosis, hypertrophy and dysfunction of SIRT2 knockout [37].

Although most of these studies described HDACs as important epigenetic regulatory enzymes that can reduce cardiac fibrosis, some authors advocate the beneficial effects of pan-HDAC inhibitors such as MPT0E014 in a rat model of heart failure. MPT0E014 improved myocardial function, decreased the migration and proliferation of cardiac fibroblast, as well as the expression of TGF $\beta$  [38]. More clarity on the mechanism underlying the action of HDACs inhibitors would clarify this controversy. The influence of histone acetylation on TGF $\beta$ -related cardiac fibrosis also involves a chromatin-binding protein.

Bromodomain and extra-terminal (BET) acetyl-lysine proteins recognize acetylated chromatin and influence gene transcription in the process of pathological fibrosis. The BET family member associated with TGF $\beta$  pro-fibrotic signaling in cardiac fibroblasts is the bromodomain-containing chromatin reader protein 4 (BRD4) [39]. TGF $\beta$  triggers BRD4 recruitment to regulatory regions of fibrosis-driving genes [40]. The BRD4 inhibitor JQ1 reduces fibrosis and other functional features of the heart in a heart failure model. Following JQ1 administration, downregulation of most target genes of the TGF $\beta$  pathway were observed [39]. The chromatin-reader BRD4 rises as a critical effector of TGF $\beta$  in the epigenetic control of pathological cardiac fibrosis, although interestingly its inhibition does not involve the regulation of canonical intracellular effectors of TGF $\beta$  [41].

#### 2.4. Post-transcriptional epigenetic regulation of TGF $\beta$

Increasing evidence implicates post-translational and transcriptional modifications in the modulation of chromatin structure, gene transcription and TGF $\beta$ -related protein expression. Among these epigenetic regulatory processes, the actions of noncoding RNAs (ncRNAs) are the most extensively studied, with several members implicated in TGF $\beta$ -dependent fibroblast activation in cardiac remodeling. The Encyclopedia of DNA Elements Consortium (ENCODE) regularly provide lists of functional elements in the human genome. The ENCODE project has recently revealed that about 80% of human DNA is not transcribed into proteins but into ncRNAs [42]. The ncRNAs are classified into two groups attending to their regulatory roles, the ubiquitous housekeeping ncRNA with generic cellular functions, and the regulatory ncRNAs [43]. The most studied regulatory ncRNAs affecting cardiac fibrosis are the small (around 22 nucleotides) single-stranded microRNAs (miRNAs). They are complementary to mRNAs and inhibit mRNAs mostly by

attenuating translation and by mRNA degradation. Other ncRNAs studied in cardiac fibrosis are long non-coding RNAs (lncRNAs) that have more than 200 nucleotides and can regulate sets of miRNA; and circular RNAs (circRNAs) whose circular structure also manages to trap miRNAs to inhibit their actions. NcRNAs regulate gene expression at epigenetic, transcriptional, and post-transcriptional levels. The mechanism of action of different ncRNAs conforms a wide range of interacting regulatory possibilities [43]. The regulatory ncRNAs most implicated in the control of TGF $\beta$  expression in the context of cardiac fibrosis are the miRNAs.

##### 2.4.1. MiRNAs

MiR-29b and miR-122 function by binding to the 3'UTR region of TGF $\beta$  and appear to be the most direct tools in the downregulation of TGF $\beta$  protein expression [44,45]. MiR-29b protects cardiac fibroblasts from hypertension generated after chronic Ang-II administration *in vivo* and *in vitro* and is associated with differential molecular, structural and functional remodeling patterns in mice and patients with aortic stenosis [45]. Interestingly, sex-specific regulation of miR-29b has been studied. In females, miR-29b was observed as a pro-fibrotic factor, whereas in males it is a protective factor in the myocardium subjected to pressure overload (TAC model) [46]. This sex-specificity points to new perspectives for miRNAs as gender biomarkers of disease. MiR-122 is downregulated in aortic stenosis patients with exacerbated myocardial interstitial fibrosis and TGF $\beta$  is one of its targets in cardiac fibroblasts [44]. These two miRNAs negatively regulate cardiac fibrosis, but only miR-29 could be considered as a link in between classical epigenetic regulation and ncRNA regulation. The epigenetic network existing between miRNAs and histone methylation in cardiac fibroblasts could be represented by an epigenetic target sensitive to canonical TGF $\beta$  signaling that is H4K20me3, and its negative regulator miR-29 [47] that contributes to cellular senescence in cardiac aging.

##### 2.4.2. LncRNAs

LncRNAs are a large and heterogeneous class of transcribed RNA molecules that act as epigenetic modifiers performing different functions. They can recruit transcription factors, bind to DNA-binding proteins, are chromatin modifiers and can regulate miRNAs expression. One of these lncRNAs that is associated with myocardial infarction is the myocardial infarction associated transcript (MIAT) located in the nucleus and described as a new potential biomarker for the diagnosis of acute myocardial infarction. The presence of single nucleotide polymorphisms (SNPs) in MIAT are associated with a risk of myocardial infarction in cardiac patients [48]. Furthermore, comprehensive study of MIAT expression in infarcted myocardium revealed that it is abnormally upregulated. MIAT knockdown inhibits interstitial fibrosis by inhibiting collagen production and cardiac fibroblast proliferation [49]. The molecular mechanism of MIAT is related to the TGF $\beta$  cascade via Furin. Furin is an endopeptidase that cleaves the TGF $\beta$  precursor providing a dimer of mature TGF $\beta$  linked by disulfide bridges [50]. Furin has been found to be a target of miR-24 that can reduce cardiac fibrosis [51]. MIAT decreases the level of miR-24 myocardial infarct border regions and cardiac fibroblasts. This action leads to the progression of cardiac fibrosis with a clear role of MIAT as a pro-fibrotic factor [49].

A similar situation involving Furin occurs with the lncRNA called metastasis-associated lung adenocarcinoma transcript 1 (MALAT1). MALAT1 is a highly conserved nuclear-retained lncRNA that is abundantly expressed in cells and tissues and has been shown to play a role in gene regulation at both the transcriptional and post-transcriptional levels in a context-dependent manner [52]. MALAT1 is upregulated in patients with myocardial infarction and targets miR-145, which in turn targets Furin. Thus, MALAT1 downregulation increases miR-145 controlling Furin expression, which ameliorates MI-impaired cardiac function and was shown to prevent Ang-II-induced fibroblast proliferation, and collagen production [53]. These results and the following indicate the importance of ECM-related proteins, such as Furin, in epigenetics

affecting cardiac fibroblasts.

The Wnt-related integration site (WNT, also named as Cellular Communication Network Factor (CCN) family of proteins [54], features inducible proteins such as WNT1 inducible signaling pathway protein 2 (Wisp2), which is a member of the ECM-associated proteins involved in intercellular signaling that induces apoptosis in cardiac myofibroblasts, but not in cardiomyocytes or fibroblast [55]. Wisp2-associated lncRNA super-enhancer Wisper emerges as another pro-fibrotic factor that promotes the differentiation of cardiac fibroblasts to myofibroblasts and subsequent collagen overproduction *in vivo*. Wisper expression correlates with cardiac fibrosis in a mouse model of myocardial infarction and in patients with aortic stenosis [56]. Wisper is related to T-cell intracellular antigen-1 (TIA1)-related protein (TIAR), a splicing factor related to tissue fibrosis through its ability to regulate the expression of pro-collagen lysine 2-oxoglutarate 5-dioxygenase (Plod2). Plod2 is involved in collagen cross-linking and matrix stabilization [57]. These characteristics indicate that Wisper lncRNA as a good candidate to be a biomarker of cardiac fibrosis and a target for reducing fibrosis.

### 2.4.3. CircRNAs

The circRNAs are another group of ncRNAs with a unique covalently closed circular shape derived from exons, introns or both. The broad functional mechanisms of circRNAs include acting as miRNA sponges, interacting with proteins, regulating gene splicing or transcription, translating proteins, or peptides and epigenetic regulation [43]. Accordingly, circRNA 010567 has been found to be pro-fibrotic as it directly blocks miR-141 which is an anti-fibrotic inhibitor of TGF $\beta$  [58]. This study proposed the 3' UTR of TGF $\beta$  as a target of miR-141. Deletion of circRNA 010567 leads to elevated miR-141 levels in Ang-II-treated cardiac fibroblasts and diabetic mice with myocardial fibrosis [58].

## 3. TGF $\beta$ receptors

Once TGF $\beta$  is released from the ECM, it triggers the pro-fibrotic signal at the plasma membrane. To initiate the pro-fibrotic cascade, TGF $\beta$  binds to constitutively phosphorylated TGF $\beta$ RII and triggers the trans-phosphorylation of TGF $\beta$ RI [59,60].

### 3.1. TGF $\beta$ RI histone modification and post-transcriptional regulation

#### 3.1.1. Histone modification

Little has been described on the TGF $\beta$ RI-related epigenetic regulation of HDAC in cardiac fibroblasts. Chromatin remodeling provided by histone acetylation promotes the binding of reader proteins containing acetyl-lysine recognition domains as is the case of the aforementioned TGF $\beta$ -related cardiac nuclear stress effector BRD4. In TGF $\beta$ -induced EndMT in cardiac fibrosis, pro-fibrotic BRD4 recruits RNA Pol II and initiates transcription of pro-fibrotic genes. Inhibition of BRD4 down-regulates EndMT-related transcription factors and attenuates TGF $\beta$ -activated TGF $\beta$ RI expression [61].

#### 3.1.2. Post-transcriptional regulation

Post-transcriptional epigenetic regulation of TGF $\beta$ RI occurs to transmit the TGF $\beta$  signal into the cell. TGF $\beta$ RI, which is targeted by miR-22, let-7, miR-101a and miR-384-5p in the fibrotic heart [62–65], is also targeted by miR-22, miR-98, miR-675, let-7, miR-101a and miR-384-5p in cultured cardiac fibroblasts [63–67]. This post-transcriptional regulation of TGF $\beta$ RI controls the pro-fibrotic gene expression, proliferation, contractility, myofibroblast transdifferentiation and cell migration [62–67]. One of the best characterized miRs is let-7, whose action leads to the reduction of the aortic stenotic process [62]. Mechanistically, let-7 has been described to directly target TGF $\beta$ RI in human cardiac fibroblasts [62], and competing with a lncRNA promotes reduced collagen deposition, and improved cardiac function *in vivo* [68]. The lncRNA that competes with let-7 is termed pro-fibrotic lncRNA (lncRNAPFL) and is up-regulated in mouse hearts in response to

myocardial infarction, as well as in fibrotic cardiac fibroblasts [68]. lncRNAPFL inhibits the anti-fibrotic activity of let-7 and as a consequence fibrosis occur [68]. The pro-inflammatory lipid mediator named Platelet Activating Factor Receptor (PTAFR) was found to be a target of let-7 in mouse cardiac fibroblasts [68], but while PTAFR was not related to myocardial fibrosis, its ligand PTAf was associated with cardiac dysfunction occurring under various cardiovascular stress situations [69]. Thus, it is highly probable that PTARF is involved in the disease and more experiments are needed to confirm its role.

Multiple stimuli that trigger fibrosis stimulate signalling cascades that share the same miRs to epigenetically regulate fibrosis. The most obvious cooperation occurs between TGF $\beta$  signaling and the phylogenetically glyco-lipoprotein cysteine-rich highly conserved Wntless/Int (Wnt) cascade. The importance of the Wnt cascade was observed by targeting the Wnt/ $\beta$ -catenin pathway. Inhibition of Wnt prevents pressure overload-induced cardiac hypertrophy [70]. In cardiac fibrosis, the mutual interaction of TGF $\beta$  and Wnt signaling has been implicated in ECM production, generating a transactivation loop during cardiac fibroblast activation. MicroRNAs, lncRNAs and circRNAs can interact with the TGF $\beta$ /Wnt signaling axis to affect cardiac fibrosis [71]. This is the case of miR-384-5p whose target sequences are present in TGF $\beta$ RI and in various receptors and ligands of the Wnt pathway, such as Lrp6, Fzd1, and Fzd2. MiR-384-5p simultaneously targets key receptors of the TGF $\beta$ /Wnt transactivation circuit and significantly attenuates both TGF $\beta$ -induced cardiac fibroblast activation and ischemia-reperfusion-induced cardiac fibrosis [64]. MiR-384-5p decreases phosphorylation of downstream effector of Wnt, such as Glycogen synthase kinase  $\beta$ ser9 (GSK3 $\beta$ ser9) and the downstream Wnt coactivator  $\beta$ -catenin [64].

Another example of this multiple inhibition is produced by the anti-fibrotic activity of miR-101. In ischemic-stimulated cardiac fibroblasts, miR-101 has been associated not only with downregulation of TGF $\beta$ RI [65], but also with the FBJ proto-oncogene Osteosarcoma Oncogene (c-FOS). The transcription factor c-Fos regulates TGF $\beta$  expression and proliferation of cardiac fibroblast, and is inhibited by miR-101 which ultimately decreases TGF $\beta$  expression [72]. The idea of targeting multiple components of different pro-fibrotic cascades has great therapeutic potential in the process of cardiac fibrosis. The anti-fibrotic potential of miRs could be increased by targeting more than one cascade or several modulators of the same cascade, as is the case of the anti-fibrotic miR-15 that targets multiple components of the TGF $\beta$  pathway, including TGF $\beta$ RI and the intracellular mediator SMAD3 [73].

### 3.2. TGF $\beta$ RII pre- and post-transcriptional regulation

#### 3.2.1. Epigenetic studies on TGF $\beta$ RII largely focus on the role of ncRNAs

MiR-19a/miR-19b-3p, and miR-9 target TGF $\beta$ RII in cultured cardiac fibroblasts [74,75] controlling pro-fibrotic protein expression [75], proliferation, viability [74], migration, invasiveness [75] and trans-differentiation of myofibroblast [74,75]. These are broad regulatory actions, which in the case of miR-19-a/b could be due to its involvement in autophagy-related fibrogenesis in human cardiac fibroblasts [75], and could contribute to the final outcome of the fibrotic process.

The regulation of TGF $\beta$ RII also includes an interesting positive modulator, muscleblind like splicing regulator 1 (MBNL1), which is an RNA splicing protein. The MBNL1 protein which specifically binds to double-stranded CUG RNA expansions, has been shown to maintain TGF $\beta$ RII transcript levels by binding to its 3' UTR. MBNL1 and miRNAs utilize the same mechanism of action however, while miRNAs have inhibitory actions, MBNL1 promotes the protection and elongation of TGF $\beta$ RII transcripts [76]. The regulation of MBNL1 appears to be intimately linked to the process of cardiac remodeling. Overexpression of MBNL1 appears after myocardial infarction and *in vivo* MBNL1 leads to weakening of the heart wall after cardiac damage [77]. Furthermore, addition of TGF $\beta$  *in vitro* to cardiac fibroblasts also promotes upregulation of MBNL1 [76].

It is common for some miRNAs to act in cells other than fibroblasts

thus affecting fibrosis. The regulatory action of miR-20a in endothelial cells affects cardiac fibrosis by directly targeting TGF $\beta$ RI and TGF $\beta$ RII. Downregulation of miR-20a increases TGF $\beta$ RI and TGF $\beta$ RII expressions and stimulates the transformation of endothelial cells into cells with a more fibroblast-like phenotype [78]. MiR-20 also participates in the subcellular localization of SMAD2 by targeting SMAD anchor for receptor activation (SARA), which ubiquitously expressed [78], facilitating the kinase action of TGF $\beta$ RI [79].

### 3.3. TGF $\beta$ RIII post-transcriptional regulation

The TGF $\beta$  decoy receptor TGF $\beta$ RIII, also known as betaglycan, prevents the correct formation of the TGF $\beta$  receptor protein complex [80]. The epigenetic regulation of TGF $\beta$ RIII is focused on post-transcriptional modifications. These are mainly carried out by two miRs that directly target TGF $\beta$ RIII mRNA with pro-fibrotic effects, miR-328 and miR-21 [81,82]. Interesting observations related to miR-328 describe its colocalization with the scar formed after a myocardial infarction and its correlation with the degree of fibrosis severity [81]. *In vitro* experiments in cardiac fibroblasts suggest that miR-328 increases TGF $\beta$  signaling by enhancing collagen expression [81]. These characteristics make miR-328 a good candidate to be a biomarker of cardiac fibrosis. Another miRNA that was pointed as a biomarker is miR-21. MiR-21 participates in non-canonical TGF $\beta$  signaling by targeting Sprouty homology 1 (SPRY1), the negative regulator of the ERK-MAP kinase pathway. As ERK-MAP kinase signaling is required for fibroblast survival and activation [83,84], the inhibition of SPRY1 by miR-21 augments ERK-MAP kinase activity that promotes growth factors secretion. Through this mechanism, miR-21 seems to control the extent of interstitial fibrosis, cardiac fibroblasts survival, and collagen deposition in TAC and heart failure models [85,86]. Another direct target of miR-21 is the tumor suppressor Phosphatase and Tensin homolog (PTEN) whose downregulation decreases the repression of the extracellular regulator of TGF $\beta$  and collagen degrader, metalloproteinase 2 (MMP2) *in vivo* with pro-fibrotic consequences [87].

## 4. SMAD2/3 canonical mediators

SMAD2/3 protein complex is the canonical cytoplasmic downstream effector of TGF $\beta$  during the fibrotic process [88,89]. This protein complex is considered the main regulator of TGF $\beta$  intracellular signaling whose phosphorylation breaks its association with TGF $\beta$ RI by forming a heterotrimeric complex with SMAD4. SMAD2/3/4 complex translocates to the nucleus, binds to DNA, couples to transcription factors, and drives the pro-fibrotic response in cardiac fibroblasts. Excessive TGF $\beta$ -SMAD2/3/4 signaling or long-lasting effects of TGF $\beta$  stimulus in cardiac fibroblasts are thought to underlie the pathophysiology of cardiac fibrosis [1]. Suppression of SMAD2/3 has been shown to inhibit the fibrotic gene program in cardiac fibroblasts and ECM remodeling [90]. With this in mind, SMAD proteins are important targets in the reduction of fibrosis. In cardiac fibrosis, downregulation of SMAD2, induces the action of SMAD3 to compensate for the lack of SMAD2 activity [90]. Thus, the few descriptions of classical epigenetic regulation of canonical TGF $\beta$  mediators in cardiac fibroblasts focus on SMAD3.

### 4.1. Histone methylation related to SMAD3

H3K4me3 and H3K36me3 are histone methylations associated with transcription activation. The use of plant extracts offers a new method to suppress histone methylation.) Treatment with *Salvia miltiorrhiza* and *Carthamus tinctorius* (SCE) downregulates H3K4me3 and H3K36me3 levels in the Smad3 promoter region in cardiac fibroblasts, leading to inhibition of Smad3 transcription, thus promoting prevention of myocardial fibrosis and adverse remodeling after myocardial infarction [91]. There is a coactivator that produces an opposite effect. Activating Signal Co-integrator-2 (ASC-2) also called HMT mixed lineage leukemia

(MLL3), is a multifunctional coactivator that can function as an essential adaptor for recruiting HMTs. ASC-2 participates as a part of a complex of methyltransferases in the H3K4me and H3K36me in the SMAD3 promoter. This epigenetic modification appears in response to pressure overload in the TAC mouse model and dilated cardiomyopathy in patients, which activates SMAD3 transcription (Table 1) [92].

### 4.2. Histone acetylation related to SMAD3

Acetylation/de-acetylation of specific lysine residues in Smad2/3 has been shown to regulate TGF- $\beta$  signaling by altering its transcriptional activity. This on/off system has been described for SMAD3 in cardiac fibrosis [93–96], and has been shown to govern the expression of many pro-fibrotic genes associated with disease progression [94,97–99]. Activation of the NAD<sup>+</sup> dependent class III HDAC family named SIRT promotes the reduction of fibrosis, as demonstrated in the following examples. In cardiac fibroblasts, activation of SIRT3 by resveratrol (RSV), a polyphenol compound with antioxidant properties, inhibits nuclear localization of TGF $\beta$ -activated SMAD3, thereby ameliorating cardiac fibrosis in the TAC mouse model and *in vitro* transformation into myofibroblast in response to Ang-II [97]. The cardioprotective action of SIRT1 was also observed in the mouse model of TAC-induced cardiac fibrosis by administration of a small molecule (SRT1720) that dramatically increases de-acetylase activity of SIRT1 by affecting Smad2/3 transactivation [93]. In addition, SIRT6-deficient mice exhibit augmented SMAD3 phosphorylation leading to increased cardiac fibrosis and cardiac fibroblasts (Table 2) [94]. All these results suggest that the action of different SIRT isoforms could prevent cardiac fibrosis and fibroblast-to-myoblast transformation by affecting TGF $\beta$ /Smad3 pathway.

### 4.3. SMAD2/3 post-transcriptional modifications

Post-transcriptional modifications of non-coding RNAs influence SMADs. The miR-15 family, comprising miR-15a/b, -16, -195 and -497 is highly expressed in cardiomyocytes and fibroblasts following pro-fibrotic stimuli, and is also overexpressed in patients with pressure overload and in experimental models [73]. The miR-15 family has many predicted targets within TGF $\beta$  signaling effectors, among which SMAD2, SMAD3 and SMAD4 have been reported. In cardiac fibroblasts, exogenous miR-15 downregulates SMAD2, although blockage of miR-15 does not lead to upregulation of SMAD2 and SMAD4 [73]. Interestingly, inhibition of miR-15 increases the expression of other TGF $\beta$ -related targets, such as TGF $\beta$ RI/II, SMAD3, the type I membrane glycoprotein Endoglin (part of the TGF $\beta$  receptor complex), the TGF $\beta$  cytoplasmic signaling inhibitor SMAD7, the TNF receptor-associated factor 6 (TRAF6), TGF $\beta$ -activated kinase 1 (TAK1) of the MAPK family, and p38 MAPK [73]. This multifunction indicates that different components of the miR-15 family may exhibit different functions, and blockade of the entire family would not provide clear results in cardiac fibrosis.

On the other hand, miR-155 is considered a pro-fibrotic regulatory factor in several fibrotic diseases including the Ang-II-derived hypertension model [100–103]. It has been suggested that cardiac fibroblasts do not endogenously express their own miR-155 in response to Ang-II, but Ang-II-stimulated macrophages-derived exosomes can transfer miR-155 to cardiac fibroblasts [101]. Cardiac fibroblasts from an *in vivo* high glucose model were induced to increase collagen deposition through TGF $\beta$ /SMAD2 signaling, which was mediated by miR-155. Furthermore, depletion of miR-155 mitigates these effects [100]. SMAD3 can be downregulated by miR-15 and miR-29, and upregulated by miR-433 activity in cardiac fibroblasts *in vivo* and *in vitro* [45,73,104]. MiR-433 has been described as a potential target for the amelioration of cardiac fibrosis. MiR-433 targets a regulator of decarboxylases for polyamine synthesis named Antizyme inhibitor (Azin1). A reduced level of Azin1 activates SMAD3 through TGF $\beta$ . In the fibrotic process, upregulation of SMAD3 occurs targeting Azin1 with miR-433



[105]. The SMAD3 regulatory network includes downregulation of miR-433. Sponge RNAs, as we previously mentioned, contain binding sites complementary to a miRNA of interest. MiR-433 blockage leads to a decrease in cardiac fibrosis *in vivo*. In TGF $\beta$ -mediated primary cardiac fibroblasts, the circRNA named circular RNA nuclear factor-1B (circNF1B) acts as a sponge for miR-433 by inhibiting the pro-fibrotic action of miR-433 [106], collaborating in the indirect regulation of SMAD3. The broad regulation of SMAD3 also involves lncRNAs, whose action can activate or suppress SMAD3 activity.

The previous mentioned lncRNA MALAT1, which is considered a pro-fibrotic molecule in cardiac fibrosis, was found to be overexpressed in an *in vivo* model of myocardial infarction and in cardiac fibroblasts treated with Ang-II [53]. The lncRNA MALAT1 is able to block miR-145, which targets SMAD3 and diminishes its expression [53,107]. The lncRNA Colorectal Neoplasia Differentially Expressed (lnc CRNDE), a known oncogenic lncRNA, can regulate SMAD3 more directly by blocking its binding to DNA promoters and subsequent expression of fibrotic markers in cardiac fibroblasts stimulated with TGF $\beta$  [108].

Moreover, there is an interesting relationship between a transcription repressor and a lncRNA highly related to TGF $\beta$ -activated cardiac fibroblasts. As mentioned above, there are areas of DNA prone to be methylated such as CpG. The methylated CpG-binding protein 2 (MeCP2) is a transcriptional repressor that binds to methylated sequences of its gene target promoter and recruits transcriptional repressors to silence gene expression [109]. MeCP2 is highly expressed in cardiac fibrosis tissue and has been associated with different cardiac pro-fibrotic cascades [110]. MeCP2 triggers cardiac fibroblast activation involving Smad3. In TGF $\beta$ -induced cardiac fibroblasts this occurs through inactivation of an anti-fibrotic lncRNA called growth arrest-specific transcript 5 (lncRNA GAS5) [111]. All these modifications and interrelationships indicate extensive epigenetic regulation of the TGF $\beta$  environment in the context of cardiac fibrosis.

## 5. Nuclear epigenetic regulation of TGF $\beta$ canonical signaling

### 5.1. SMAD4 nuclear complex acetylation

The main canonical mediator of TGF $\beta$  signaling in the nucleus is SMAD4. It is a transcription factor of the TGF $\beta$  cascade that binds SMAD2/3 and translocates the complex to the nucleus. HAT p300, a transcriptional co-activator that is often recruited to transcriptional enhancers to regulate gene expression through chromatin acetylation, behaves as an important epigenetic regulator in cardiac fibrosis [112]. CREB-binding protein (CBP) is a transcriptional co-activator protein that plays a central role in the coordination and integration of events with the transcription apparatus. SMAD3 has a dramatically increased affinity toward TGF $\beta$ -activated p300/CBP, mediating full activation of gene transcription [113]. The discovery that co-repressors contain HDAC transcriptional activity and that co-activators such as CBP/p300 contain HAT activity acting on histone tails in the nucleosome has increased the evidence of a link between histone acetylation and transcription activation in the case of the nuclear SMAD2/3/4 complex [114]. The organic small molecule L002, which is a specific inhibitor of p300, is considered a novel anti-fibrotic candidate tested in Ang-II hypertensive mice, in a renovascular hypertensive mouse model, and in human and rat cardiac fibroblasts [112,115].

In line with the finding that co-repressors contain HDAC transcriptional activity, Ski (Sloan-Kettering Institute) and SnoN (Ski novel) are SMAD-interacting proteins that negatively regulate the TGF $\beta$  signaling pathway by disrupting SMAD2/3/4 complex formation as well as inhibiting SMAD association with p300/CBP coactivators. They form an inhibitory complex that positions on the SMAD-binding elements of the promoters of pro-fibrotic genes. These complexes recruit HDACs and other co-repressors to inhibit gene expression [116]. Ski has been shown to counteract fibrotic processes by regulating the expression of ECM proteins in cardiac fibroblasts and myofibroblasts [117–119]. Moreover,

overexpression of Ski reduces myofibroblast contractility and promotes apoptosis amplifying the effect of its anti-fibrotic action (Table 2) [118,120]. Binding of SMADs to transcriptional co-repressors, including Ski/SnoN, could induce their degradation by the ubiquitin proteasome pathway (UPP), leading to increased pro-fibrotic signaling [116].

### 5.2. Post-transcriptional regulation of SMAD nuclear complex

MiRNAs such as miR-21, -29 and -155 are upregulated in cardiac fibrosis and can target the aforementioned Ski and SnoN co-repressors [121–124]. For example, miR-155 blocks Ski expression in cardiac fibroblasts, promoting ECM protein expression [121]. MiR-34 targets and inhibits SMAD4. siRNA silencing of miR-34 leads to increased SMAD4 and collagen expression in primary cardiac fibroblasts and in a myocardial infarction model, as would be expected [125]. Silencing of the miR-34 family (miR-34a, -34b, and -34c) may protect the heart against pathological cardiac remodeling and improve its function {Bernardo, 2012 #681} [126]. As in the case of miR-15 family, some components of the miR-34 family could be involved in anti-fibrotic actions and others in pro-fibrotic actions. SIRT1 promotes cardio-protection, as we have already reviewed in previous sections, and also exerts anti-apoptotic effects in the heart [127]. MiR-34 can down-regulate SIRT1 and promote fibrosis [127], indicating a complex role for this miR in cardiac fibrosis.

The zinc finger protein, specificity protein 1 (Sp1), is one of the TGF $\beta$ /SMAD-associated transcription factors that is subjected to epigenetic regulation. At the collagen I- $\alpha$ 2-promoter, SP1 and SMAD3/4 have a consensus binding site, and upon stimulation of TGF $\beta$ -SMAD3/4 signaling, fibrosis increases [128]. Prior to these events, SP1 expression can also be regulated by a lncRNA that indirectly affects cardiac fibroblast proliferation. One of the lncRNAs related to the composition and configuration of ECM elements is lncRNA plasmacytoma variant translocation 1 (lncPVT1) [105]. It is overexpressed in fibrotic human hearts and in murine models acting as a “RNA sponge” through a complementary region which can bind and sequester miR-128-3p. MiR-128-3p targets SP1 reducing heart fibrosis [129].

## 6. Conclusion

The epigenetic mechanisms of several fibrosis modifiers related to canonical TGF $\beta$  signaling and their cooperative action in cardiac fibroblasts have been described. Modulation of epigenetic processes in cardiac fibrosis includes epigenetic imbalances through DNA methylation, histone methylation and acetylation. These alterations involve TGF $\beta$ -mediated pro-fibrotic action of DNMT1, 3 [20,21], reduction of cardiac fibrosis by SET1 depletion [26], or by inhibition of class I and II HDACs [33]; pro-fibrotic action of KDM3a demethylase [27], and anti-fibrotic action of some SIRT isoforms [36,93,94,97,126]. The well-defined pro-fibrotic actions and emerging anti-fibrotic effects of HDACs in fibroblasts has gathered interest in controlling cardiac fibrosis by specific inhibition of pro-fibrotic isoforms of HDACs [32–36,38].

Understanding the interrelationship of different epigenetic modulators could help to generate anti-fibrotic cocktails that augment the efficacy of future treatments. Some of these cooperative actions include miRNAs with key cross-talk actions. This is the case of miR-384-5p, of particular interest for its potential in reducing fibrosis by controlling the TGF $\beta$  and Wnt/ $\beta$  catenin cascades [64]. A more indirect regulation controlling fibrosis is performed by circRNA 010567 [58] or circNF1B [106] which act as miRNAs sponges on TGF $\beta$  and SMAD3 respectively. Another example is the interesting epigenetic interplay between miR-29 and histone H4K20me3 methylation in cardiac fibroblasts to control cell senescence [47].

We have reviewed several epigenetic modifiers that are related to TGF $\beta$  and TGF $\beta$ RI, especially HDAC modifiers such as the MPT0E014 inhibitor of class I, II and IV HDAC [38], the chromatin reader BRD4, whose TGF $\beta$ - and TGF $\beta$ RI-related inhibition in fibroblasts ensures

downregulation of fibrosis [39–41], or the presence of SIRT1, 2, 3 and 6 isoforms whose downregulation promotes cardiac fibrosis [37,93,94,97,127].

In the cytoplasm of cardiac fibroblasts, the canonical mediator SMAD3 presents a clear platform for classical and post-transcriptional epigenetic regulation in both pro- and anti-fibrotic pathways. Such examples are the SMAD3 co-repressors containing HDAC activity Ski and SnoN [117–120] and the methyltransferase ASC-2 complex [92], which participate in the H3K4me and H3K36me of the SMAD3 promoter giving rise to anti- and pro-fibrotic epigenetic effects respectively. Other examples reviewed here are indirect pro-fibrotic regulation of SMAD3 from lncRNA MALAT1 [52,53,107], and direct anti-fibrotic regulation of SMAD3 from lncRNA CRNDE [108].

Cell-specific studies utilizing ncRNAs are slowly increasing. The focus of ncRNA studies is on generating new anti-fibrotic drugs that target epigenetically TGF $\beta$  signaling in cardiac fibrosis. Post-transcriptional epigenetic regulation driven by ncRNAs exhibits extensive control over TGF $\beta$ , TGF $\beta$ RI, TGF $\beta$ RII and their canonical cytoplasmic mediators SMAD2/3/4 in cardiac fibroblasts. Interestingly, there are proteins such as MBNL1 [76,77] that act as a miRNA on TGF $\beta$ RII, whose action increases the post-transcriptional epigenetic regulation of TGF $\beta$  signaling. TGF $\beta$ -related epigenetic regulation in fibroblasts indicates that future studies will likely define new consolidated targets for controlling TGF $\beta$ -activated cardiac fibrosis.

In addition to defining new targets in cardiac fibrosis, there is a growing interest in finding reliable biomarkers knowing that dysregulation of the specific H3K27me3 HMT enhancer (EZH2) [27] in cardiac embryonic cells is a predisposing factor for pathological cardiac remodeling in the adult. TGF $\beta$ -related lncRNAs, such as MIAT [48,49] or Wisper [56,57] are emerging as biomarkers of myocardial infarction and cardiac fibrosis, respectively.

Although different epigenetic modifiers and biomarkers have been related to TGF $\beta$ , further studies describing epigenetics modifications of the canonical TGF $\beta$  cascade in fibroblasts would garner more interest in the field. The action of these modifications behind TGF $\beta$ -dependent fibrosis would highlight key sets of changes that will clearly influence cardiac epigenetics. The challenge of epigenetic editing in very well-defined specific cellular targets could open up promising therapeutic opportunities for the coming years.

## Disclosures

None.

## Acknowledgments

This work was supported by the Agencia Estatal de Investigación, Spain (RTI2018-095214-B-I00; and BIO2015-72124-EXP), and the IDIVAL InnVal 17/22, NextVal 18/11 Thanks to the University of Cantabria and the IDIVAL (UC-IDIVAL Fellows program; grant number PREVAL19/05: Maestro D and UC: Algeciras L) for financial support.

We thanks Andrina Chambers for her contribution to the text.

## References

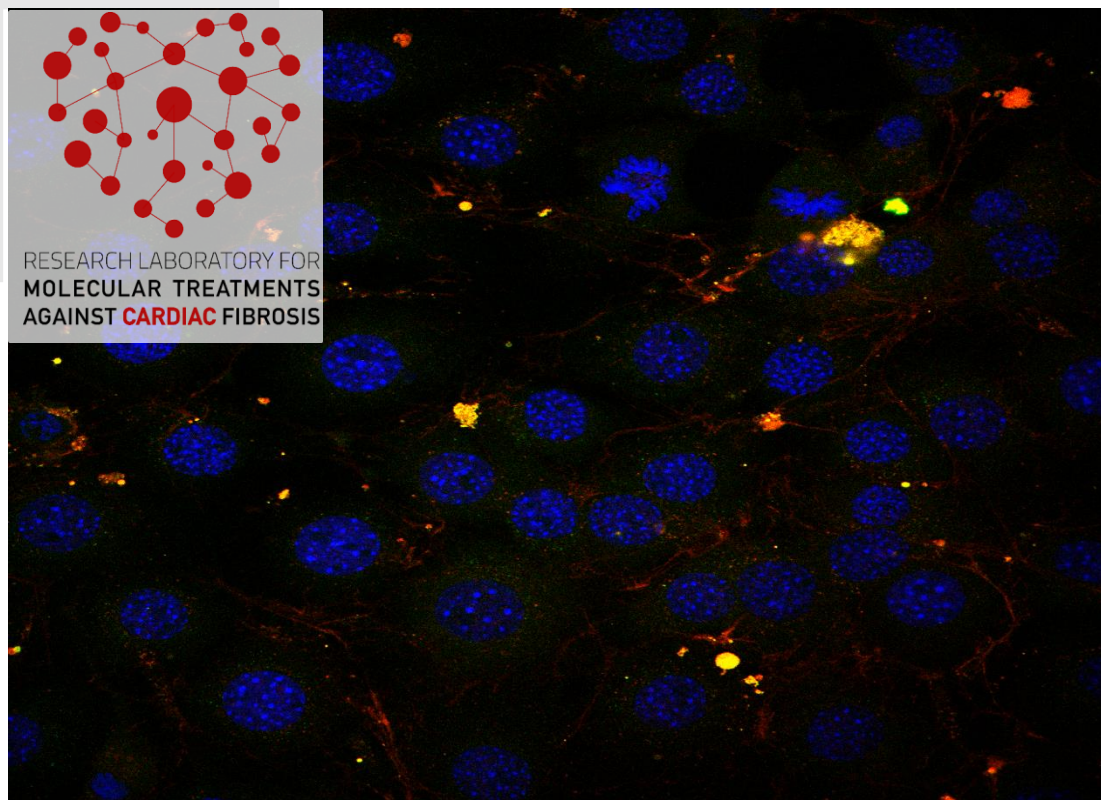
- [1] S. Hinderer, K. Schenke-Layland, Cardiac fibrosis - A short review of causes and therapeutic strategies, *Adv. Drug Deliv. Rev.* 146 (2019) 77–82.
- [2] N. Garamszegi, S.P. Garamszegi, P. Samavarchi-Tehrani, E. Walford, M. M. Schneiderbauer, J.L. Wrana, et al., Extracellular matrix-induced transforming growth factor-beta receptor signaling dynamics, *Oncogene*. 29 (2010) 2368–2380.
- [3] J. Massagué, S.W. Blain, R.S. Lo, TGFbeta signaling in growth control, cancer, and heritable disorders, *Cell*. 103 (2000) 295–309.
- [4] X. Xu, L. Zheng, Q. Yuan, G. Zhen, J.L. Crane, X. Zhou, et al., Transforming growth factor- $\beta$  in stem cells and tissue homeostasis, *Bone Res.* 6 (2018), 017–0005.
- [5] H.M. Arthur, S.D. Bamforth, TGF $\beta$  signaling and congenital heart disease: Insights from mouse studies, *Birth Defects Res A Clin Mol Teratol.* 91 (2011) 423–434.
- [6] T. Doetschman, J.V. Barnett, R.B. Runyan, T.D. Camenisch, R.L. Heimark, H. L. Granzier, et al., Transforming growth factor beta signaling in adult cardiovascular diseases and repair, *Cell Tissue Res.* 347 (2012) 203–223.
- [7] A.B. Roberts, Molecular and cell biology of TGF-beta, *Miner. Electrolyte Metab.* 24 (1998) 111–119.
- [8] M.B. Felisbino, T.A. McKinsey, Epigenetics in Cardiac Fibrosis: Emphasis on Inflammation and Fibroblast Activation, *JACC Basic Transl Sci.* 3 (2018) 704–715.
- [9] C. Lu, S. Sidoli, K. Kulej, K. Ross, C.H. Wu, B.A. Garcia, Coordination between TGF- $\beta$  cellular signaling and epigenetic regulation during epithelial to mesenchymal transition, *Epigenetics Chromatin* 12 (2019) 019–0256.
- [10] J. Ma, G. Sanchez-Duffhues, M.J. Goumans, P. Ten Dijke, TGF- $\beta$ -Induced Endothelial to Mesenchymal Transition in Disease and Tissue Engineering, *Front Cell Dev Biol.* 8 (2020).
- [11] J. Xu, S. Lamouille, R. Derynck, TGF-beta-induced epithelial to mesenchymal transition, *Cell Res.* 19 (2009) 156–172.
- [12] A.V. Sigel, M. Centrella, M. Eghbali-Webb, Regulation of proliferative response of cardiac fibroblasts by transforming growth factor-beta 1, *J. Mol. Cell. Cardiol.* 28 (1996) 1921–1929.
- [13] N. Cho, S.E. Razipour, M.L. McCain, Featured Article: TGF- $\beta$ 1 dominates extracellular matrix rigidity for inducing differentiation of human cardiac fibroblasts to myofibroblasts, *Exp. Biol. Med.* 243 (2018) 601–612.
- [14] F. Rizvi, R. Siddiqui, A. DeFranco, P. Homar, L. Emelyanova, E. Holmuhamedov, et al., Simvastatin reduces TGF- $\beta$ 1-induced SMAD2/3-dependent human ventricular fibroblasts differentiation: Role of protein phosphatase activation, *Int. J. Cardiol.* 270 (2018) 228–236.
- [15] R. Vivar, C. Humeres, C. Muñoz, P. Boza, S. Bolivar, F. Tapia, et al., FoxO1 mediates TGF-beta1-dependent cardiac myofibroblast differentiation, *Biochim. Biophys. Acta* 1 (2016) 128–138.
- [16] K. Tominaga, H.I. Suzuki, TGF- $\beta$  Signaling in Cellular Senescence and Aging-Related Pathology, *Int. J. Mol. Sci.* 20 (2019).
- [17] G. Sengle, R.N. Ono, T. Sasaki, L.Y. Sakai, Prodomains of transforming growth factor beta (TGFbeta) superfamily members specify different functions: extracellular matrix interactions and growth factor bioavailability, *J. Biol. Chem.* 286 (2011) 5087–5099.
- [18] I. Saif, Y. Kasmi, K. Allali, M.M. Ennaji, Prediction of DNA methylation in the promoter of gene suppressor tumor, *Gene*. 651 (2018) 166–173.
- [19] V. Grimaldi, M.R. De Pascale, A. Zullo, A. Soricelli, T. Infante, F.P. Mancini, et al., Evidence of epigenetic tags in cardiac fibrosis, *J. Cardiol.* 69 (2017) 401–408.
- [20] Y. He, S. Ling, Y. Sun, Z. Sheng, Z. Chen, X. Pan, et al., DNA methylation regulates  $\alpha$ -smooth muscle actin expression during cardiac fibroblast differentiation, *J. Cell. Physiol.* 234 (2019) 7174–7185.
- [21] X. Pan, Z. Chen, R. Huang, Y. Yao, G. Ma, Transforming growth factor  $\beta$ 1 induces the expression of collagen type I by DNA methylation in cardiac fibroblasts, *PLoS One* 8 (2013) 1.
- [22] J. Stenzig, Y. Schneeberger, A. Löser, B.S. Peters, A. Schaefer, R.R. Zhao, et al., Pharmacological inhibition of DNA methylation attenuates pressure overload-induced cardiac hypertrophy in rats, *J. Mol. Cell. Cardiol.* 120 (2018) 53–63.
- [23] A. Vujic, E.L. Robinson, M. Ito, S. Haider, M. Ackers-Johnson, K. See, et al., Experimental heart failure modelled by the cardiomyocyte-specific loss of an epigenome modifier, DNMT3B, *J. Mol. Cell. Cardiol.* 82 (2015) 174–183.
- [24] H. Tao, Z.Y. Song, X.S. Ding, J.J. Yang, K.H. Shi, J. Li, Epigenetic signatures in cardiac fibrosis, special emphasis on DNA methylation and histone modification, *Heart Fail. Rev.* 23 (2018) 789–799.
- [25] T. Zhang, S. Cooper, N. Brockdorff, The interplay of histone modifications - writers that read, *EMBO Rep.* 16 (2015) 1467–1481.
- [26] L. Yu, G. Yang, X. Weng, P. Liang, L. Li, J. Li, et al., Histone Methyltransferase SET1 Mediates Angiotensin II-Induced Endothelin-1 Transcription and Cardiac Hypertrophy in Mice, *Arterioscler. Thromb. Vasc. Biol.* 35 (2015) 1207–1217.
- [27] Q.J. Zhang, T.A.T. Tran, M. Wang, M.J. Ranek, K.M. Kokkonen-Simon, J. Gao, et al., Histone lysine dimethyl-demethylase KDM3A controls pathological cardiac hypertrophy and fibrosis, *Nat. Commun.* 9 (2018) 018–07173.
- [28] P. Delgado-Olguin, Y. Huang, X. Li, D. Christodoulou, C.E. Seidman, J. G. Seidman, et al., Epigenetic repression of cardiac progenitor gene expression by Ezh2 is required for postnatal cardiac homeostasis, *Nat. Genet.* 44 (2012) 343–347.
- [29] L.R. Filgueiras, S.L. Brandt, T.R. Ramalho, S. Jancar, C.H. Serezani, Imbalance between HDAC and HAT activities drives aberrant STAT1/MyD88 expression in macrophages from type 1 diabetic mice, *J. Diabetes Complicat.* 31 (2017) 334–339.
- [30] A.J. Bauer, K.A. Martin, Coordinating Regulation of Gene Expression in Cardiovascular Disease: Interactions between Chromatin Modifiers and Transcription Factors, *Front Cardiovasc Med.* 4 (2017).
- [31] I.V. Gregoretti, Y.M. Lee, H.V. Goodson, Molecular evolution of the histone deacetylase family: functional implications of phylogenetic analysis, *J. Mol. Biol.* 338 (2004) 17–31.
- [32] Y. Sixto-López, M. Bello, J. Correa-Basurto, Exploring the inhibitory activity of valproic acid against the HDAC family using an MMGBSA approach, *J. Comput. Aided Mol. Des.* 34 (2020) 857–878.
- [33] R.F. Li, S.S. Cao, W.J. Fang, Y. Song, X.T. Luo, H.Y. Wang, et al., Roles of HDAC2 and HDAC8 in cardiac remodeling in renovascular hypertensive rats and the effects of valproic acid sodium, *Pharmacology*. 99 (2017) 27–39.
- [34] J. Hu, T. Shen, J. Xie, S. Wang, Y. He, F. Zhu, Curcumin modulates covalent histone modification and TIMP1 gene activation to protect against vascular injury in a hypertension rat model, *Exp Ther Med.* 14 (2017) 5896–5902.

- [35] K.B. Schuetz, M.S. Stratton, W.W. Blakeslee, M.F. Wempe, F.F. Wagner, E. B. Holson, et al., Overlapping and divergent actions of structurally distinct histone deacetylase inhibitors in cardiac fibroblasts, *J. Pharmacol. Exp. Ther.* 361 (2017) 140–150.
- [36] Y. Zhang, F. Gao, Y. Tang, J. Xiao, C. Li, Y. Ouyang, et al., Valproic acid regulates Ang II-induced pericyte-myofibroblast trans-differentiation via MAPK/ERK pathway, *Am. J. Transl. Res.* 10 (2018) 1976–1989.
- [37] M. Sarikhani, S. Maity, S. Mishra, A. Jain, A.K. Tamta, V. Ravi, et al., SIRT2 deacetylase represses NFAT transcription factor to maintain cardiac homeostasis, *J. Biol. Chem.* 293 (2018) 5281–5294.
- [38] Y.H. Kao, J.P. Liou, C.C. Chung, G.S. Lien, C.C. Kuo, S.A. Chen, et al., Histone deacetylase inhibition improved cardiac functions with direct antifibrotic activity in heart failure, *Int. J. Cardiol.* 168 (2013) 4178–4183.
- [39] Q. Duan, S. McMahon, P. Anand, H. Shah, S. Thomas, H.T. Salunga, et al., BET bromodomain inhibition suppresses innate inflammatory and profibrotic transcriptional networks in heart failure, *Sci. Transl. Med.* 9 (2017).
- [40] M.S. Stratton, S.M. Haldar, T.A. McKinsey, BRD4 inhibition for the treatment of pathological organ fibrosis, *F1000 Res* 28 (2017). F1000-15.
- [41] M.S. Stratton, R.A. Bagchi, M.B. Felisbino, R.A. Hirsch, H.E. Smith, A.S. Riching, et al., Dynamic Chromatin Targeting of BRD4 Stimulates Cardiac Fibroblast Activation, *Circ. Res.* 125 (2019) 662–677.
- [42] P.J. Feingold, et al., The ENCODE (ENCyclopedia Of DNA Elements) Project, *Science.* 306 (2004) 636–640.
- [43] P. Zhang, W. Wu, Q. Chen, M. Chen, Non-Coding RNAs and their Integrated Networks, *J Integr Bioinform.* 16 (2019), 2019–0027.
- [44] J. Beaumont, B. López, N. Hermida, B. Schroen, G. San José, S. Heymans, et al., microRNA-122 down-regulation may play a role in severe myocardial fibrosis in human aortic stenosis through TGF- $\beta$ 1 up-regulation, *Clin. Sci.* 126 (2014) 497–506.
- [45] Y. Zhang, X.R. Huang, L.H. Wei, A.C. Chung, C.M. Yu, H.Y. Lan, miR-29b as a therapeutic agent for angiotensin II-induced cardiac fibrosis by targeting TGF- $\beta$ /Smad3 signaling, *Mol. Ther.* 22 (2014) 974–985.
- [46] R. García, A.B. Salido-Medina, A. Gil, D. Merino, J. Gómez, A.V. Villar, et al., Sex-specific regulation of miR-29b in the myocardium under pressure overload is associated with differential molecular, structural and functional remodeling patterns in mice and patients with aortic stenosis, *Cells.* 9 (2020).
- [47] G. Lyu, Y. Guan, C. Zhang, L. Zong, L. Sun, X. Huang, et al., TGF- $\beta$  signaling alters H4K20me3 status via miR-29 and contributes to cellular senescence and cardiac aging, *Nat. Commun.* 9 (2018), 018–04994.
- [48] R. Ma, X. He, X. Zhu, S. Pang, B. Yan, Promoter polymorphisms in the lncRNA-MIAT gene associated with acute myocardial infarction in Chinese Han population: a case-control study, *Biosci. Rep.* 40 (2020).
- [49] X. Qu, Y. Du, Y. Shu, M. Gao, F. Sun, S. Luo, et al., MIAT is a pro-fibrotic long non-coding RNA governing cardiac fibrosis in Post-infarct myocardium, *Sci. Rep.* 7 (2017).
- [50] C.M. Dubois, M.H. Laprise, F. Blanchette, L.E. Gentry, R. Leduc, Processing of transforming growth factor beta 1 precursor by human furin convertase, *J. Biol. Chem.* 270 (1995) 10618–10624.
- [51] J. Wang, W. Huang, R. Xu, Y. Nie, X. Cao, J. Meng, et al., MicroRNA-24 regulates cardiac fibrosis after myocardial infarction, *J. Cell. Mol. Med.* 16 (2012) 2150–2160.
- [52] G. Arun, D. Aggarwal, D.L. Spector, MALAT1 long non-coding RNA: functional implications, *Noncoding RNA.* 6 (2020).
- [53] S. Huang, L. Zhang, J. Song, Z. Wang, X. Huang, Z. Guo, et al., Long noncoding RNA MALAT1 mediates cardiac fibrosis in experimental postinfarct myocardium mice model, *J. Cell. Physiol.* 234 (2019) 2997–3006.
- [54] D. Jeong, M.A. Lee, Y. Li, D.K. Yang, C. Kho, J.G. Oh, et al., Matricellular protein CCN5 reverses established cardiac fibrosis, *J. Am. Coll. Cardiol.* 67 (2016) 1556–1568.
- [55] A. Huang, H. Li, C. Zeng, W. Chen, L. Wei, Y. Liu, et al., Endogenous CCN5 participates in angiotensin II/TGF- $\beta$ (1) networking of cardiac fibrosis in high angiotensin II-induced hypertensive heart failure, *Front. Pharmacol.* 11 (2020).
- [56] R. Micheletti, I. Plaisance, B.J. Abraham, A. Sarre, C.C. Ting, M. Alexanian, et al., The long noncoding RNA Wisper controls cardiac fibrosis and remodeling, *Sci. Transl. Med.* 9 (2017).
- [57] H.N. Yeowell, L.C. Walker, D.M. Mauger, P. Seth, M.A. Garcia-Blanco, TIA nuclear proteins regulate the alternate splicing of lysyl hydroxylase 2, *J Invest Dermatol.* 129 (2009) 1402–1411.
- [58] B. Zhou, J.W. Yu, A novel identified circular RNA, circRNA\_010567, promotes myocardial fibrosis via suppressing miR-141 by targeting TGF- $\beta$ 1, *Biochem. Biophys. Res. Commun.* 487 (2017) 769–775.
- [59] R. Derynck, TGF-beta-receptor-mediated signaling, *Trends Biochem. Sci.* 19 (1994) 548–553.
- [60] P. ten Dijke, K. Miyazono, C.H. Heldin, Signaling via hetero-oligomeric complexes of type I and type II serine/threonine kinase receptors, *Curr. Opin. Cell Biol.* 8 (1996) 139–145.
- [61] S. Song, L. Liu, Y. Yu, R. Zhang, Y. Li, W. Cao, et al., Inhibition of BRD4 attenuates transverse aortic constriction- and TGF- $\beta$ -induced endothelial-mesenchymal transition and cardiac fibrosis, *J. Mol. Cell. Cardiol.* 127 (2019) 83–96.
- [62] P.Y. Chen, L. Qin, C. Barnes, K. Charisse, T. Yi, X. Zhang, et al., FGF regulates TGF- $\beta$  signaling and endothelial-to-mesenchymal transition via control of let-7 miRNA expression, *Cell Rep.* 2 (2012) 1684–1696.
- [63] Y. Hong, H. Cao, Q. Wang, J. Ye, L. Sui, J. Feng, et al., MiR-22 may suppress fibrogenesis by targeting TGF $\beta$ R I in cardiac fibroblasts, *Cell. Physiol. Biochem.* 40 (2016) 1345–1353.
- [64] H.H. Seo, S. Lee, C.Y. Lee, J. Lee, S. Shin, B.W. Song, et al., Multipoint targeting of TGF- $\beta$ /Wnt transactivation circuit with microRNA 384-5p for cardiac fibrosis, *Cell Death Differ.* 26 (2019) 1107–1123.
- [65] X. Zhao, K. Wang, Y. Liao, Q. Zeng, Y. Li, F. Hu, et al., MicroRNA-101a inhibits cardiac fibrosis induced by hypoxia via targeting TGF $\beta$ R1 on cardiac fibroblasts, *Cell. Physiol. Biochem.* 35 (2015) 213–226.
- [66] R. Cheng, R. Dang, Y. Zhou, M. Ding, H. Hua, MicroRNA-98 inhibits TGF- $\beta$ 1-induced differentiation and collagen production of cardiac fibroblasts by targeting TGFBR1, *Hum. Cell* 30 (2017) 192–200.
- [67] L. Wang, P. Jiang, Y. He, H. Hu, Y. Guo, X. Liu, et al., A novel mechanism of Smads/miR-675/TGF $\beta$ R1 axis modulating the proliferation and remodeling of mouse cardiac fibroblasts, *J. Cell. Physiol.* 234 (2019) 20275–20285.
- [68] H. Liang, Z. Pan, X. Zhao, L. Liu, J. Sun, X. Su, et al., lncRNA PFL contributes to cardiac fibrosis by acting as a competing endogenous RNA of let-7d, *Theranostics.* 8 (2018) 1180–1194.
- [69] G. Montrucchio, G. Alloati, G. Camussi, Role of platelet-activating factor in cardiovascular pathophysiology, *Physiol. Rev.* 80 (2000) 1669–1699.
- [70] W.Y. Wei, Q. Zhao, W.Z. Zhang, M.J. Wang, Y. Li, S.Z. Wang, et al., Secreted frizzled-related protein 2 prevents pressure-overload-induced cardiac hypertrophy by targeting the Wnt/ $\beta$ -catenin pathway, *Mol. Cell. Biochem.* 472 (2020) 241–251.
- [71] F. Yousefi, Z. Shabaninejad, S. Vakili, M. Derakhshan, A. Movahedpour, H. Dabiri, et al., TGF- $\beta$  and WNT signaling pathways in cardiac fibrosis: non-coding RNAs come into focus, *Cell Commun Signal.* 18 (2020) 020–00555.
- [72] Z. Pan, X. Sun, H. Shan, N. Wang, J. Wang, J. Ren, et al., MicroRNA-101 inhibited postinfarct cardiac fibrosis and improved left ventricular compliance via the FBJ osteosarcoma oncogene/transforming growth factor- $\beta$ 1 pathway, *Circulation.* 126 (2012) 840–850.
- [73] A.J. Tjissen, I. van der Made, M.M. van den Hoogenhof, W.J. Wijnen, E.D. van Deel, N.E. de Groot, et al., The microRNA-15 family inhibits the TGF $\beta$ -pathway in the heart, *Cardiovasc. Res.* 104 (2014) 61–71.
- [74] J. Li, Y. Dai, Z. Su, G. Wei, MicroRNA-9 inhibits high glucose-induced proliferation, differentiation and collagen accumulation of cardiac fibroblasts by down-regulation of TGFBR2, *Biosci. Rep.* 36 (2016).
- [75] M. Zou, F. Wang, R. Gao, J. Wu, Y. Ou, X. Chen, et al., Autophagy inhibition of hsa-miR-19a-3p/19b-3p by targeting TGF- $\beta$  R II during TGF- $\beta$ 1-induced fibrogenesis in human cardiac fibroblasts, *Sci. Rep.* 6 (2016).
- [76] J. Davis, N. Salomonis, N. Ghearing, S.C. Lin, J.Q. Kwong, A. Mohan, et al., MBNL1-mediated regulation of differentiation RNAs promotes myofibroblast transformation and the fibrotic response, *Nat. Commun.* 6 (2015).
- [77] Y. Xu, C. Liang, Y. Luo, T. Zhang, MBNL1 regulates isoproterenol-induced myocardial remodeling in vitro and in vivo, *J. Cell. Mol. Med.* 25 (2021) 1100–1115.
- [78] A.C. Correia, J.R. Moonen, M.G. Brinker, G. Krenning, FGF2 inhibits endothelial-mesenchymal transition through microRNA-20a-mediated repression of canonical TGF- $\beta$  signaling, *J. Cell Sci.* 129 (2016) 569–579.
- [79] T. Tsukazaki, T.A. Chiang, A.F. Davison, L. Attisano, J.L. Wrana, SARA, a FYVE domain protein that recruits Smad2 to the TGFbeta receptor, *Cell.* 95 (1998) 779–791.
- [80] O. Eickelberg, M. Centrella, M. Reiss, M. Kashgarian, R.G. Wells, Betaglycan inhibits TGF-beta signaling by preventing type I-type II receptor complex formation. Glycosaminoglycan modifications alter betaglycan function, *J. Biol. Chem.* 277 (2002) 823–829.
- [81] W. Du, H. Liang, X. Gao, X. Li, Y. Zhang, Z. Pan, et al., MicroRNA-328, a potential anti-fibrotic target in cardiac interstitial fibrosis, *Cell. Physiol. Biochem.* 39 (2016) 827–836.
- [82] H. Liang, C. Zhang, T. Ban, Y. Liu, L. Mei, X. Piao, et al., A novel reciprocal loop between microRNA-21 and TGF $\beta$ RIII is involved in cardiac fibrosis, *Int. J. Biochem. Cell Biol.* 44 (2012) 2152–2160.
- [83] D.T. Dudley, L. Pang, S.J. Decker, A.J. Bridges, A.R. Saltiel, A synthetic inhibitor of the mitogen-activated protein kinase cascade, *Proc. Natl. Acad. Sci. U. S. A.* 92 (1995) 7686–7689.
- [84] G. Pagès, P. Lenormand, G. L'Allemain, J.C. Chambard, S. Meloche, J. Pouységur, Mitogen-activated protein kinases p42mapk and p44mapk are required for fibroblast proliferation, *Proc. Natl. Acad. Sci. U. S. A.* 90 (1993) 8319–8323.
- [85] M. Cheng, G. Wu, Y. Song, L. Wang, L. Tu, L. Zhang, et al., Celastrol-induced suppression of the MiR-21/ERK signalling pathway attenuates cardiac fibrosis and dysfunction, *Cell. Physiol. Biochem.* 38 (2016) 1928–1938.
- [86] T. Thum, C. Gross, J. Fiedler, T. Fischer, S. Kissler, M. Bussen, et al., MicroRNA-21 contributes to myocardial disease by stimulating MAP kinase signalling in fibroblasts, *Nature.* 456 (2008) 980–984.
- [87] S. Roy, S. Khanna, S.R. Hussain, S. Biswas, A. Azad, C. Rink, et al., MicroRNA expression in response to murine myocardial infarction: miR-21 regulates fibroblast metalloprotease-2 via phosphatase and tensin homologue, *Cardiovasc. Res.* 82 (2009) 21–29.
- [88] J. Massagué, TGF-beta signal transduction, *Annu. Rev. Biochem.* 67 (1998) 753–791.
- [89] J. Massagué, TGF $\beta$  signalling in context, *Nat. Rev. Mol. Cell Biol.* 13 (2012) 616–630.
- [90] H. Khalil, O. Kanisicak, V. Prasad, R.N. Correll, X. Fu, T. Schips, et al., Fibroblast-specific TGF- $\beta$ -Smad2/3 signaling underlies cardiac fibrosis, *J. Clin. Invest.* 127 (2017) 3770–3783.
- [91] J. Yang, B. Wang, N. Li, Q. Zhou, W. Zhou, Z. Zhan, Salvia miltiorrhiza and carthamus tinctorius extract prevents cardiac fibrosis and dysfunction after



- myocardial infarction by epigenetically inhibiting Smad3 expression, *Evid. Based Complement. Alternat. Med.* 30 (2019).
- [92] D.S. Jiang, X. Yi, R. Li, Y.S. Su, J. Wang, M.L. Chen, et al., The histone methyltransferase mixed lineage leukemia (MLL) 3 may play a potential role on clinical dilated cardiomyopathy, *Mol. Med.* 23 (2017) 196–203.
- [93] A. Bugyei-Twum, C. Ford, R. Civitarese, J. Seegobin, S.L. Advani, J.F. Desjardins, et al., Sirtuin 1 activation attenuates cardiac fibrosis in a rodent pressure overload model by modifying Smad2/3 transactivation, *Cardiovasc. Res.* 114 (2018) 1629–1641.
- [94] S. Maity, J. Muhamed, M. Sarikhani, S. Kumar, F. Ahamed, K.M. Spurthi, et al., Sirtuin 6 deficiency transcriptionally up-regulates TGF- $\beta$  signaling and induces fibrosis in mice, *J. Biol. Chem.* 295 (2020) 415–434.
- [95] T.K. Sin, A.P. Yu, B.Y. Yung, S.P. Yip, L.W. Chan, C.S. Wong, et al., Modulating effect of SIRT1 activation induced by resveratrol on Foxo1-associated apoptotic signalling in senescent heart, *J. Physiol.* 592 (2014) 2535–2548.
- [96] M.S. Stratton, T.A. McKinsey, Epigenetic regulation of cardiac fibrosis, *J. Mol. Cell. Cardiol.* 92 (2016) 206–213.
- [97] T. Chen, J. Li, J. Liu, N. Li, S. Wang, H. Liu, et al., Activation of SIRT3 by resveratrol ameliorates cardiac fibrosis and improves cardiac function via the TGF- $\beta$ /Smad3 pathway, *Am. J. Physiol. Heart Circ. Physiol.* 308 (2015) 19.
- [98] A.K. Ghosh, S.E. Quaggin, D.E. Vaughan, Molecular basis of organ fibrosis: potential therapeutic approaches, *Exp. Biol. Med.* 238 (2013) 461–481.
- [99] K. Tian, Z. Liu, J. Wang, S. Xu, T. You, P. Liu, Sirtuin-6 inhibits cardiac fibroblasts differentiation into myofibroblasts via inactivation of nuclear factor  $\kappa$ B signaling, *Transl. Res.* 165 (2015) 374–386.
- [100] W. He, H. Huang, Q. Xie, Z. Wang, Y. Fan, B. Kong, et al., MiR-155 knockout in fibroblasts improves cardiac remodeling by targeting tumor protein p53-inducible nuclear protein 1, *J. Cardiovasc. Pharmacol. Ther.* 21 (2016) 423–435.
- [101] C. Wang, C. Zhang, L. Liu, B. Chen, Y. Li, et al., Macrophage-derived mir-155-containing exosomes suppress fibroblast proliferation and promote fibroblast inflammation during cardiac injury, *Mol. Ther.* 25 (2017) 192–204.
- [102] Y. Wei, X. Yan, L. Yan, F. Hu, W. Ma, Y. Wang, et al., Inhibition of microRNA-155 ameliorates cardiac fibrosis in the process of angiotensin II-induced cardiac remodeling, *Mol. Med. Rep.* 16 (2017) 7287–7296.
- [103] D. Zhang, Y. Cui, B. Li, X. Luo, Y. Tang, miR-155 regulates high glucose-induced cardiac fibrosis via the TGF- $\beta$  signaling pathway, *Mol. Biosyst.* 13 (2016) 215–224.
- [104] L. Tao, Y. Bei, P. Chen, Z. Lei, S. Fu, H. Zhang, et al., Crucial Role of miR-433 in regulating cardiac fibrosis, *Theranostics.* 6 (2016) 2068–2083.
- [105] N. Akbari Dilmaghani, H. Shoori, G. Sharifi, M. Mohaqiq, J. Majidpoor, M. E. Dinger, et al., Non-coding RNAs modulate function of extracellular matrix proteins, *Biomed. Pharmacother.* 136 (2021) 19.
- [106] Y. Zhu, W. Pan, T. Yang, X. Meng, Z. Jiang, L. Tao, et al., Upregulation of circular RNA CircNFIB attenuates cardiac fibrosis by sponging miR-433, *Front. Genet.* 10 (2019).
- [107] Y. Xiang, Y. Zhang, Y. Tang, Q. Li, MALAT1 modulates TGF- $\beta$ 1-induced endothelial-to-mesenchymal transition through downregulation of miR-145, *Cell. Physiol. Biochem.* 42 (2017) 357–372.
- [108] D. Zheng, Y. Zhang, Y. Hu, J. Guan, L. Xu, W. Xiao, et al., Long noncoding RNA Crnde attenuates cardiac fibrosis via Smad3-Crnde negative feedback in diabetic cardiomyopathy, *FEBS J.* 286 (2019) 1645–1655.
- [109] D.H. Yasui, S. Peddada, M.C. Bieda, R.O. Vallero, A. Hogart, R.P. Nagarajan, et al., Integrated epigenomic analyses of neuronal MeCP2 reveal a role for long-range interaction with active genes, *Proc. Natl. Acad. Sci. U. S. A.* 104 (2007) 19416–19421.
- [110] X. Li, Y. Yang, S. Chen, J. Zhou, J. Li, Y. Cheng, Epigenetics-based therapeutics for myocardial fibrosis, *Life Sci.* 271 (2021) 9.
- [111] H. Tao, P. Shi, X.D. Zhao, H.Y. Xuan, X.S. Ding, MeCP2 inactivation of LncRNA GAS5 triggers cardiac fibroblasts activation in cardiac fibrosis, *Cell. Signal.* 74 (2020) 4.
- [112] R. Rai, T. Sun, V. Ramirez, E. Lux, M. Eren, D.E. Vaughan, et al., Acetyltransferase p300 inhibitor reverses hypertension-induced cardiac fibrosis, *J. Cell. Mol. Med.* 23 (2019) 3026–3031.
- [113] R. Janknecht, N.J. Wells, T. Hunter, TGF- $\beta$ -stimulated cooperation of smad proteins with the coactivators CBP/p300, *Genes Dev.* 12 (1998) 2114–2119.
- [114] P. Qiu, R.P. Ritchie, X.Q. Gong, Y. Hamamori, L. Li, Dynamic changes in chromatin acetylation and the expression of histone acetyltransferases and histone deacetylases regulate the SM22 $\alpha$  transcription in response to Smad3-mediated TGF $\beta$ 1 signaling, *Biochem. Biophys. Res. Commun.* 348 (2006) 351–358.
- [115] R. Rai, S.K. Verma, D. Kim, V. Ramirez, E. Lux, C. Li, et al., A novel acetyltransferase p300 inhibitor ameliorates hypertension-associated cardio-renal fibrosis, *Epigenetics.* 12 (2017) 1004–1013.
- [116] A.C. Tecalco-Cruz, D.G. Ríos-López, G. Vázquez-Victorio, R.E. Rosales-Alvarez, M. Macías-Silva, Transcriptional cofactors Ski and SnoN are major regulators of the TGF- $\beta$ /Smad signaling pathway in health and disease, *Signal Transduct Target Ther.* 3 (2018), 018–0015.
- [117] R.H. Cunnington, J.M. Northcott, S. Ghavami, K.L. Filomeno, F. Jahan, M. S. Kavosh, et al., The Ski-Zeb2-Meox2 pathway provides a novel mechanism for regulation of the cardiac myofibroblast phenotype, *J. Cell Sci.* 127 (2014) 40–49.
- [118] R.H. Cunnington, B. Wang, S. Ghavami, K.L. Bathe, S.G. Rattan, I.M. Dixon, Antifibrotic properties of c-Ski and its regulation of cardiac myofibroblast phenotype and contractility, *Am. J. Phys. Cell Phys.* 300 (2011) 13.
- [119] J. Wang, L. Guo, D. Shen, X. Xu, S. Han, W. He, The Role of c-SKI in regulation of TGF $\beta$ -induced human cardiac fibroblast proliferation and ECM protein expression, *J. Cell. Biochem.* 118 (2017) 1911–1920.
- [120] M.R. Zeglinski, J.J. Davies, S. Ghavami, S.G. Rattan, A.J. Halayko, I.M. Dixon, Chronic expression of Ski induces apoptosis and represses autophagy in cardiac myofibroblasts, *Biochim. Biophys. Acta* 6 (2016) 31.
- [121] R. Kishore, S.K. Verma, A.R. Mackie, E.E. Vaughan, T.V. Abramova, I. Aiko, et al., Bone marrow progenitor cell therapy-mediated paracrine regulation of cardiac miRNA-155 modulates fibrotic response in diabetic hearts, *PLoS One* 8 (2013) 1.
- [122] S. Teichler, T. Illmer, J. Roemhild, D. Ovcharenko, T. Stiewe, A. Neubauer, MicroRNA29a regulates the expression of the nuclear oncogene Ski, *Blood.* 118 (2011) 1899–1902.
- [123] J. Wang, W. He, X. Xu, L. Guo, Y. Zhang, S. Han, et al., The mechanism of TGF- $\beta$ /miR-155/c-Ski regulates endothelial-mesenchymal transition in human coronary artery endothelial cells, *Biosci. Rep.* 37 (2017) 31.
- [124] J. Li, L. Zhao, X. He, T. Yang, K. Yang, MiR-21 inhibits c-Ski signaling to promote the proliferation of rat vascular smooth muscle cells, *Cell. Signal.* 26 (2014) 724–729.
- [125] Y. Huang, Y. Qi, J.Q. Du, D.F. Zhang, MicroRNA-34a regulates cardiac fibrosis after myocardial infarction by targeting Smad4, *Expert Opin. Ther. Targets* 18 (2014) 1355–1365.
- [126] B.C. Bernardo, X.M. Gao, C.E. Winbanks, E.J. Boey, Y.K. Tham, H. Kiriazis, et al., Therapeutic inhibition of the miR-34 family attenuates pathological cardiac remodeling and improves heart function, *Proc. Natl. Acad. Sci. U. S. A.* 109 (2012) 17615–17620.
- [127] M. Yamakuchi, MicroRNA Regulation of SIRT1, *Front. Physiol.* 3 (2012).
- [128] A.C. Poncelet, H.W. Schnaper, Sp1 and Smad proteins cooperate to mediate transforming growth factor-beta 1-induced alpha 2(I) collagen expression in human glomerular mesangial cells, *J. Biol. Chem.* 276 (2001) 6983–6992.
- [129] F. Cao, Z. Li, W.M. Ding, L. Yan, Q.Y. Zhao, LncRNA PVT1 regulates atrial fibrosis via miR-128-3p-SP1-TGF- $\beta$ 1-Smad axis in atrial fibrillation, *Mol. Med.* 25 (2019) 019–0074.





La tesis aquí escrita pretende abordar el estudio de la fibrosis cardíaca patológica, con el objetivo de esclarecer y contribuir al desarrollo de nuevas aproximaciones a su tratamiento. Los medios para alcanzar estos objetivos se basan en la utilización de nanomateriales dirigidos por proteínas como herramienta teragnóstica, así como la implementación de un sistema de expresión genética dirigido. Como rasgo distintivo de este estudio, se establecerá un sistema de investigación traslacional, mediante la utilización y evolución de los sistemas utilizados en el trabajo, con el claro objetivo final, de que el trabajo aquí presentado pueda ser utilizado para futuras investigaciones.

This thesis aims to address the study of pathological cardiac fibrosis, with the objective of clarifying and contributing to the development of new approaches to its treatment. The means to achieve these objectives are based on the use of protein-targeted nanomaterials as a theragnostic tool, as well as the implementation of a targeted gene expression system. As a distinctive feature of this study, a translational research system will be established through the use and evolution of the systems used in the work, with the clear final objective that the work presented here can be used for future research.